SYNTHESIS AND EVALUATION OF METAL-SILICA CORE-SHELL NANOMATERIALS FOR CATALYSIS

by

Lu Zhang Whaley

B.S. in Chemical Engineering, South China University of Technology, 2005

M.S. in Chemical Engineering, University of North Dakota, 2007

Submitted to the Graduate Faculty of

Swanson School of Engineering in partial fulfillment

of the requirements for the degree of

Doctor of Philosophy

University of Pittsburgh

2011

UNIVERSITY OF PITTSBURGH

SWANSON SCHOOL OF ENGINEERING

This dissertation was presented

by

Lu Zhang Whaley

It was defended on

August 19th, 2011

and approved by

Robert M. Enick, Ph.D., Professor, Department of Chemical and Petroleum Engineering

Joseph J. McCarthy, Ph.D., Professor, Department of Chemical and Petroleum Engineering

Rongchao Jin, Ph.D., Professor, Department of Chemistry, Carnegie Mellon University

Dissertation Director: Götz Veser, Ph.D., Professor, Department of Chemical and Petroleum Engineering

SYNTHESIS AND EVALUATION OF METAL-SILICA CORE-SHELL NANOMATERIALS FOR CATALYSIS

Lu Zhang Whaley, Ph.D.

University of Pittsburgh, 2011

Nanocatalysts have drawn considerable interest because of their high selectivity and reactivity compared with conventional catalysts. However, the catalyst deactivation due to the sintering under moderate/high temperature operation and coke formation in hydrocarbon participating systems poses a challenge for their usage. Our work focuses on solving the above issues by designing and developing a series of metal core silica shell materials. The fundamental understanding of core shell materials is facilitated by systematic investigation via synthesis, characterization (XRD, TEM, BET, EDX) and catalytic tests (CO oxidation, ethylene hydrogenation, CO methanation and catalytic partial oxidation of methane).

The synthesis and post-treatment methods for this newly developed core shell material are optimized and standardized. We demonstrate fine control over the key structural elements of nickel core silica shell material. Two different nickel core silica shell structures are obtained with the distinction of a pronounced cavity in the core. The synthesis route is not limited to nickel particles, but also applied for a range of other metals (e.g. Cu, Co, Pd). The pore size of silica shell is around ~1nm independent of the shell thickness and structure difference. The thermal stability of nickel particles as a function of particle size as well as silica support is thoroughly studied. The nickel particles in core shell materials are stabilized under 5nm up to 1000°C with the comparison of strong sintering of unprotected nickel particles beyond 10nm as low as 500°C. The stable core shell material not only shows its advantage for stable operation under high

temperature reactive condition (>800°C), but also possesses the highly coking resistant property in fuel participating reactions. Even though the presence of silica shell is beneficial for improving stability of nickel particles, it brings up significant mass transfer limitation when shell thickness is beyond 10nm.

We not only demonstrate the capability to synthesize the well controlled nanocatalysts with high temperature stability and minimal mass transfer limitation, but also understand the structure correlated reactivity in several reaction systems. Additionally, we highlight the correlation between sintering, mass transfer and coking properties of the catalysts.

TABLE OF CONTENTS

LIST OF TABLES

LIST OF FIGURES

ACKNOWLEDGMENTS

First and foremost I would like to thank Dr. Veser for his help in transforming me from a student to a researcher. Your knowledge and guidance throughout my time at the University of Pittsburgh will help shape my professional life. The foundation you have laid will give me the ability to go into the workforce with a solid scientific background and proficient work habits. It has been a pleasure to grow and learn in your research group.

Thank you to all of my past and present lab mates. We spent many long hours in the lab together and my time spent with you will stand as some of my fondest memories at Pitt. Rongwen, Anmin, Yanan, Rahul and Yi learning from your experience and passion has made me a stronger researcher. Shuang, Michelle, Sen and Saurabh growing and learning with you has been an experience I will always cherish.

Thank you to the staff of the Chemical Engineering, Mechanical Engineering and Materials Science departments at Pitt, especially Al Stewart and Cole Van Ormer. The technical training I received and useful discussions we shared were a great benefit.

Thank you to the Department of Energy for giving us the funding to explore this project.

Finally, I would like to say thank you to my parents and Zach. Without your support and encouragement I would never had made it through this process. I love you and will always work hard and do my best to make you proud.

1.0 INTRODUCTION AND PROJECT SCOPE

1.1 NANOMATERIALS AND NANOCATALYSTS

Nanomaterials, which have characteristic dimensions below 100nm, have gained increasing attention because of their novel and improved reactivity, strength, optical characteristics, electrical and mechanical properties. They are applied in a wide range of areas, including cosmetics, coatings, hard cutting tools, displays, information storage, biosensors, drug delivery, medical imaging, fuel cells and catalysts [1-8]. The main reason that nanocatalysts are more effective than conventional catalysts is their high reactivity and selectivity due to the presence of under-coordinated atoms for structure sensitive reactions [1, 9, 10]. Another reason is the high surface area-to-volume ratio, which improves the efficiency of the material usage since the number of active sites per gram metal to active components is significantly increased. The global market for nanocatalysts is projected to reach $6 billion by 2015, which is almost twice as much as 2003 [11]. The largest end user of nanocatalysts is petrochemical industry, followed by chemicals/pharmaceuticals, food processing and environmental remediation [12]. The main challenges for the application of nanocatalysts are the decreased reactivity due to mass transfer limitation and deactivation due to poor thermal stability and coking in high temperature fuel processing environment.

1.2 LIMITATIONS OF NANOCATALYSTS

1.2.1 Thermal stability

Thermal stability is a major concern for catalysts, especially for high temperature processing in the petrochemical industry. Even though smaller particles are desired for high reactivity, they sinter more easily than larger particles. The low stability of small particles is not only because of a thermodynamic driving force to minimize surface energy [13, 14], but also because of a melting point depression in which the melting point of nanoparticles is hundreds of degrees lower than the corresponding bulk material [15]. The reduction in the active surface area due to sintering will result in decreased reactivity. One of the solutions to enhance the stability of the metal particles is to cap or embed nanoparticles in ceramic matrix. Our group has used BHA (Barium Hexa-aluminate) as a stabilizing matrix for metal nanoparticles at high temperatures [16]. 10nm platinum particles are stabilized by the BHA matrix via a microemulsion template sol-gel method (Figure 1-a). The platinum particle size is under 5nm before 600°C. Increasing temperature makes the metal particles mobile and grow. The particles stop growing around 10-15nm between 700°C and 1000°C due to a "caging effect" of the BHA support (Figure 1-b). This "caging effect" occurs because the pore neck of the BHA limits the growth of the metal particles (Figure 1-c). The size of metal particles determined from the TEM images agrees with the pore size distribution of the support from the BET measurements (Figure 1-d), which verifies that the pore neck structure of the BHA support stabilizes the metal particles at the high temperature. Even though the BHA matrix is able to limit the growth of particles to some extent, the platinum particle size still has a significant increase from 5nm to 15nm.

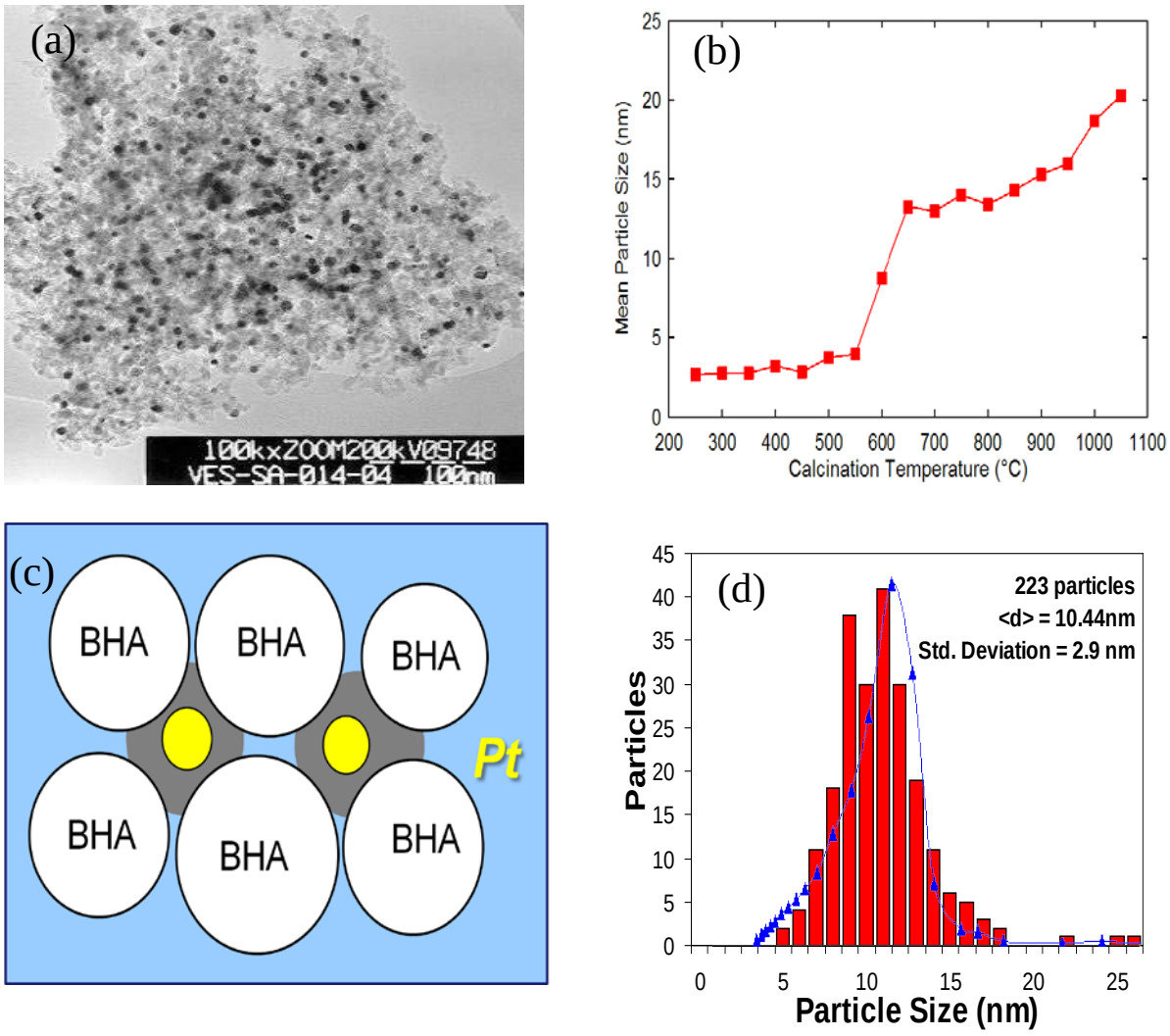

Figure 1: (*a) TEM of Pt-BHA;(b) Nickel particle sizes with increasing calcination temperatures; (c) The scheme of "caging effect";(d) The agreement of pore size distribution of BHA and platinum particle size [17]*

Another solution for stabilizing nanoparticles is to coat metal particles with an inert and stable ceramic support (e.g. silica, ZrO_2). For instance, silica-coated Rh catalysts have been shown to be much more stable compared with materials prepared via sol-gel method and impregnation method [18]. Not only does the coated Rh show minimal particle size increase after thermal treatment in air at 900°C for 12 hours, but it also has the highest BET surface area before and after calcination among these materials. Hence, a decreased activity of Rh supported silica

catalysts after thermal treatment was observed in NO-CO reaction with the exception of silica-coated Rh, which showed high sintering resistance [18]. Another example is silica coated Fe_3O_4 with 15.5 ± 2.0nm cores and 4.5 ± 1.0nm shells. The material maintains its structure (i.e. unchanged Fe_3O_4 particle size) after calcination at 700°C for 6 hours in air, while a decreased micropore volume and BET surface area is observed. The prolonged stability through cyclic redox with CH_4 and O_2 is also demonstrated [19]. Park et al. compared the thermal stability of silica-coated Pd (Pd@SiO_2) and impregnated Pd/SiO_2 material with comparable Pd particle sizes of 2-4nm. A decreased activity of Pd/SiO_2 after the thermal treatment at 700°C for 6 hours in air was also observed in CO oxidation as well as in acetylene hydrogenation in contrast with a minimal reactivity decrease in Pd@SiO_2 [20]. Joo et al. reported that Pt@SiO_2 (14nm core @17 nm shell) particles with 2.3nm pore size were thermally stable at high temperature for ethylene hydrogenation and CO oxidation [21]. They stressed an interesting observation that after 750°C calcination some silica particles possess larger Pt cores or multiple Pt cores while some form Pt-free cavity structure, which indicates that Pt particles diffuse through the mesoporous silica shell to the neighboring Pt@SiO_2 particles [21]. The Schüth group reported the ~15-17nm Au coated zirconia (Au@ZrO_2) shows exceptional stability compared with Au impregnated on zirconia (Au/ZrO_2). The reactivity of Au@ZrO_2 after thermal treatment at 800°C is exactly the same as the fresh samples, while there is a significant decrease in reactivity for Au/ZrO_2 due to sintering [22, 23]. Figure 2 shows some examples of these metal core silica shell materials.

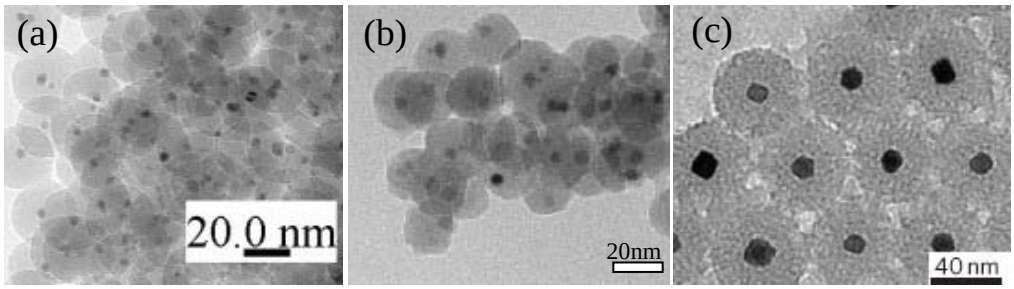

Figure 2: *Selected examples of metal-cores silica-shell materials (a) Rh@SiO_2 [18] (b) Pd@SiO_2 [20] (c) Pt@SiO_2 [21]*

1.2.2 Mass transfer limitation

A novel, stable catalyst is not only required to maintain its catalytic activity after high-temperature treatment, it should also present no substantial mass transfer resistance. However, the active sites of some nanocatalysts are located within torturous nanosized pores, which will result in significant internal transport limitations. The core shell material, which is a promising candidate as a high temperature stable nanocatalyst, brings up concern for the presence of mass transfer limitation due to the formation of the silica shell. A few researchers have mentioned the potential existence of mass transfer between reactants and active sites in core shell type nanomaterials [20, 22, 23], but this has never been systematically investigated. It was claimed that there is no mass transfer resistance in Au@ZrO_2 core shell materials with 20nm shell thickness and 3-4nm pore size [22]. However, there is no experimental data supporting the absence of mass transfer limitation. Hori et al. observed selective mass transfer limitations of hydrocarbons (methane, ethane, etc) for combustion in Pt core silica shells with less than 1nm pore size and 12nm shell thickness, which is the thinnest shell among all synthesized core shell material to-date [24]. They found mass transfer limitation of iso-butane is more severe in thicker shell (25nm) than in 12nm shell. The dramatic decrease in the reaction rate of benzyl chloride in

a thicker shell (80nm) compared to a 4nm silica shell with several angstrom pore sizes showed clear evidence of a reduced accessibility of the core [25]. Additionally, Min-Woong Ryoo observed severe mass transfer limitation in methane combustion in Pd supported microporous FAU zeolite (0.8nm) compared to 3nm MCM41 zeolite [26]. To improve mass transfer to the active sites, researchers have tried to increase the porosity of silica by adding a porogen C_{18}TMS (n-octadecyl trimethoxysilane) during synthesis [27, 28]. However, a lower reactivity of Pd@SiO_2 with 10nm shell thickness synthesized when utilizing the porogen is still observed in CO oxidation compared with Pd/SiO_2 [28]. Even for conventional mesoporous catalyst, Nyugen and co-workers found mass transfer limitation of perovskite embedded inside mesoporous silica in methane combustion due to the long monodimensional channel of the support [29]. This finding is supported by the decreased apparent activation energy from 25.5 kcal/mol to 18.5 kcal/mol for higher temperature (>380°C).

1.2.3 Coking

Another challenge for nanocatalysts is coking, especially in high C/H or C/O condition, such as the CPOM (catalytic partial oxidation of methane) or CO methanation reactions [30-35]. It is reported that nickel has the highest carbon deposition rate compared to Pd, Rh and Ir [36]. Coking is the carbon formation on metal surface. The carbon can be deposited either from methane decomposition or the Boudouard reaction (CO disproportion). Carbon deposition from CO disproportion occurs at lower temperature; while it is from CH_4 dissociation (>1020K) at higher temperature [36]. Two types of the carbon formation could be found on nickel catalysts: “whisker” and “encapsulated/graphic” carbons. Encapsulating carbon consists a thin CH_x film or a few layers of graphite covering the active site of nickel particles, resulting in a rapid

deactivation of the catalysts [37]. Whisker carbon does not necessarily result in an immediate deactivation of the catalyst, but it leads to the catalyst destruction or reactor blockage [38, 39]. Depending on the location of the carbon formation, coking can also be categorized as “site blocking” or “pore-mouth plugging”. “Site blocking” means that the carbon deposits on the metal surface cover the active sites, while “pore-mouth plugging” describes carbon accumulation at the entrance of the pores to block access to the active components. The deactivated catalyst from coking can be regenerated either via oxidation in air or steam gasification. Amiridis and co-workers discussed the pros and cons of these two regeneration processes [39, 40]. The oxidation process is faster than the steam gasification but will cause a high temperature front which can result in destruction of the catalyst. Another disadvantage for the oxidation process is the conversion from metallic nickel to nickel oxide, which requires a further regeneration step of reduction before the next reaction cycle. Conversely the steam gasification process maintains a uniform temperature profile in the catalyst bed and the catalyst preserves its metallic nickel form at the end of the process, but it requires external energy supply.

To design coking resistant nickel catalysts, efforts have been made to increase the O_2 availability on the metal surface by adding rare earth element like ceria. Ceria, which has high oxygen storage capacity, can facilitate carbon removal via supply of lattice oxygen [41, 42]. The basicity of the support can also be modified to increase the adsorption of CO_2, which can promote its reaction with deposited carbon. Addition of basic elements like lanthanum or synthesis of a solid solution like $MgAl_2O_4$ can make the support more basic [43]. The reduction of nickel ensemble size is another method to enhance coking resistance. Kim et al. found that the nickel particles under 10nm show high resistance to carbon deposition even under a fuel rich environment [44]. It was further confirmed by Zheng that Ni particles larger than 10nm

deactivate fast even at low space velocity ($18000h^{-1}$), while Ni particles under 9.5nm are stable at high space velocity up to $54000h^{-1}$ [45]. Lercher et al. suggested that the rate of carbon formation is proportional to the particle size of Ni, in which the rate of carbon formation slows down dramatically below a critical Ni particle size (diameter < 2 nm) [46]. Ponzi et al. reported that the minimum diameter of the Ni particles for the formation of whisker carbon is about 8~10 nm [47, 48]. Beside synthesizing small sized mono-metallic nickel particles, the addition of noble metal as such as Pd [49, 50], Pt [51], Rh [52] can also increase the dispersion and reduce the particle size, hence improving the coking resistance of the catalyst.

1.3 MATERIAL SYNTHESIS

1.3.1 Nano-sized nickel and nickel based catalysts

A number of metals could be used as active components in catalysts including noble metals (e.g. Pt, Pd, Au and Rh) and transition metals (e.g. Ni, Co, Cu, and Fe). Compared with noble metals, transition metals are much less costly. Our work has focused on nickel since nickel is an excellent catalyst for a number of hydrogen production reactions, such as steam reforming reaction [27, 37, 53, 54] and partial oxidation of methane [55-57]. However, the synthesis of small nickel particles under 5nm is challenging due to a strong magnetic dipole-dipole interaction between particles [58, 59]. The synthesis routes for nickel and nickel-based catalysts especially the size range under 5nm are briefly reviewed below.

One approach is to synthesize different sized nickel particles by controlling the nickel nucleation and growth rate. One example is to adjust the molar ratio of reducing agent and nickel

salt. It is found that the mean diameter of nickel particles decreases with the increasing ratio of [hydrazine]/[$NiCl_2$] and approaches a constant (around 10nm) when [hydrazine]/[$NiCl_2$] is greater than 12 [60, 61]. Another idea to control nickel particle size is to use different capping agents to adjust the growth rate of the nuclei [62]. Nickel particles are controlled from 3nm to 11nm by varying ratio of hexadecylamine (HDA) and trioctylphosphine oxide (TOPO), which were used as the capping agents to tune the growth of nanoclusters [59]. In a similar manner, nickel particles ranging from 2-30nm are synthesized by adjusting the ratio of oleylamine(OA) and trioctylphospine (TOP) when using $Ni(acac)_2$ as a salt precursor [63]. Park also suggested the use of different phosphines to obtain different nickel particle sizes since phosphines act as both the solvent and the surfactant [64]. 2nm sized nickel particles are obtained by using bulky tri-octylphosphine (TOP), while 5nm and 7nm sized nanoparticles were produced by using less bulky tributylphosphine (TBP) and triphenylphosphine (TPP) [64]. ~4-16nm Ni nanoparticles were also synthesized by chemical reduction of nickel salts $Ni(CH_3COO)_2$ or $Ni(acetylacetonate)_2$ [65, 66]. The variables such as the ligand type (e.g. oleic acid, n-trioctylamine), molar ratio of ligands to nickel salt, types of nickel salt and reaction temperatures were studied [65, 66]. Another method to synthesize small sized nickel particles is by wet-impregnation [45, 67, 68] or deposition-precipitation method [69, 70]. In wet-impregnation method, the final size of nickel particle is highly dependent on the type of nickel salt precursor. Generally, the nickel size is in the order nickel ehtylenediamine complex (2-3nm) < nickel acetylacetonate dehydrate (~10nm) <nickel acetate (16nm) <nickel nitrate (50nm) [45, 67, 68]. In deposition-precipitation method, an appropriate pH end point is essential to obtain the small sized nickel particles [71].

As summarized, the synthesis route for nickel particles under 5nm is complicated and tedious with the exception of the impregnation method [45, 59, 63-65, 72]. Hence, a simplified method to obtain the controlled nickel particles needs to be developed.

1.3.2 Core shell materials

In general, there are two ways to synthesize metal core silica shell materials: coating of pre-synthesized nanoparticles called “two-step synthesis” [19, 27, 73-80] and the microemulsion method [18, 24, 81-85] called coating in-situ synthesized nanocrystals or “one-step synthesis”. The critical step in the two-step synthesis is to transfer pre-synthesized colloids from aqueous solution to ethanol where a Stöber or a modified Stöber process is performed. For example, PVP which is an amphiphilic polymer is able to stabilize colloidal particles in water. PVP coated particles can be transferred into a mixture of water-ammonia-ethanol and be directly coated with silica shells via tetraethyl orthosilicate (TEOS) hydrolysis and condensation. Au and silver coated silica are demonstrated by this method [80]. The impact of different PVP length on the metal stabilization and particle sizes have been discussed as well [73] . Somorjai group also used TTAB instead of PVP as a capping agent to synthesize $Pt@SiO_2$ with 2.3nm core size [31]. However, the challenge for this method is to determine the optimum TEOS amount. Insufficient TEOS results in multiple cores, while excessive TEOS results in empty cores [31].

Microemulsion is defined as a thermodynamically stable and optically transparent mixture of water, organic solvent (oil), and surfactant. Constant exchange between the content of droplets and the surfactant molecules at the interfaces facilitates chemical reactions involved in the particle synthesis. There are two types of microemulsion including normal (oil droplets dispersed in water) and reverse (water droplets dispersed in oil) microemulsion. In the reverse

microemulsion method, nanoreactore-like water droplets dissolve both inorganic salts and organometallic. Water is not only used to stabilize micelles, but also serves as a reactant for TEOS hydrolysis. Silica nucleation is in a better control in “one-step synthesis” compared to “two-step synthesis”, since silica nucleation and growth occur within the boundaries of the nanometer-sized droplets.

Besides traditional dense core-shell materials, core-shell materials with hollow structures have drawn considerable attention in recent years. The advantage of a hollow core-shell structure is that more surface area of active components is exposed to reactants, which is desirable as a heterogeneous catalyst. Hollow core-shell materials are typically prepared by selective etching the core particles [27, 86] or the shells [22, 87-89]. For example, HCl is able to diffuse through the silica shell to etch away nickel starting from 37nm down to an empty core [27]. Co@SiO_2 and Fe@SiO_2 hollow structured materials are also demonstrated in this way [27]. Gold particle sizes can be tailored from 120nm down to an empty core by the use of different amounts of etchants KCN [86]. For the shell etching, double shells composed of different materials are coated on a core followed by a selective removal of the inner shell using solvents or calcinations procedures. For example, hollow structure Au/ZrO_2 is formed by the use of NaOH to remove silica shell from the original SiO_2/ZrO_2 layered shells [22]. Hollow Au@SiO_2 and Fe@SiO_2 are also synthesized in a way that Na_2CO_3 is used to etch the shell with higher condensation degree of silicate species [89]. Other routes to create hollow structures include spontaneous dissolution–regrowth of silica in NaBH4 solution at 51°C for 6 hours [90], incorporation of nanoparticles into hollow colloidal particles [91] and the Kirkendall effect [92, 93]. In general, all of these routes to create hollow structures in a core shell material involve complex, multi-step synthesis.

1.4 REACTION APPLICATIONS

1.4.1 CO oxidation

CO oxidation is relevant to the practice of automotive exhaust reduction and also used for purification H_2 stream production. This is one of the simplest catalytic reactions and serves as a model for our understanding of catalysts. The global reaction is written as

$2CO+O_2=2CO_2$

The catalytic sequence is as follows [94-96]:

$CO_g \rightleftharpoons CO_{ads}$ (1)

$O_{2,g} \longrightarrow 2O_{ads}$ (2)

$CO_{ads}+O_{ads} \longrightarrow CO_{2,g}$ (3)

The reaction follows Langmuir-Hinshelwood mechanism at room temperature, in which the surface is primarily covered with CO and the reaction rate is controlled by the desorption of CO. However, the mechanism may be changed when the reaction condition is different. For example, Bergeld suggested adsorbed O_2 can directly react with CO to form CO_2 following an alternative "autocatalytic reaction path" at low temperature (180K~230K).

A number of metals such as Au, Pt, Pd and Ni are extensively studied for this reaction [96-98]. CO oxidation is reported as a structure insensitive reaction from experimental data as well as density functional theory (DFT) calculations [97, 99, 100]. The insensitivity of the reaction is explained by the insensitivity of total bonding energy of CO and O to surface structure. One of the key parameters in CO oxidation is the ratio of O_2/CO. It is reported that higher O_2/CO is preferred for higher CO conversion since excessive CO will poison the active

sites of the metals [101]. However, the higher O_2/CO results in the decrease in reaction rate due to the formation oxide species which act as active site blockers on the surface [96].

1.4.2 Ethylene hydrogenation

Ethylene hydrogenation reaction has served as a basis for numerous kinetic studies of metal catalysts (e.g. platinum, nickel or palladium) [102-104]. The mechanism of the ethylene hydrogenation reaction can be described as the following elementary processes [105, 106]:

$H_2 + 2* \rightleftharpoons 2H_{ads}$ (1)

$C_2H_4 + 2* \rightleftharpoons C_2H_{4,ads}$ (2)

$C_2H_{4,ads} + C_2H_{4,ads} \rightleftharpoons C_2H_{5,ads} + *$ (3)

$C_2H_{5,ads} + H_{ads} \rightleftharpoons C_2H_{6,ads} + *$ (4)

$C_2H_{6,ads} \rightleftharpoons C_2H_6 + *$ (5)

Where * is the empty surface site. The rate-determining step is either reaction (3) or (4).

It is reported that the reaction is close to first order in hydrogen and zero order in ethylene at lower temperature (<170^{o}C). However, the reaction becomes first order in ethylene above 170^{o}C [106]. The difference of kinetics is explained by different surface concentrations of hydrogen and ethylene atoms in different temperature regions. At low temperatures, less free surface sites are available for hydrogen dissociation since the surface is almost completely covered by ethylene. A higher temperature results in a decreased concentration of adsorbed ethylene, which enables the more adsorption and dissociation of hydrogen. The reaction is typically operated in a hydrogen-rich environment to avoid the formation of acetylene residues on the surface [107].

1.4.3 CO methanation

CO methanation has attracted considerable interest since Sabatier and Senderens first brought up the concept more than 100 years ago [108]. It is the final clean-up step for the feed gas for ammonia synthesis [109]. It can be also used to produce methane from synthesis gas in connection with coal gasification [110], in relation to Fischer–Tropsch synthesis [111] and hydrogen purification for PEM fuel cells [112, 113]. The reaction equation is as follows:

$CO+3H_2=CH_4+H_2O$ (ΔH^0_{298K} =-206 kJ/mol)

A number of researchers have attempted to understand the mechanism of CO methanation, and there are several different opinions regarding whether the process is structure sensitive or not. Goodman et al. concluded it is a structure insensitive process since the reaction rate per Ni atom on Ni(111) is comparable with that on Ni(100) as well as on supported Ni catalysts. The rate limiting step is carbide formation or carbide hydrogenation in sufficient low H_2-to-CO ratio or low pressures [114-116]. However, Nielson, Nørskov and Chorkendorff suggested this is a structure sensitive process as evidenced by both DFT calculations as well as ultra-high vacuum experiments. The reasoning is that the rate limiting step in this condition is CO dissociation, which occurs only on under-coordinated sites [31, 117-119]. It is also suggested that 4nm Ni particles have the highest reactivity for this reaction [120]. The design of a coking resistant catalyst for this reaction is critical since carbon deposition is a challenging and relevant issue [30-33].

1.4.4 Catalytic partial oxidation of methane reaction (CPOM)

CPOM is a promising alternative process to the traditional industrial route for synthesis gas production-steam reforming of methane (SRM). It is a much less energy intensive process compared with SRM since it is a mildly exothermic process. Additionally, the product syngas ratio (H_2/CO=2) is suitable for the downstream Fischer–Tropsch reaction.

In CPOM, methane reacts directly with oxygen or air to form synthesis gas (CO and H_2) in a one-step reaction:

$CH_4 + 0.5\ O_2 = CO + 2\ H_2$ $\quad \Delta H_R^0 = -37$ kJ/mol

A high conversion of syngas is achieved only at high temperature (>700^{o}C) since it is a mildly exothermic reaction. At lower temperature, CO_2 and H_2O are the main products from the major competing methane combustion reaction.

$0.5\ CH_4 + O_2 = 0.5\ CO_2 + H_2O$ $\quad \Delta H^0_{298K} = -800$kJ/mol

Other competing reactions include methane steam reforming and water-gas-shift reactions.

$CH_4 + H_2O = CO + 3H_2$ $\quad \Delta H^0_{298K} = 206$kJ/mol (steam reforming)

$CO + H_2O = H_2 + CO_2$ $\quad \Delta H^0_{298K} = -41$kJ/mol (water-gas-shift)

There are two main categories of catalysts: noble metals like Pt, Rh, or Ru [16, 121-123] and transition metals like Ni and Co [55, 56, 124-128]. Even though noble metals show high activity and selectivity in CPOM reaction, their high cost limits their application. Hence, more attention is drawn to the advancement of transition metals. Nickel and cobalt-based catalysts have similar activity. However, cobalt deactivates faster than nickel since cobalt oxidizes more

easily and forms an inactive cobalt oxide phase [129]. Overall, a nickel-based catalyst is a good candidate for CPOM reaction because of its high reactivity and affordable price.

The ideal nickel-based catalyst is thermally and chemically stable with high reactivity and selectivity. However, the deactivation of nickel catalyst is commonly caused by the change of oxidation state [124, 130-132], sintering [123, 133, 134] and coking [37] . In CPOM, metallic nickel rather than NiO is the active site for the reaction [135, 136]. The metallic state nickel is responsible for high selectivity of CO and H_2. However, during the reaction, metallic nickel will react with O_2 to form NiO which will decrease its activity and selectivity [124, 130-132]. Hence, it is important to enhance nickel tolerance against oxidation during the reaction to sustain its reactivity. Another issue is poor thermal stability of the nickel catalyst since CPOM is a thermodynamically favored high temperature reaction. Loss of catalytic active surface area due to sintering will result in decreased reactivity [123, 133, 134]. To enhance thermal stability, efforts should be made to modify support composition or enhance metal support interaction [137-140]. An alternative way to stabilize metal particles is to create a cage-like structure by either embedding metals in a ceramic matrix or coating metals with an inert shell, such as silica [16, 27].

1.5 PROJECT SCOPE

Large surface areas and a high population of under-coordinated atoms make nanocatalysts advantageous over traditional catalysts. However, catalyst deactivation due to sintering under moderate/high temperature operation and coke formation in hydrocarbon participating systems poses a challenge for their practical usage. Our work focuses on solving

these issues by designing and developing a series of core-shell materials. A fundamental understanding of core-shell materials is facilitated by systematic investigation via synthesis, characterization, and catalytic tests. Synthesizing well-defined nanomaterials is crucial for our project since the catalytic properties of nanocatalysts are highly dependent on its size and shape. Material characterization serves as a bridge to communicate microscope structure with our understanding and to help steer the direction for synthesizing the targeted structure. Characterization also provides powerful scientific evidence to explain structure correlated reactivity. Reaction testing is important to show the impact of microscope structure on a macroscope level and to demonstrate significance for industrial applications of these nanocatalysts. Overall, the research aims to optimize the synthesis conditions to achieve well-defined nanocatalysts with good thermal stability and minimal internal mass transfer limitations; to be able to tailor the characteristic length scales of nanocomposites; and to evaluate and understand the properties of the materials and their applications.

2.0 EXPERIMENTAL

2.1 SYNTHESIS

Standard synthesis procedures include solution synthesis, surfactant removal by calcinations, external nickel removal by etching, and finally surface cleaning for materials used for reactive testing.

2.1.1 Solution synthesis

Ni core silica shell (denoted as Ni@SiO_2) material is synthesized in a reverse-microemulsion mediated sol-gel process. A mixture of 10g Brij58 (≥99%, Aldrich) and 50 mL cyclohexane (≥99%, Aldrich) in 250 mL three-neck flask was heated up to 50^{o}C in oil bath under stirring (with stirring rate 240 rpm). The nickel nitrate aqueous solution (1.5 mL, 1.0 M stock solution made from Aldrich) was added dropwise. Under stirring, hydrazine hydrate (1.5mL, Aldrich) was added dropwise and the mixture was stirred for another hour. Next, ammonium hydroxide solution (3 mL, 28 wt.%) was added dropwise to the previous solution. After 1 hour stirring, 10g tetraethoxysilane (TEOS, ≥99%, Aldrich) was added dropwise to the microemulsion. Hydrolysis and condensation of the silica precursors were allowed to proceed for 2 hours at 50°C. Then Ni@SiO_2 was precipitated by adding 2-propanol and washed three times

by centrifugation and redispersion. Figure 3 shows the synthesis scheme and the solution color along with the synthesis. The green color is from Ni^{2+} and the pink color indicates the formation of a nickel hydrazine complex [141].

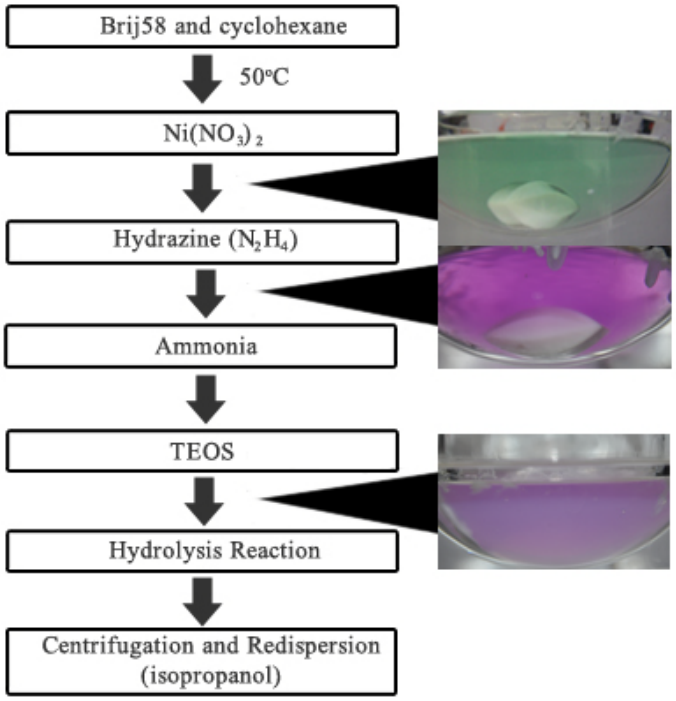

Figure 3: *The synthesis scheme and the color of the solution during the reaction*

2.1.2 Surfactant removal

The wet $Ni@SiO_2$ sample was transferred to a plastic weight boat under the hood for overnight drying. After that, the powdered catalysts were calcined at 500°C for 2 hours under 0.5 SLM air stream in a Thermolyne 79300 tube furnace. The temperature program for this calcination process and the sample color after different steps are shown in Figure 4. The temperature ramping rate must be slow (1°C/min) especially between 200°C to 300°C to avoid abrupt reactions, because a significant amount of surfactants are trapped in the silica pores and must be burned off slowly. A sharp increase in BET surface area from 200°C to 300°C (inserted

picture in Figure 4-left) indicates the temperature range in which most surfactants will be removed is 200°C to 300°C. For each calcination cycle, only 0.1g of dried pink powdered sample should be loaded per calcination boat to avoid explosion. The color of calcined sample is grey indicating the formation of NiO. For selected sample used in reactive testing, the oxidized sample is reduced in H_2 at 700°C for 30 minutes before an etching process. The color of reduced sample is black, which is consistent with the color of metallic nickel.

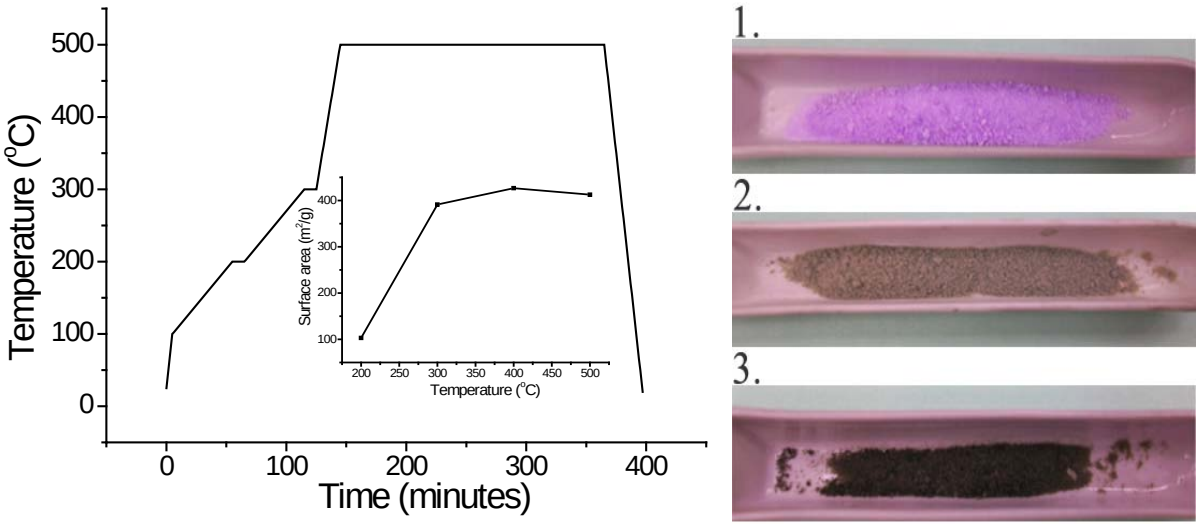

Figure 4: *(a) Calcination temperature program with the inserted image showing BET surface area as a function of temperature (b) The powdered sample before the calcination, after calcination in the air and after reduction in the H_2*

2.1.3 Etching process and surface purification

The reduced material is etched with HNO_3 (Aldrich) to remove any external nickel outside of the silica shell, especially when a high concentrated nickel precursor is used. In the standard procedure, 0.2g catalyst is treated in 10ml HNO_3 diluted with 10mL D.I. H_2O under a stirring rate 240rpm for 30 minutes. Afterwards, the etched material is washed with D.I. water by centrifuge and redispersion three times. Then the sample is redispersed in ethanol and

centrifuged before drying in the oven at 80°C for 4 hours. The reason to use ethanol in the last step is to shorten the drying process since ethanol is highly volatile and yet does not interfere with the properties of silica. The results in section 3.5.1.2 suggest that 30 minutes is an appropriate etching time to assure the removal of external nickel and the retainment of internal nickel in cavity sample. Another calcination cycle needs to be performed to remove the water, acid and impurities. The sample is calcined in the air (0.2 SLM) at 773K for 1 hour with the heating rate 20°C/min.

Among above synthesis steps, etching is the most sensitive step. The etching step in the core shell material without cavity structure is especially complex due to difficult control of etching rate and degree of etching. The external nickel is not necessarily etched away before starting etching internal nickel. Figure 99 in appendix shows even after 2 hour etching, there is still significant leftover external nickel while some internal nickel is etched away. The yield of one batch synthesis from solution synthesis to the final product is about 40%~80% depending on the silica shell thickness and the loss during the etching step. 50%~ 100% silica conversion is achieved during solution synthesis step, in which the actual hydrolysis degree will determine its conversion. In calcination step, around 20% sample weight is lost due to the removal of surfactant. The yield for etching step is about 80% weight due to the loss of the sample during centrifuge and redispersion steps. The final product weight in one batch synthesis is about 1~1.5g depending on the silica shell thickness.

As comparison materials, IMP-Ni/SiO_2 (wet-impregnation method), DP-Ni/SiO_2 (deposition-precipitation method) and sol-gel Ni/SiO_2 are also synthesized. The synthesis condition of these materials is found in Appendix B.1.

2.2 CHARATERIZATION

2.2.1 Nitrogen sorption

Catalyst surface area and porosity are determined using a Micromeritics ASAP 2020 in our lab as well as a Quantachrome autosorb1 apparatus in NETL facility. The Micromeritics ASAP 2020 only gives the pore size distribution greater than 2nm while Quantachrome autosorb1 is able to measure pore size distribution in micro porous range. In ASAP 2020, samples are degassed for 3 hours at 200°C under high vacuum prior to each test. In Quantachrome autosorb1, samples are degassed for 12 hours at 200°C before each test. Both nitrogen adsorption/desorption measurements were performed at liquid nitrogen temperature (77 K). The typical test involved a 6-point Brunauer- Emmett-Teller (BET) analysis for total surface area measurement in the relative pressure range $0.1<P/P_0<0.35$.

2.2.2 Transmission electron microscopy (TEM)

Catalyst morphology is determined by both TEM (JEOL-2000FX electron microscope) and a high resolution transmission electron microscopy (HRTEM, JEOL-2100). In the preparation step, a small portion of the sample was grinded in the mortar and dispersed in ethanol. The suspension was sonicated about 1 minute for better dispersion. One drop of the sample is placed on a copper type-B support grid (Ted Pella Inc.), followed by air drying to remove the solvent. To achieve better contrast, the sample can be reduced in H_2 before TEM especially for small sized nickel particles. For example, 1nm nickel particles embedded in silica sample are barely discernible in an oxidized sample compared to a reduced sample.

Measurement of mean nickel particle diameter from TEM micrographs was performed by hand using ImageJ software [142].

2.2.3 X-ray powder diffraction (XRD)

X-ray diffraction measurements were performed with a high-resolution powder X-ray diffractometer (Phillips PW1830, USA) in line focus mode using a monochromatic Cu radiation at the wavelength of 1.54 Å. The beam voltage was 40kV at a current of 30mA. The XRD patterns were recorded between 10° and 80° (2θ) in steps of 0.08° intervals with a minimum 0.2s counting time at each step. XRD should be performed right after the sample is fully reduced to avoid the reoxidaton of nickel after air exposure. Figure 100 in the appendix shows that NiO peaks were detected after the fully reduced sample exposure to the air for 1 week.

2.2.4 Temperature programmed reduction (TPR)/ Temperature programmed oxidation (TPO)

TPR/TPO is performed to investigate the reducibility and oxidation capability of the nickel particles in different structured material. The flow rate of each gas (30 cm^3 min^{-1}) is controlled by mass flow controllers. The catalyst (30mg) is loaded in a quartz reactor. Before TPR/TPO, the fresh sample is pretreated by 5% O_2 in He at 500°C for 1 hour to remove the moisture and impurities on catalyst surface with a subsequent flush with He. In TPR, the catalyst is reduced in hydrogen flow (10% H_2 in argon) in the temperature range from 30°C to 900°C with 5°C/min ramping rate. In TPO, the catalyst is oxidized by 5% O_2 in He from 30°C to 500°C with the same ramping rate. The temperature is measured by a type K thermocouple inside the

catalyst bed. The signal is recorded by a Balzers Quadstar GSD 300 mass spectrometer as well as a Micromeritics Chemisorb 2750 chemisorption system. The detailed procedure for the TPR/TPO can be found in Appendix A.1.

2.2.5 Chemisorption

Chemisorption experiments for metal dispersion and total nickel surface area determination for the nanocatalyst are conducted on a Micromeritics AutoChem 2920 in NETL (National Energy Technology Laboratory) facility with collaboration with Dr. Shi. Samples are reduced for 30 minutes at 700°C in 10% H_2/Ar with a subsequent flush with He while the chamber is cooling down. N_2O and H_2 pulsing with He as a carrier gas at room temperature is performed.

2.3 REACTIVE TESTING

2.3.1 CO oxidation

Powdered catalytic materials are inserted into a 5 mm ID quartz glass tube. The catalysts are supported within the tube on either end by plugs of quartz glass felt. The tube is placed within a high temperature tube furnace such that the catalyst zone is fully within the heated zone of the furnace. A K-type thermocouple (Omega) is used to monitor reaction temperature and it was inserted such that the tip of the thermocouple is within 1 mm of the end of the catalyst zone. The temperature in the reaction zone is controlled by the temperature of the furnace. Mass flow

controllers (MKS Instruments Inc.) are used to feed a 3% CO and 9% O_2 in balance of pure helium (Valley National Gas). The nickel needs to be reduced at 700°C for 30 minutes under a hydrogen flow with a flow rate of 30 mL min^{-1} before the reaction. The contact time is ~0.14-0.2s from 200°C to 400°C with the total flow rate 26 mL min^{-1} (the mixture O_2:CO= 3:1 in the balance of He with 23 mL min^{-1}). The total flow rate of gas is adjusted to normalize the contact time if the length of the catalyst bed is varied in some cases. Typically, the prepared Ni@SiO_2 sample (0.038g) is diluted with SiO_2 (0.013g) to ensure the catalyst bed is about 7 mm. The nickel mass (1.5mg) and the space velocity (18000h^{-1}) maintain the same in each run. A specific order of valve manipulation is used to avoid the explosive region in the mixture of CO and O_2. The order to turn on the mixture is first helium, then O_2 followed by CO. The order to turn off the mixture is first CO, then O_2 and helium. The products were analyzed by an Agilent 3000A Micro GC equipped with thermal conductivity detectors (TCD). The carbon balance is typically within +/-5%. Example calculations of conversion and carbon balance are found in Appendix A.2.1.

2.3.2 Ethylene hydrogenation

Powdered catalytic materials are inserted into a 5 mm ID quartz glass tube. The catalysts are supported within the tube on either end by plugs of quartz glass felt. The tube is placed within a high temperature tube furnace such that the catalyst zone is fully within the heated zone of the furnace. A K-type thermocouple is used to monitor reaction temperature and it was inserted such that the tip of the thermocouple is within 1 mm of the end of the catalyst zone. The temperature in the reaction zone is controlled by the temperature of the furnace. Mass flow controllers (MKS Instruments Inc.) are used to feed the gas containing 10% ethylene and 30% H_2

with a balance of He with a flow rate of 100 mL min^{-1}. The contact time is 0.08s. The nickel needs to be reduced at 700°C for 30 minutes under a hydrogen flow with a flow rate of 30 mL min^{-1} before the reaction. Typically, the prepared Ni@SiO_2 sample (0.0207 g) was diluted with SiO_2 (0.0760 g). The nickel mass (4.8mg) and the space velocity (45000h^{-1}) are maintained the same in each run. The products were analyzed by an Agilent 3000A Micro GC equipped with thermal conductivity detectors (TCD). The carbon balance is typically within +/-5%. Example calculations of conversion and carbon balance are found in Appendix A.2.2.

2.3.3 CO methanation

CO methanation reaction were performed in a fixed bed continuous flow reactor operated at atmospheric pressure. In a typical run, 0.038g nickel core shell material blended with 0.012g commercial silica powders (Aldrich) was placed in a tube reactor made of quartz glass with 5 mm ID. The catalyst bed length is about 7mm. The nickel mass (1.5mg) and the space velocity (24000h^{-1}) are maintained the same in each run. After pre-treatment at 700°C for 30 minutes under a hydrogen flow with a flow rate of 30 mL min^{-1}, a mixture of H_2/CO=3.6 in a balance of 70% Helium (Valley National Gas) was introduced by mass flow controllers (MKS Instruments Inc.). The contact time is ~0.12s-0.15s. The exit gases pass through a U tube filled with the silica gel desiccant (Fisher Scientific) to eliminate H_2O from the stream. The products were analyzed by both Balzers Quadstar GSD 300 mass spectrometer (MS) and Agilent 3000A Micro GC equipped with thermal conductivity detectors (TCD). For the reactivity tests of different catalysts in section 6.2, a total flow rate of 25 mL min^{-1} is used. For thermal stability test in section 4.4.2, total flow rate 12.5 mL min^{-1} was introduced. The reactor was heated from room temperature to 450°C with the ramping rate 20°C /min and held at 450°C for 1.5 hour. The

carbon balance is typically within +/-5%. Example calculations of conversion and carbon balance are found in Appendix A.2.3.

2.3.4 CPOM

CPOM reaction is performed in fixed bed reactor made of quartz glass tube with inner diameter 5 mm at ambient pressure. The catalysts are supported within the tube on either end by plugs of quartz glass felt. The tube is placed within a high temperature tube furnace with the upper limit 1100°C (model type TF55035A, VWR) where the catalyst zone is fully within the heated zone of the furnace (usually 7 inch away from the furnace inlet) to allow adequate pre-heating of the reaction gas mixture. The catalyst bed temperature is measured by a 24 inch grounded K-type thermocouple (model type KMQXL-020G-24, Omega). This type of thermocouple is thermally stable up to 1200°C and is coking resistant. The thermocouple is placed about 1/3 of catalyst bed length away from the entrance of the catalyst to increase the accuracy of catalyst bed temperature measurement. Even though the ideal situation is to conduct the reaction in isothermal condition, it is hard to achieve the isothermality in this case. For example, efforts made to increase the flow rate of dilution gas (He) results in no/low reactivity of catalyst. The reason the thermocouple is placed closer to the catalyst entrance is because of the reaction mechanism described as the exothermic methane combustion followed by the endothermic steam reforming, in which results in a higher temperature closer to the catalyst entrance than the downstream catalyst bed [143, 144]. The temperature difference between catalyst bed and oven set temperature can be as high as 70°C depending on the extent of the reaction. The temperature in the reaction zone is controlled by the temperature of the furnace, which is typically between 300°C and 1000°C. Mass flow controllers (MKS Instruments Inc.)

are used to feed a mixture of CH_4 (8.9 cm^3 min^{-1}) and Air (21.8 cm^3 min^{-1}) (0.1 Grade, Valley National Gas). The exit gases pass through a U tube filled with the silica gel desiccant (Fisher Scientific) to eliminate H_2O from the stream. The products composition were monitored by Balzers Quadstar GSD 300 mass spectrometer (MS) and analyzed by Agilent 3000A Micro gas chromatography (GC) equipped with thermal conductivity detectors (TCD). Nitrogen is used as an internal standard to calculate the total gas flow rate after water condensation and to back-calculate the concentration of each product.

Typically, 0.03g $Ni@SiO_2$ sample was diluted with 0.04g fumed silica (Aldrich) to adjust the catalyst bed to be 14mm. The mass of nickel (1.2mg) and space velocity (6551h^{-1}) were the same for each run. The contact time is ~0.14s-0.21s from 500°C to 900°C. To make sure the gas mixture is outside of the explosion range (~5%-15% CH_4 in air) at any time; methane is always turned on before air and turned off after air. Figure 5 shows the flow chart of the reactor set-up for CPOM reaction.

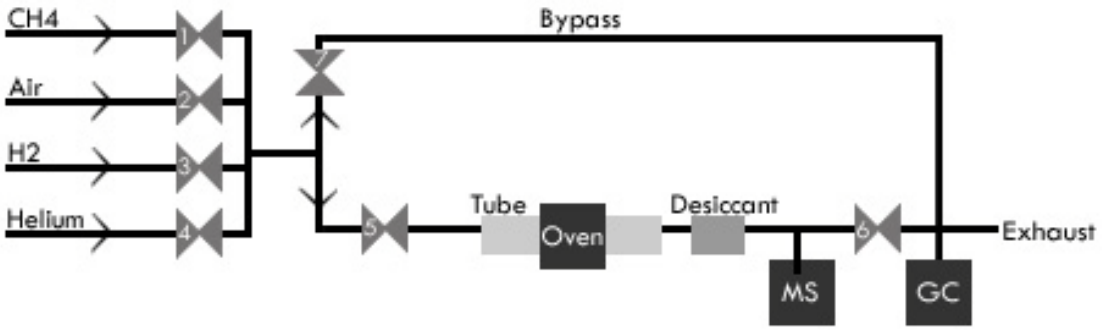

Figure 5: *The flow chart of the reactor set-up*

The standardized procedure for the ignition and extinction operation in section 6.3.1 is described as follows. The sample is reduced in H_2 (30 cm^3 min^{-1}) at 700°C for half an hour before switching to helium to purge the system. CH_4 is turned on followed by air, and the system is held ~5-10 minutes to make sure $CH_4/O_2=2$ by taking a data point using GC. In the ignition

branch, the oven is heated up from room temperature to the oven set point temperature with a heating rate of 20°C/min, then held for 30 minutes before moving on to another oven set point temperature. Once the catalyst ignites, the extinction branch is measured. The oven set point temperature is stepwise decreased to a lower temperature and allowed to stabilize for 20 minutes. To shut off the reactor, helium (30 cm^3 min^{-1}) is turned on first to prevent nickel coking in pure methane environment. Then air is turned off followed by methane. The carbon balance is typically within +/-5%. Example calculations of conversion, selectivity and atom balance are found in Appendix A.2.4.

2.3.5 In-situ TPO/TPR

In-situ TPO in section 4.4.2 and section 5.4 is performed to qualitatively determine the carbon formation on the catalyst surface by comparing the CO_2 peak area. Before performing TPO, the reactor is cooled down to room temperature with helium flow. Air with 99.9% purity (Valley National Gas) is introduced to the reactor with a flow rate of 20 mL min^{-1}. Once the MS (mass spectroscopy) signals that all gases have reached steady state, the oven is heated from room temperature to 1173K with the ramping rate 20K/min and held at 1173K for 1 hour to make sure all the carbon is depleted.

In-situ TPR is performed in section 6.3.3 to qualitatively compare the fraction of metallic nickel in the cavity Ni@SiO_2 with 7nm and 20nm shell thicknesses at 800°C in extinction branch. H_2 signal is recorded by Balzers Quadstar GSD 300 mass spectrometer (MS). The detailed procedure for in-situ TPR can be found in Appendix A.3.

3.0 STRUCTURE CONTROL, FORMATION MECHANISM AND THEIR PROPERTIES

In this chapter, we will demonstrate the fine dimensional control of the core shell material by adjusting the synthesis parameters, elaborate chemistry in the synthesis system, propose and verify the hypothesis for the mechanism of structure formation. The properties of this new type of materials are also evaluated for their possible applications.

3.1 NICKEL CORE SILICA SHELL MATERIAL

Figure 6 shows the well-controlled morphology of the nickel core silica shell material from nano-scale to macro-scale. The diameter of the spherical particle is ~30nm. The grey ring is silica shell with a thickness ~10nm. The inner wall of silica shell is decorated with a dark ring of small nickel clusters (<2nm). There is a pronounced cavity structure, which is 10nm in diameter. The material is a grey powdered sample.

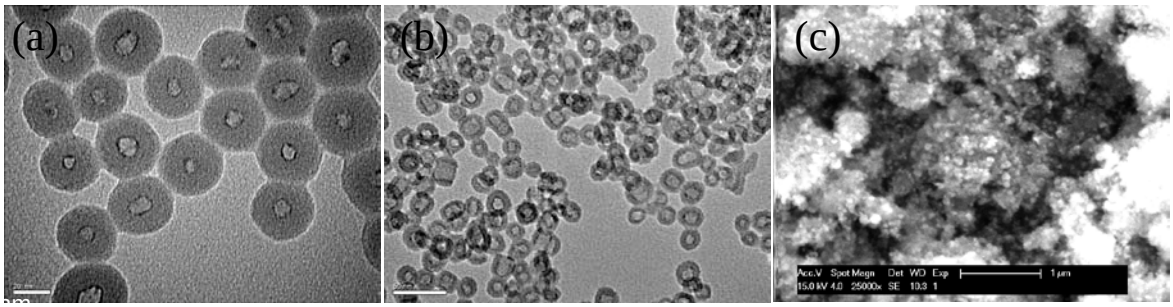

Figure 6: *(a, b) TEM images of Ni@SiO_2 (c) SEM image of the macro-pore structure*

Electron tomography is used to probe the three-dimensional structure of the nanoparticles in collaboration with G. Zhao and P. Zhang in the Structure Biology Department at University of Pittsburgh. Sample tomographic slices (Figure 7-A) and the surface-rendered 3D tomogram (Figure 7-B,C) reveal that the Ni@SiO_2 indeed possesses the hollow spherical structure comprising sub-nanometer nickel clusters decorated on the inner wall of silica shell.

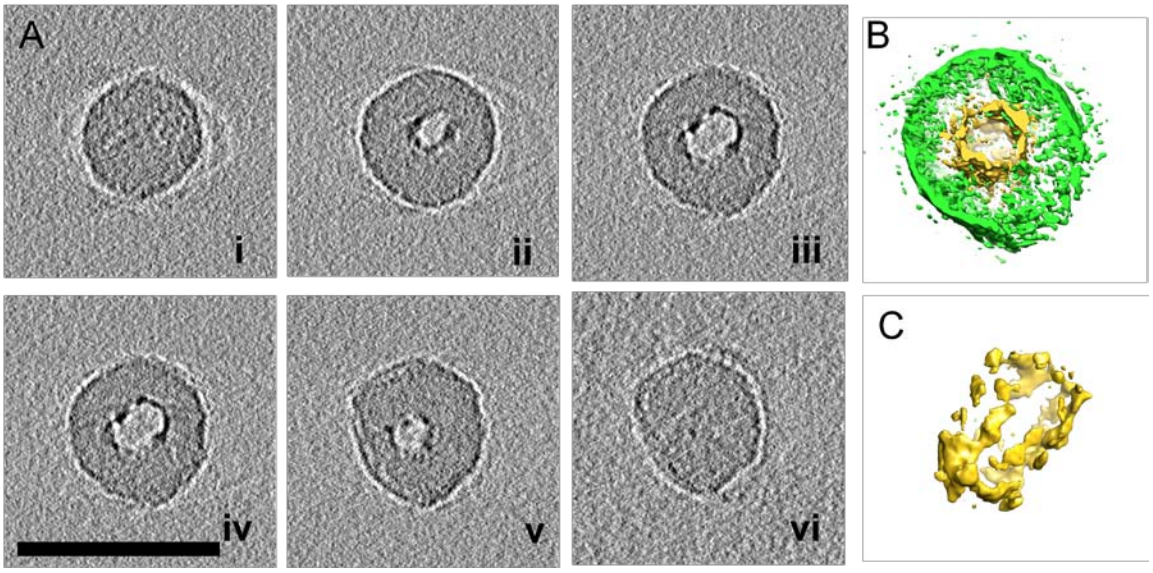

(Data courtesy of G. Zhao)

Figure 7: *(A) X-Y computational slices (i-vi) of a 3D tomographic volume containing a silica nanoshell, in which the inner surface is decorated with Ni, shown in every 3.9 nm through the volume. Scale bar is 50 nm. (B) 3D surface rendering of the whole nanoshell. Outer shell is colored as green and inner shell is colored as yellow. (C) Surface rendering of the inner core.*

3.2 STRUCTURAL CONTROL

3.2.1 Shape control

The core shell material is spherical in shape as seen in Figure 6-a when following the standard synthesis procedure described in section 2.1. The spherical shape can be tailored to an elongated shape by changing surfactant/water ratio or the synthesis temperature.

3.2.1.1 Surfactant /water ratio

By increasing surfactant-to-water ratio from 2.38-5.88, the shape of hollow Ni@SiO_2 particles transitions from spherical hollow structures to elongated rod-shaped hollow structures and to high aspect tubes. First, a small increase in surfactant-to-water ratio results in a mixture of spherical shape and rod-shaped structure (Figure 8-a). Upon further increase of the surfactant-to-water ratio, the shape of the nanoparticles changes to elongated cavities with a length of ~40-52nm corresponding to an aspect ratio of ~3-4 (Figure 8-b), and finally to tube-like structures with a length of ~90-112 nm and an aspect ratio of ~6-7 (Figure 8-c). In all cases, the inner walls of the hollow structures are decorated by sub-nanometer nickel clusters.

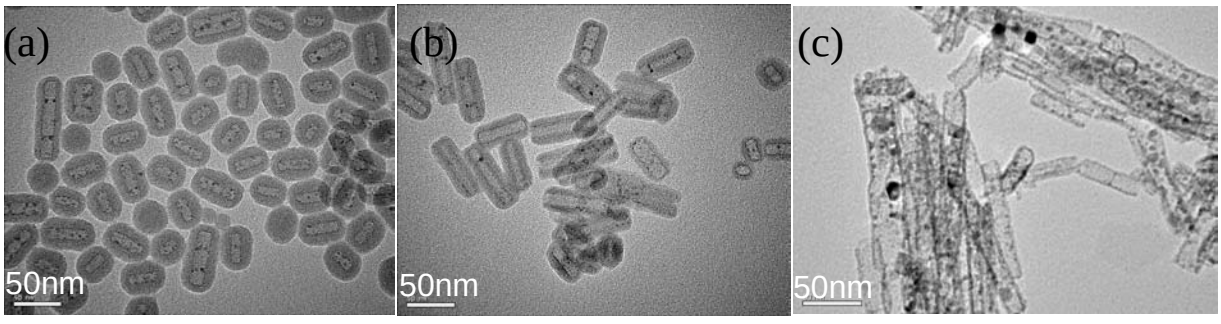

(Images a and b provided by courtesy of R. Lu)

Figure 8: *Different shapes of hollow Ni@SiO_2 nanoparticles*

However, further decrease in surfactant-to-water ratio less than 2 results in the non-stable microemulsion system, leading to poor uniformity of core shell materials (Figure 79 in appendix B). It is worth mentioning that the hollow structure is formed before the calcination step to remove the surfactant (Figure 80 in appendix B).

3.2.1.2 Temperature

The reaction temperature in the standard method is 50°C. The temperature needs to be less than 100°C to avoid evaporation of the solvent. When the reaction temperature increases to 70°C, the length of tube-like structure is over 300nm with high aspect ratio over 10. Figure 9 shows the TEM pictures of the particles under 70°C reaction temperature at different scales.

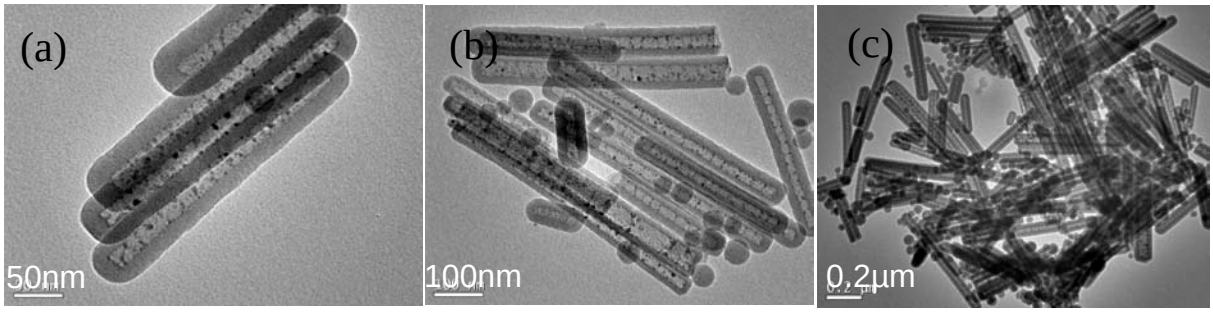

Figure 9: *TEM pictures of Ni@SiO_2 synthesized at 70°C*

3.2.2 Size control-silica shell

There are three ways to control silica shell thickness: reaction time, TEOS amount and ammonia concentration. The silica-particle growth is reaction-control by the slow hydrolysis of TEOS rather than fast TEOS condensation [145]. Fogler further systematically investigated the kinetics of silica particle formation in nonionic reverse microemulsion system and found out that TEOS hydrolysis rate is approximately first order with respect of aqueous ammonium concentration and TEOS [146, 147].

3.2.2.1 Reaction time

Figure 10 shows the silica shell thickness as a function of reaction time. The silica shell thickness is tailored from 3nm to 15nm by the increasing reaction time from 20 minutes to 27 hours with a TEOS amount of 5g. The cavity diameter remains constant at 14.65 ± 3.82 nm. The rate of the silica shell growth is initially very fast and reaches plateau after 10 hours since the silica growth rate is limited by the TEOS and water amount. Water not only serves as a reactant for TEOS hydrolysis, it also stabilizes micelles in the reverse microemulsion system. The silica shell growth in this case is also 1st order with respect of TEOS concentration and the apparent rate constant for silica-particle growth (k_c) is determined via the following equations [147]:

$$1- \frac{V_p(t)}{V_p(\infty)} = exp(-k_c t)$$

$$V_p(t) = \frac{4}{3}\pi(r^3 - {r_o}^3)$$

$$V_p(\infty) = \frac{4}{3}\pi(R^3 - {r_o}^3)$$

Where k_c is the specific rate constant for silica particle growth; $V_p(t)$ and $V_p(\infty)$ are the volume of silica particles at time t and at the end of reaction; r_o (~7.5nm) is the radius of cavity structure; r is the time dependent shell thickness of the particles from TEM measurement; R (~14nm) is the final shell thickness at the end of the reaction since the growth of silica shell thickness approaches plateau after 5 hours.

The apparent silica shell growth rate (k_c) is determined to be 0.19h^{-1} from the linear data points before 5 hours. The different value of k_c in our case from the reported value (0.032h^{-1}) could be due to the different ammonia concentrations [147]. The same trend of time dependent silica shell growth, in which the particle growth is rapid during initial reaction period and then levels off, is also observed when the silica precursor amount increases from 5g from 20g in appendix B.4.1 (Figure 81 and Figure 82).

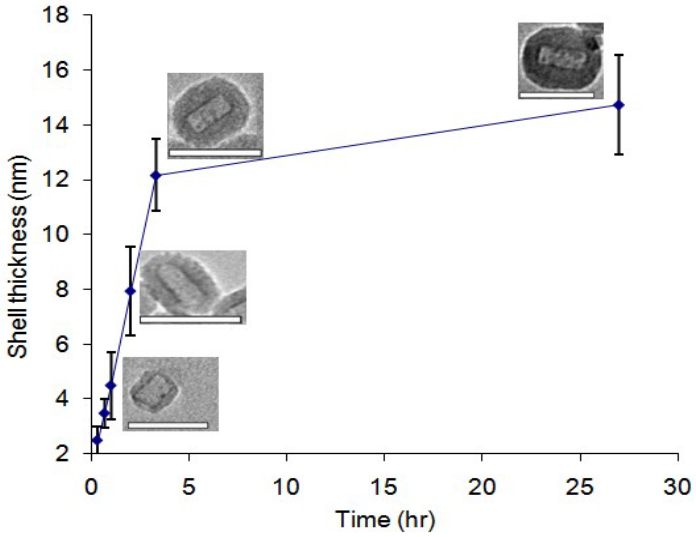

Figure 10: *Silica shell thickness vs. reaction time. Synthesis condition: 5g TEOS, 3mL 16.5M ammonia solution.*

3.2.2.2 TEOS amount

The same phenomena is observed that silica shell thickness (3nm to 9nm) goes up with the increase of TEOS amount (1g to 10g) while cavity size maintains constant 10.86 ± 1.29 nm (Figure 11). The reason for cavity size independent from reaction time will be discussed in detail in Section 3.3. Even when the TEOS amount is increased from 10 g with 1 hour reaction to 20g with 24 hour reaction time, the silica shell thickness is only increased to 18nm. This small increase in silica shell thickness could be resulted from the availability of water, which not only serves as the reactant for TEOS hydrolysis but also used to stabilize micelle. The overall reaction for TEOS hydrolysis and condensation is as follows:

$Si(OC_2H_5)_4+2H_2O = SiO_2 + 4C_2H_5OH$

In the solution, the molar ratio $M[H_2O]/M[TEOS]$ is 2.51 (when 20g TEOS is used) which is slightly higher than the required stoichiometry ratio since the excessive water is needed for stabilizing micelles.

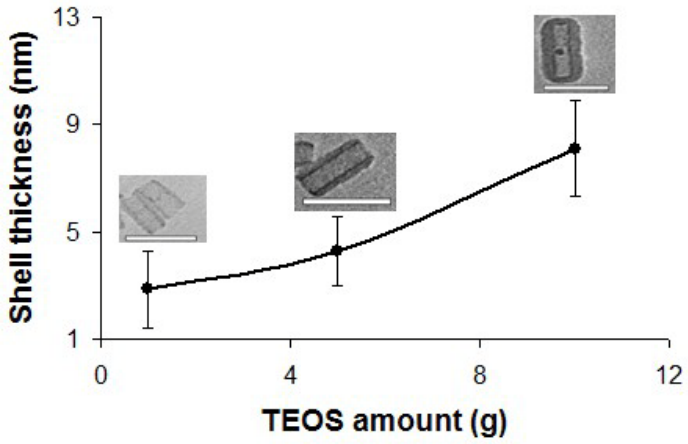

Figure 11: *Silica shell thickness vs. TEOS amount. Synthesis condition: reaction time 1hr, 3mL 16.5M ammonia solution.*

3.2.2.3 Ammonia solution

Besides TEOS amount and synthesis time, varying ammonia concentration is another way to adjust the thickness of silica shell. The core shell structure with poor uniformity is formed without the addition of ammonia solution (Figure 12-left), which serves as a base catalyst for TEOS hydrolysis [146, 147]. The silica shell thickness increases with the increasing of ammonia concentration from 0.25M to 8M (Figure 12-right). TEM pictures of materials with different ammonia concentrations could be found in Figure 83 in appendix. The growth rate of silica shell reaches plateau due to the limited availability of both water and TEOS amount. Also, higher uniformity is obtained at higher concentration. When it comes to change the pH of the solution by adding ammonia solutions, the water amount needs to be adjusted to maintain the same surfactant-to-water ratio.

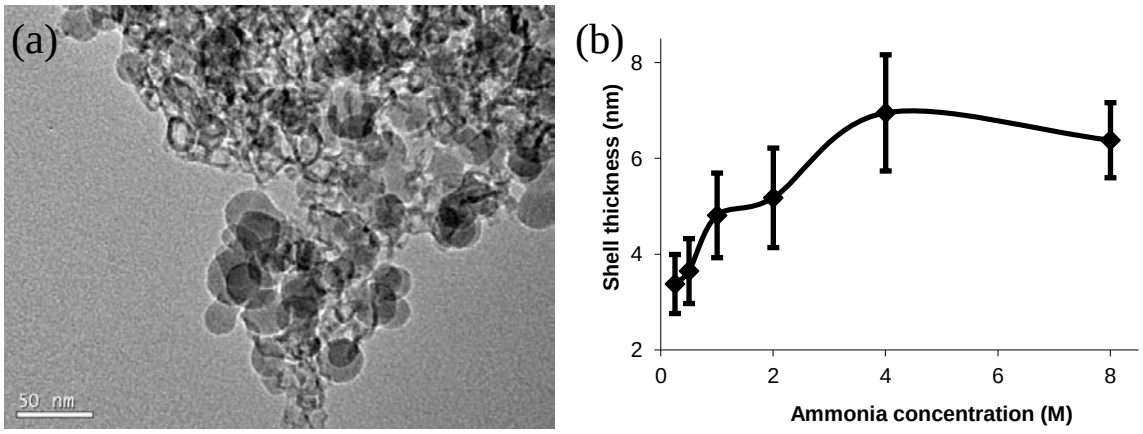

Figure 12: *(a) TEM images of $Ni@SiO_2$ without ammonia solution. (b) Silica shell thickness vs. ammonia solution concentrations. Synthesis condition: TEOS 10g, hydrolysis time 1hr.*

Even though the silica shell thickness can be tailored by adjusting synthesis parameters (reaction time, TEOS amount and the ammonia concentration), it is more difficult to achieve dimensional control on lower or higher end (eg. below 5nm or beyond 15 nm within ±1nm deviation) compared with middle range. Thinner shell under 5nm could not be achieved by only decreasing reaction time or TEOS amount. For example, a lot of open structures result from decreasing reaction time <40 minutes or decreasing TEOS to 1g (Figure 84 in appendix). This is because of the insufficient time for the nucleation and growth of silica or the lack of enough TEOS to form the shell. By carefully adjusting both parameters, shell thickness under 5nm can be tailored. Shells thicker than 15nm could not be achieved with increased TEOS and reaction time since the availability of water limits the growth of the silica shell. The solution is to increase the water amount while adjusting the surfactant amount at the same time to maintain a constant surfactant-to-water ratio. The importance of a fixed surfactant-to-water ratio is required because any variation will affect the shape of micelles, or it can compromise the stability of the microemulsion. However, increases in the surfactant amount are also limited since undissolved surfactant will lump together when it exceeds its solubility at 50^{o}C. A disrupted microemulsion

results in inhomogeneous silica particles. Figure 85 shows TEM pictures of particles with 20~50nm silica shell thickness with a wide size distribution and inhomogeneous particle shapes. Table 1 below listed the parameters to synthesize different shell thickness.

Table 1: *Key parameters to synthesize well-defined shell thickness from 3nm to 20nm*

Shell thickness	TEOS (g)	Time (hours)
3nm	3	1
4nm	2	2
5nm	3	2
7nm	5	2
10nm	10	2
12nm	10	24
20nm (*)	20	24

Note: Other parameters are the constant: surfactant 10.5g, 1.5mL 1M $Ni(NO_3)_2$, 1.5mL hydrazine hydrate, 3mL $NH_3.H_2O$. (*) additional 0.7g H_2O.

3.2.3 Size control- nickel particles

Initial attempts to control the nickel particle size in above hollow structures included increasing nickel precursor concentration, decreasing the amount of reducing agent hydrazine or slowing down the addition rate of hydrazine. These approaches were based on the idea that the concentrations of nickel ions and reducing agent would affect the rate of nickel nucleation and growth, which would eventually result in different sized nickel particles [60, 61, 148]. Unfortunately, the subnanometer nickel clusters are always obtained regardless of these changes to the synthesis system (Figure 86). Moreover, the hollow structure always co-exists with these subnanometer nickel clusters.

However, nickel particles size ranging from 1nm to 7nm embedded in silica shell were synthesized by a combination of changing hydrazine addition order or the absence of hydrazine and changing the nickel concentration. Without adding hydrazine, 1nm nickel particles embedded in silica shell were obtained. By increasing nickel nitrate concentration from 1M to

4M, 3nm nickel particles were synthesized. An alternative way to obtain 3nm nickel particles while keeping hydrazine in the system is to change the addition order of hydrazine and ammonia solution. An increase in $Ni(NO_3)_2$ concentration from 1M to 4M will result in the even larger nickel particles (7nm). The formation mechanism of different sizes of nickel particles will be discussed in detail in Section 3.3. Figure 13 shows the TEM of $Ni@SiO_2$ with different nickel particles sizes and their particle size distribution counted from at least 200 particles. The spherical structures are silica support. The black dots in bright field TEM pictures (Figure 13 a-e-1) are embedded nickel particles, which are also characterized as the bright dots in high-angle annular dark-field (HADDF) TEM pictures (Figure 13 a, b-2). Table 7 in appendix listed the synthesis conditions for obtaining different nickel particle sizes in these materials.

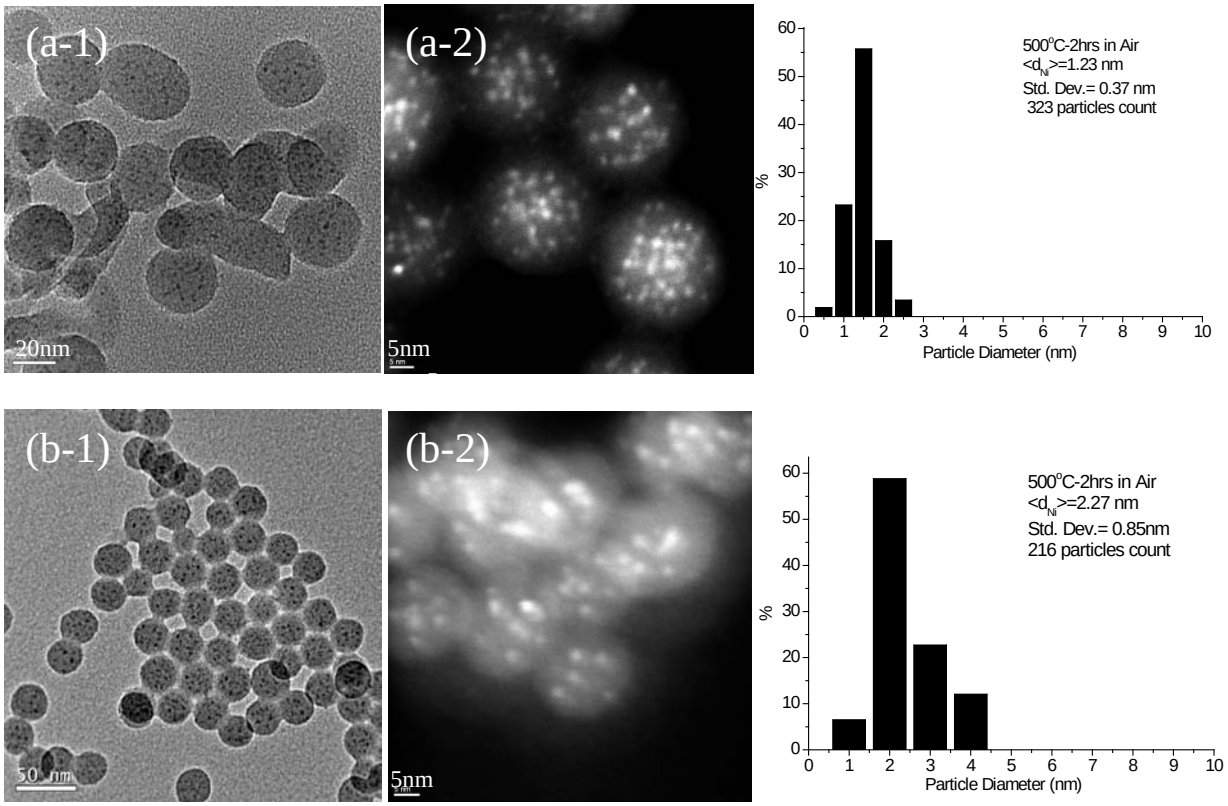

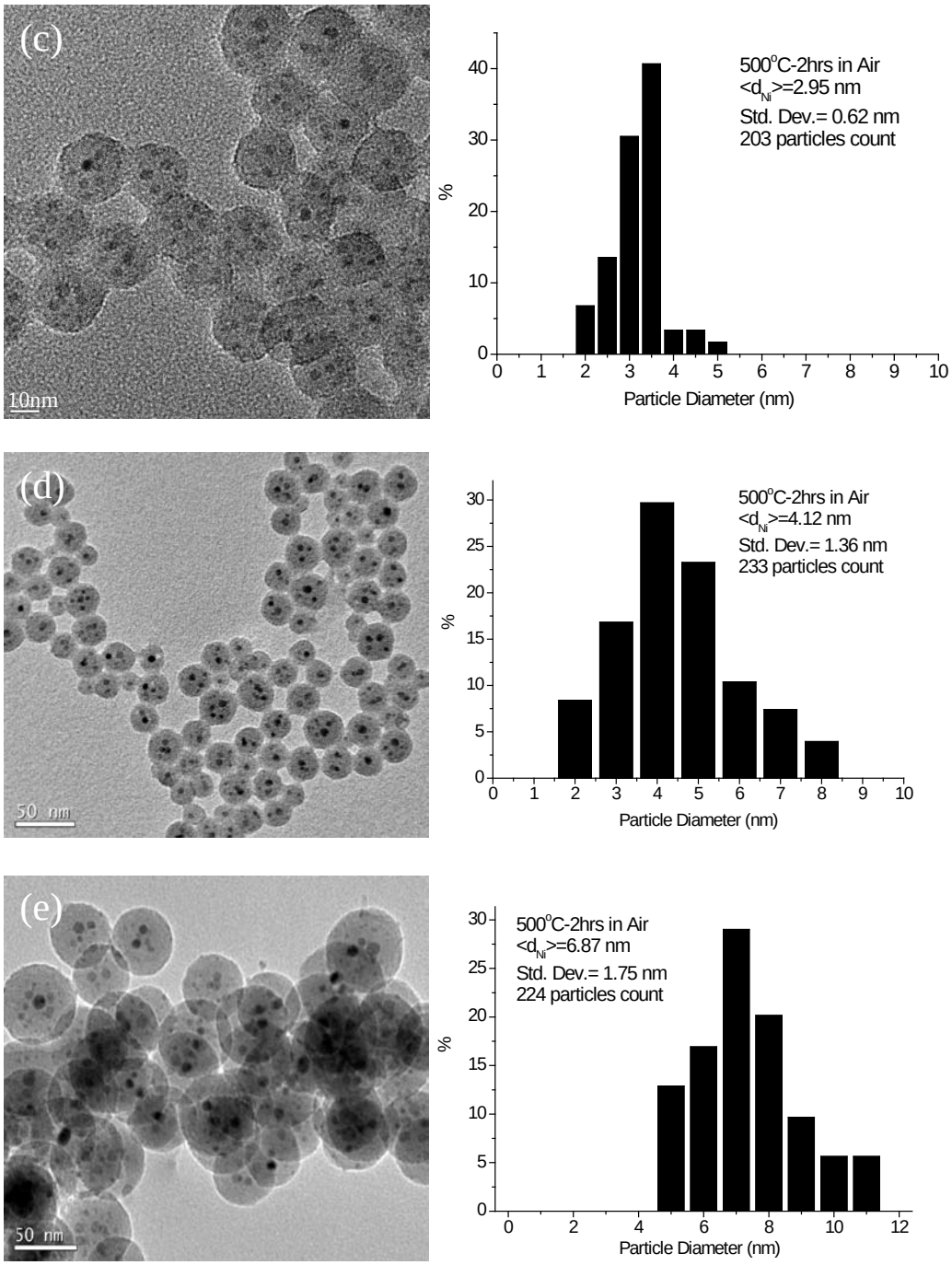

HADDF TEM pictures are provided by L. Shuang.

Figure 13: *(left) TEM images and (right) particles size distribution of different nickel sizes in (a) 1nm Ni@SiO_2, (b) 2nm Ni@SiO_2, (c) 3nm Ni@SiO_2, (d) 4nm Ni@SiO_2, (e) 7nm Ni@SiO_2*

Besides adjustment of the synthesis parameters (e.g. surface/water, TEOS amount), a number of other conditions (e.g. surfactant type, silica precursor type) were also studied to understand the chemistry of the system (Figure 87 and Figure 88 in appendix).

3.3 MECHANISM OF PARTICLE FORMATION

Based on the results in Section 3.2, the mechanisms of the hollow formation and the direction of silica shell growth are proposed. Our hypothesis is that the existence of nickel hydrazine complex stabilizes the micelles resulting in the formation of hollow structure; silica shell growths outwards the water oil interfaces due to the formation of hydrophilic silanol group. An illustration of the proposed mechanism is given below (Figure 14).

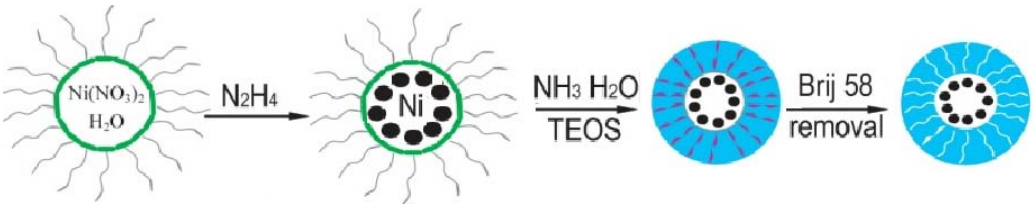

Figure 14: *Scheme of proposed mechanism for cavity and pores formation*

Firstly, micelles form within the oil phase following the addition of aqueous salt solution. The dissolved nickel nitrate remains within aqueous environment of these micelles and hence makes the microemulsion green in color. Subsequent addition of hydrazine formed Ni hydrazine complex $Ni(N_2H_4)_2^{2+}$, which shows pale violet color [149]. The addition of ammonia, which creates the basic environment, is able to reduce nickel ion by the reaction [60, 150, 151]: $Ni^{2+}+N_2H_4+4OH^-=2Ni+N_2+4H_2O$. The released gas bubbles were observed when adding ammonia solution to the microemulsion, which indicates a nitrogen release from the reaction. It

is noted that the reducing ability of hydrazine only occurs in basic environment, since the standard reduction potential for hydrazine in basic solution is -1.16V which is lower than that of Ni^{2+} (-0.25) while the reduction potential of hydrazinium ion in acidic solution is -0.23V [152]. However, the pale violet color does not disappear after the addition of ammonia in this case, which indicates that there is some extra nickel hydrazine complex existing in the system. The nickel hydrazine complex stabilizes the surfactant shell via hydrogen bonding, resulting in a reinforced oil/water interface membrane of reverse micelle and preventing it from collapse during the sol-gel process of silica sources [153].

To verify our hypothesis that nickel hydrazine complex plays an important role in the formation of hollow structure, synthesis with different chemical combinations are performed. Without the addition of nickel precursor, non-hollow silica spheres are obtained (Figure 15-a), indicating that hollow structures will not be formed without nickel species. Without addition of hydrazine, 1nm nickel particles embedded in a dense but porous silica spheres are obtained (Figure 13-a), indicating that neither nickel ion or nickel ammonia complex $Ni(NH_3)_6^{2+}$ is able to stabilize micelles and form hollow structures. Without addition of ammonia, no uniform core shell structure was formed. However, some of the hollow structures are formed (Figure 12-left), which indicates nickel hydrazine complex is able to stabilize micelles to some extent. Figure 15 shows the fraction of hollow particle among all particles (including dense and hollow particles) as a function of the nickel precursor concentration. When the concentration of $Ni(NO_3)_2$ is 0.1M, only 20% of the SiO_2 has cavity structure. When the concentration of $Ni(NO_3)_2$ increases to 1M, nearly all silica particles have cavity structures. Higher percentage of silica particle with cavity structure at higher nickel loading could be explained by the presence of more Ni hydrazine

complex to stabilize the micelles. 1M nickel nitrate is sufficient to achieve all particles with cavity structure without resulting excessive nickel outside of the silica particles.

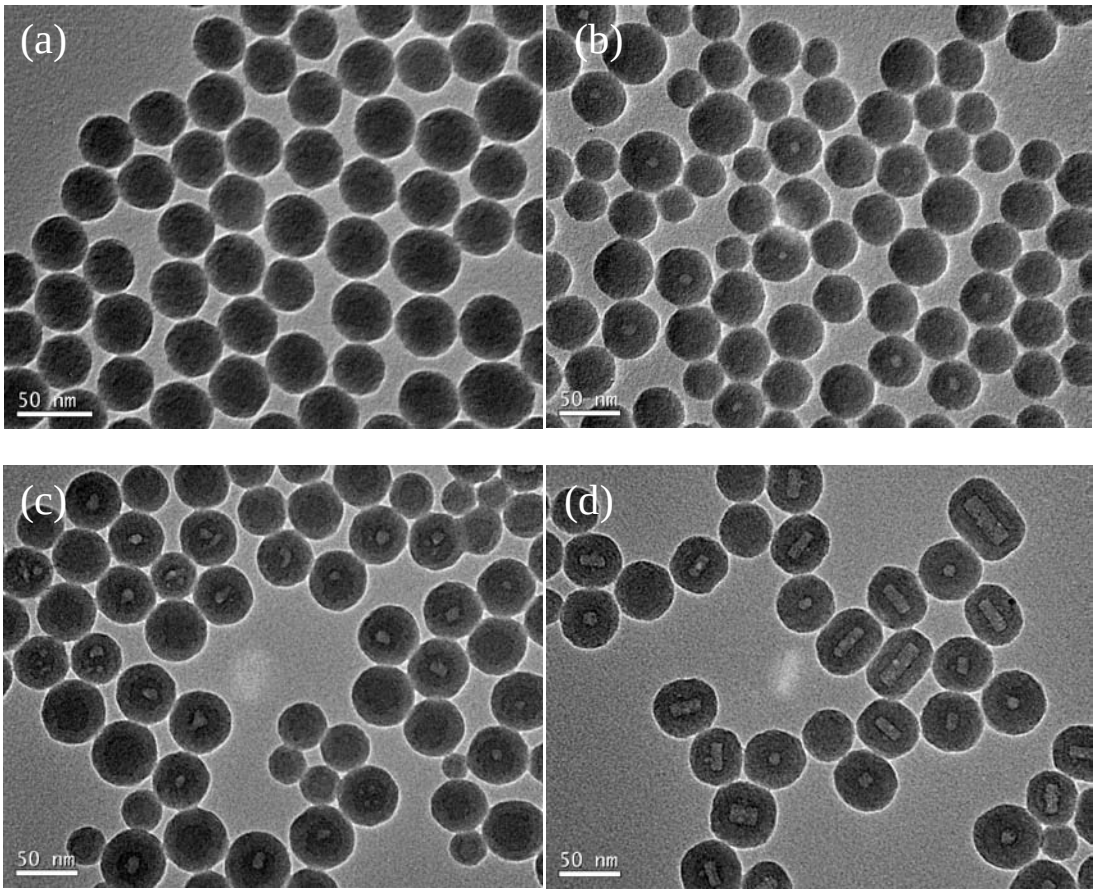

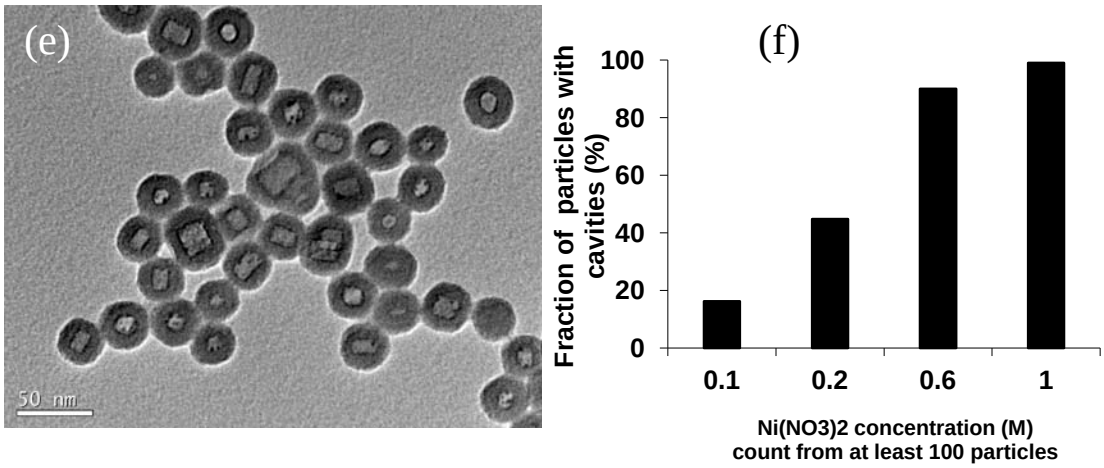

Figure 15: *TEM images of Ni@SiO_2 with different nickel nitrate concentrations with constant volume 1.5mL: a) 0M, b) 0.1M, c) 0.2M, d) 0.6M, e) 0.8M, f) fraction of particles with cavities (counted particle number>100)*

An alternative way to verify the hypothesis is to transform the non-cavity structure to cavity structure by replacing $Ni(NH_3)_6^{2+}$ with $Ni(N_2H_4)_2^{2+}$. Large nickel particles (3nm) were formed with the disappearance of the cavity structure when the addition order of hydrazine and ammonia solution is changed (i.e. ammonia addition before hydrazine). The formation of different nickel particle sizes could be explained by the different redox potential of Ni^{2+} (-0.25) and $Ni(NH_3)_6^{2+}$ (-0.476). $Ni(NH_3)_6^{2+}$ (blue color) is formed immediately by adding ammonia solution after nickel nitrate solution. A lower redox potential value means that the ion is more difficult to be reduced to Ni particles; the reduction rate of Ni ammonia complex is much slower than Ni ion. This is why when using the same amount of hydrazine, subnanometer Ni clusters were formed because of the fast reduction, and 3nm Ni particles were formed because of the slow reduction. Also $Ni(NH_3)_6^{2+}$ is not able to stabilize micelle, hence no hollow structures were formed in this case. However, the cavity structure can be formed again when the hydrazine amount is increased dramatically from 1.5mL to 10mL (Figure 16) since ligands in nickel ammonium complex are substituted by hydrazine ligands due to the hydrazine excess. It is noted

that the core shell structures are no longer uniform since large hydrazine volumes (10mL) will disturb the stability of the microemulsion system (50mL).

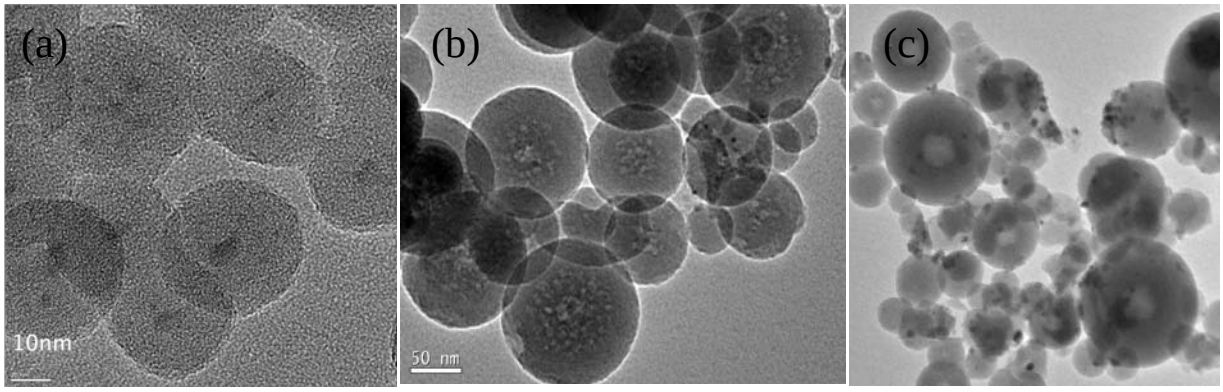

Figure 16: *TEM images of Ni@SiO_2 with the various amount of hydrazine a) 1.5mL, b) 4mL, c) 10mL*

Our hypothesis that silica shell grows outwards from the interface is verified by a study of the evolution of silica shell thickness with time (Figure 10), which shows silica shell thickness increases with reaction time while the cavity size is constant. TEOS, which has non-polar structure, diffuses from non-polar oil to react with water on the oil-water interface. Partially hydrolyzed TEOS has hydrophilic silanol group. Since silanol group is hydrophilic, water is still able to penetrate and diffuse through the hydrophilic interface to continuously react with fresh TEOS. In this way, we understand that silica grows outward from the water/oil interface, leaving the cavity size unchanged.

3.4 EXTENSION TO OTHER METALS

3.4.1 Monometallic Nanoparticles

To increase our understanding of synthesis mechanisms and to broaden availability of materials for applications, other metal cores were synthesized by replacing the nickel nitrate precursor with other metal salt precursors. $Co@SiO_2$, $Cu@SiO_2$, $Pd@SiO_2$, $Ag@SiO_2$ were synthesized by using corresponding metal nitrate salt. The color of the powdered sample with different metals before and after air calcination can be found in Figure 89. The synthesis procedure can be found in appendix B.7.1.

$Co@SiO_2$ and $Cu@SiO_2$ both have cavity structures in the core; $Ag@SiO_2$ partially has cavity structure, while $Pd@SiO_2$ only has non-hollow silica sphere structure. This could be explained by the different reducibility of metals and coordination bonding between hydrazine (Standard redox potential of Pd^{2+}=0.951>Cu^{2+}=0.341>Ag^{+}=-0.15>Ni^{2+}=-0.257>Co^{2+}=-0.28) [154]. Noble metals are more easily reduced while the alkali metals are more difficult to reduce (Figure 18). For example, palladium ion can easily be reduced by ammonia solution alone without the addition of hydrazine, and a similar structure of $Pd@SiO_2$ is still obtained (Figure 90). Even though a small portion of $Ag@SiO_2$ has cavity structure, this brings the question of obtaining more uniform cavity formation by simply adjusting reduction rate. Other metals such as Sn, Fe and Pb could also possibly form cavity structure since their redox potentials are between Cu^{2+} and Co^{2+}. However, the difficulty to obtain such a cavity structure might also be avoiding the transient state of the same metal which is beyond the workable range. For example, the redox potential of Fe^{2+} is much lower than that of Fe^{3+} and is beyond the workable range.

The concentration of metal salt solution does not determine whether the hollow structure will be formed or not. Decrease in the metal salt will only result in more silica spheres without metal cores (Figure 91 and Figure 92).

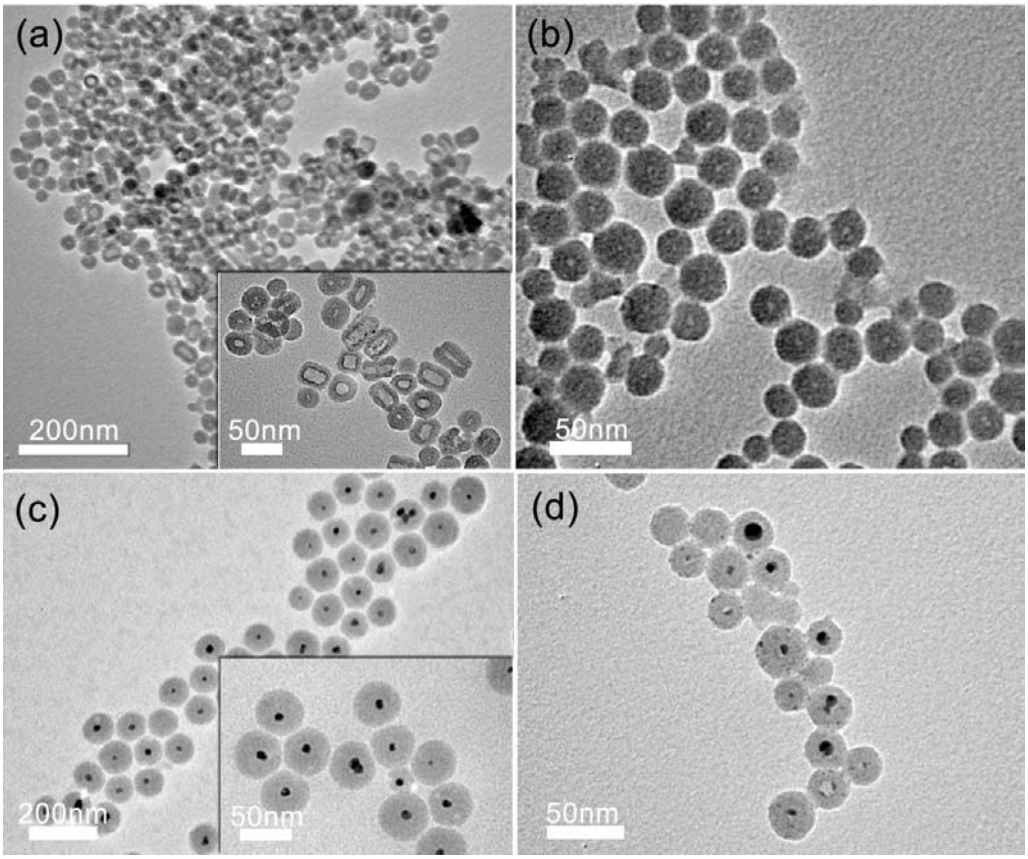

Figure 17: *TEM images of a series of metal core silica shell: a) Co@SiO_2, b) Cu@SiO_2, c) Pd@SiO_2, d) Ag@SiO_2*

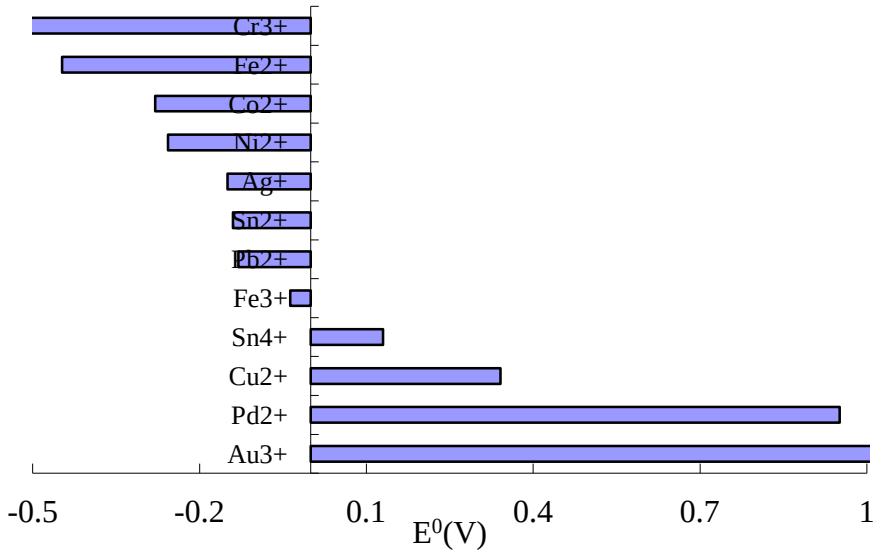

Figure 18: *Standard reduction potential of metal ions at 25^{o}C [154]*

3.4.2 Dual and Bimetallic nanoparticles

Ni@SiO_2 and Pd@SiO_2 that are synthesized following the same synthesis route possess different structures. This inspired us to synthesize dual NiPd@SiO_2. It is reported that bimetallic FePt was formed by simultaneous reduction of Fe and Pt ions with hydrazine in a reverse microemulsion system with Brij 52/56 and iso-octane [155]. Unfortunately, no bimetallic NiPd particles form in our case when combining $Ni(NO_3)_2$ and $Pd(NO_3)_2$; the different redox potentials of Ni^{2+} (-0.257) and Pd^{2+} (0.951) prevent the two ions from being reduced at the same time. Figure 19 shows dual NiPd@SiO_2 particles with different Ni/Pd molar ratios. The NiPd@SiO_2 inherited the structural features of both Ni@SiO_2 and Pd@SiO_2, in which the sub-nanometer clusters coated on the inner wall of hollow structures are nickel particles and the large particles (5-10nm) are palladium. A higher Ni/Pd molar ratio creates more core shell materials with a cavity structure in the total population as expected, since Ni hydrazine complex is responsible for the cavity formation.

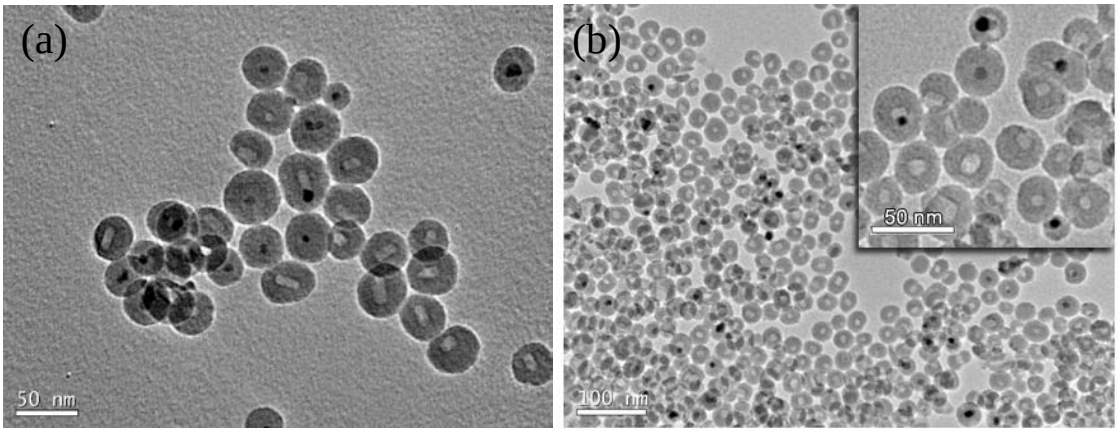

Figure 19: *(a) Pd/Ni=5.45:1 and (b) Pd/Ni=1:1 in dual Pd/Ni@SiO_2*

Bimetallic NiPd@SiO_2 can be synthesized using another synthesis route: two-step synthesis. 3nm NiPd bimetallic particles protected by PVP are synthesized following a method developed by Toshima group [156]. This synthesis procedure can be found in appendix B.8.1. Next, the PVP-protected NiPd particles are transferred to a Stöber solution consisting of an ethanol-ammonia-water mixture to coat with silica. Figure 20 shows the HRTEM and lattice spacing data of bimetallic NiPd particles. The (111) lattice spacing of the Ni/Pd nanoclusters (0.214nm) calculated from HRTEM is between pure Ni (0.2035nm) and pure Pd (0.2283nm), which indicates the formation of a NiPd alloy. Figure 21 shows the formation of a 50nm silica shell on pre-synthesized bimetallic NiPd particles after the Stöber reaction and the EDX spectrum confirms the existence of both Ni and Pd species in silica particles. The disadvantage of this method is that the silica shell thickness is not sensitive to the reaction time. 50nm silica shell is formed even though the reaction time is only 30 minute instead of 20 hours (Figure 93). The capability to synthesize bimetallic NiPd@SiO_2 opens opportunities to understand property difference between dual and bimetallic NiPd nanoparticles.

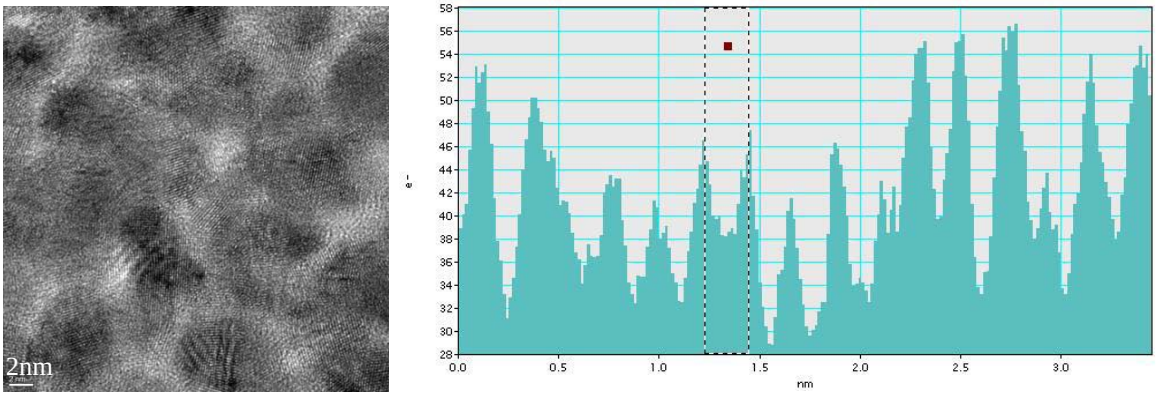

Figure 20: *(left) HRTEM image (right) Lattice spacing of Ni/Pd nanoclusters (Pd/Ni=3:2)*

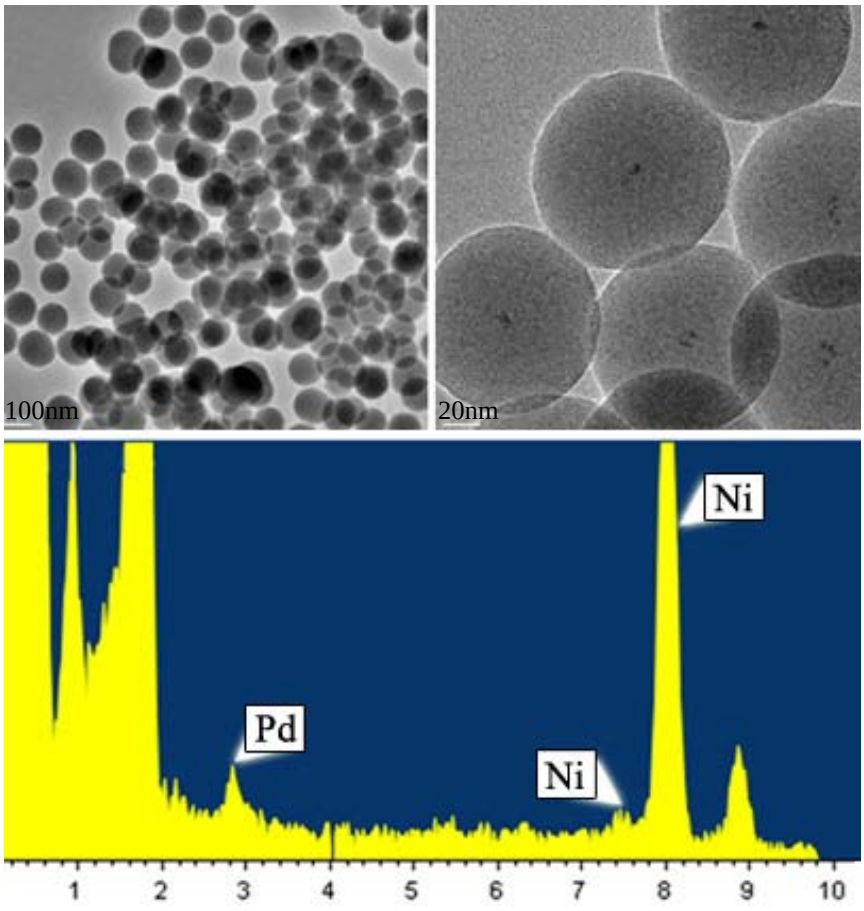

Figure 21: *NiPd@SiO_2 by Stöber method at different scales*

3.5 PROPERTIES

3.5.1 Porosity

3.5.1.1 Nitrogen sorption

One of the most important properties is the porosity of the support, which determines whether the material can be used as a catalyst. The reactants (gas or liquids) need to be able to diffuse though the torturous channels of support matrix to react with active components, which are usually embedded or capped by such matrix. The higher porosity will facilitate the transport of reactants and enable the surface reactions. The absence of pores or low porosity will block the active sites of the catalysts or pose mass transfer limitation, which results in no or lower reactivity of catalysts. The BET surface area and pore size distribution of core shell materials with and without cavity structure in comparison with pure silica particles synthesized from microemulsion system are measured from ASAP2020 instrument (Figure 22).

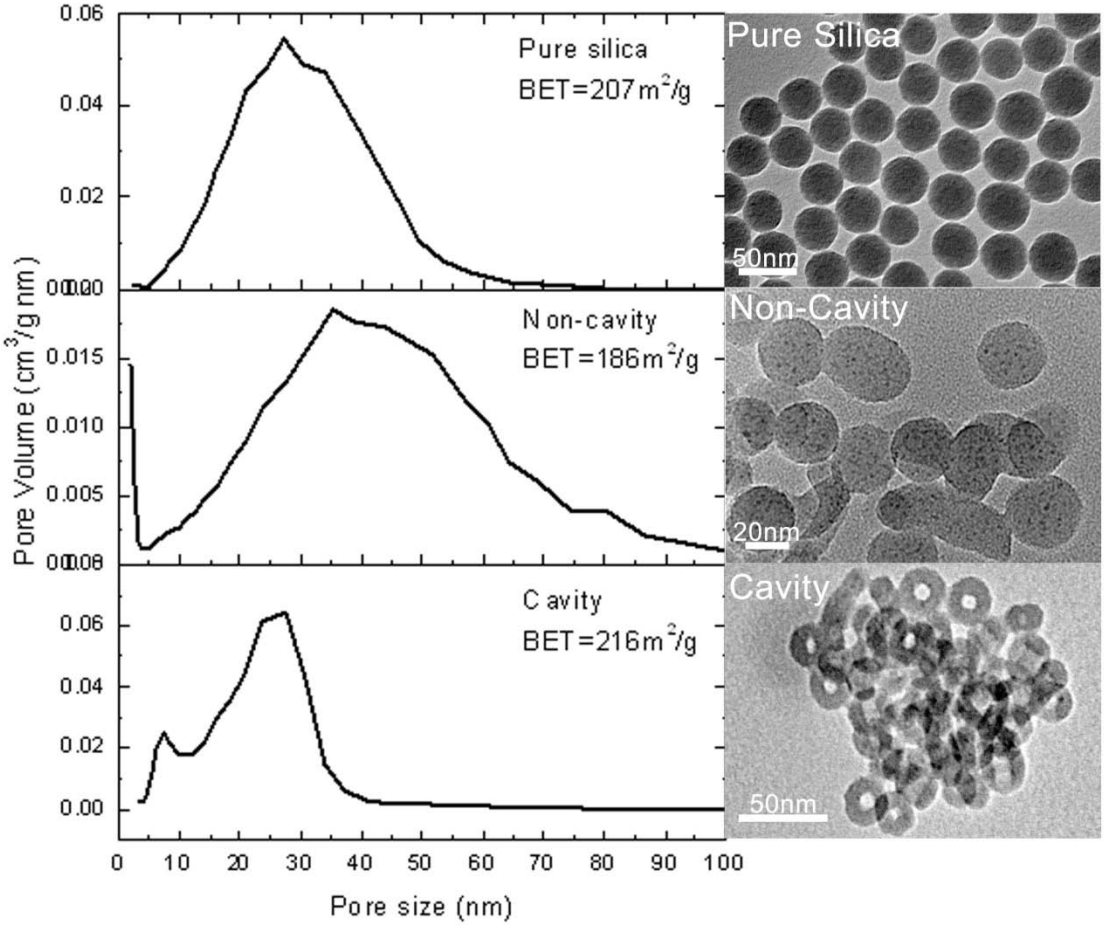

Figure 22: *(left) BET surface area and pore size distribution of Ni@SiO_2 with cavity structure, non-cavity and pure silica; (right) TEM of the corresponding material*

In the cavity sample, there are two pronounced peaks at 8nm and ~20-30nm. The peak at 8nm indicates the dimension of the cavity structure, which is 8nm in diameter. The peak between ~20-30nm results from the interparticle void spaces between the spherical particles. By contrast, there is only one big broad peak in the non-cavity and pure silica samples. The peak of the non-cavity sample shift slightly to a larger pore size compared with pure silica sample since the non-cavity particle (d~30nm) is slightly larger than that of pure silica particle (d~20-30nm). Figure 23-left also shows the pore size distribution and BET surface of the cavity-Ni@SiO_2 as a function of silica shell thickness. All the core shell materials with cavity structure have the pore

size at 8nm since they have similar cavity dimensions. The peak at ~20-30nm pore size shifts to a higher value at thicker shell as expected since the increase in the diameter of the whole silica particles creates a larger interparticle void space. The decrease in BET surface area at thicker shell can be explained by a heavy overlapping of the silica matrix which blocks the pore openings (Figure 23-right).

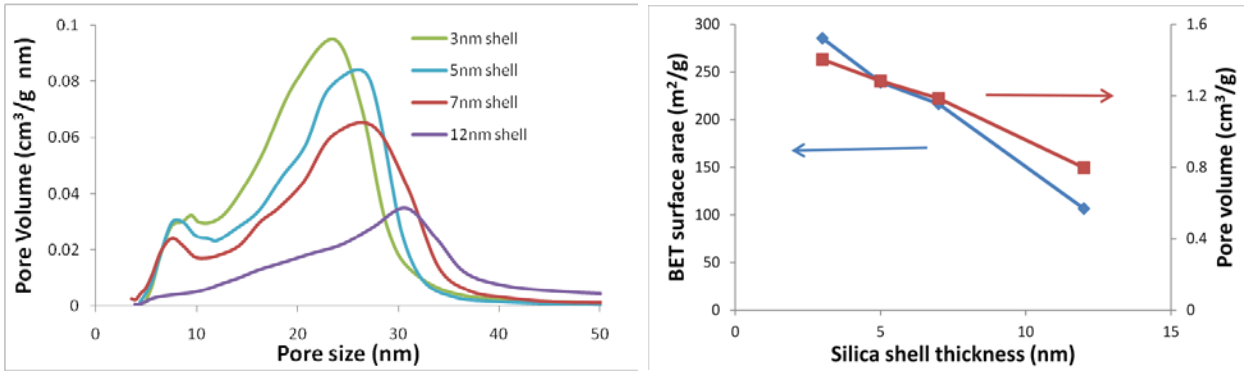

Figure 23: *(left) Pore size distribution and (right) BET surface area and pore volume of cavity Ni@SiO_2 with different shell thickness*

The ASAP2020 is not capable of detecting pore size distributions in microporous range (<2nm) since the system does not have enough vacuum system to reach the pressure range less than 0.01 P/P_o. However, it still gives an accurate BET surface area for both micorpores and mesopores. This is because the pressure range required to obtain data for total BET surface area (0.05 to 0.3 P/P_o) is much higher than that for micropore size distribution ($10e^{-7}$ to 10 e^{-2} P/P_o). To obtain the pore size distribution in microporous range, the samples are analyzed in Quantachrome autosorb1 instrument in NETL facility with collaboration with Dr. Fan Shi. Figure 24 shows the pore size distribution in non-cavity core shell materials with different nickel sizes and cavity materials with different shell thicknesses.

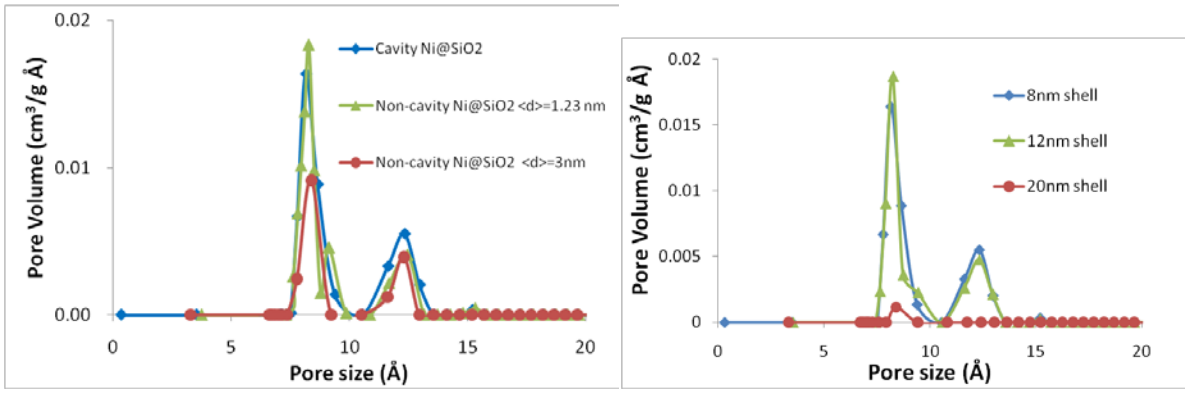

Figure 24: *Pore size distribution of microporous range in (left) both cavity and non-cavity Ni@SiO$_2$ structure (right) different shell thickness*

The pore size in the microporous range indicates the porosity of the silica shell. Figure 24-left shows not only that the core shell material with and without cavity structure have a pore size around 0.8nm, but also that the non-cavity Ni@SiO$_2$ with different sized nickel particles share the same silica pore size. This result indicates that the presence of nickel clusters embedded in the silica matrix does not attribute to the porosity of silica shell. The silica pore size is independent of the silica shell thickness in the cavity-Ni@SiO$_2$, which could be explained by the formation of silica pores via the removal of surfactants templates (Figure 24-right). Hence the same type of the surfactant used in all synthesis creates similar pore structures independent of the shell thickness or structure differences.

3.5.1.2 Accessibility of the cores-liquid phase

Not only are gases able to diffuse through the pores of silica shell, liquids are also able to diffuse through the silica pores. Nickel cores can be etched away by HCl, H_2SO_4 and HNO_3 at a range of concentrations without compromising the structures of the silica shell. The nickel loading and TEM images of materials after various etching times using different acids are given in appendix from Figure 94 to Figure 97 in appendix C.1.1. The acids molecules are dissociated

to the corresponding ions to diffuse through the silica pores and react with nickel. The ionic diameters of Cl^-, NO_3^- and SO_4^{2-} are 0.36nm, 0.38nm, 0.49nm respectively [157]. The decreased nickel loading as determined by EDX after etching with H_2SO_4 in Figure 98 indicates that the pore size of silica shell is at least 0.5nm since nickel particles inside of the shell have been etched away. Figure 25 shows the TEM images of the intact core shell structure during etching process.

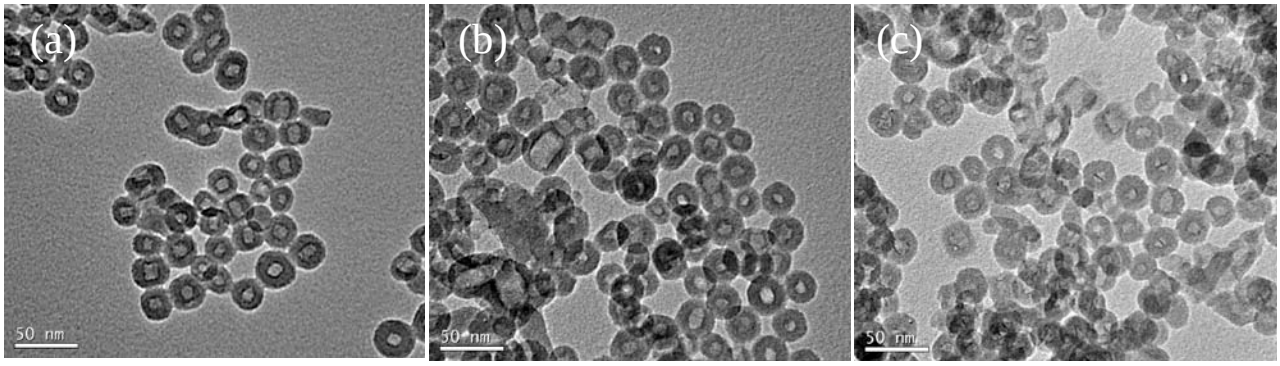

Figure 25: *TEM images of $Ni@SiO_2$ (a) before etching, (b) after etching for 1hr and (c) after etching for 12hrs with HCl (3M 10mL)*

Even though the liquids are able to diffuse through the silica pores, the initial nickel etching rate of $Ni@SiO_2$ core shell materials is much slower than that of Ni/SiO_2 obtained from impregnation method with external nickel outside of silica support (Figure 26). The difference of etching rate, which is due to the small pores of silica shell, indicates a strong diffusion limitation for core shell materials. The unchanged nickel loading after 5 hours etching can be explained by the possible strong interaction between nickel and silica support. There are two possible explanations for the higher final nickel loading of $Ni@SiO_2$ than that of nickel impregnated on commercial silica support (>99.5%, 10-20nm silica spheres from Aldrich). The first is that subnanometer nickel clusters are more likely anchored on the silica surface than large nickel particles, which may lead to an etching resistance. The other possibility is that the silica surface

derived from the microemulsion synthesis might lead to the higher interaction between nickel and silica support.

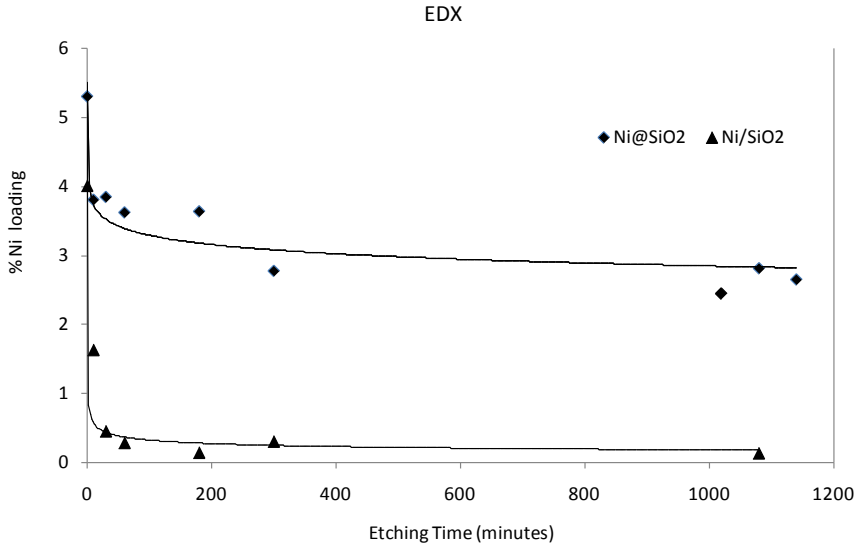

Figure 26: *Nickel loading from EDX with various etching time using 3M 10mL HCl of Ni@SiO_2 and IMP-Ni/SiO_2*

3.5.2 Crystallinity of nickel particles

The XRD patterns of Ni@SiO_2 with different structure and different nickel particle sizes are shown in Figure 27. The broad peak between 20° and 30° is amorphous silica. No nickel peak is detected in both cavity-Ni@SiO_2 and 2nm Ni@SiO_2 since the nickel crystal size is too small. The characteristic peaks at 44.38° and 51.75° in 4nm Ni@SiO_2 sample correspond to planes Ni (111) and Ni(200) according to JCPDS-ICDD 4-850. XRD needs to be performed immediately after reduced since the nickel particles are easily oxidized after exposure to air (see Figure 100).

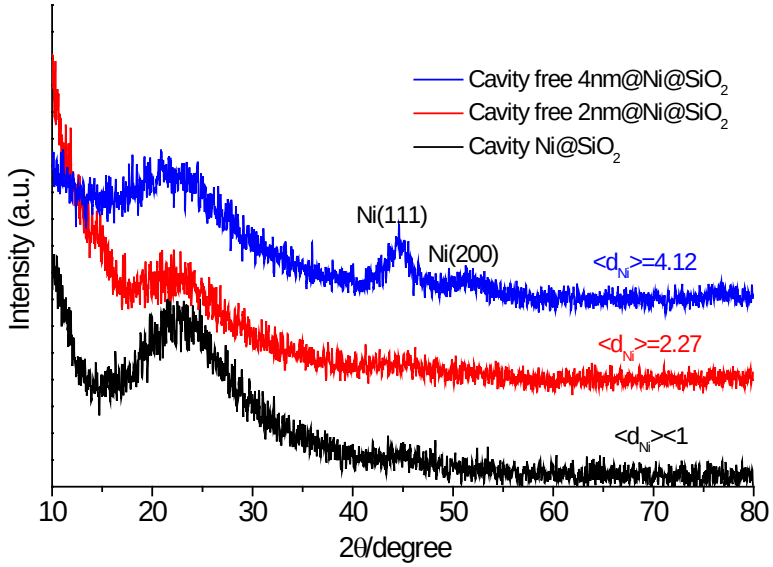

Figure 27: *XRD patterns of cavity-Ni@SiO₂, non-cavity 2nm Ni@SiO₂ and non-cavity 4nm Ni@SiO₂*

3.5.3 Reducibility and oxidation capability of nickel particle

TPR is employed to understand the particle size dependent reducibility as well as the nickel particles in different configurations (i.e. attached but not encapsulated nickel in cavity structure versus fully encapsulated nickel in non-cavity structure). There is no specific temperature value, but rather a temperature range for the reduction peak for different nickel species since the peak locations depend on many factors: the nature of nickel precursor [70], support [70], nickel loading [158], incorporation method (impregnation, deposition-precipitation, ion-exchange, etc) [159] and heating rate [160]. Table 2 lists the peak location for different Ni supported silica materials from literature. In general, TPR peaks shift to lower temperature at larger particles and shift to higher temperature with a stronger metal-support interaction [70, 158, 161, 162]. The peaks at a lower temperature range (between 200°~400°C) usually result from the

reduction of bulk NiO to metallic nickel [163]; while peaks in the range between 400°C to 800°C denote nickel silicate species or the stronger nickel support interaction [70, 158, 161].

Table 2: *TPR peak locations and assignments of nickel on silica catalysts from literature*

Sample	Ni particle size	Ramping rate (K/min)	TPR peak max (°C)	Peak assignments
[(a)] Ni on MCM41 by wet-impregnation	<3nm and 10nm	10	277~327, 527~627	bulk NiO (277~327°C), small nickel particles (527~627°C)
[(b)] Ni/SiO_2 by deposition-precipitation	3.5nm	10	610~770	strong interaction-nickel silicate formation
[(c)] Ni on silica by sol-gel	4nm	5	400~500, 700	n.a.
[(d)] Ni/SiO_2 by wet-impregnation	29.9	10	327,452	larger particle (327°C), well-dispersed Ni with stronger interaction (452°C)
[(e)] Ni/SiO_2 by wet-impregnation	2.5nm	5	one broad peakat at 470	n.a.
	5.7nm	5	one broad peak at 500	n.a.
	10.2nm	5	320, 570	bulk NiO (320°C), nickel hydrosilicate(570°C)
[(f)] Ni/SiO_2 by wet-impregnation	n.a.	12	400, 500~550	large bulk NiO with little interaction with support(400°C); small NiO stongly attached to support (500°C)
[(f)] above catalyst after 900°C calcination	n.a.	12	new peak >600	deeper chemical interaction with silica support

Note: literature sources[(a)][163],[(b)][69],[(c)][164],[(d)][162],[(e)][158],[(f)][159]

Figure 28 shows the TPR of the cavity-Ni@SiO_2 as well as non-cavity Ni@SiO_2 with two different nickel particles sizes. For comparison, the TPR profiles of IMP-Ni/SiO_2 and DP-Ni/SiO_2 are also studied. There are two distinct peaks in all core shell materials (i.e. synthesis from the microemulsion system). The peak at ~300-400°C is bulk NiO with weaker interaction with silica support and the peak at ~400-500°C is from the NiO in intimate contact with the silica support. There is only one low temperature peak in DP-Ni/SiO_2, which indicates for nickel particles located on the external surface of silica spheres weakly interacted with the silica support. This peak becomes wider and shifts to even lower temperature (~200°-300°C) for IMP-Ni/SiO_2, which could be explained by a wide range of nickel particle distributions at larger sizes. Overall, there are two types of NiO present for all nickel core shell materials while only one reduction

peak at lower temperature region is present for DP-Ni/SiO_2. The absence of a high temperature reduction peak in DP-Ni/SiO_2 resulting from the stronger interaction between the metal and support could explain the lower thermal stability of nickel particles in DP-Ni/SiO_2. The correlation between TPR and nickel stabilization are discussed in section 4.3.

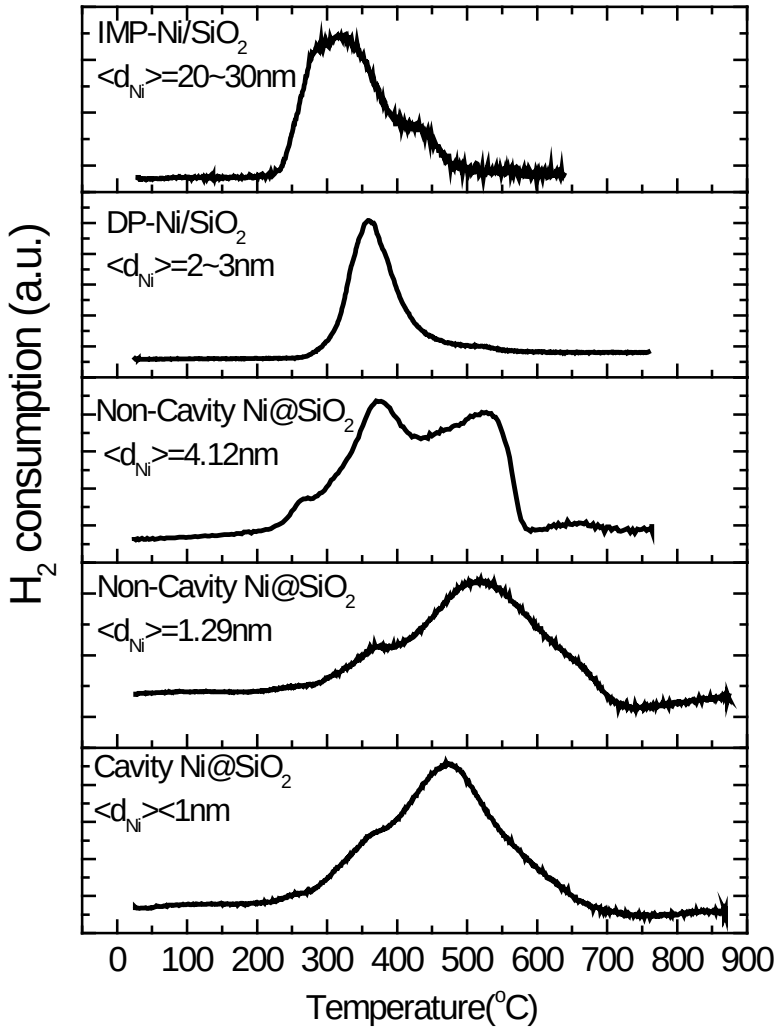

Figure 28: *TPR as a function of nickel particle sizes in non-cavity Ni@SiO_2, cavity-Ni@SiO_2, DP-Ni/SiO_2 and IMP-Ni/SiO_2*

The TPO of all core shell materials does not have any distinct peak in contrast with IMP-Ni/SiO_2 which has a wide TPO peak around 300°C (Figure 101 in appendix) [165]. A reason for this could be nickel clusters that in core shell materials are easily oxidized after its exposure to air at the room temperature.

3.5.4 Chemisorption

Three gases (N_2O, H_2 and CO) are commonly used as probe molecules to determine the metallic surface area. Room temperature H_2 chemisorption is the most common technique to determine the metallic surface area for nickel supported on alumina or silica catalysts. It is reported that N_2O and H_2 give comparable results for copper-based catalysts [166, 167]. Even though the formation of $Ni(CO)_4$ at 298K limits the usage of CO as a chemisorption gas for nickel catalysts, a number of researchers still use CO as a probe gas [67, 168]. It is also reported CO chemisorption can be performed at 273K to avoid $Ni(CO)_4$ formation [169]. Table 3 lists the H_2 and N_2O chemisorption results of cavity-$Ni@SiO_2$ and non-cavity $Ni@SiO_2$ as well as IMP-Ni/SiO_2 and commercial HiFuel Ni catalyst. The metal dispersion ($D\% = 96.7/d_{Ni}$, nm) and surface area based on nickel particle sizes determined from TEM images are also included in the table for comparison.

Table 3: *H_2 and N_2O chemisorption data for cavity-Ni@SiO_2, non-cavity Ni@SiO_2, IMP Ni/SiO_2 and HiFuel Ni catalysts*

		H_2 Chemisoprtion		N_2O Chemisoprtion		Theoretical calculation	
Sample	Ni loading	Disperson	Metallic surface area (m^2/g_{Ni})	Disperson	Metallic surface area (m^2/g_{Ni})	Disperson	Metallic surface area (m^2/g_{Ni})
Cavity $<d_{Ni}><$1nm,20nm shell[(1)]	1.20%	1.30%	8.8	3.92%	26.08	96.70%	674.16
Cavity $<d_{Ni}><$1nm,20nm shell[(2)]	1.20%	7.24%	48.2	16.90%	112.7	96.70%	674.16
Cavity,$<d_{Ni}><$1nm,6nm shell[(1)]	4.45%	2.88%	19.2	1.03%	6.87	96.70%	674.16
Cavity,$<d_{Ni}><$1nm,6nm shell[(2)]	4.45%	n.a.	n.a.	9%	59.9	96.70%	674.16
Non-cavity,$<d_{Ni}>$=1.23nm	4.24%	n.a.	n.a.	670%	190	78.60%	548.10
Non-cavity,$<d_{Ni}>$=1.95nm	6.70%	3.00%	20.1	0.47%	3.12	49.50%	345.72
Non-cavity, $<d_{Ni}>$=4.12 nm	12.40%	1.66%	11.04	1.61%	10.69	23.40%	163.63
IMP Ni/SiO_2,$<d_{Ni}>$=20~30 nm	20%	1.23%	8.21	1.01%	6.75	4.83%	33.71
Commercial Hifuel Ni	10%	0.85%	5.62	n.a.	n.a.	3.22%	22.47

[(1),(2)]separate runs for the same sample. Data provided by Dr. Fan Shi in NETL

One can see that the analyzed chemisorption value is much lower than the theoretical calculated value. One of the reasons for this unreasonably low dispersion and metal surface area could be inapplicable H_2 and N_2O adsorption stoichiometry for core shell materials. It is reported that the H/Ni_S=1 is only valid when nickel loading is higher than 3% and the nickel dispersion is between 15~50% [169]. By comparison, the dispersion of cavity-Ni@SiO_2 and non-cavity Ni@SiO_2 with small nickel particle sizes are well above the applicable dispersion range according to theoretical calculated values. Another reason for the low chemisorption data could be a strong interaction between the nickel and silica support, which prohibits or slows down the adsorption process of probe gases. A number of researchers also reported that the dispersion of small nickel particles (<5nm) is lower than 5% (Table 4) [124] [170] [171].

Besides the under-valued data, another observation is inconsistent results between repeat runs and different probe gases. The reason for the discrepancy could be the nickel particles are so small (<2nm) that H_2 and N_2O absorb poorly on nickel surface. In contrast, the H_2 and N_2O data

is comparable in non-cavity Ni@SiO_2 with 4.12nm nickel particle size and IMP-Ni/SiO_2 since they have sufficient nickel loading and nickel particles are large enough to coordinate with both H_2 and N_2. The dispersion of IMP-Ni/SiO_2 in our case is comparable with the reported data in literature [162, 172]. Another reason for the inconsistent results between different runs in cavity-Ni@SiO_2 could be the dynamic adsorption process. It is reported that that the amount of irreversibly adsorbed H_2 on Ni/SiO_2 varies significantly depending on nickel crystallite sizes [169].

Table 4: *The dispersion and surface area per gram metal of the catalyst with different nickel sizes and loading from literature*

Nickel particle size from XRD	Nickel loading	Support	Probe gas	Dispersion	Metallic surface area (m^2/g_{Ni})
[(a)] 2~3nm	5%	SiO_2	CO	37%	280
[(b)] <5nm	3.70%	Al_2O_3	H_2	2.20%	n.a
[(b)] <5nm	11%	Al_2O_3	H_2	2.80%	n.a
[(b)] 7nm	40%	Al_2O_3	H_2	11%	n.a
[(b)] 16nm	75%	Al_2O_3	H_2	5.40%	n.a
[(c)] 1.4nm layer	5%	Al_2O_3	H_2	3.21%	2.29
[(d)] 8.2nm	16.30%	MgO	H_2	1%	n.a
[(e)] 21.8nm	3.90%	SiO_2	H_2	2.70%	0.59
[(f)] 2.6nm	3.60%	SiO_2	H_2	37%	n.a
[(f)] 2.9nm	13.50%	SiO_2	H_2	41%	n.a
[(g)] 29.9nm	5%	SiO_2	H_2	2.80%	18.2

Note: Literature sources [(a)][67], [(b)][124], [(c)][170], [(d)][171], [(e)][172], [(f)][169],[(g)][162]

The results suggest that we are currently not able to obtain the reasonable dispersion and nickel surface area data for core shell materials via chemisorption technique. The possible explanation could be the classic chemisorption model (i.e. $H/Ni_S=1$) is not applicable for sub-nanometer nickel clusters.

3.6 SUMMARY

The presence of an inert silica shell, which is supposed to prevent nickel particles from sintering at moderate or high temperatures, motivates us to synthesize core shell materials. Two types of core shell materials with the distinction of the cavity structure are introduced. The uniqueness of our core shell material is the cavity structure and the formation of sub-nanometer nickel particles sizes. The cavity structure in core shell material not only facilitates the accessibility of nickel particles with reactants due to the open space, but also potentially simplifies the diffusion pathway of reactants. The diffusion pathway in cavity $Ni@SiO_2$ is consistent for all nickel particles while it varies in non-cavity $Ni@SiO_2$ since nickel particles are dispersed through the entire silica matrix with different distances to the exterior surface. The formation of sub-nanometer nickel particles not only provides high surface-to-volume ratio, but also potentially possesses some unique catalytic properties due to increased active steps and terrace sites. More importantly, the synthesis approach to achieve both cavity structure and sub-nanometer nickel particles is simple and straightforward. Other single (Co, Pd, etc) or double-metal (Pd/Ni, etc) cores are also easily obtained from this synthesis route, which opens up the opportunities for a wide range of reactive system applications.

The presence of hydrazine and its addition before ammonia are crucial for the formation of a cavity structure. The formation of a cavity structure is attributed to the formation of a nickel hydrazine complex, which is able to stabilize micelles that lead to the cavity structure. We also demonstrated the fine control over the key dimensional elements of core shell materials, such as

silica shell thickness (~3-20nm), nickel particle sizes (~7nm), and shape of the particles. The silica shell grows outwards from the water-oil interface in a positive relationship with reaction time, TEOS amount, and ammonia concentration, yet is limited by the availability of water in the microemulsion system. The well controlled core shell materials enable us to systematically investigate size dependent catalytic properties as well as mass transfer limitation as a function of shell thickness for future studies.

4.0 THERMAL STABILITY OF CORE SHELL MATERIALS

We are able to fabricate core shell materials with controllable dimensions (i.e. nickel particles size and shell thickness) in different configurations (i.e. cavity and non-cavity structure). Now let's study the thermal stabilities of core shell materials by understanding the behavior of both nickel particles as well as porosity variation of silica shell at different temperatures either in air or H_2. The materials, which will be studied in this chapter, are non-cavity structure with the particle size 1nm, 2nm and 4nm as well as cavity structure with the particles size under 1nm. As comparison materials, nickel supported on silica materials from wet-impregnation method (IMP-Ni/SiO_2) as well as deposition-precipitation method (DP-Ni/SiO_2) were used. The materials are calcined at different temperature between 600°C and 1000°C. The heating rate is 20°C/min and the set-point temperature is held for 2 hours prior to characterization. The samples, at different stages of the sintering process of the catalysts, are characterized by BET, TEM, XRD and TPR. Finally, the stability of core shell materials and IMP-Ni/SiO_2 were compared in reactive applications as catalysts for both ethylene hydrogenation and CO methanation reaction systems.

4.1 NICKEL PARTICLES

The stability of core shell material includes both the stability of nickel particles and the silica support. Instability of nickel particles means the agglomeration from small particles into large particles, which results in a loss of nickel surface area and decreased reactivity. Understanding the stability of nickel particles in different configurations will help us to understand their performance in more complex reaction systems, as well as help guide us to design catalysts with a more enhanced stability.

Nickel sintering behavior is studied by calcining core shell materials in H_2 flow at specific temperatures for 2 hours. Conducting thermal testing predominantly in a reducing environment provides a worst case perspective of stability since nickel is less thermally stable in H_2 compared to air due to the strong interaction between NiO and SiO_2 [173]. The average nickel particle size as well as its size distribution after each temperature treatment is measured from TEM nnn and XRD. One can expect the nickel particles in core shell materials to be more stable than those in DP-Ni/SiO_2 due to the presence of a protective silica shell. A number of research groups have demonstrated the efficiency of a silica shell for stabilizing metal particles at high temperature [18-23]. However, these studies were only conducted on materials with single metal core (above 5nm) larger than pore size of the support. The successful synthesis of a wide range of nickel particle (from <1nm~7nm) enables us to compare nickel stability when its size is smaller or comparable with silica support (pore size 0.8nm). Moreover, the introduction of core shell with cavity structure allows us to compare nickel particles in different configurations (e.g. the nickel particle interaction with the silica support depending on the degree of encapsulation).

4.1.1 Non-cavity structure

4.1.1.1 1nm $Ni@SiO_2$

The initial nickel particle size is narrowly distributed with the average particle size 1.23nm (Figure 29-a1). The nickel particles grow slightly to 2.46nm after the thermal treatment at 800°C and vacate to leave behind some cavity structures in the silica spheres (Figure 29-b1). The newly formed cavity structure is the key difference between 1nm $Ni@SiO_2$ and 2nm $Ni@SiO_2$. When the size of nickel particles is smaller than silica pore size, they are able to easily diffuse through the silica matrix and collide with neighboring nickel without disturbing silica matrix. When the nickel particles are larger than silica pore size, their diffusion will induce the reconstruction of silica matrix. From particle size distribution, one can see a small portion of nickel particles in 1nm $Ni@SiO_2$ with sizes smaller than silica pore size while all nickel particles in 2nm $Ni@SiO_2$ are larger than silica pore size (Figure 29-a2, Figure 32-a2). This could explain why some cavity structure is newly formed in 1nm $Ni@SiO_2$ after 800°C treatments, which is not observed in 2 nm $Ni@SiO_2$. Even though the nickel particles seem to be fully encapsulated with silica shell from the TEM image (Figure 29-a1), it might still have some open space around them since TEM image only gives us 2-D projection. One can imagine that a silica support with such irregular tortuosity would hardly cover the regular-shaped nickel spheres without any space. It is possible that one nickel particle diffuses though the matrix to “join” the neighboring nickel and leaves an empty space. The newly formed larger nickel particle would remain in the same position and yet would occupy more empty space (see Figure 30).

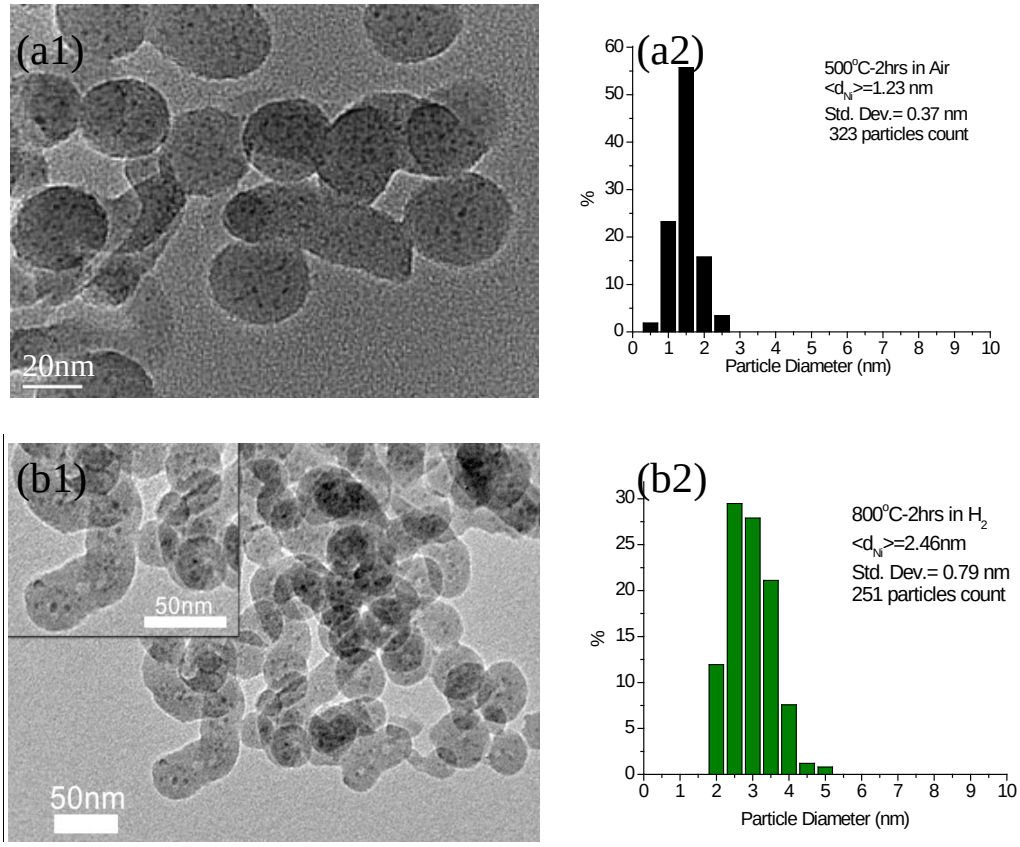

Figure 29: *TEM and nickel particle size distribution of 1nm Ni@SiO_2 (a) before and (b) after thermal treatment at 800°C for 2hrs in H_2*

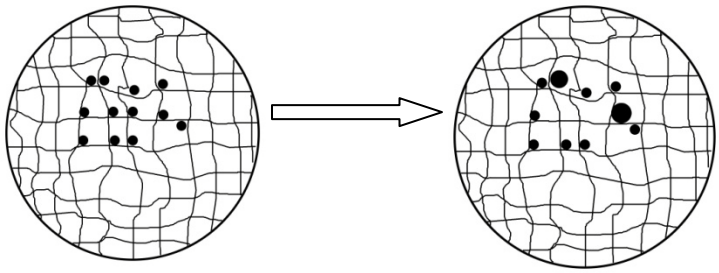

Figure 30: *Scheme of the cavity formation during sintering for nickel particles smaller than silica pore size*

4.1.1.2 2nm Ni@SiO_2

Since the diffusion of nickel particles through silica pores is observed when the nickel particle sizes are smaller or comparable with the pore size of silica shell, the core shell material

with initial nickel particle size slightly larger than silica pore size is studied. Figure 31 shows the TEM images and particle size distribution of sintered nickel particles after thermal treatment at different temperatures. There is hardly any discernible change of nickel particle size after thermal treatment at 700°C. The distinction from 1nm Ni@SiO_2 is no cavity structure is observed in 2nm Ni@SiO_2 since silica shell is more efficient to stabilize nickel particles when their sizes are larger than the pore size. XRD also shows the corresponding nickel size growth (Figure 32). No nickel peak is detected at 500°C since the nickel size is too small and below XRD detection limit. The appearance of Ni (111) and (200) peaks after thermal treatment at 1000°C indicates the nickel size increase, which agrees with TEM observations. Another interesting observation is that the sintered nickel particles move towards the center of the silica particles to merge from multiple nickel cores to a single core.

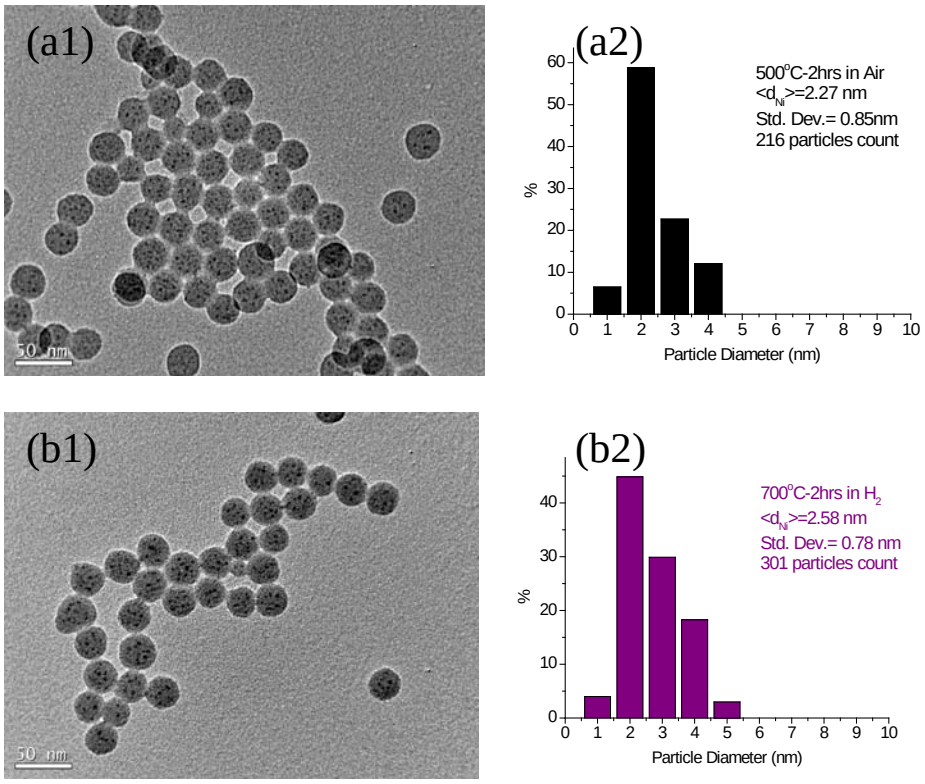

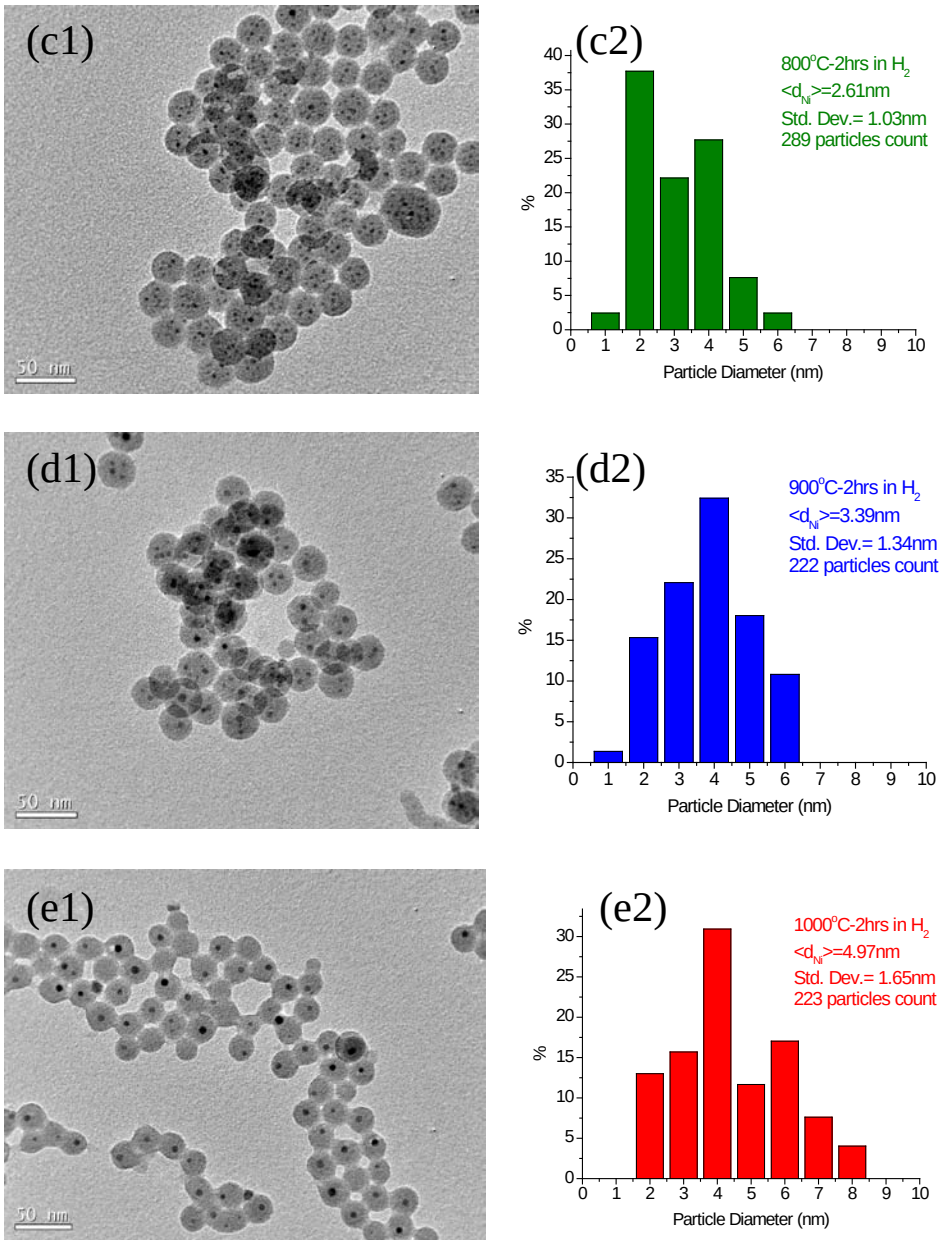

Figure 31: *TEM and particle size distribution of 2nm Ni@SiO_2 before (a) and after thermal treatment at (b) 700°C, (c) 800°C, (d) 900°C and (e) 1000°C for 2hrs in H_2*

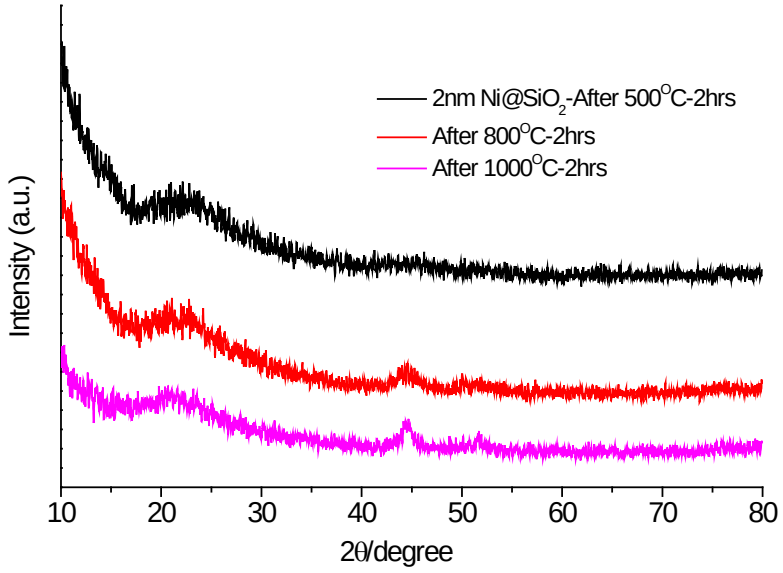

Figure 32: *XRD pattern for 2nm Ni@SiO_2 before and after thermal treatment for 2hrs in H_2 at 800°C and 1000°C*

4.1.1.3 4nm Ni@SiO_2

The same trend of nickel growth in 2nm Ni@SiO_2 during sintering process is also observed in core shell material with other larger nickel particle sizes. Figure 33 shows the TEM pictures and particle size distribution of sintered nickel particles in 4nm Ni@SiO_2 after thermal treatments. The increase in nickel particle size accompanies the merging multiple cores to a single core towards the center of the silica particles. This trend is quantified in Figure 34 by the temperature dependence of the percentage of the nickel core numbers in silica spheres. There is a wide range of nickel core numbers at 500°C and 800°C. After 900°C, the majority of silica particles only have single nickel core. After 1000°C, the silica particle is either in absence of nickel particles or has only one nickel particle in the center. Some nickel particles diffuse out of the silica shell resulting in nickel-free silica spheres.

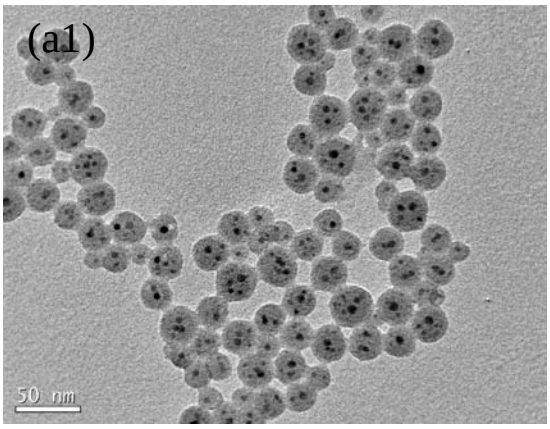
(a1)
50 nm

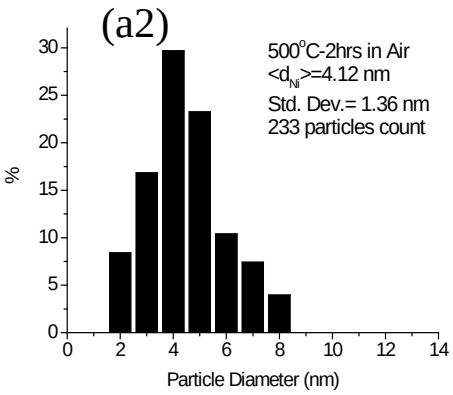
(a2)
500°C-2hrs in Air
<d_Ni>=4.12 nm
Std. Dev.= 1.36 nm
233 particles count
%
Particle Diameter (nm)

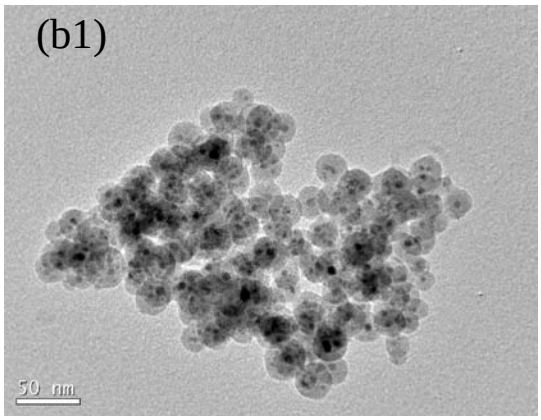
(b1)
50 nm

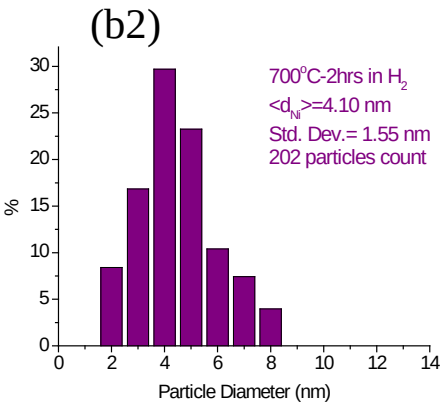
(b2)
700°C-2hrs in H2
<d_Ni>=4.10 nm
Std. Dev.= 1.55 nm
202 particles count
%
Particle Diameter (nm)

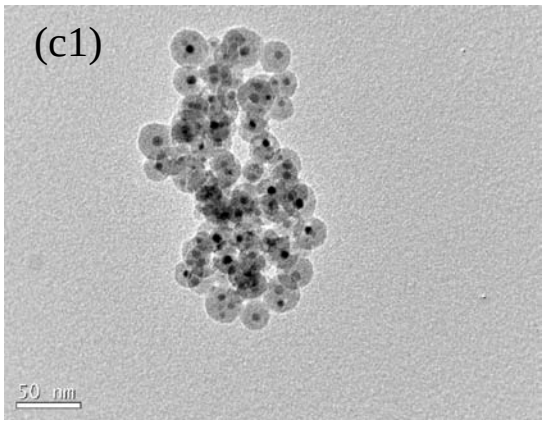
(c1)
50 nm

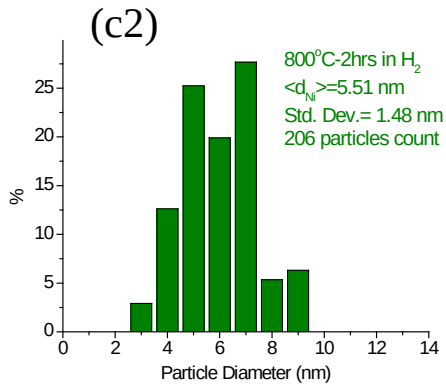
(c2)
800°C-2hrs in H2
<d_Ni>=5.51 nm
Std. Dev.= 1.48 nm
206 particles count
%
Particle Diameter (nm)

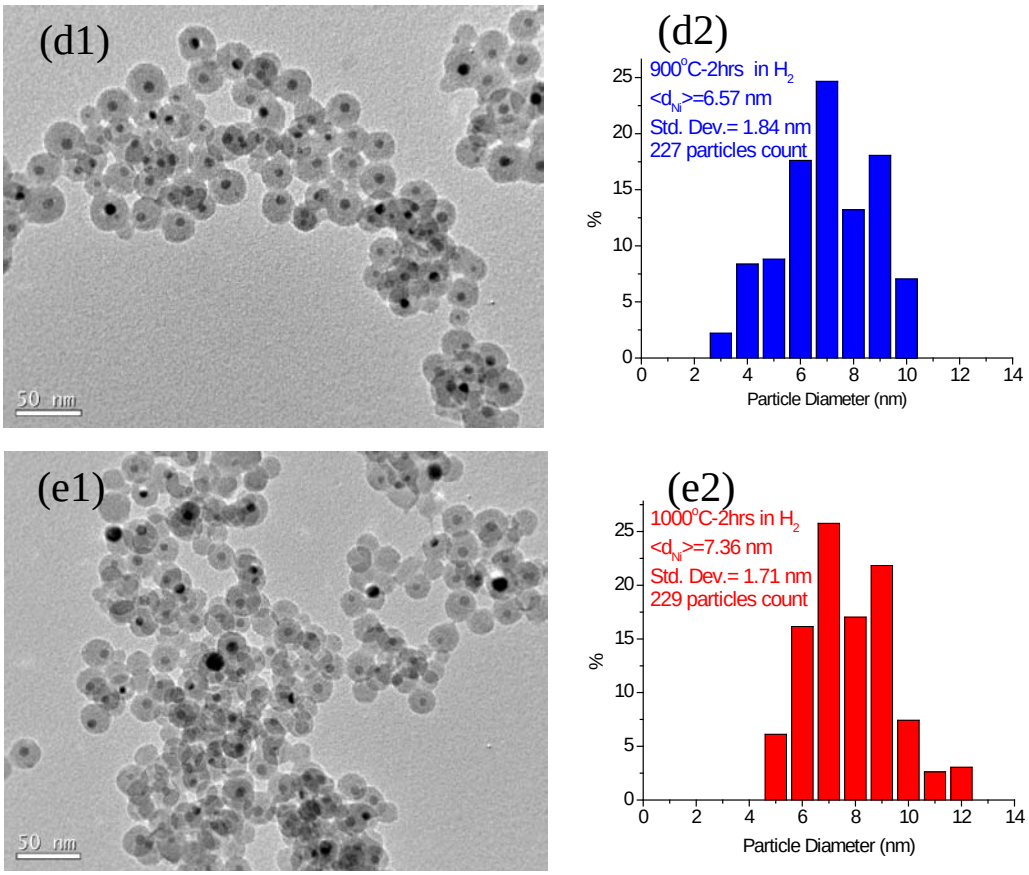

Figure 33: *TEM and particle size distribution of 4nm Ni@SiO_2 before (a) and after thermal treatment at (b) 700°C, (c) 800°C, (d) 900°C and (e) 1000°C for 2hrs in H_2*

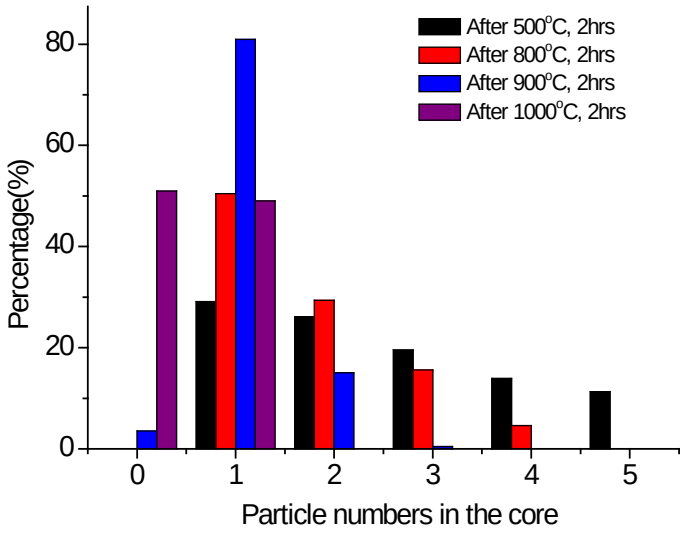

Figure 34: *Fraction of nickel core numbers in silica particles for 4nm Ni@SiO_2 sample as starting material (500°C, 2hrs in air) and after treatment in H_2 for 2hrs at 800°C, 900°C, 1000°C*

XRD patterns for 4nm Ni@SiO_2 after different calcination temperatures agree with our observation in the TEM pictures (Figure 35). The peaks become narrower and sharper at higher temperature indicating the growth of nickel particles. At 1000°C, there are three diffraction peaks at 44.5°, 51.8° and 76.4 ° indicating metallic nickel with cubic (FCC) structure, relative to planes (111), (200) and (220). The nickel crystallite sizes were estimated according to Scherrer's equation based on the full width at half maximum (FWHM) of the plane (111) (Table 5). Scherrer's equation is described as follows [174]:

$$D=\frac{\lambda k}{(B-B_o)\cos(\theta)}$$

Where D (Å) is the mean diameter of the crystallite, λ=1.54Å, k=0.89, B_o=0.1°, and B is the width at half maximum.

The discrepancy between the average nickel particle sizes determined from TEM and calculated from XRD patterns is less than 20%, hence validating the accuracy of nickel sizes counted from TEM.

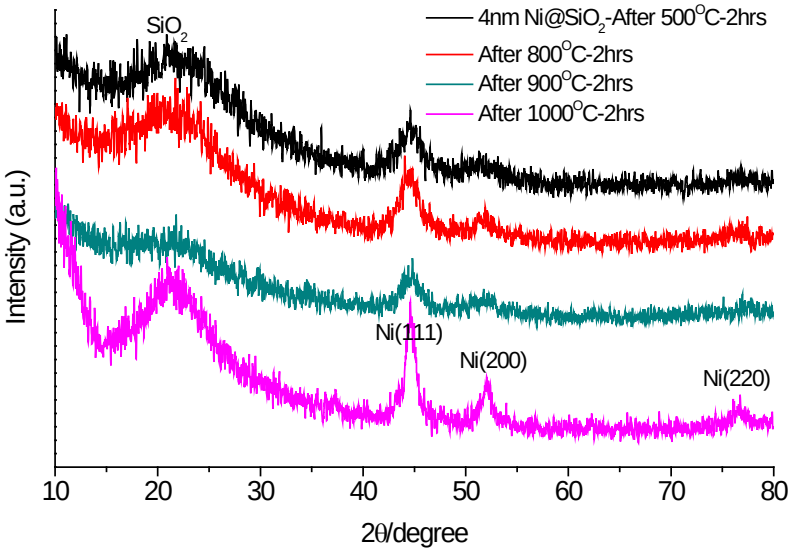

Figure 35: *XRD pattern for 4nm Ni@SiO_2 before and after thermal treatment for 2hrs in H_2 at 800°C, 900°C and 1000°C*

Table 5: *Average nickel crystallite sizes counted by TEM and determined from Scherrer equation*

Sample	d_{TEM} (nm)	d_{XRD} from Scherrer Equation (nm)
500°C-2hrs	4.12	4.90
800°C-2hr	5.51	5.73
900°C-2hr	6.57	6.78
1000°C-2hr	7.36	7.28

4.1.2 Cavity structure

The key difference between core shell materials with and without cavity structure is whether the nickel particles are fully encapsulated in the silica shell. Figure 36 shows TEM images and temperature dependence of the particle size distribution of sintered nickel particles in

cavity-Ni@SiO_2 after thermal treatment. Even though nickel particles are not fully encapsulated by a silica shell, they are surprisingly stable and remain in the sub-nanometer range even after thermal treatment at 800°C. This might be explained by a strong interaction between nickel and silica support, which would inhibit the agglomerations of nickel particles. The nickel particles in cavity structure grow to a single nickel core after 900°C, similar to 2nm Ni@SiO_2. However, the difference between cavity and non-cavity structure is that the sintering of nickel particles in cavity structure will not modify the diffusion pathway through silica shell. The XRD patterns agree with our observation in TEM pictures (Figure 37). No nickel peaks are detected in XRD until 900°C since nickel particles are too small to be detected [175]. The sharper Ni (111) and (200) peaks are detected at 1000°C, which indicates an increase in nickel particle size. The sintered nickel particle size in cavity sample at 1000°C is comparable with that of 2nm Ni@SiO_2, which is much smaller than that of 4nm Ni@SiO_2. This indicates the particle size during the sintering process highly depends on the nickel loading (i.e. higher nickel loading will result in larger sintered particles).

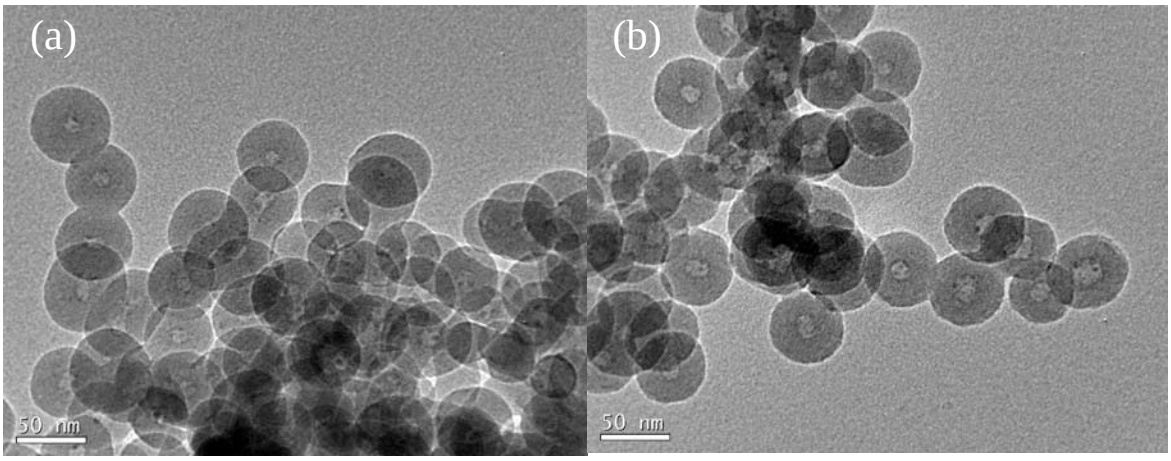

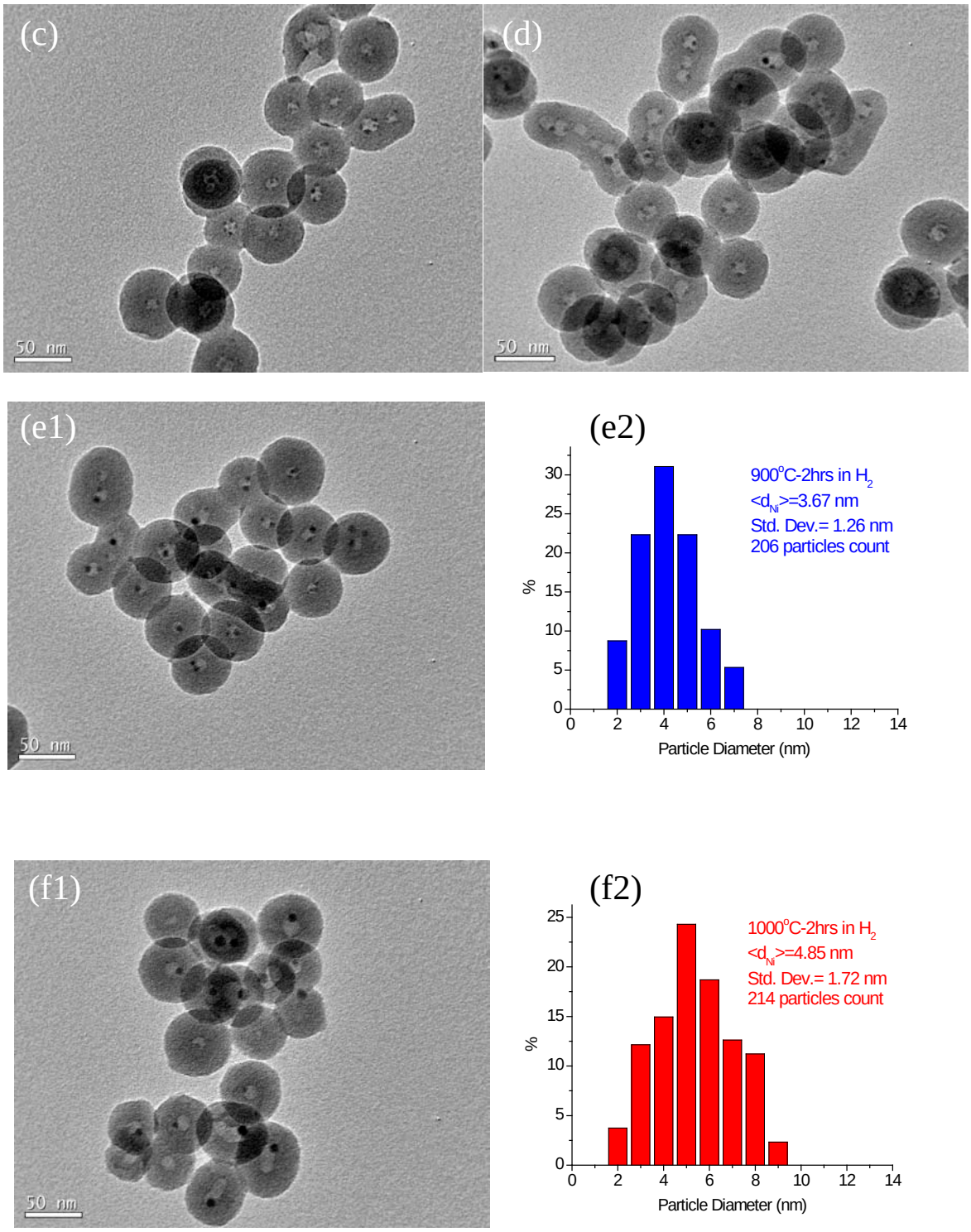

Figure 36: *TEM and particle size distribution of cavity-Ni@SiO_2 before (a) and after thermal treatment at (b) 600°C, (c) 700°C, (d) 800°C, (e) 900°C and (f) 1000°C for 2hrs in H_2*

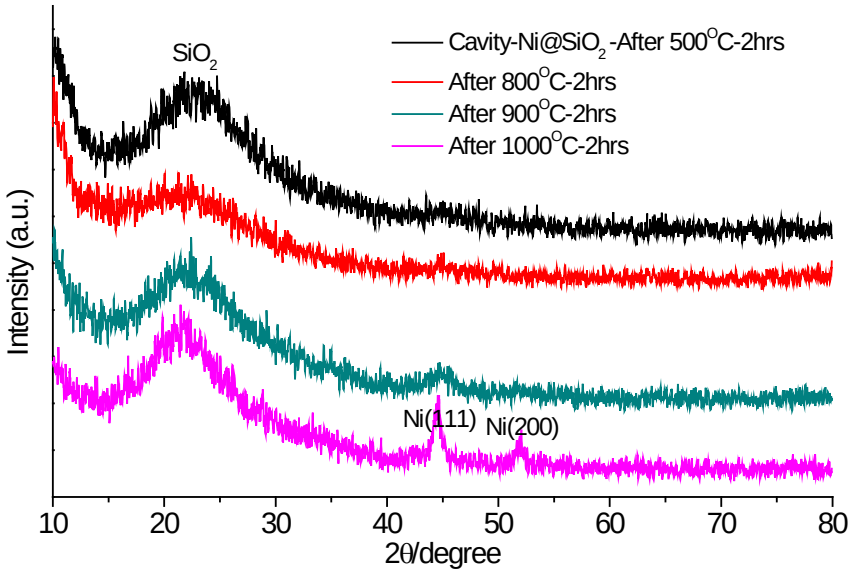

Figure 37: *XRD pattern for cavity-Ni@SiO_2 before and after thermal treatment for 2hrs in H_2 at 800°C, 900°C and 1000°C*

Nickel particles in cavity structure have similar thermal behavior with those in non-cavity structure. However, the difference between these two structures is the changed location of sintered nickel particles, which might result in the elongated diffusion pathway in non-cavity structure (see Figure 38). Nickel particles agglomerate into a single nickel locating more towards the center of silica particles in non-cavity structure, while the sintered nickel remains in the same spot in cavity structure. Additionally, the cavity structure facilitates the diffusion of reactants from different directions since reactants diffuse much faster though the cavity than porous solids.

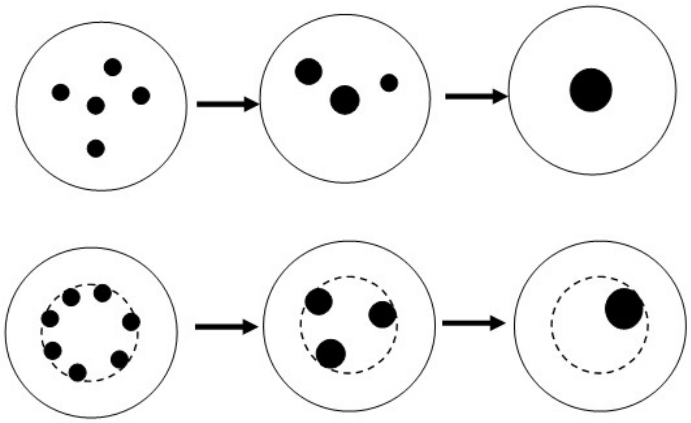

Figure 38: *Scheme of the nickel particle sintering in (above) non-cavity Ni@SiO_2 (bottom) cavity-Ni@SiO_2*

TEM images of core shell materials after thermal treatment in air can be found in appendix (Figure 102).

4.1.3 Ni/SiO_2 from deposition-precipitation (DP-Ni/SiO_2)

To compare nickel sintering behavior, DP-Ni@SiO_2 material was thermally treated at the same temperatures as core shell material. The synthesis procedure of DP-Ni@SiO_2 can be found in appendix B.1.2. The initial nickel particles (<2 nm), with comparable size to that of cavity Ni@SiO_2, are located on the external surface of silica shell (Figure 39-a). The sintering of DP-Ni@SiO_2 occurs as low as 500°C, in which nickel particle size significantly increases to around 12 nm.

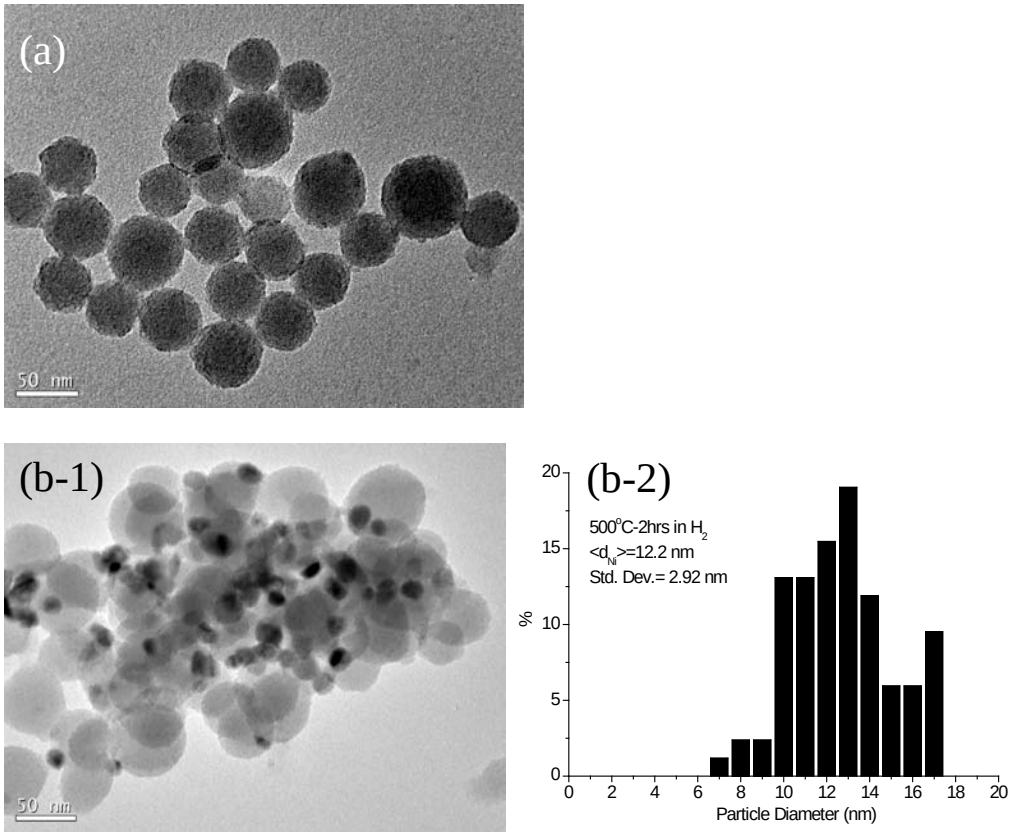

Data provided by the courtesy of M. Najera

Figure 39: *TEM images and particle size distribution of DP-Ni@SiO_2 (a) before and (b) after thermal treatment at 500°C for 2hrs in H_2*

It is clear that the presence of silica shell significantly suppresses the nickel sintering. Regardless of cavity or non-cavity structure, the nickel particles are stabilized under 5nm at 800°C and are maintained well below 10nm at 1000°C. In contrast, the nickel particles sinter strongly above 10nm at temperatures as low as 500°C in DP-Ni/SiO_2 material.

4.2 SILICA SHELL

Our next question pertains to changes in the silica structure after thermal treatment. Specifically, will the diffusion of the nickel particles that are larger than silica pores in non-cavity core shell material will affect the silica structure or not?

Figure 40 shows the BET surface area, porosity, and pore size distribution of silica in non-cavity core shell structure after different thermal exposures. There is a decrease in BET surface area and micropore volume with the increasing temperatures as expected due to the sintering of silica pores. Surprising, the silica pore diameter does not shift after different temperatures exposures, meaning that diffusion of nickel particles through pores does not force pores to become wider despite the larger size of the particles. However, the peak area does decrease, which indicates a loss of microporous surface area due to pore collapse. It is noted that the sintered nickel particle size (>2nm) in the non-cavity core shell material is always larger than the pore size of silica shell (< 2nm) during the sintering process, which indicates that the silica shell is not able to constrain the growth of the nickel particle to its own pore size. The increase in nickel particle size beyond the pore size of silica shell could be attributed to the structure rearrangement of the support material. Sehested also observed that the nickel particle size grows beyond the pore size of alumina support with no indication that the final size of sintered nickel particles will be equal to the pore size of the carrier [134].

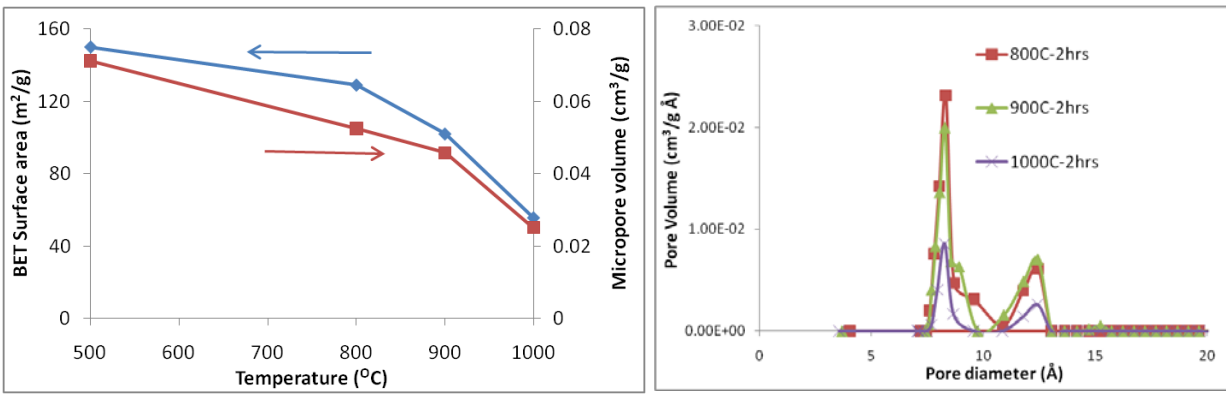

Figure 40: *(left) BET surface area and pore volume (right) pore size distribution of silica shell in non-cavity Ni@SiO_2 after different calcination temperatures*

After studying the robustness of silica support at different temperatures, long term stability of the materials was also studied. The material is heated under H_2 flow at 800^{o}C from 2 hours to 12 hours. The pore size and the pore volume do not change significantly for non-cavity Ni@SiO_2, and the BET surface area only decreases slightly from 129m^2/g to 124m^2/g (Figure 41-left). The BET surface area of cavity-Ni@SiO_2 with different shell thickness as a function of temperature and time can also be found in appendix E.1.2. A similar trend of the minor BET surface area reductions of non-cavity Ni@SiO_2 is also observed. The pore size distribution in the silica shell in non-cavity Ni@SiO_2 is also similar to cavity Ni@SiO_2 after thermal treatment at 800°C for 12 hours (Figure 41-right). This indicates the reconstruction process of the silica shell is not affected by the presence of the embedded nickel particles.

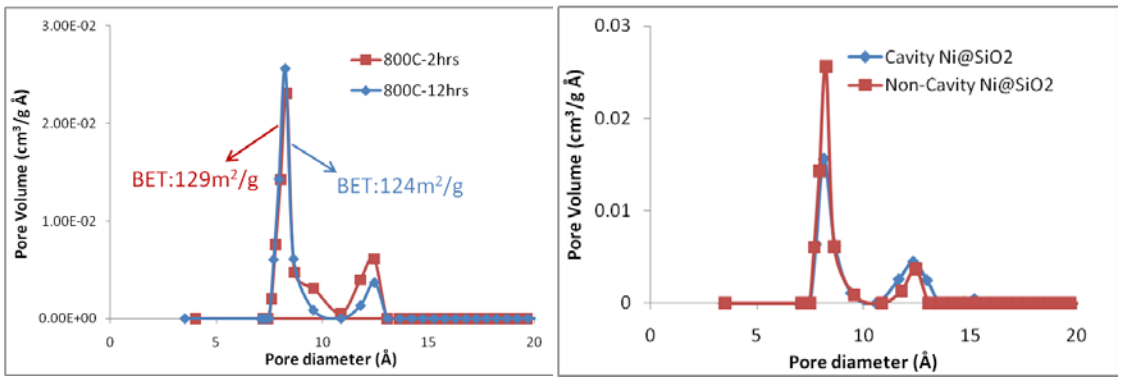

Figure 41: *Pore size distribution of silica shell in (left) non-cavity Ni@SiO_2 after thermal treatment at 800℃ for 2hrs and 12hrs; (right) both cavity and non-cavity core shell materials after thermal treatment at 800℃ for 12hrs*

4.3 REDUCIBILITY

To further understand the nickel sintering behavior for different morphological configurations, the TPR of core shell material with and without cavity structure as well as DP-Ni/SiO_2 after the thermal treatment at the corresponding temperatures is studied (Figure 42-Figure 44). Based on our interpretation of TPR in section 3.5.3, the lower temperature peak (300-400°) is assigned to the reduction of bulk NiO while the peak at higher temperature (400- 500°C) is either assigned to a strong nickel-support interaction or the formation of nickel silicate. One distinct difference in TPR between core shell materials and DP-Ni/SiO_2 before thermal treatment is the absence of the higher temperature peak in DP-Ni/SiO_2. There are two peaks in core shell materials regardless of the cavity structure. It is well known that stronger metal support interaction facilitates the stabilization of metal particles [176]. The absence of this nickel-support interaction in DP-Ni/SiO_2 could explain why the nickel particles are so easily sintered as low as 500°C.

The general trend of TPRs in non-cavity 4nm Ni@SiO_2 is the peaks shift to lower temperature, which is also observed in DP-Ni/SiO_2. The lower temperature peak shift could be explained by the increased nickel particle size with increasing temperature. The exception is the appearance of a new peak at 1000°C, which could be attributed to a strong chemical interaction between nickel and the silica support after calcination at 1000°C [159]. TPR for cavity-Ni@SiO_2 also shifts to left at higher temperature due to the growth of the nickel particles. The difference between core shell materials with and without cavity structure is the peak shifts to higher temperature for the cavity sample at 800°C while the peak shifts to lower temperature for the non-cavity sample. One explanation for this higher temperature peak shift is the possible presence of another form of nickel silicate after annealing small sized nickel (<2nm) with silica in the cavity structure. A similar trend is also observed by Yoshida that the reduction peak shifts to higher temperature after calcination temperature at 800°C [161].

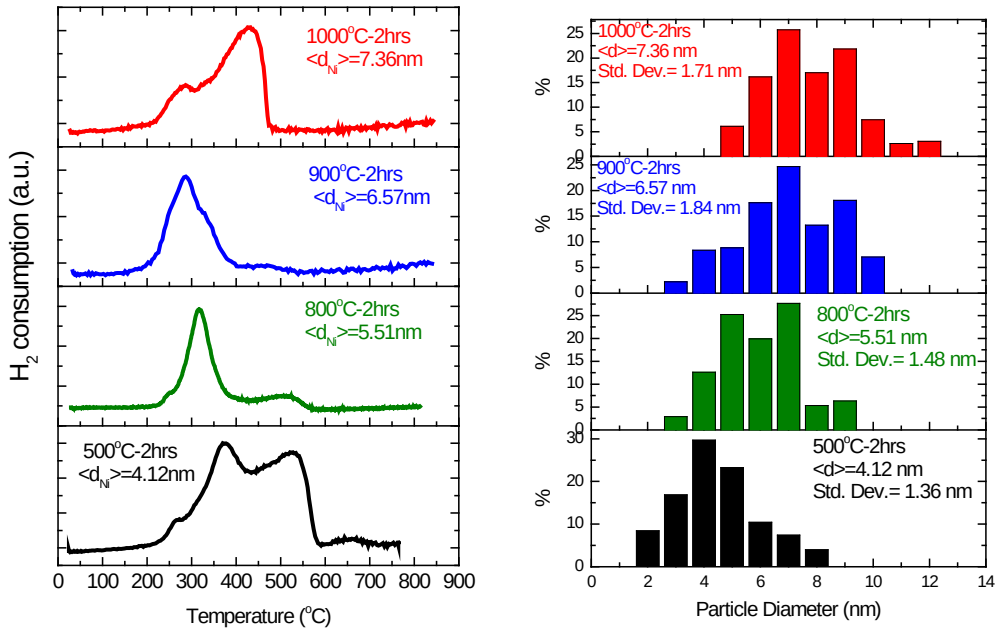

Figure 42: *(left) TPR profile and (right) particle size distribution of 4nm Ni@SiO_2 before and after thermal treatment at 800°C, 900°C and 1000°C for 2hrs in H_2*

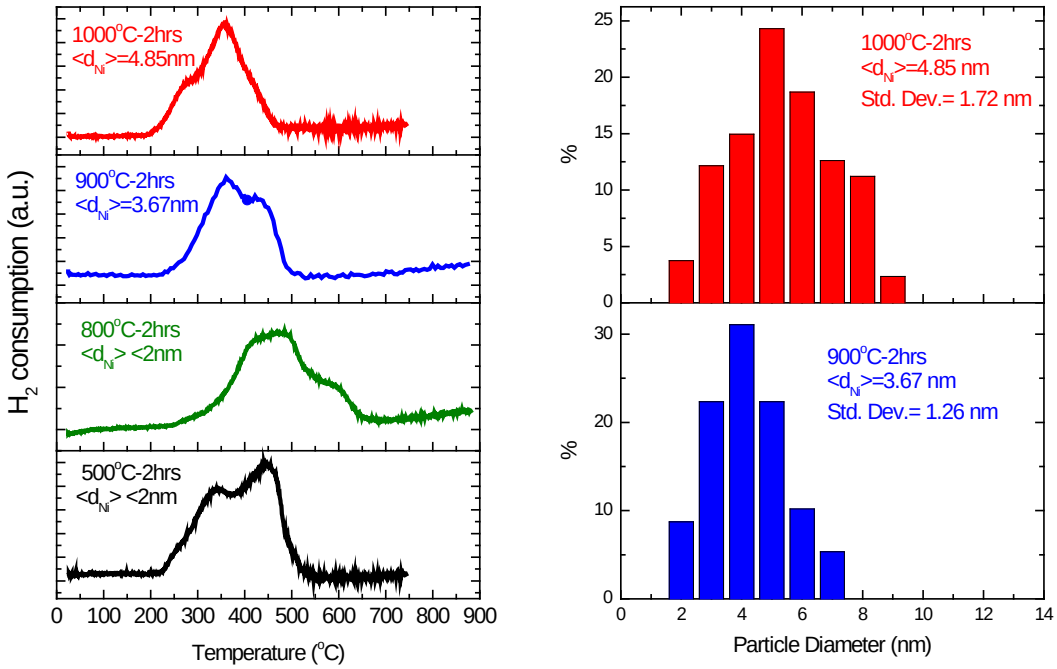

Figure 43: *(left) TPR profile and (right) particle size distribution of cavity Ni@SiO_2 before and after thermal treatment at 800°C, 900°C and 1000°C for 2hrs in H_2*

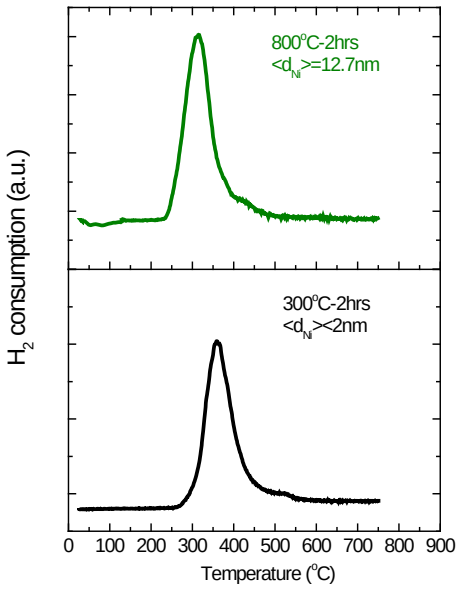

Data provided by the courtesy of M. Najera

Figure 44: *TPR profile of DP Ni/SiO_2 before and after thermal treatment at 800°C for 2hrs in H_2*

The TPRs are compared as a function of temperature and time. The TEM pictures and particle size distributions of non-cavity Ni@SiO_2 after thermal treatment at 800°C from 2 hours to 12 hours can be found in Figure 104. The TPR of the samples treated at the corresponding conditions are shown in Figure 45. There is a decrease in the TPR peak area which corresponds with the nickel sintering process from 2 hour to 12 hours. A reduction of peak area, which indicates that less nickel particles are able to be reduced, suggests the formation of larger nickel particles.

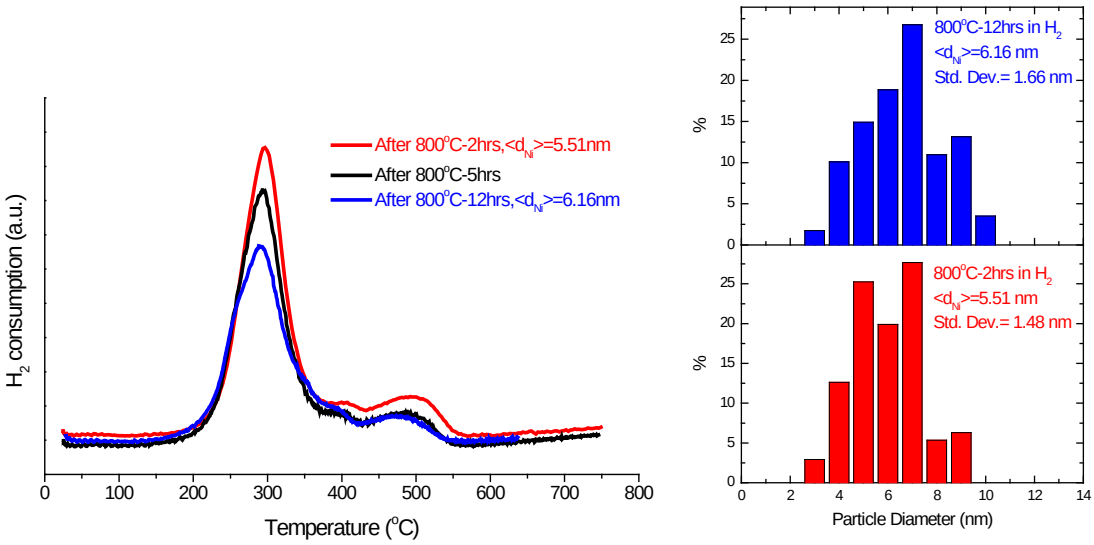

Figure 45: *TPR and particles size distribution of 4nm Ni @SiO_2 calcined in H_2 at 800°C for 2hrs, 5hrs and 12hrs.*

Overall, the TPR peak at lower temperature region becomes more dominate with increasing calcination temperatures as nickel particles grow. However, there is an exception at 1000°C where a deeper chemical reaction possibly occurs resulting in the formation of new nickel-silica species. The particle size dependent nickel support interaction, which is weaker in larger nickel particles than smaller nickel particles, is responsible for the shift of TPR profiles.

Besides that, less nickel particles are able to be reduced at a larger size which suggests that smaller sized nickel particles have higher reactivity.

4.4 REACTIVE APPLICATION

4.4.1 Ethylene hydrogenation

The ethylene hydrogenation reaction is an exothermic and structure insensitive reaction. The reaction is performed in a fixed bed reactor with a contact time 0.08s to investigate the reactivity and thermal stability of the $Ni@SiO_2$ core shell materials. The total flow rate is 100 cm^3 min-1 with the volumetric ratio C_2H_4:H_2:He=1:3:6. The nickel mass is constant at 4.8mg for each run. As a comparison catalyst, IMP-Ni/SiO_2 was synthesized from conventional wet-impregnation method following the procedure in appendix B.1.1. The detailed experimental procedure can be found in section 2.3.2. The catalyst reactivity in terms of ethylene conversions is plotted as a function of reaction temperature (Figure 46). The ignition of the reaction on $Ni@SiO_2$ occurs at room temperature and is much lower than that of IMP-Ni/SiO_2 by 20°C difference. This indicates hollow $Ni@SiO_2$ is more reactive than IMP-Ni/SiO_2. The high reactivity of $Ni@SiO_2$ is likely a result of the formation of small sub-nanometer nickel clusters, which facilitates a much higher active surface area than the conventional catalyst. Besides its high reactivity, the $Ni@SiO_2$ also shows high stability at elevated temperatures. After 12 hours thermal treatment at 700°C, the reactivity of $Ni@SiO_2$ was maintained while the conventional catalyst quickly deactivates to a high degree. This deactivation of conventional catalyst is resulted from particle sintering from 20nm to 50nm (Figure 47).

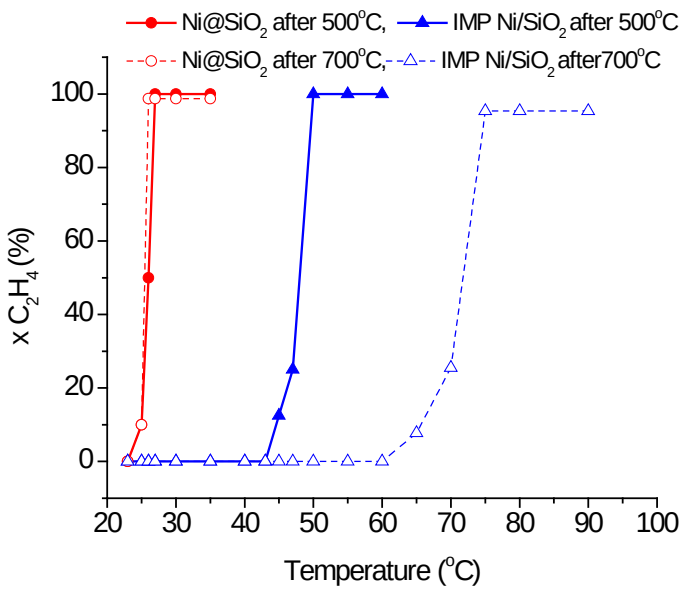

Figure 46: *Ethylene conversion measured at different temperatures for $Ni@SiO_2$ and IMP-Ni/SiO_2 before (calcined in air at 500°C for 2hrs) and after thermal treatment in air at 700°C for 12hrs*

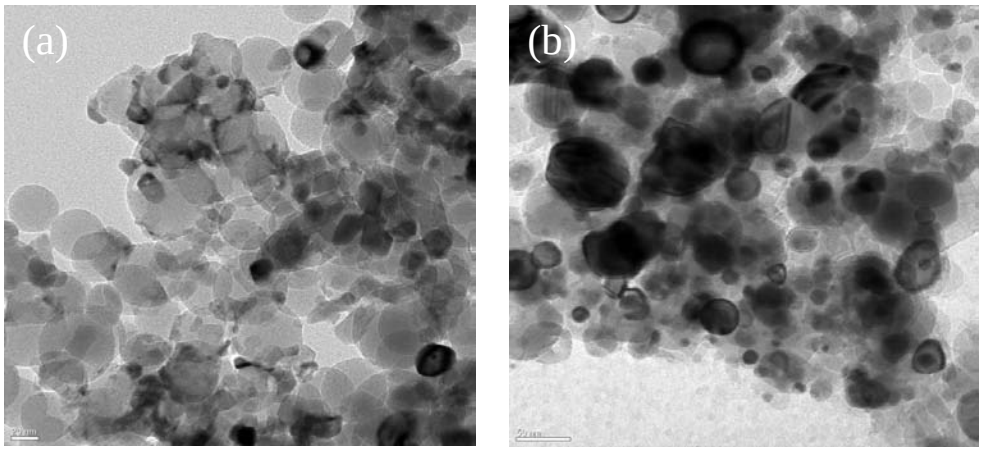

Figure 47: *TEM images of IMP-Ni/SiO_2 (a) before and (b) after thermal treatment in the air at 700°C for 12hrs.*

4.4.2 CO Methanation

To further demonstrate the thermal stability of the core shell materials, the core shell material with and without cavity structure as well as the comparison catalyst IMP-Ni/SiO_2 were

tested in the CO methanation reaction. CO methanation is an exothermic reaction and carbon formation due to methane dissociation is a challenging issue when using nickel catalysts. The reaction is performed in a fixed bed reactor at 450°C for 1 hour with the contact time 0.12s. The total flow rate is 12.5 mL min^{-1} with volumetric ratio CO: H_2: He as 1:3.6:10.8. A nickel mass (1.5mg) is maintained the same for each run. The detailed experimental procedure can be found in section 2.3.3. The reactivity of core shell materials and conventional IMP-Ni/SiO_2 before (solid line) and after 12 hours thermal treatment at 800°C (dashed line) are compared (Figure 48). The higher initial reactivity of Ni@SiO_2 compared with that of IMP- Ni/SiO_2 can be attributed to the smaller nickel particles (<2nm) in both core shell materials which result in larger nickel active surface area. Another distinct difference in reactivity between these three catalysts before thermal treatment is the decreasing reactivity in IMP- Ni/SiO_2 with reaction time, while the reactivity of both core shell materials is maintained. The deactivation in IMP-Ni/SiO_2 results from carbon formation on nickel surface since methane is a primary product. The formation of whisker carbon on the deactivated IMP-Ni/SiO_2 confirms this (Figure 49-left). A similar decreasing reactivity is observed in non-cavity Ni@SiO_2 as well as IMP-Ni/SiO_2 after thermal treatment. An in-situ TPO is performed following each reaction test to qualitatively compare the amount of carbon formation. A significant amount of CO_2 is detected for the deactivated catalysts while no CO_2 is observed for cavity-Ni@SiO_2 after reaction (Figure 49-right), which indicates there is no coke formation on cavity-Ni@SiO_2. The suppression of coke formation is due to the small nickel particles (<5nm) in core shell materials [10, 45, 177, 178]. Another reason for the reduced coke formation is the strong nickel-support interaction, which might slow down the CH_4 chemisorption rate nickel surface [179-181]. The TPR peak shifts in Figure 42 and Figure 43 indicate the stronger metal-support interaction in cavity Ni@SiO_2 compared to non-

cavity Ni@SiO_2 after thermal treatment at 800°C for 12 hours, which could inhibit the carbon formation on sintered cavity Ni@SiO_2. Besides the catalyst deactivation due to carbon formation, the initial reactivity of non-cavity Ni@SiO_2 and IMP-Ni@SiO_2 after thermal treatment decreases significantly while the reactivity of cavity Ni@SiO_2 remains the same before and after thermal treatment. The decrease in reactivity of IMP-Ni@SiO_2 is due to the loss of nickel surface area during sintering process. The reason for the reduced reactivity of non-cavity Ni@SiO_2 after thermal treatment could be explained by mass transfer limitations of reactants in addition to the nickel surface area loss. The mass transfer limitation is due to the elongated diffusion pathway when nickel particles migrate to the center of silica particles during sintering process (see Figure 38). In contrast, the unchanged reactivity of cavity Ni@SiO_2 is due to the stable sub-nanometer nickel clusters after thermal treatment as well as the unaffected diffusion pathway of the reactants.

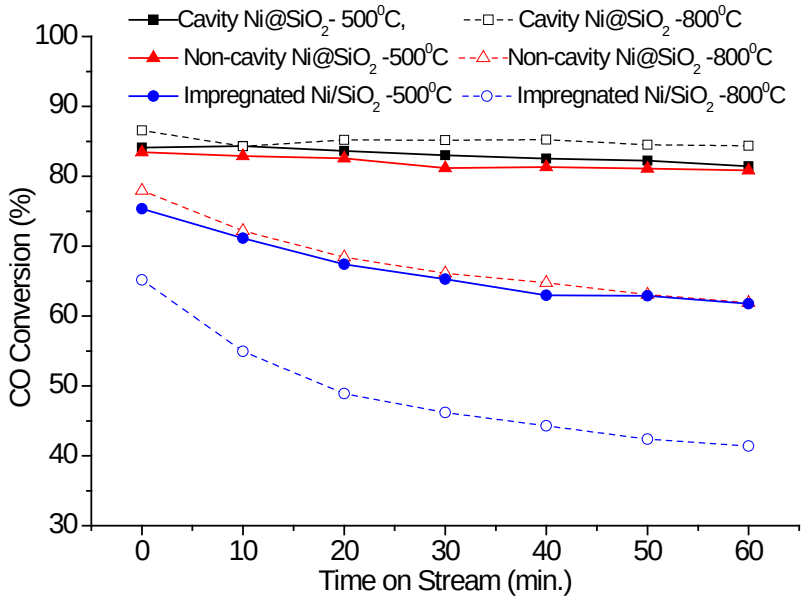

Figure 48: *CO methanation reaction over cavity Ni@SiO_2, non-cavity Ni@SiO_2, and conventional impregnated Ni/SiO_2 (IMP-Ni/SiO_2) before (solid line) and after (dashed line) thermal treatment at 800°C for 12hrs*

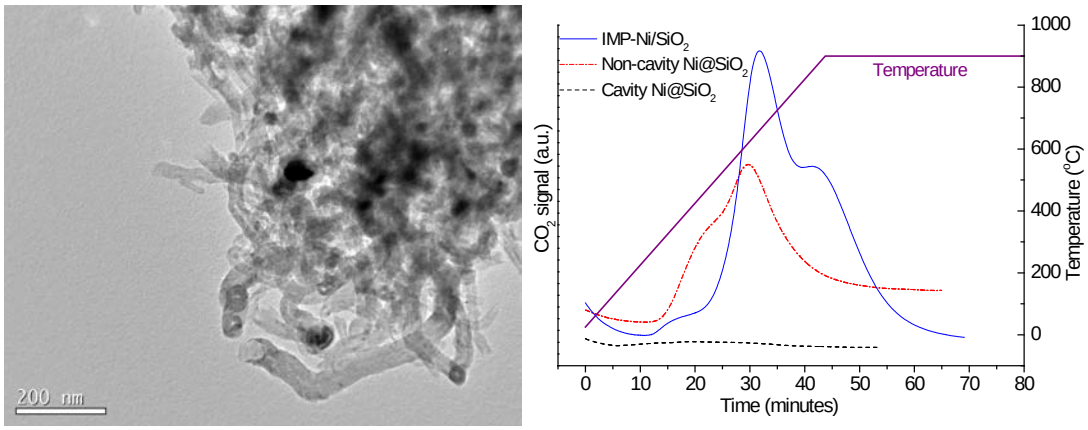

Figure 49: *The TEM image of IMP-Ni/SiO_2 after the CO methanation reaction (left); CO_2 signal of TPO after CO methanation reactions of cavity-Ni@SiO_2, non-cavity Ni@SiO_2 and IMP-Ni/SiO_2 after thermal treatment at 800^oC for 12hrs (right)*

4.5 SUMMARY

We demonstrated highly stable nickel catalyst by encapsulation nickel particles with silica shell. The nickel particles are stabilized under 5nm even at 1000°C while there is a dramatic size increase in nickel particles in DP-Ni/SiO_2 as low as 500°C. The silica shell significantly decreases the nickel sintering rate. However, major differences are observed in core shell materials with different nickel particle sizes and configurations depending on the presence of cavity structure. The results suggest that core shell material with cavity structure is the most desirable configuration in terms of thermal stability since the slight agglomeration of nickel particles will not interfere the silica structure or the diffusion pathway of the reactants. The core shell material with nickel particles size (~1nm) smaller than silica pore size is the least stable among core shell materials since nickel particles easily diffuse through silica matrix. Even though a larger silica pore diameter could facilitate transport of the reactants, one should be

aware of the trade-off between the stability and mass transfer. The diffusion of nickel particles with smaller size than silica pore size suggests that larger pores are not desired for stabilizing small sized nickel particles. The benefit of stabilizing nickel particles is not only to maintain its active surface area and reactivity, but also to retain its unique property such as high coking resistance only when nickel particles are under 5nm. Overall, the results suggest that the core shell material would be a good candidate for a high temperature fuel processing catalyst due to its high temperature stability and its potential for coking resistance.

5.0 STABLE AND COKING RESISTENT CPOM CATALYST

We demonstrated previously the enhanced stability of $Ni@SiO_2$ in ethylene hydrogenation and CO methanation reactions. The significance of synthesizing and stabilizing nickel particles under 5nm to suppress coking formation is also mentioned in last chapter. Our next focus it to test core shell materials in CPOM reactive system. There are several reasons why we chose CPOM as a test reaction. First, the reaction itself is one of emerging industrial processes for hydrogen production. It is a much less energy intensive process compared with steam reforming of methane since it is a mildly exothermic process. Second, the product syngas ratio (H_2/CO=2) is also suitable for the downstream Fischer–Tropsch reaction. Third, nickel is a well-researched and popular catalyst for the reaction with decent reactivity and affordable prices compared to noble metals such as Pt, Rh, or Ru [16, 27, 121-123, 133, 182-189]. Fourth, the thermodynamically favored high temperature operation condition of CPOM reaction allows further investigations of the stability of the core shell materials. Fifth, the deactivation of nickel-based catalysts due to coking is a critical issue for this reaction. In this chapter, we will discuss the structure dependent stability and coking behaviors of core shell materials in comparison with IMP-Ni/SiO_2, sol-gel Ni/SiO_2 and commercial steam reforming HiFuel nickel catalyst. The synthesis procedures for IMP-Ni/SiO_2 and sol-gel Ni/SiO_2 can be found in appendix B.1.1 and B.1.3.

5.1 CATALYST CHARATERIZAION

Morphologies of catalysts used in the CPOM reaction and the porosity information of the silica support are shown in Figure 50. Small nickel clusters (<2nm) decorate the inner wall of the silica shell in Ni@SiO_2. There is a pronounced cavity structure centered in the particle with 8nm silica shell thickness. This “nanobubble” structure is confirmed by its pore size distribution. The peak at 8nm, which agrees with the dimensions of cavity structure, confirms the presence of cavity structure. The peak between 20nm to 30nm is from the void space between the silica spheres. The nickel particles in sol-gel Ni/SiO_2, which are about 3nm, are embedded in silica matrix. The silica matrix has irregular mesopores (5nm and 12nm) which render the nickel particles highly accessible by reactants. In IMP-Ni/SiO_2, the broad peak between 20nm to 40nm is from the void space between silica spheres. All the above nickel silica supported catalysts exhibit a high surface area (>200 m^2/g). Figure 51 shows the TEM image and the chemical composition of HiFuel nickel catalyst, of which the support is calcium-alumina oxide. The nickel loading of each sample, as determined by EDX, is included on each individual TEM picture.

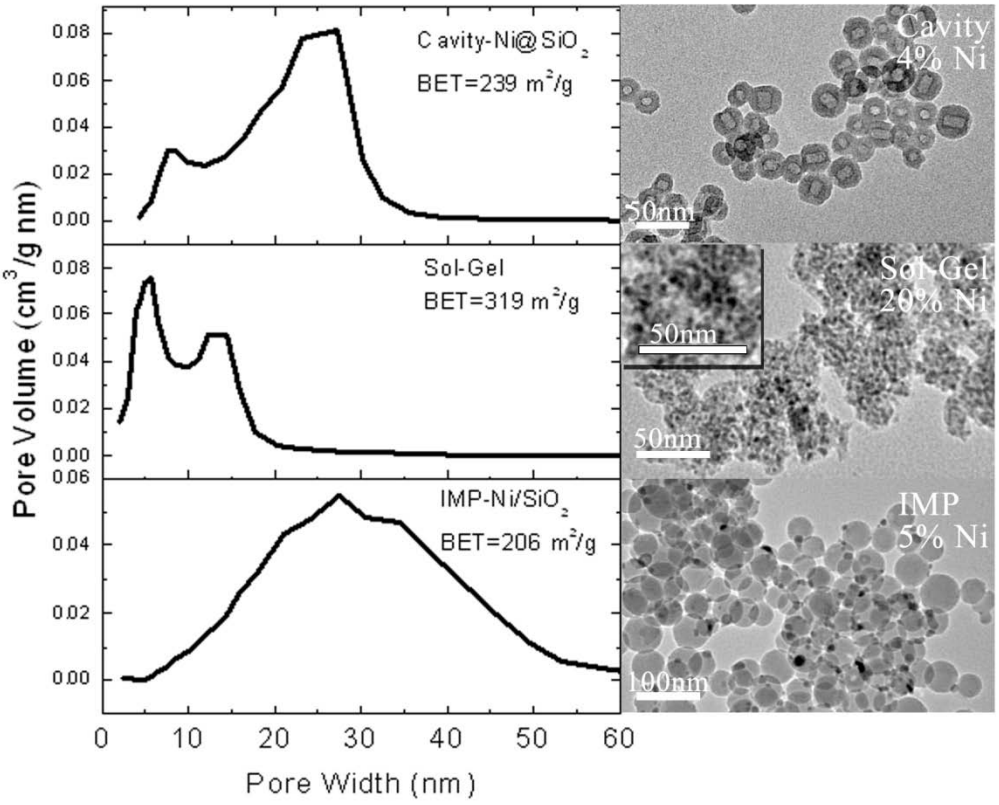

Figure 50: *TEM images, pore size distribution and BET surface area of (a) core-shell Ni@SiO_2 (b) sol-gel Ni/SiO_2 (c) IMP-Ni/SiO_2*

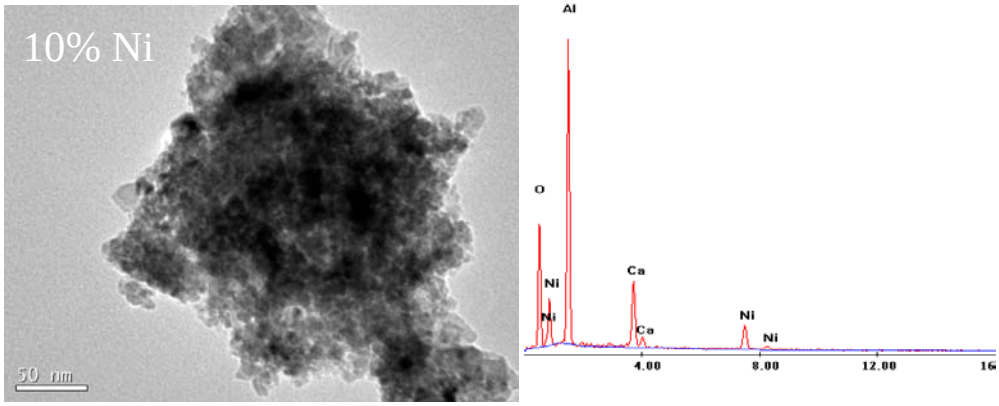

Figure 51: *(left) TEM image and (right) EDX of HiFuel commercial nickel catalysts*

The nickel crystallite information of Ni@SiO_2, IMP-Ni/SiO_2 and sol-gel Ni/SiO_2 were shown in Figure 52. Nickel clusters in Ni@SiO_2 are too small to be detected by XRD. The broad and weak Ni (111) peak in XRD spectrum indicates the small sized nickel particles in sol-gel Ni/SiO_2 catalyst. In contrast, the sharp Ni (111) and (200) peaks of IMP-Ni/SiO_2 indicate the

formation of large nickel particles (~20nm). The nickel particle size calculated from the Scherrer equation based on Ni (111) at 44.38° and Ni (200) at 51.75° agrees with our observation in TEM images (Table 6).

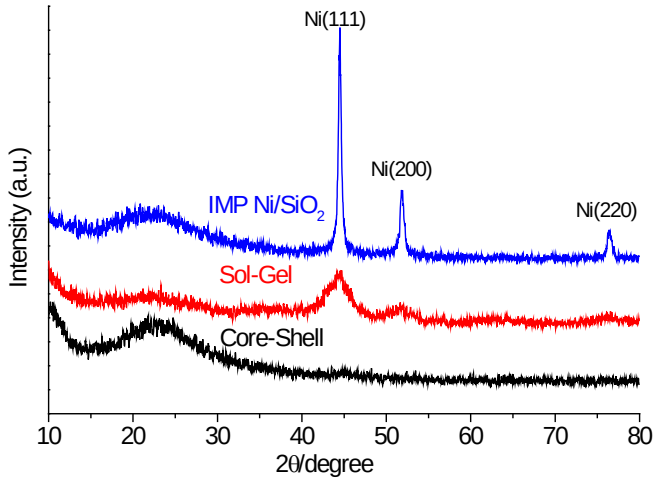

Figure 52: *XRD patterns of catalysts (IMP, sol-gel and core-shell) before reaction*

Table 6: *Nickel particle size from TEM images and calculated from Scherrer equation based on two peaks at 44.38° and 51.75° in XRD pattern*

Sample	TEM (nm)	Peak Location (degree)	XRD from Scherrer Equation (nm)
Sol-Gel	3	44.38	3.60
		51.75	4.30
IMP Ni/SiO2	19.8	44.38	20.50
		51.75	18.90

TPR is also employed to understand the nickel reducibility in different catalysts (Figure 53). There are two distinct peaks in all silica supported nickel catalysts. The peak at lower temperature is assigned to the bulk NiO and the higher temperature peak is coming from the nickel-silica interaction. The peak ratio between the high temperature peak and the lower temperature peak decreases with the increasing nickel particle size as expected. The reduction peaks in HiFuel catalyst with calcium-alumina oxide support locate at a much higher temperature, which suggests a stronger nickel support interaction.

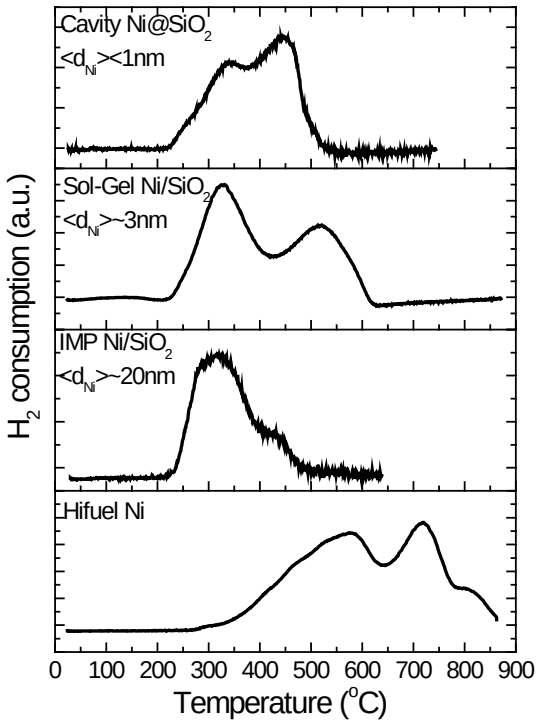

Figure 53: *TPR profiles of different catalysts of core-shell, sol-gel, IMP and HiFuel Nickel catalysts*

5.2 REACTIVITY

The catalytic activities of different nickel silica supported catalysts are compared with state-of-art HiFuel catalyst with the same nickel mass (1.2mg) and the space velocity ($6551h^{-1}$) (Figure 54). The conversions of methane for core-shell and sol-gel nickel catalysts, which is similar with the HiFuel catalyst, are very close to equilibrium curve as low as 800°C, and they reach complete methane conversion at 900°C. In contrast, methane conversion for IMP nickel catalyst is below 40% at 900°C and only reaches 60% at as high as 1100°C. Besides the high reactivity of core-shell and sol-gel catalysts, they also have comparable CO selectivity with

HiFuel nickel catalyst, which reaches the equilibrium levels during the whole range of operation. The high reactivity and selectivity of core-shell and sol-gel catalysts are attributed to the presence of small sized nickel particles, which provide much higher active nickel surface area than IMP-Ni/SiO_2.

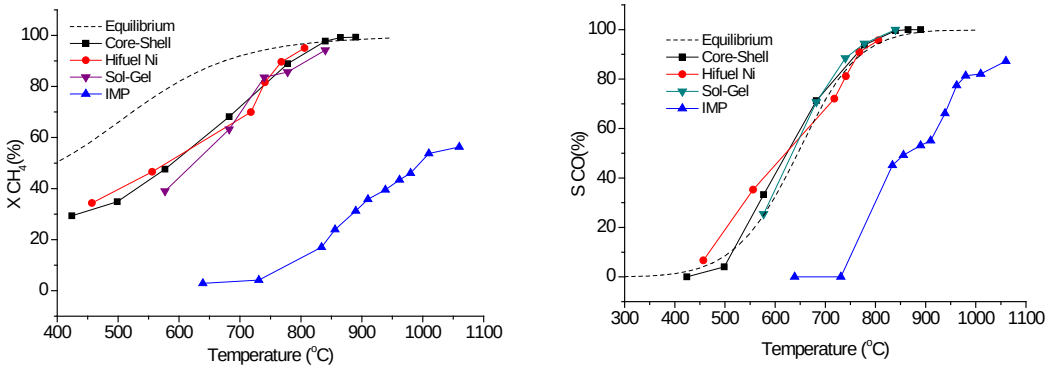

Figure 54: *CH_4 conversion and CO selectivity of core shell, sol-gel, IMP and HiFuel nickel catalysts at 400-1100℃ (feed in gas CH_4/O_2=2)*

Besides the core shell material with cavity structure, the reactivity and selectivity of non-cavity core shell materials with various nickel particle sizes were also studied (Figure 55). The lower reactivity and selectivity of non-cavity Ni@SiO_2 compared with cavity-Ni@SiO_2 is a result of the limited mass transfer of reactants in the silica structure. One of the important steps during a catalytic reaction is the transport of the reactants through the porous support media to the active components. The longer diffusion pathway of reactants from outer surface of the support to the active components would slow down the overall reaction, leading to a lower reactivity. In non-cavity structures, the nickel particles are dispersed though the entire silica particles from the edges to the center, which generates several different diffusion pathways for reactants. The dimension of silica particles is about 24nm in non-cavity core shell material, which means the longest pathway for reactant could be as far as 12 nm assuming there is no tortuosity in non-cavity and cavity structures. In contrast, the nickel particles which are coated on

the inner wall of silica shell in cavity structure have the same distance to the outer surface of the support. Since the diffusion pathway in non-cavity structure is much longer than that in cavity structure (4nm), this could explain why their reactivity is much lower than that of cavity structures. Additionally, the reactivity and selectivity of non-cavity 3nm Ni@SiO_2 is lower than that of 1nm Ni@SiO_2. The reason for this could be the nickel particles sitting towards the edges of silica particles are more accessible by reactants. The population of small, highly reactive nickel particles close to the edge of silica particles in 1nm Ni@SiO_2 is much higher than that of 3nm Ni@SiO_2, which results in a shorter total diffusion pathway of reactants and hence a higher reactivity (see Figure 13). A more detailed discussion of the impact of the diffusion pathway on the reactivity will be found in section 6.3.3.

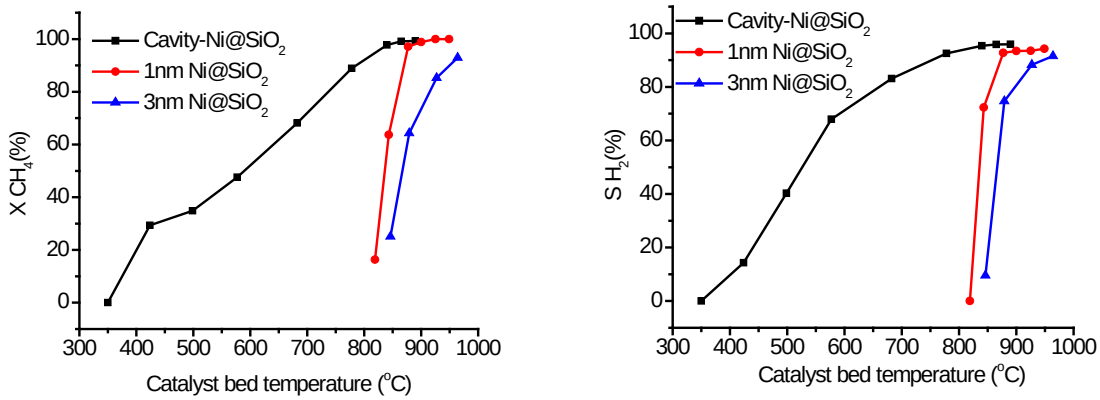

Figure 55: *CH_4 conversion and H_2 selectivity of cavity-Ni@SiO_2, non-cavity 1nm Ni@SiO_2 and 3nm Ni@SiO_2 at different temperatures (feed in gas CH_4/O_2=2)*

5.3 STABILITY

The superior thermal stability of core shell materials was demonstrated in a reducing environment (H_2 flow) in Chapter 4.0 in which nickel particles are stabilized under 5nm at

temperatures as high as 1000°C. This motivates us to further test the stability of core shell materials in reactive stream at high temperature condition. The on-stream stability of core shell material in comparison with unprotected nickel supported silica material will be tested in CPOM reaction operated at 800°C for 10 hours as well as multiple start-up and shut-down cycles. It is expected that the reactivity of the core shell material will not change at those conditions due to the stabilization of nickel particles and silica structure at 800°C, while deactivation occurs with unprotected nickel supported silica material due to the sintering.

5.3.1 Long time on-stream operation

The long term thermal stability of sol-gel Ni/SiO_2, core shell materials with and without cavity structure is compared with a stoichiometric ratio (CH_4/O_2=2) of CPOM at 800°C for 10 hours. Figure 56 shows the reactivity and selectivity as a function of time as well as the TEM images of the corresponding catalyst after the reaction. While a strong deactivation is observed in sol-gel Ni/SiO_2 and non-cavity Ni@SiO_2, the reactivity and selectivity of cavity-Ni@SiO_2 remains constant during 10 hours of operation. The deactivation in sol-gel catalyst is due to a severe sintering of nickel particles, which are embedded in silica matrix rather than being isolated by silica shell. The sintered nickel particles in sol-gel catalyst are ~10 nm in size, which is much larger than that of cavity-Ni@SiO_2 after reaction. The sharper Ni peaks of sol-gel catalyst in XRD after reaction shown in Figure 57-left confirms the significant increase in nickel size. In contrast, the nickel particles in cavity Ni@SiO_2 catalyst still remain under 5nm after reaction, which is indicated by the broad peak at Ni (111) with the absence of Ni (200) and Ni (220) peaks in XRD pattern (Figure 57-right). There are two reasons for the stability of the small

nickel particle sizes in cavity-Ni@SiO_2: one reason is that the nickel loading is sufficiently low and the second reason is that the presence of the silica shell prevents nickel particles from sintering.

The deactivation of sol-gel Ni/SiO_2 is expected since there is no protection for nickel particles. However, it is surprising to see there is a decrease in reactivity of non-cavity core shell material during the first 3 hours subsequently followed by a sudden drop. The deactivation cannot be simply explained by the nickel sintering since the sintering of nickel particles is significantly slowed down by the presence of silica shell and the nickel particles only slightly grow from 5.51nm to 6.16nm at 800°C from 2 hours to 12 hours (Figure 104 in appendix). The gradual decrease in the first three hours is due to the slow increase in nickel size. Yet during the sintering process, the multiple nickel cores also agglomerate into single nickel core by migrating towards the center of the silica particles and hence elongating the diffusion pathway of the reactants (see Figure 38). In addition, O_2/CH_4 is likely higher towards the center of silica particles than the edges due to the preferential O_2 diffusion. More detailed discussion regarding the preferential O_2 diffusion versus the silica shell thickness will be found in section 6.3.3. An oxygen rich environment allows the nickel particles to be more easily oxidized. The abrupt deactivation observed could hence be explained by the formation of NiO resulting from the elongated diffusion pathway during sintering process. The NiO formation is confirmed by the catalyst color change from black (Ni) to grey (NiO) after reaction. Once the nickel is oxidized, the reactivity and selectivity dropped significantly to the same level as the fully oxidized catalyst. In CPOM reaction, metallic nickel is the active component and is responsible for high reactivity and selectivity. Deactivation from NiO formation during the CPOM reaction is quite common [130, 132]. Kishida's group also observed a dramatic decrease of catalyst reactivity after just 1

hour reaction time due to the formation of NiO, which was confirmed by the XANES spectrum [132].

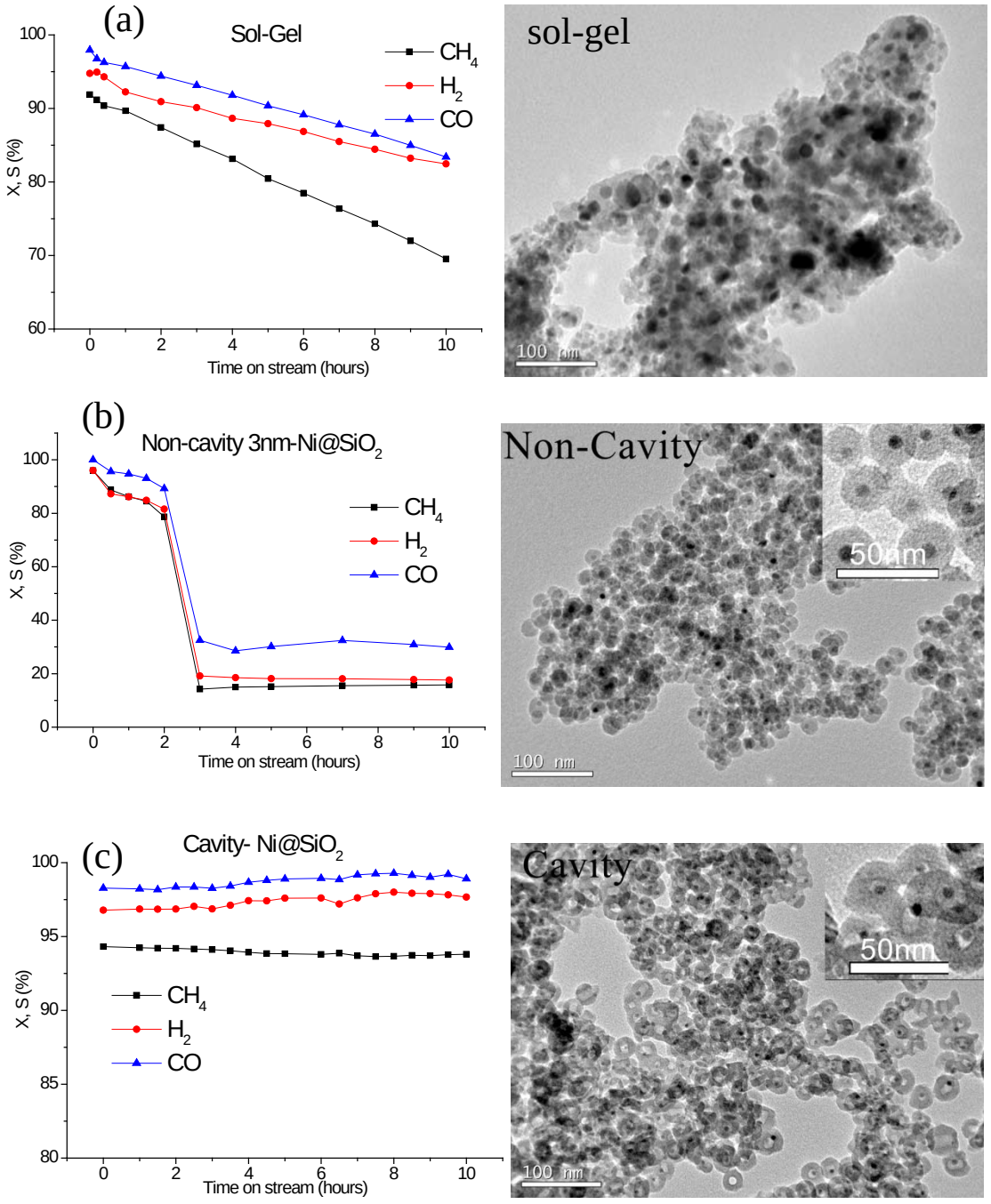

Figure 56: *(left) Methane conversion, H_2 and CO selectivity of (a) sol-gel (b) non-cavity $Ni@SiO_2$ (c) cavity-$Ni@SiO_2$ at 800℃ for 10hrs on-stream reaction (CH_4/O_2=2, contact time=0.15s); (right) TEM images of the corresponding catalysts after reaction*

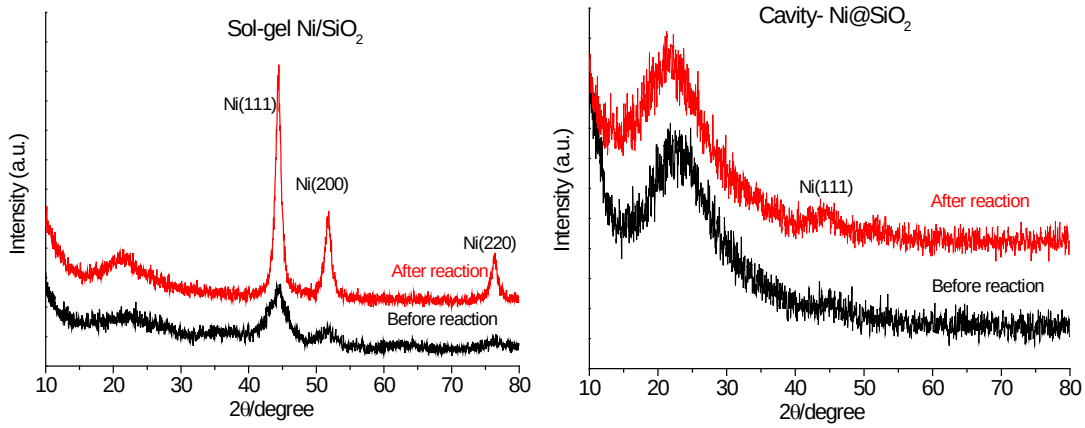

Figure 57: *XRD pattern of (left) sol-gel Ni/SiO$_2$ (right) cavity-Ni@SiO$_2$ before and after reaction for 10hrs at 800°C*

5.3.2 Cyclic operation

To further test the stability of core shell materials, several start-up and shut-off cycles were also conducted. Cyclic operation is both a realistic practice in industry operation and a worst case test for stability through multiple ignition and extinction cycles. One of the reasons for this is that multiple cycles enable us to study other factors affecting catalyst stability, such as the changes in Ni oxidation state during the operation or water condensation on silica structure during cooling.

The reactivity of cavity Ni@SiO$_2$ does not change up to the 12th cycles (Figure 58-a). However, the reactivity of non-cavity Ni@SiO$_2$ with 1nm Ni or 3nm Ni decreases significantly in the second cycle (Figure 58-b, c). The deactivation of non-cavity Ni@SiO$_2$ is likely due to the formation of NiO. After undergoing a 1st cycle at as high as 1000°C, the agglomerated nickel particles move towards the center of silica particles. Figure 59 shows that well-dispersed nickel clusters in non-cavity Ni@SiO$_2$ agglomerate and move towards the center of silica particles after

the 1st reaction cycle. The altered diffusion pathway of reactants accompanying with nickel sintering makes the nickel particles more susceptible to oxidation. In contrast, nickel sintering of cavity $Ni@SiO_2$ does not affect the diffusion pathway.

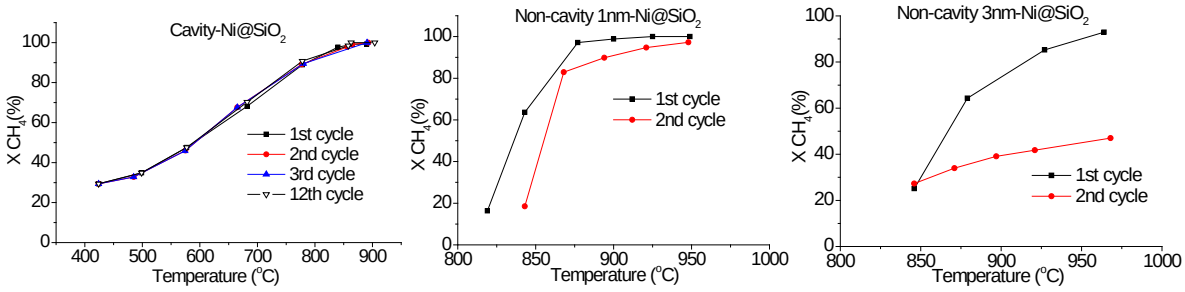

Figure 58: *CH_4 conversion of cavity-$Ni@SiO_2$, non-cavity 1nm $Ni@SiO_2$ and 3nm $Ni@SiO_2$ during multiple cycles (feed in gas CH_4/O_2=2)*

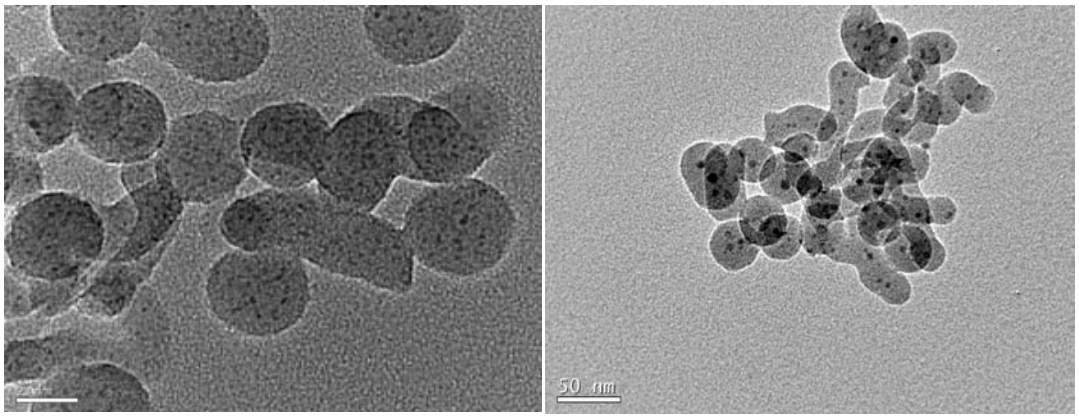

Figure 59: *TEM pictures of 1nm $Ni@SiO_2$ (left) before the reaction and (right) after the 1st cycle of the reaction*

5.4 COKING RESISTANCE

Another challenge for nickel based catalyst applied in CPOM reaction is coking. We tested both cavity-$Ni@SiO_2$ and commercial HiFuel Ni catalyst in a severe fuel rich environment (CH_4/O_2=3) at 800°C to study their coking behavior. Commercial HiFuel catalyst is designed for

higher coking resistance through the high basicity of the support via the addition of Ca and an enhanced metal-support interaction as suggested by TPR in section 5.1. It is reported that the stronger metal-support interaction is beneficial for decreased carbon deposition [179-181]. The reason could be that the stronger chemical bonding between Ni and the support prevents the detachment of the nickel from the support, thereby preventing the formation of carbon filaments. However, the HiFuel catalyst could not survive from coking at our fuel rich reaction condition (CH_4/O_2=3) even though its nickel-support interaction is stronger than that in cavity-Ni@SiO_2 as measured in TPR. The outlet flow rate decreases within ten minutes after the HiFuel catalyst is exposed to the reactant stream and drops to 70% after 20 minutes, indicating a reactor blockage by severe carbon formation (Figure 60-right). A TEM image of HiFuel catalyst after the reaction indicates that both graphic carbon and whisker carbon are formed (Figure 61). In contrast, the activity and selectivity of the core shell material remain constant over five hours of operation (Figure 60-left). A decrease in methane conversion is observed at 5th hour when the CH_4 to O_2 ratio is changed from 2.5 to 3, while minimal change of CO selectivity occurs. This decrease in methane conversion, which is also reported by other researchers, is attributed to the increased methane partial pressure [190, 191]. Based on stoichiometric calculations for solely CPOM reaction, the maximum conversion of CH_4 increases from 0.67 to 0.8 with the decreased feed in ratio CH_4/O_2 from 3 to 2.5. The agreement of the experimental results with stoichiometric calculations indicates the absence of carbon formation on core shell catalyst from methane decomposition reaction. To qualitatively compare the amount of carbon formation on the nickel surface, in-situ TPO is performed after the reaction. The CO_2 peak area in HiFuel catalyst is much larger than that of core shell material, which indicates more severe carbon formation, and agrees with our observation in the reaction. Thus, even though TPR indicates a stronger

interaction between nickel and the support for HiFuel catalyst, it still did not overcome the coking issue. The formation and stabilization of small sized nickel particles (under 5nm) in core shell material are responsible for the inhibition of carbon formation. Both experimental observations and DFT calculations suggest that the growth of graphite is suppressed on small nickel particles (<5nm) since nucleation cannot proceed on the facets and step edges of small particles [10, 178, 192] [46] [47].

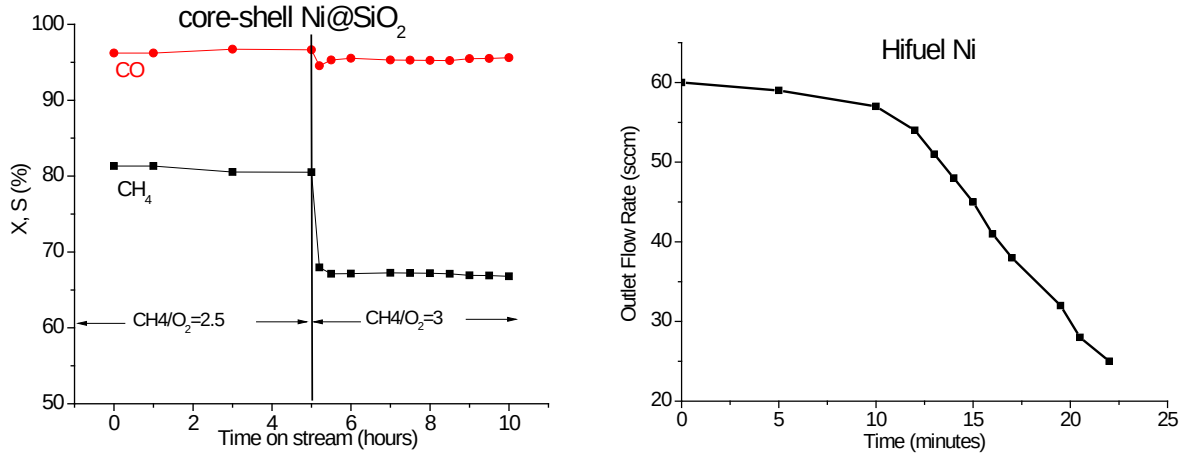

Figure 60: *(left) Methane conversion and CO selectivity of core-shell material at 800℃ from CH_4/O_2=2.5 to CH_4/O_2=3; (right) Total outlet flow of HiFuel catalyst at 800℃ (CH_4/O_2=3)*

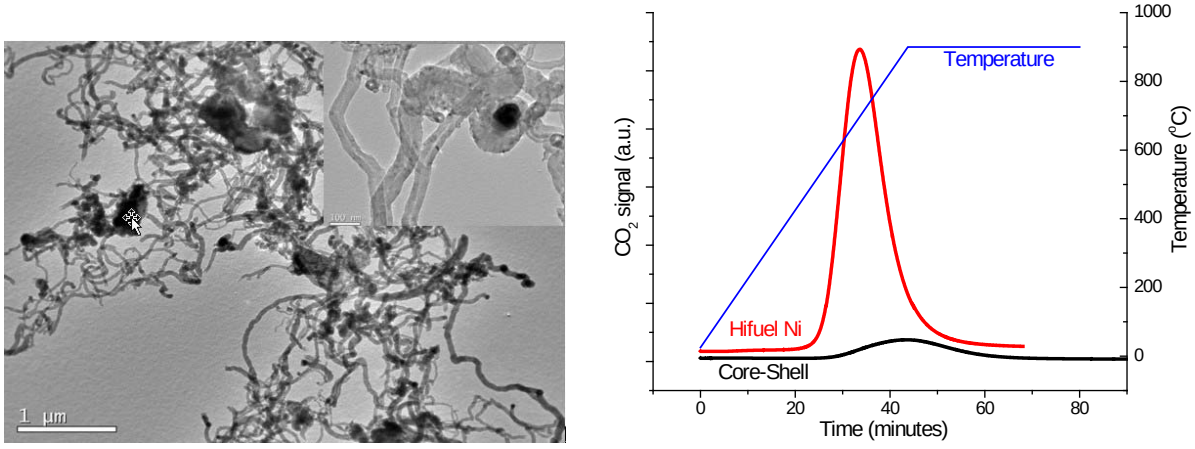

Figure 61: *(left) TEM of HiFuel catalyst after reaction (CH_4/O_2=3); (right) In-situ TPO profile in core-shell and HiFuel nickel catalysts after reaction (CH_4/O_2=3)*

5.5 SUMMARY

We demonstrate the excellent thermal stability and high coking resistance of the core shell material with cavity structure in comparison to both nickel silica supported catalysts and the commercial HiFuel catalyst. The results suggest that cavity Ni@SiO_2 is a promising CPOM catalyst with high activity and selectivity and temperature stability at comparable levels to the HiFuel catalyst. Its coking-free property in the fuel rich environment makes it even more advantageous over the HiFuel catalyst, which undergoes a fast and severe coking ultimately leads to the reactor blockage. The minimal coking of core shell material is attributed to the small nickel particles (under 5nm), which suppress the carbon nucleation and growth on the steps and terraces. The challenge lies in the stabilization of the as-synthesized small nickel particles, which sinter more easily. The deactivation of sol-gel Ni/SiO_2 exemplifies a strong nickel sintering during continuous high temperature operations. In contrast, the nickel particles in cavity Ni@SiO_2 are efficiently stabilized by the presence of silica shell and achieve stable continuous on-stream operations as well as cyclic operations. Surprisingly, a deactivation is observed in non-cavity Ni@SiO_2 material even though the nickel sintering is also minimized by silica shell. The deactivation is due to NiO formation resulting from an increased diffusion pathway when nickel particles agglomerate from the edges of the silica particles towards the center. This suggests that cavity Ni@SiO_2 is superior to non-cavity Ni@SiO_2 since changes to the diffusion pathway do not occur. Overall, the present study confirms the stability and robustness of cavity Ni@SiO_2 in high temperature reaction system. A key to overcome catalyst deactivation, which could be due to sintering, NiO formation or coking, is to stabilize nickel particles under 5nm while maintaining the unchanged diffusion pathway of the reactants within a hollow core.

6.0 MASS TRANSFER LIMITATION

Core-shell material with sub-nanometer nickel clusters and a robust silica shell has an advantage of thermal stability and coking resistance. However, a mass transfer limitation due to the presence of the silica shell potentially limits its application. This chapter will discuss the impact of the different shell thicknesses on the reactivity. The reactivity of the core shell materials as a function of shell thickness is investigated in three different reaction systems. The BET surface area, nickel loading and TEM pictures of the catalysts used in this chapter are given in appendix F.1.1 (Figure 105 and Table 8).

6.1 CO OXIDATION

CO oxidation is one of the simplest reaction models to study the catalyst reactivity and is hence used to study the impact of silica shell thickness. The reaction is performed in a fixed bed reactor with a contact time of 0.4s (calculated at room temperature) and the mixture of 3% O_2 and 1% CO in balance of helium.

6.1.1 Optimum reaction condition

Reaction parameters of contact time and the O_2/CO ratio are optimized to achieve reasonable CO conversion (>80%). The CO conversion increases significantly when the contact time increases from 0.1s to 0.4s (calculated at 298K) as expected (Figure 62-left). Higher CO conversion is achieved for metallic nickel versus NiO since metallic nickel is the active component in the reaction [193] (Figure 62-left). In CO oxidation, bonding energy of surface oxygen determines the catalyst activity. The higher oxygen bonding energy in Ni (452kJ/mol) than NiO (113kJ/mol) could explain why metallic Ni has higher reactivity than NiO in this reaction [194]. The O_2/CO ratio is also adjusted to determine the optimum condition with the highest CO conversion since it is reported that excessive CO will poison the active sites of the metal and reduce its activity [101]. Our results show that the reactivity of core shell material is independent of the O_2/CO ratio from 1 to 7, in which CO is the limiting reactant since the stoichiometry ratio O_2/CO is 0.5 (Figure 62-right). Goodman reported that the reaction for Pd and Ir is first-order with respect to CO partial pressure when O_2/CO>12; whereas the reaction became negative-first order with respect to CO when O_2/CO<12 under ultrahigh vacuum condition [195]. Hertl and Farrauto found that the reaction is first order to CO and zero order to oxygen on Cu [196]. It is also reported that the reaction is first order with respect to CO and independent of O_2 pressure for NiO catalyst [197]. The similar reactivity between different O_2/CO ratios in our case suggests that the reaction is zero order to O_2. This could be explained by a trade-off between catalyst poisoning in fuel rich condition and the formation of NiO in fuel lean environment. The optimum reaction condition is a contact time of 0.4s and an O_2/CO ratio as 3. The operation procedure is found in section 2.3.1.

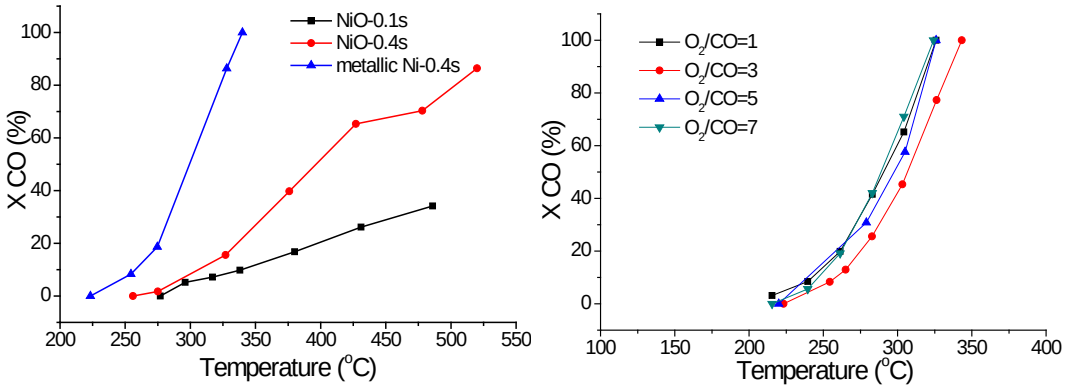

Figure 62: *(left) different contact times and nickel oxidation states; (right) different O_2/CO ratio*

6.1.2 Impact of shell thickness

The reactivity in terms of CO conversion is compared between the cavity Ni@SiO_2 materials with shell thicknesses of 7nm, 12 nm and 20nm (Figure 63). The thinner shells achieve higher CO conversion at lower temperature, i.e. complete CO conversion is achieved at 350°C for a 7nm shell, while only 30% CO conversion is obtained for a 20nm shell. The thinner shell not only shows higher activity, but also has a steeper increase in the CO conversion with rising temperature which indicates higher activation energy. The apparent activation energy for both 7nm shell and 20nm shell is calculated from Arrhenius equation when the CO conversion is under 30%. The higher apparent activation energy in thinner shell (84.7kJ/mol) than thicker shell (66.3kJ/mol) indicates the mass transfer limitation in core shell materials. It is reported that the activation energy for Ni/Al_2O_3 catalyst is 28.9 kJ/mol in 1% CO and 37.7 kJ/mol in 2.2% CO before 340°C [193].

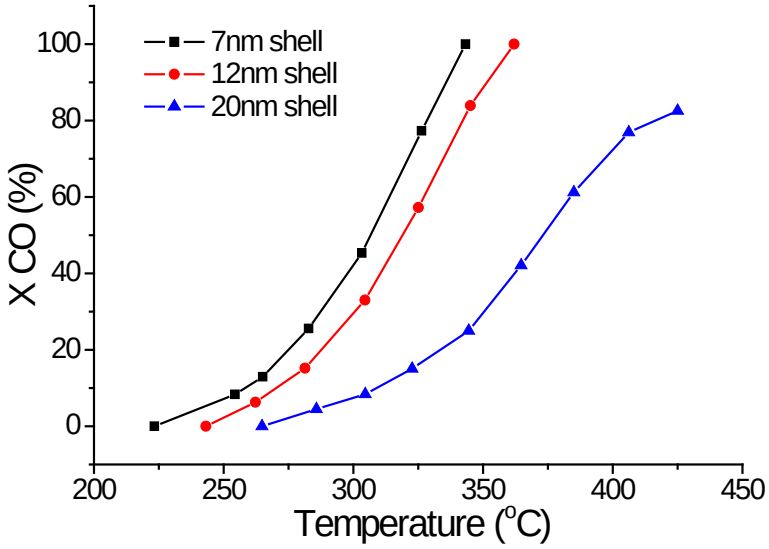

Figure 63: *CO conversion versus temperature for CO oxidation over nickel core silica shell materials with different shell thickness (O_2: CO=3:1 in the balance of He, contact time=0.4s at 25 ^oC)*

6.2 CO METHANATION

After observing mass transfer limitation in one of the simplest reaction system-CO oxidation, we tested whether a similar phenomena for a more complex reactive system with more industrial significance: CO methanation reaction. CO methanation is the final step to purify gas reactant streams for ammonia production and also used to produce methane from coal gasification. The results in chapter 4.4.2 suggest that cavity-Ni@SiO_2 is a potential CO methanation catalyst since it is coking resistant. This motivates us to determine the most desirable core shell configuration for higher reactivity by studying silica shell. The reaction is performed in a fixed bed reactor with the contact time from ~0.12s-0.15s. It is assumed that the morphology of nickel clusters is consistent regardless of shell thickness. The nickel mass (1.5mg) is kept constant for each run to utilize a similar nickel surface area. To determine the reaction

condition, the reactivity of the catalyst under different H_2/CO ratios can be found in appendix F.1.2. A H_2/CO ratio of 3.6 is used in our case and the detailed operation procedure is located in section 2.3.3.

The CO conversion increases to its maximum around ~450°C-550°C and then decreases with increasing temperature since the reaction is exothermic. A higher CO conversion is achieved at lower temperatures for a 7nm shell compared to a 12nm shell. The conversions of both these materials are much higher than the material with a 20nm shell, which reaches less than 10% conversion during the whole temperature range (Figure 64). In addition, the ignition curve of the thinner shell is much steeper than that of the thicker shell. The higher onset temperature and more gradual ignition curve in thicker shell are due to a mass transfer limitation.

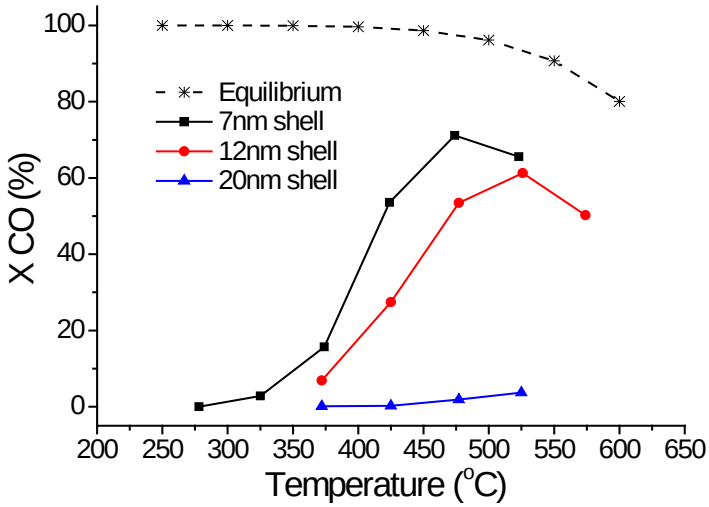

Figure 64: *The CO conversions of cavity-Ni@SiO_2 with different shell thickness (7nm, 12nm, 20nm) (total flow rate 25sccm, H_2/CO=3.6)*

6.3 CPOM REACTION

After observing mass transfer limitation for thicker silica shells in low temperature CO oxidation and moderate temperature CO methanation, we further investigate the core shell materials in high temperature CPOM reaction.

6.3.1 Hysteresis phenomenon in core shell material

Temperature hysteresis is described as the conversion of a reactant measured as a function of temperature is different when increasing the temperature versus decreasing the temperature [198]. One cause for this is insufficient heat removal in exothermic reactions. When cooling off the reactor, the heat released from the reaction is harder to remove due to the poor heat transfer which produces a higher degree of the conversion [198, 199]. The hysteresis can also result from the formation of metallic nickel active sites; the active nickel sites in this reaction are responsible for the higher conversion and selectivity in cooling cycle than heating cycle in CPOM reaction [200-202].

Following the operation procedure in section 2.3.4, the conversion of methane and CO selectivity as a function of catalyst bed temperature were measured during ignition and extinction operations. The arrows in the graphs show the direction of temperature change. The hysteresis loop, which is observed in all core shell material, could be explained by the formation of metallic nickel active site in the extinction branch (Figure 65) [130, 203]. A catalyst color change accompanying with the hysteresis, which is also observed by van Looij and Geus [130], indicates a change in the nickel oxidation state from NiO to metallic nickel. The color of NiO is grey while the metallic nickel is black. The grey color at 850°C in ignition branch indicates the

pre-reduced nickel catalyst is slowly oxidized to form NiO during the reaction [202] (Figure 66-a). At a certain high temperature, it is reduced rapidly by the dissociated CH_4 to the metallic state which agrees with the black color at 850°C in extinction branch [144, 204] (Figure 66-b). The formation of metallic Ni results in a higher selectivity for CO and H_2 in the CPOM dominant reaction during the extinction cycle. The dynamic formation of metallic Ni proceeds only after catalyst ignition. It achieves at least 5 hours of stable operation as low as 500°C. Figure 107 in appendix shows 5-hours stable operation at 500°C, 600°C and 700°C in extinction branch.

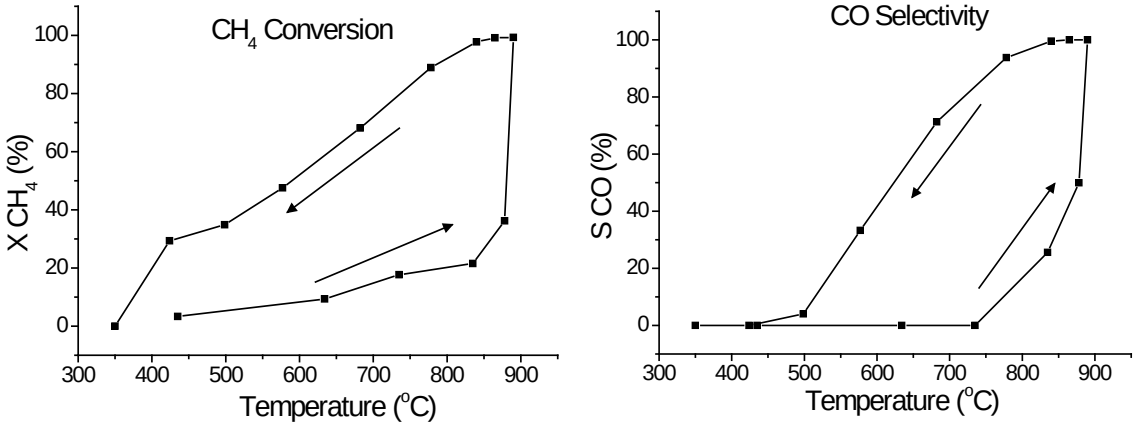

Figure 65: *CH_4 conversion and CO selectivity at different temperatures in CPOM reaction for $Ni@SiO_2$ with a 4nm silica shell (the arrows mark the increase and the decrease in temperature). Reaction condition: CH_4/O_2=2, a mixture of methane and air with flow rate 8.98sccm and 22.3sccm at 1atm*

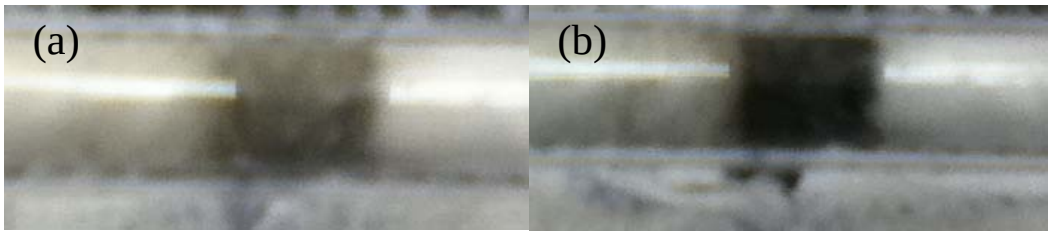

Figure 66: *The color of cavity-$Ni@SiO_2$ at (a) ignition curve and (b) extinction curve at 850°C*

Since it is a challenge to achieve truly isothermal conditions, the conversion and selectivity are also measured as a function of catalyst bed temperature during the complete

ignition and extinction operation in HiFuel catalyst or IMP-Ni/SiO_2 material with the same reactor configuration. No hysteresis is observed in either catalyst (Figure 67) even though the difference between catalyst bed temperature in HiFuel catalyst and oven-set temperature is as high as 70°C once the catalyst ignites. The absence of hysteresis loop in HiFuel catalyst is because of a higher oxidation resistance for the nickel particles, which is the result of the strong interaction between nickel and the modified support. In other words, nickel is more difficult to oxidize once it is fully reduced and remains in the metallic state during ignition process. To further support that the hysteresis resulted from the nickel oxidation state rather than insufficient heat removal, the reactivity of fully oxidized and fully reduced HiFuel catalyst only in ignition operation is compared. One can see that there is a dramatic increase in CH_4 conversion and corresponding CO selectivity at 650^{o}C in fully oxidized catalyst, which is different from the fully reduced catalyst (Figure 68). The abrupt increase is because of NiO decomposition for the formation of metallic nickel at such high temperature which is responsible for higher reactivity and selectivity. Once the metallic nickel is formed (above 650^{o}C), the reactivity and selectivity are the same regardless of the initial nickel state. The absence of hysteresis loop in IMP-Ni/SiO_2 is because of its low reactivity. The nickel particles, which are oxidized to NiO during ignition operation, are not able to reduce back to a metallic state since methane dissociation is not initiated due to the low reactivity (only 40% methane conversion at 900°C). This result suggests that the hysteresis loop exists only when the nickel catalyst has high reactivity and low oxidation resistance.

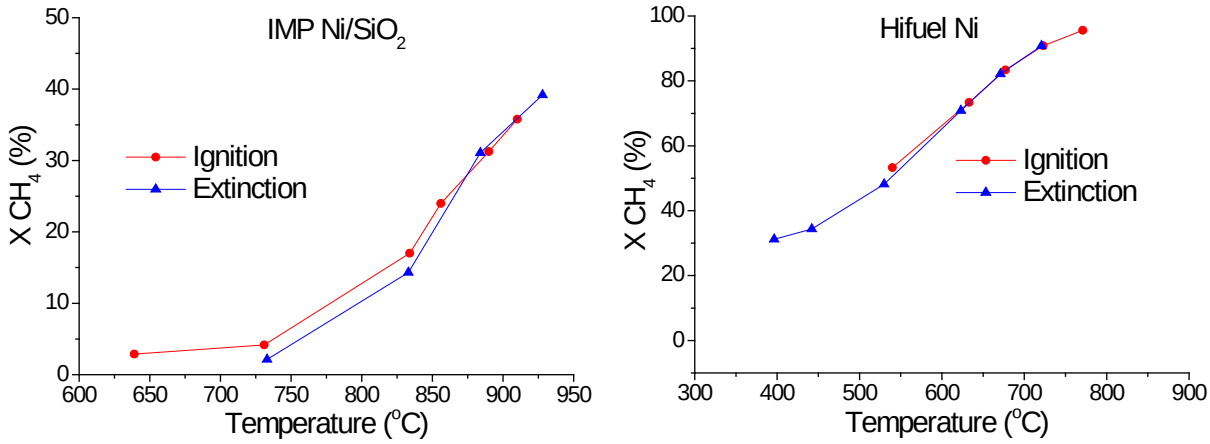

Figure 67: *CH_4 conversion as a function of catalyst bed temperatures for (left) IMP-Ni/SiO_2 and (right) HiFuel Ni catalyst between ignition and extinction operation (CH_4/O_2=2)*

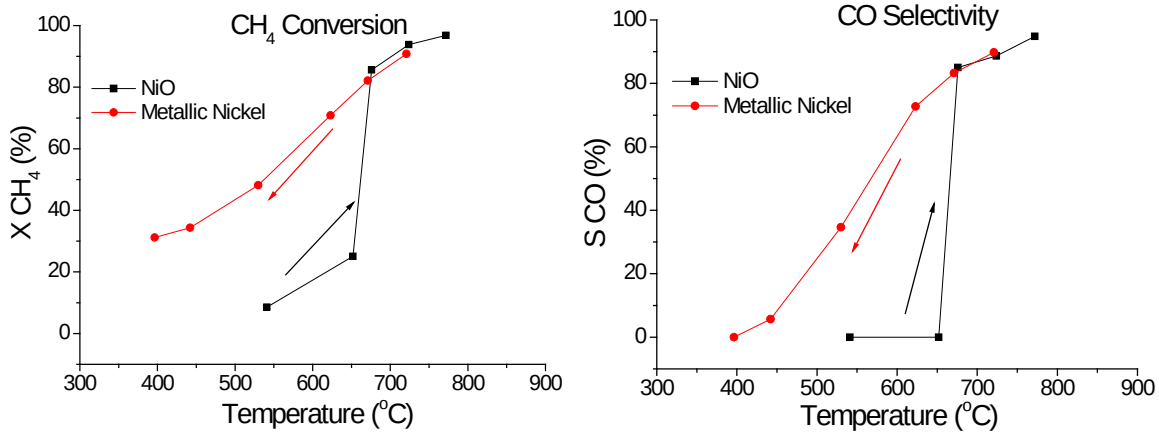

Figure 68: *CH_4 conversion and CO selectivity as a function of catalyst bed temperatures for HiFuel of initial NiO and metallic nickel during ignition operation (CH_4/O_2=2)*

6.3.2 Effect of nickel oxidation state

6.3.2.1 Ignition-extinction between NiO and metallic nickel catalysts

To further understand the impact of nickel oxidation state on reactivity and verify our hypothesis that the hysteresis is due to the change between NiO and metallic nickel, we test fully oxidized and reduced cavity-Ni@SiO_2 in the complete ignition-extinction cycle. Based on the TPO and TPR result, the fully oxidized catalyst is oxidized in air at 500°C for 1 hour and fully

reduced catalyst is reduced in H_2 at 700°C for 30 minutes. Regardless of the initial oxidation state, both catalysts follow similar trends in ignition as well as extinction branch (Figure 69). This indicates that the initial metallic state nickel in the fully reduced sample is quickly oxidized to NiO and shows much lower activity and selectivity in ignition branch than that of extinction branch. A steep increase in conversion occurs at 900°C accompanied with the high syngas selectivity, due to the formation of metallic nickel.

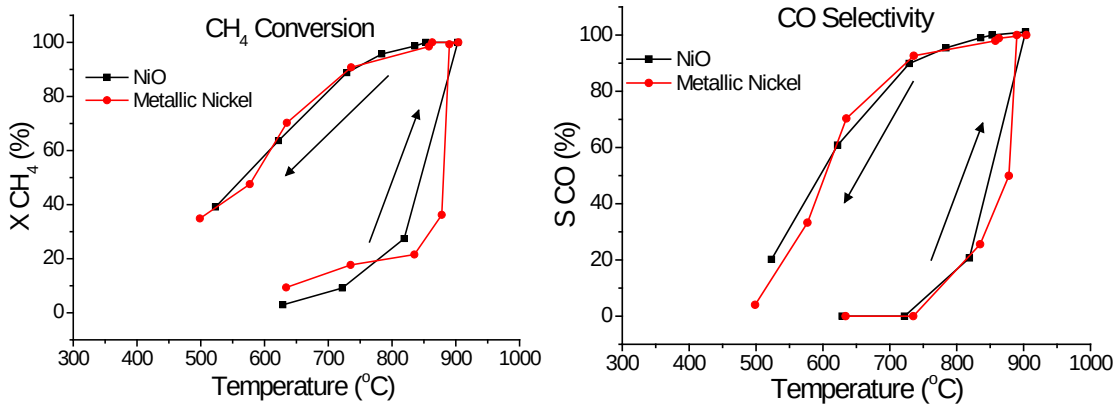

Figure 69: *CH_4 conversion and CO selectivity at different temperatures for cavity-Ni@SiO_2 of initial NiO and metallic nickel during ignition and extinction operation (CH_4/O_2=2)*

Even though there is little difference in terms of the conversion and selectivity in the ignition branch between these two catalysts, there is a distinct difference in MS signal of O_2 at the reactor effluent (Figure 70-left). The oxygen level reaches the steady state very fast (within 1 minute) in the fully oxidized sample once the oven reaches its set-point temperature. In contrast, initially there is a sharp O_2 consumption peak followed by the slow increase in the O_2 level in the fully reduced sample. The oxygen level does not reach the steady state for over two hours. The consumption of the O_2 is one order of magnitude higher than that for complete oxidation of nickel catalyst (see appendix F.1.4 for calculations), which indicates the O_2 consumption is not solely from the nickel oxidation process. The reason for a dramatic decrease in O_2 consumption

at the beginning is because most of the nickel is metallic state initially, which is the active component for the reaction. As the reaction proceeds, the nickel is oxidized to NiO, which results in a lower reactivity and slowing down O_2 consumption rate. Thus, the O_2 consumption is the combination result from the proceeding reaction and the nickel oxidation process. The time to takes O_2 level to reach steady state at 600°C is much longer than that at 800°C. The reason for that is because all the metallic nickel is oxidized to NiO at 800°C, while there is still a co-existence of NiO and metallic nickel in the catalyst at 600°C. At 900°C, there is fast change of O_2 since all of the O_2 is consumed and the catalyst ignites at that temperature.

As described above, the system reaches steady state very slowly in the ignition branch when the initial state of catalyst is metallic nickel. In contrast, the system reaches a steady state very fast (less than 1 minute) in the extinction branch when the oven reaches the set-temperature (Figure 70-right). The faster steady state attainment in extinction branch is because of the remained metallic Ni state due to the high syngas yield as well as the complete O_2 consumption. In the extinction branch, all the oxygen is consumed during the whole operation range (600°C-800°C) while the unconverted methane amount increases with the decreasing temperature. The increase in CH_4 amount at lower temperature is because of the transition from a CPOM dominant reaction to methane combustion dominant reaction due to thermodynamic constraint. The stoichiometry ratio of CH_4 to oxygen is 2:1 from the CPOM reaction and 1:2 from the methane combustion reaction.

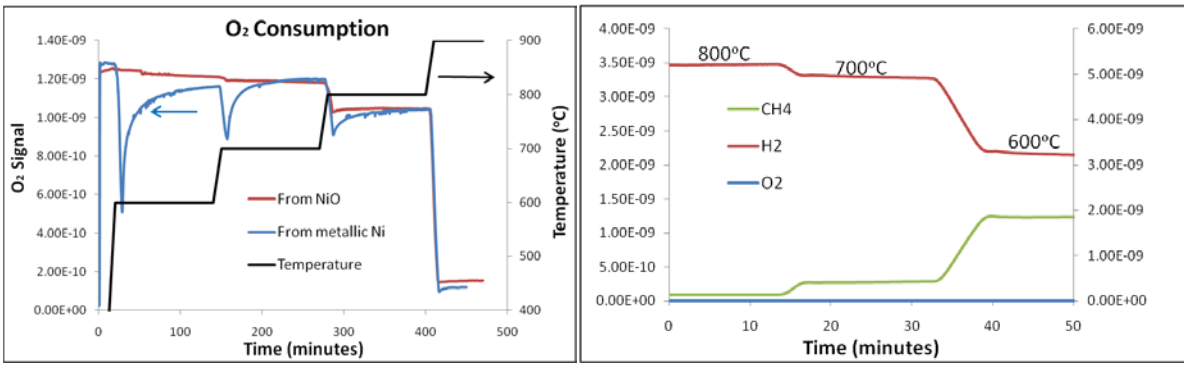

Figure 70: *Oxygen consumption in (left) ignition operation and (right) extinction operation*

6.3.2.2 Impact of different operation approaches

Based on the above discussion, it is clear that the higher reactivity in the extinction branch is due to a formation of metallic nickel from methane dissociation. Hence it is interesting to compare the conversion and selectivity of the extinction branch and the pre-reduced nickel catalyst at the same oven set temperature. The operation for the detainment of pre-reduced nickel catalysts at different oven set temperatures (~500-800°C) can be found in Appendix A.4.

The reactivity of the catalysts in these two different operation procedures is comparable at the higher temperature region (above 700°C), while the methane conversion in extinction branch is higher than that of the protected metallic nickel at lower temperature (under 600°C) (Figure 71). This suggests that a higher fraction of metallic nickel in the catalyst is oxidized to NiO within the alternative approach since the temperature is not high enough to form metallic nickel while introducing oxygen to the system. In the extinction branch, the metallic state of the nickel is simultaneously regenerated by the production of syngas. In this approach, the catalyst bed temperature will increase immediately and stabilize around 760°C within 1 minute at the oven set point temperature of 700°C. This indicates the immediate ignition of the nickel catalyst. The immediate ignition is also observed when oven-set temperature is 600°C. Yet at 800°C,

although the catalyst does ignite, the catalyst bed temperature does not increase much compared with the oven-set temperature due to dominate CPOM reaction over methane combustion. Conversely, at 600°C and 700°C, the strongly exothermic methane combustion is responsible for the large increase in catalyst bed temperature. At an oven set point of 500°C, little temperature increase in the catalyst bed is observed since the catalyst has very low reactivity.

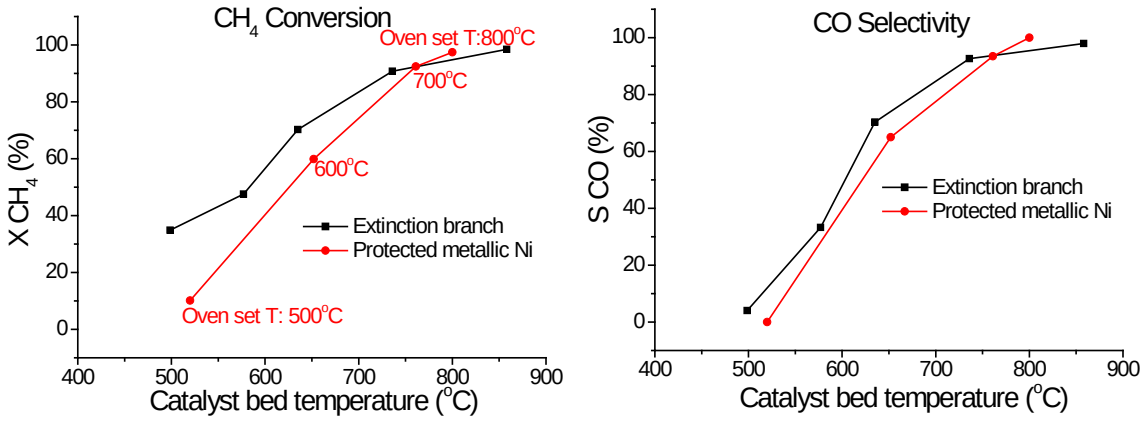

Figure 71: *CH_4 conversion and CO selectivity for cavity-Ni@SiO_2 during extinction operation and protected metallic Ni at different temperatures (CH_4/O_2=2)*

Another approach is to study the impact of different heating rates on catalyst reactivity. Since the nickel will be oxidized to NiO once it is exposed to gas stream during the heating cycle, it is hypothesized that shortening the time that the catalyst exposed to the oxygen would avoid all metallic nickel oxidation. The reactivity of the catalysts at 800°C using different ramping rate 20°C/min, 50°C/min, 70°C/min, 100°C/min is studied. The catalyst ignition accompanies with a fast increase in catalyst bed temperature only when using the fastest heating rate, in which it takes 5 minutes for the oven to heat from 300°C to 800°C (Figure 72). The ignition of the catalyst under this fast ramping suggests that metallic state of catalyst is retained or that a hot spot is created by the faster heating.

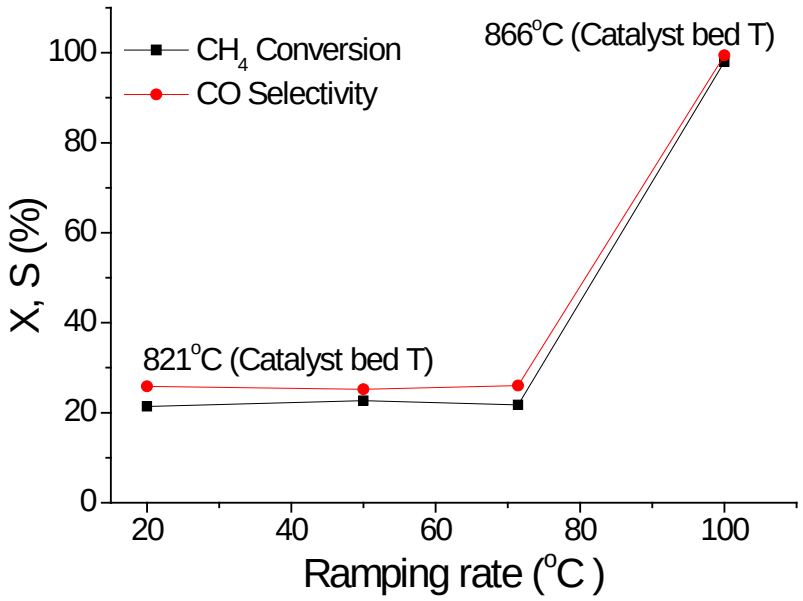

Figure 72: *Methane conversion and carbon monoxide selectivity under different ramping rates from 300°C to 800°C*

6.3.3 Impact of shell thickness

Figure 73 shows the catalyst activity and selectivity during the complete ignition and extinction cycles for several shell thicknesses. For all materials, ignition occurs at 900°C since the nickel clusters are very small and they gradually oxidize to NiO during the ignition process. In extinction branch, the conversion and selectivity is independent of shell thickness up to 10nm. However, there is a dramatic decrease in reactivity and selectivity during the extinction branch when the shell thickness is above 10nm. Since the reactivity of the nickel catalyst is highly correlated with its oxidation state, it is hypothesized that the decreased reactivity in thicker silica shells is due to the formation of NiO. The larger fraction of NiO formation among nickel species in thicker shell could be resulted from the preferential O_2 diffusion compared with methane,

which would create a higher O_2 /CH_4 ratio within the silica shell matrix.

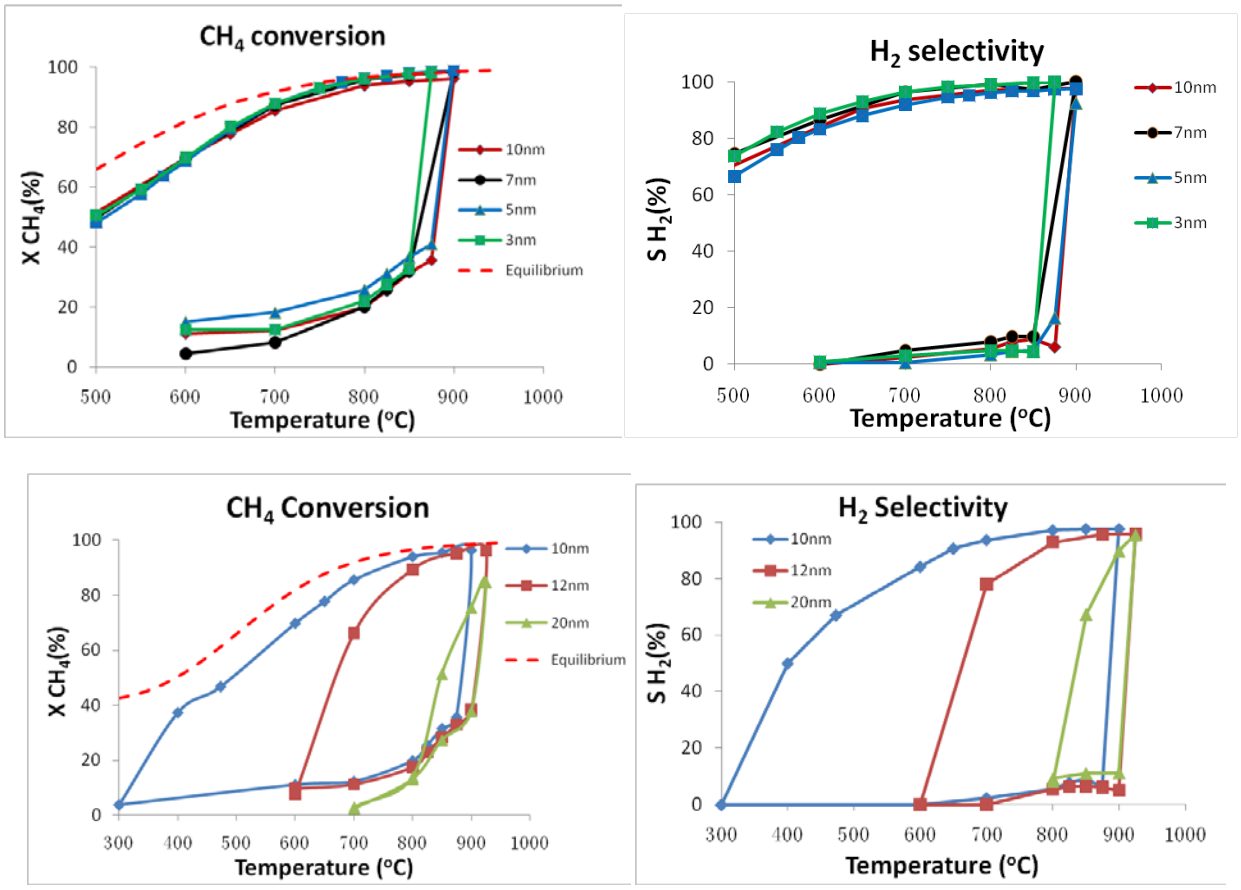

Figure 73: *CH_4 conversion and H_2 selectivity at different temperatures in the CPOM reaction for Ni@SiO_2 with different silica shell thickness: (above) 3nm, 5nm, 7nm, 10nm; (below) 10, 12nm, 20nm (CH_4/O_2=2)*

The type of diffusion in the silica shell is Knudsen diffusion. The mean free path of oxygen and methane is approximately calculated as ~200-300nm in the temperature range from 300°C to 900°C at ambient pressure, which is two orders larger than silica pores (1nm).

In Knudsen diffusion, the reacting molecules collide more often with pore walls than with each other. The Knudsen diffusion coefficient (in cm^2 s^{-1}) of a certain species it can be defined as:

$$D_{ki}=9700 r_p \sqrt{\frac{T}{M_i}}$$

Where r_p (cm) is the pore radius, T(K) is the temperature and M_i(g/mol) is the molecular weight.

This model accounts for light molecules diffusing faster than the heavy ones. However, the classic Knudsen diffusion equation does not consider any steric effect. The molecular diameters of oxygen, methane, and nitrogen are 0.338nm, 0.371nm and 0.363nm respectively [205]. Yet, larger methane molecules with tetrahedral structures could diffuse more slowly into the silica pores than linear-structured oxygen molecules.

It is well known that metallic nickel is the active site for the CPOM reaction. The change of the nickel oxidation state from metallic nickel to NiO will result in a lower reactivity and selectivity. To confirm our hypothesis that the lower activity in thicker shell is due to a larger amount of NiO formation, we need to compare the fraction of metallic nickel in thicker shell and thinner shell. However, the characterization of the core-shell material after the reaction is difficult. One limitation is its small nickel particles size (<2nm), which cannot be detected by XRD. Another commonly used technique is X-ray photoelectron spectroscopy (XPS), which has a penetration depth of only ~1-5 nm [206]. Hence, we are not able to detect nickel species since the nickel particle is coated by silica shell that is greater than 5nm. The other limitation is that the nickel clusters oxidize easily after their exposure to the air and the oxidation resistance decreases with the decrease in nickel particle size. We hence lack in-situ characterization capabilities to detect smaller sized nickel particles in the presence of a silica shell. However, we did observe the color change of the catalyst bed for a 20nm shell before the reaction (fully reduced) and at 800°C in the extinction branch with the comparison of the consistent nickel color in a thinner shell. The grey color in Figure 74-left is fully reduced catalyst and the white color indicates the formation of NiO at 800°C in extinction branch. (Note: Usually metallic nickel is black and NiO is grey color. However, the intensity/degree of the color depends on the nickel

loading as well as the shell thickness. When the nickel loading is low or the shell is thicker, the metallic nickel is more towards grey color and NiO shows white color which is more like the color of pure silica).

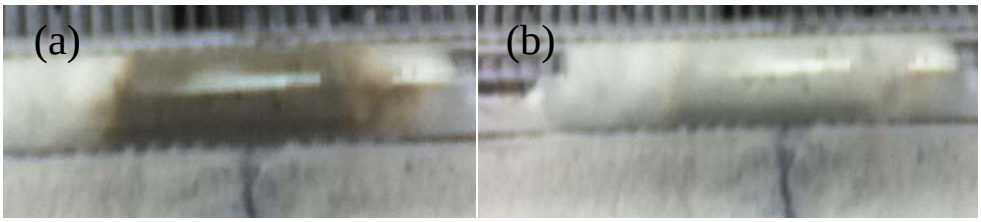

Figure 74: *Color change for $Ni@SiO_2$ with 20nm shell (a) before the reaction (fully reduced) and (b) at 800℃ in the extinction branch*

The color change of the catalyst is strong evidence that the lower reactivity of the catalyst with thicker shell is due to the NiO formation. In-situ TPR is performed to qualitatively compare the fraction of NiO formation among nickel species between the catalysts with thicker shell (20nm) and thinner shell (7nm) at 800°C in extinction branch. The procedure for in-situ TPR is found in the experimental section 2.3.5. The peak area, which indicates the amount of H_2 consumed by the catalyst, directly correlates with the amount of NiO in the catalyst. The larger peak area means that more NiO species is present in the catalyst. Figure 75 shows that the total peak area of hydrogen consumption in 7nm shell is significantly smaller than that in 20nm shell, which indicates that less NiO species present in 7nm than 20nm. The small peak area in 7nm shell indicates there is a significant of amount of metallic nickel besides NiO species in the catalyst. The co-existence of NiO and metallic nickel is consistent with the mechanism of CPOM reaction (i.e. nickel species are oxidized to the weakly bonded NiO and simultaneously reduced to the metallic nickel by the dissociation of methane [131, 136, 144]). Thus, the TPR result provides the direct evidence for our hypothesis that the lower reactivity of thicker shell compared with thinner shell in extinction branch is due to higher fraction of NiO formation.

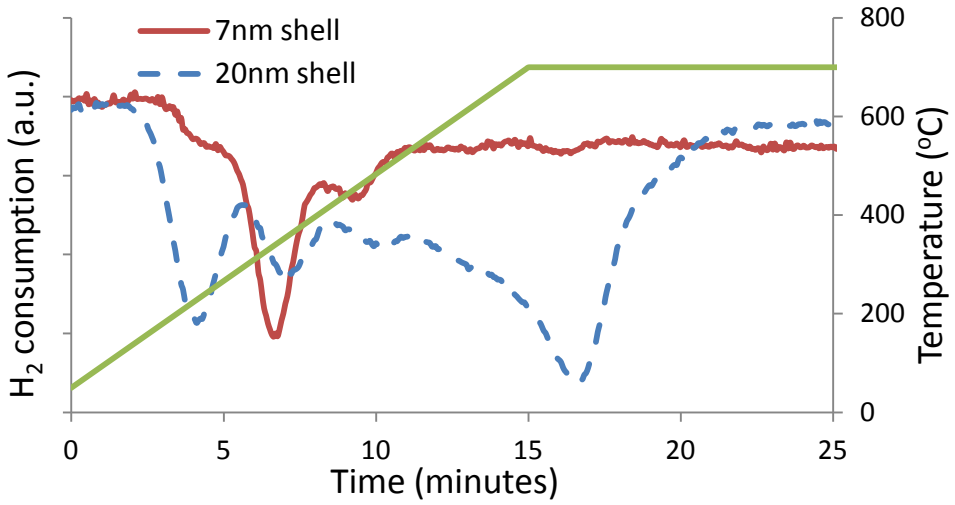

Figure 75: *In-situ TPR of cavity Ni@SiO$_2$ with 7nm and 20nm shell at 800°C in the extinction branch*

6.3.4 Impact of CH_4/O_2 ratio

To support our hypothesis that preferential O_2 diffusion occurs in the microporous silica shell, different CH_4/O_2 ratios from fuel lean to fuel rich environment are performed. The conversion and selectivity of the core shell material with a 4nm shell thickness and the commercial HiFuel catalyst are compared. Compared with the core shell material, the HiFuel Ni catalyst has a high oxidation resistance due to its larger nickel particles as well as the modified support. One of the distinct differences between these two catalysts is that there is no hysteresis for the HiFuel catalyst in any case, while hysteresis occurs when $CH_4/O_2 \geq 2$ for core shell materials (Figure 76). Another distinction, as illustrated in Figure 77-left, is that methane conversion decreases with increasing CH_4/O_2 ratio for the HiFuel catalyst while it reaches its maximum at CH_4/O_2 of 2 in the core shell material. The general trend for CPOM reaction is that methane conversion decreases from fuel lean to fuel rich environment since O_2 is limiting reactant. The exception that methane conversion is lower in the core shell material in a fuel lean

environment is because of NiO formation, which results in a lower reactivity. The reason that the methane conversion for the HiFuel catalyst is higher than that in the core shell material in a fuel rich environment (CH_4/O_2 =3) is that carbon formation occurs from methane dissociation in HiFuel catalyst. One can see that CO selectivity in HiFuel catalyst is much lower than that of cavity $Ni@SiO_2$ at higher methane conversion which indicates the carbon formation. Additionally, the ignition temperature for core shell material decreases from 900°C ($CH_4/O_2 \leq 2$) to 800°C (CH_4/O_2=3) with the contraction of hysteresis loop compared with CH_4/O_2=2. This indicates that the fuel rich environment is beneficial for preventing nickel from oxidation and maintaining its high activity during ignition branch. The results once again confirm that nickel species in the core shell material are very sensitive to oxygen and the preferential O_2 diffusion will facilitate the NiO formation.

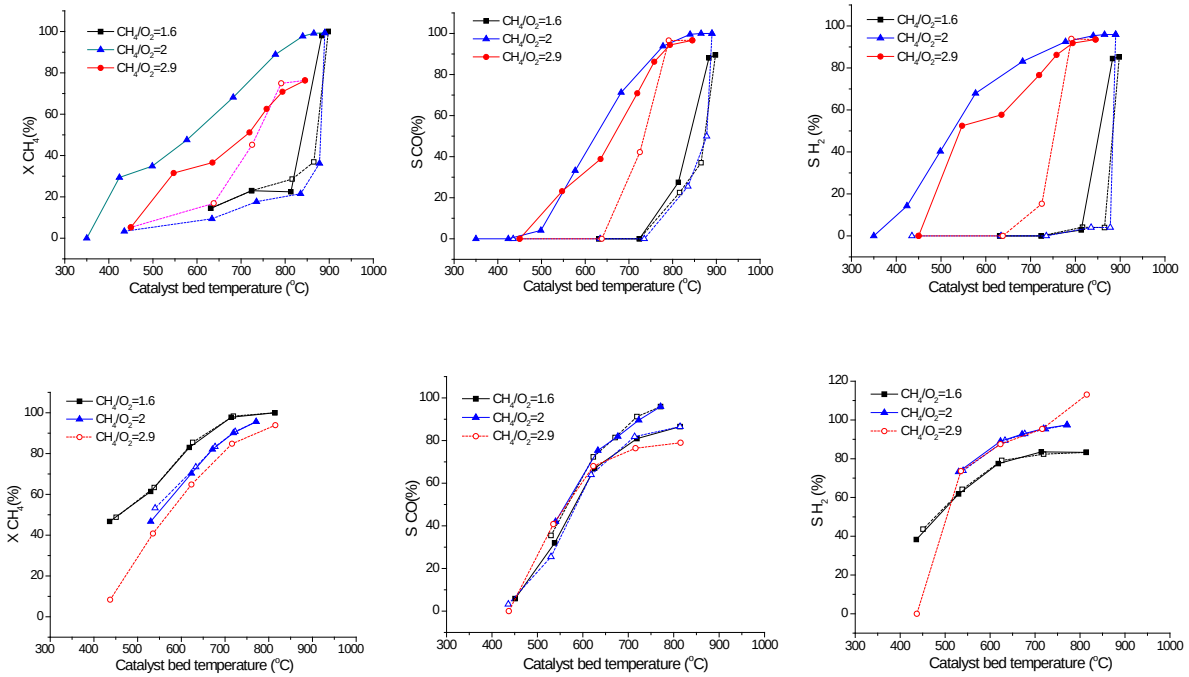

Figure 76: *Methane conversion and H_2 selectivity of different CH_4/O_2 ratios for (top) cavity-$Ni@SiO_2$ with 4nm shell and (bottom) HiFuel Ni catalyst (Dashed line: ignition branch; solid line: extinction branch)*

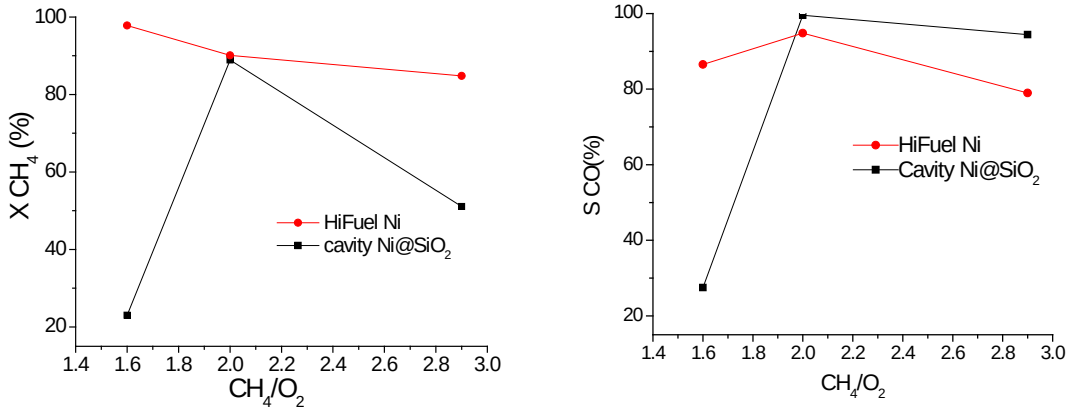

Figure 77: *Methane conversion of different CH_4/O_2 ratios for cavity-Ni@SiO2 with a 4nm shell and the HiFuel Ni catalyst at 700℃*

6.4 SUMMARY

Core shell material with microporous silica shells (pore diameter 0.8nm) is used as a nano-reactor to study the transport of different gas molecules. A delayed ignition curve with the increasing silica shell thickness is observed at multiple temperature operations: in low T CO oxidation, medium T CO methanation and the high T CPOM reaction. A steep increase in the ignition curve for the material with thinner shells is observed in both CO oxidation and CO methanation, which indicates a lower apparent activation energy in the materials with thicker shell is due to the mass transfer limitation. However, the opposite phenomenon is observed in CPOM reaction, in which a sharp decrease in ignition curve is observed in the materials with thicker shell. This difference is due to a change in nickel oxidation state in CPOM reactions beyond mass transfer limitation. The preferential O_2 diffusion through silica shell results in a higher O_2/CH_4 ratio when silica shell thickness increases. A higher O_2/CH_4 ratio facilitates the formation of NiO, which is not the active components in the CPOM reaction and hence decreases

catalyst reactivity. It is also proposed that the mass transfer limitation could be removed when shell thickness is below 10nm, which is proven by an unchanged reactivity of core shell materials with different shell thicknesses ranging from 3nm to 10nm in the CPOM reaction. This result suggests that the synthesized shell thickness should be less than 10nm to effectively mitigate mass transfer limitation. The silica shell, which serves as a porous membrane for preferential diffusion of different molecules, could achieve different gas compositions between the “nano-bubble” and the external gas stream. This possibility greatly expands our capability to study reactions into the explosion range for the “nano-bubble” with safe non-explosive regime of external gas streams in the reactor.

7.0 SUMMARY AND OUTLOOK

7.1 SUMMARY

One of the biggest challenges for nanocatalysts is thermal stability. The sintering of active components will result in a decreased reactivity due to a reduction of surface area and the disappearance of terrace/step sites. Encapsulating metal cores with porous inert shells is an efficient approach to enhance catalyst stability. However, avoidance of mass transfer limitations due to the presence of the shell is not well understood. Another area that needs development is simple and straightforward methods to synthesize core shell materials, especially the ones with cavity structures possessing small sized nickel particles (<5nm). Our goal is to synthesize well-controlled nanocatalysts with high temperature stability and to understand structure dependent properties by material characterization and reactive testing.

The synthesis and post-treatment methods for this newly developed core shell material are optimized and standardized. Our approach to obtain size and shape controlled nickel particles and silica shells is highly reproducible. The synthesis route is not limited to nickel particles, but can also be applied for a broad range of other metals (e.g. Cu, Co, Pd). The presence and addition order of hydrazine are essential in creating the unique cavity structure. The pore size of the silica shell is around ~1nm, independent of the shell thickness and structure difference, which enable gas molecules (e.g. CO_2, CH_4, C_2H_6) and small liquid molecules (e.g. H_2SO_4) to penetrate

and react with active components. Mass transfer limitations are observed when the silica shell is greater than 10nm in CO oxidation, CO methanation as well as partial oxidation of methane. The thermal stability of nickel as well as silica support is thoroughly studied. The sintering rate of nickel particles is significantly slowed down by the silica shell and the nickel particles are stabilized under 5nm up to 1000°C. The sintering of nickel particles in core shell materials with a cavity structure does not affect the transport properties compared with materials without a cavity structure. The sintered nickel particles in non-cavity core shell materials move towards the center of the silica particle, which modifies the diffusion pathway for the reactants and further decreases the catalyst reactivity. However, the reactivity and selectivity of the core shell material with cavity structure does not change during on-stream high temperature operation as well as multiple cycles in CPOM reactions even with slightly agglomerated nickel particles. The high coking resistance of the cores shell material due to the formation and stabilization of nickel particles under 5nm is also highlighted. The minimal coking in the core shell material is observed in both the CPOM reaction under fuel a rich environment and the CO methanation reaction.

We not only demonstrate the capability to synthesize well controlled nanocatalysts with high temperature stability and minimal mass transfer limitation, but we also understand the structure correlated reactivity in several reaction systems. Additionally, we highlight the correlation between sintering, mass transfer, and coking properties of the catalysts.

7.2 OUTLOOK

7.2.1 Core-shell catalysts

In Chapter 3.0, we proposed the unique structure of both nickel and palladium in nano-confinement. The potential application for this type of structure is that it might facilitate multiple reactions while minimizing undesired side reactions. For example, nickel is an excellent catalyst for steam reforming/CPOM and the main products are CO and H_2. Pd is a catalyst for methanol production from syngas. The presence of neighboring nickel and Pd particles might be able to allow these two reactions happen simultaneously at high temperature while suppressing the water gas shift reaction. The challenge of this concept is to seek multiple reactions operated in the comparable temperature range (i.e. methanol production is usually operated lower than 300^{o}C while the steam reforming reaction is higher than 700^{o}C due to thermodynamic constrain). Another direction is to study the ensemble effect of Pd by comparing the reactivity of this material with bimetallic NiPd@SiO_2 synthesized by Stöber method in Chapter 3.0 as well as the pure nickel or palladium core shell catalysts in the CPOM reaction. A number of experiments suggest that the addition of Pd in a nickel catalyst would be beneficial for the higher reactivity and low carbon deposition.

In Chapter 3.0, we also demonstrated the capability to synthesize Co@SiO_2, Cu@SiO_2, Pd@SiO_2 and Fe@SiO_2, which not only allows us to apply these monometallic catalysts to different reaction systems, but also extends the potential applications for the Pd/Ni@SiO_2 typed structure mentioned in section 3.4.2. Co-based catalysts are commonly used in Fischer-Tropsch reaction. Cu-based catalysts are known for water-gas shift reaction and Pd-based catalysts are widely used in automobile emission control. More importantly, the possible combination of the

above metals opens new opportunities to compare their activity in certain reaction systems with the reported corresponding bimetallic catalysts. For example, DFT calculations and experimental results suggest that the Ni-Fe bimetallic catalyst has much higher reactivity than the pure nickel-based catalyst in the CO-methanation reaction [207]. Ni-Co, Ni-Pd bimetallic catalysts are reported to show excellent stability, high activity, and coking resistance for CO_2 reforming of methane [49, 168].

7.2.2 In-depth properties investigation

There are two interesting observations in properties of the core shell material discussed in section 3.5.3 and section 3.5.4: nickel surface area measurement and the particle size dependent reducibility. The chemisorption measurement of the same sample batch is not reproducible even though the same standard analysis procedure is followed. This variation may be due to an inappropriate chemisorption model for the case when nickel particle under a critical size. A DFT simulation is suggested to compare with the chemisorption data from our experiments to elucidate the differences and discuss the impact of nickel particle size on the accuracy of chemisorptions results. Additionally, the hydrogen uptake peak area decreases with an increase of the nickel particles size, indicating that degree of reduction also decreases at larger particle sizes. The shift of the reduction peak to higher temperature for the core shell material after high temperature treatment might be attributed to the formation of nickel silicate species, but further evidence of this has not been found. The reduction degree and peak location determined from TPR data could be correlated with the fraction of unreduced nickel species and the chemical composition analyzed from XANES data. This would help us to further understand the chemical and physical properties of nickel species.

7.2.3 In-situ catalyst studies

Section 6.3.2 discussed the impact of oxidation state of nickel species on the reactivity in CPOM reaction. However, the small sized nickel particles and the easily oxidized metallic nickel species limit the material characterization. Our collaboration with Dr. Jeff Miller at Advanced Photon Source at Argonne National Laboratories has been initiated to investigate these materials via EXAFS/XANES. The future accessibility of XANES and in-situ XANES could provide us the direct evidence of the correlation of nickel oxidation state and catalytic activity in CPOM [132]. The in-situ XANES during core shell material synthesis could also help us to understand the synthetic pathway in Chapter 3.0. It might provide additional information regarding when and how nickel clusters are formed during the synthesis and how they contribute to the formation of cavity structure.

7.2.4 Pore diffusion simulations

Mass transfer limitation is observed when the shell is thicker than 10nm in three different reaction systems. The well understood configuration of the core shell material (i.e. the porosity, shell thickness) allows us to establish a proper simulation model. A simulation result could be compared with our experimental data to further understand transport in micropores. More importantly, a simulation is also suggested to investigate the preferential diffusion between different gas species or liquid reactants, which could correlate the reactivity and selectivity data.

7.2.5 New exploration of $Ni@SiO_2$

The high coking resistance of the core shell material is discovered and demonstrated in CPOM reaction as well as CO methanation reaction. The coking resistance is due to the formation of small sized (<5nm) nickel particles, which inhibits the carbon nucleation on the step and terrace sites of the particles. Another reaction system that is suitable to demonstrate this superior property is methane dry reforming reaction, where coking is also a limitation for nickel-based catalysts [164, 208, 209]. Besides this, the reducing environment of dry reforming avoids the complexity of nickel oxidation state change during the reaction and would hence further our understanding of the catalysts by excluding this complexity. Another reactive system is steam reforming of methane, which also involves significant coking for nickel-based catalysts [10, 35, 37]. However, the concern for this reaction is the instability of the silica support in presence of the steam due to the formation of silica hydroxide. However, a number of researchers still apply silica supported catalysts in steam reforming reactions [27, 210]. It could be a good reaction system to demonstrate the coking behavior and also study the hydrothermal stability of the material as a function of silica shell thickness. Beyond the coking resistance of the core shell material, there is a potential for strong resistance to sulfur poisoning due to the presence of the shell [211]. Trace amount of H_2S could be introduced to the stream in CPOM reaction in order to evaluate its performance.

APPENDIX A

PROCEDURES

A.1 TPR/TPO

The pretreatment (step 1 and 2) is described in Figure 78. The procedure for TPR is standardized as follows:

1) Pretreat sample in the 5% O_2 in He to remove moisture and impurities on the catalyst surface by ramping from room temperature to 500°C at 20°C/min, and holding at 500°C for 1hr.
2) At 500°C, switch the supply gas to He and hold for 30 minutes.

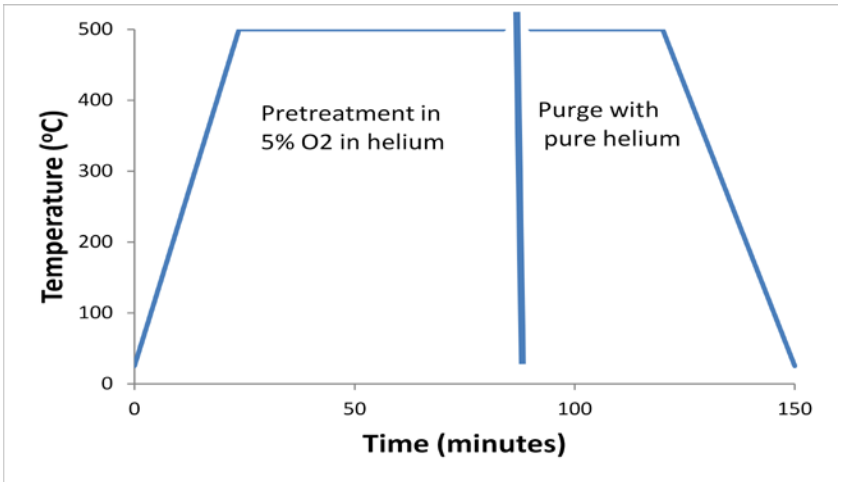

Figure 78: *Temperature programming for pre-treatment in TPR*

3) Open the furnace chamber carefully. Cool down the chamber in He flow with fan. Wait until the sample temperature reaches room temperature ~25°C-30°C.
4) Close the chamber (to ensure the sample temperature is stabilized around room temperature), switch to 10% H_2 in Ar.
5) Create a new file in the chemisorption station, wait until the baseline is stabilized
6) Ramp from room temperature to 800 °C at 5°C/min.
7) Once the temperature reaches 800°C, turn off the chemisorption station

After above TPR, TPO is performed without removing the sample.

8) Purge with He again at 500°C for 30 minutes, then repeat step 3) above.
9) Close the chamber (to ensure the sample temperature is stabilized around room temperature), switch to 5% O_2 in He.
10) Repeat step 5)-7) for TPO

To obtain a TPR of the sample after different temperature treatments in section 4.3, the sample is treated in 10% H_2 in Ar without removing the sample. For example, the following steps are done to obtain a TPR of the sample after an 800°C treatment for 2hrs in H_2.

11）After TPO, purge the system with He

12) Switch to 10% H_2 in Ar, ramping to 800°C at the rate 30°C/min and hold for 2 hours. Then repeat step 2)-10) using a modified final temperature of 900°C rather than 800°C.

A.2 CALCULATION IN REACTIONS

A.2.1 CO oxidation

Using molar quantities, CO conversion is defined as:

$$Xco = \frac{[CO]_{in} - [CO]_{out}}{[CO]_{in}}$$

Helium is used as internal standard to determine CO and CO_2 amount in the system.

Assuming CO and CO_2 are the only carbon containing species in the system, and that no coke formation occurs within the reactor, the carbon balance is calculated as

$$[CO]_{in} = [CO]_{out} + [CO_2]_{out}$$

A.2.2 Ethylene hydrogenation

Using molar quantities, C_2H_4 conversion is defined as:

$$X_{C_2H_4} = \frac{[C_2H_4]_{in} - [C_2H_4]_{out}}{[C_2H_4]_{in}}$$

Helium is used as internal standard to determine C_2H_4 and C_2H_6 amount in the system.

Assuming C_2H_4 and C_2H_6 are the only carbon containing species in the system, and that no coke formation occurs within the reactor, the carbon balance is calculated as

$$[C_2H_4]_{in} = [C_2H_4]_{out} + [C_2H_6]_{out}$$

A.2.3 CO methanation

Using molar quantities, CO conversion is defined as:

$$Xco = \frac{[CO]_{in} - [CO]_{out}}{[CO]_{in}}$$

Helium is used as internal standard to determine the amount of all species (CO, CO_2, CH_4, H_2) in the system. The carbon balance is calculated as

$$[CO]_{in} = [CO]_{out} + [CO_2]_{out} + [CH_4]_{out}$$

A.2.4 CPOM

Using molar quantities, methane conversion, H_2 and CO selectivity are defined as:

$$X_{CH4} = \frac{[CH_4]_{in} - [CH_4]_{out}}{[CH_4]_{in}}$$

$$S_{CO} = \frac{[CO]_{out}}{[CH_4]_{in} - [CH_4]_{out}}$$

$$S_{H_2} = \frac{[H_2]_{out}}{2*([CH_4]_{in} - [CH_4]_{out})}$$

N_2 is used as internal standard to determine the amount of all species (CO, CO_2, CH_4, H_2) in the system. Assuming CO, CO_2, and CH_4 are the only carbon containing species in the system, and that no coke formation occurs within the reactor. The carbon balance can be closed as:

$$[CH_4]_{in} = [CH_4]_{out} + [CO]_{out} + [CO_2]_{out}$$

A.3 IN-SITU TPR

Since MS is not sensitive to H_2, two experimental factors need to be carefully adjusted to show the proper TPR peak: the proper percentage of H_2 in helium and the suitable temperature programming. 6.3% H_2 in He with a total flow rate 32 sccm is used since a higher percentage of H_2 in He will not show a TPR peak. The temperature programming used in our case is to increase the temperature from room temperature to 700°C for 15 minutes and hold for 30 minutes. It is noted that the temperature program used in regular TPR stated in section 2.2.4 does not work since the H_2 baseline does not stabilize when increasing the temperature at lower ramping rates like 5°C/min or 10°C/min. The standardized procedure for in-situ TPR is developed and strictly followed:

1) After the reaction at 800°C in extinction curve, quickly switch the gas mixture from reactor line to bypass line to avoid any potential nickel surface change during the shutting off.
2) Turn on the helium; turn off the air followed by methane. Then switch back the helium from bypass line to reactor to purge the reactor while cooling down the reactor with fan for 30 minutes.
3) When the temperature reaches room temperature, turn on the H_2. Create a new MS file for in-situ TPR.
4) Wait another 30 minutes until H_2 baseline is stabilized
5) Heat the oven from room temperature to 700°C for 15min and hold 700°C for 30min.

A.4 OPERATION FOR THE PROTECTED METALLIC STATE CATALYSTS

The following is the procedure for the protected metallic state catalysts at different oven set temperatures (~500-800°C). For example, the same catalyst can be fully reduced in H_2 at 700°C for 30 minute, followed by a reactor purge with He while cooling down the oven. After 10 minutes, both valve 5 and 6 are closed to make sure the metallic state ndddickel is protected by He (Figure 5). Then turn off He, turn on the methane followed by air and switch the gas steam to the bypass line. Wait 10 minutes to make sure the feed in gas composition reach the CH_4/O_2 ratio as 2 (checked by GC). Heat the oven to the set-point 700°C. Once the oven reaches its set point, the feed gas is redirected from the bypass line to the reactor line and the reactor effluent is monitored. The same method is applied for multiple temperatures (i.e. 500°C, 600°C and 800°C). Since it is difficult to achieve true isothermal conditions, the catalyst bed temperature is also carefully measured.

APPENDIX B

SYNTHESIS

B.1 COMPARISON CATALYSTS SYNTHESIS

B.1.1 IMP-Ni/SiO_2

IMP-Ni/SiO_2 is synthesized from the conventional wet-impregnation method. Pure silica particles are synthesized following exactly the same reverse microemulsion route described in section 2.1.1 without the addition of nickel nitrate solution as the only difference. The dried white power sample is calcined in the air at 500°C for 2 hours to remove the surfactants as described in section 2.1.2. 0.2g above synthesized silica particles are submerged by 2mL $Ni(NO_3)_2$ (0.1M) solution in a small glass vial with overnight stirring. Afterwards, the sample in the uncapped vial is heated at 80°C while stirring until the sample is dried. The dried green powered sample is calcined again at 500°C for 2 hours with the heating rate 20°C/min. The targeted 5% nickel loading IMP-Ni/SiO_2 sample shows the grey color.

B.1.2 DP-Ni/SiO_2

Pure silica particles are synthesized following the same reverse microemulsion route described in section 2.1.1 without the addition of nickel nitrate solution as the only difference. The dried white power sample is calcined in the air at 500°C for 2 hours to remove the surfactants as described in section 2.1.2. 0.6g above silica particles are dispersed in 5mL DI water. The $NiCl_2$ stock solution is prepared by dissolving 0.55 g $NiCl_2$ in 10 mL DI water. A mixture of the above $NiCl_2$ solution and the silica particles are sonicated for better dispersion and then stirred for 20min. Ammonium hydrate is added dropwise (~3-5mL) until the pH 10.5-11 is reached. Afterwards, the solution is centrifuged and dried. The dried sample is calcined at 300°C in the air for 1 hour with the heating rate 10°C/min. (The procedure is developed by M. Najera.)

B.1.3 Sol-Gel Ni/SiO_2

Sol-gel Ni/SiO_2 is synthesized following exactly the same reverse microemulsion route described in section 2.1.1 with a change in the $Ni(NiO_3)_2$ concentration and the TEOS amount. 1.5mL 1.5M $Ni(NO_3)_2$ stock solution is added into the mixture of 10.5g Brij58 and 50mL cyclohexane at 50°C. When adding TEOS, only 1g is added for 2 hours hydrolysis reaction. The dried power sample is calcined in the air at 500°C for 2 hours to remove the surfactants as described in section 2.1.2.

B.2 SURFACTANT/WATER

The shape of the core shell material changes from spherical structure to long tubes when increasing surfactant/water ratio. However, no uniform structure is formed when the surfactant/water ratio is lower than 2.

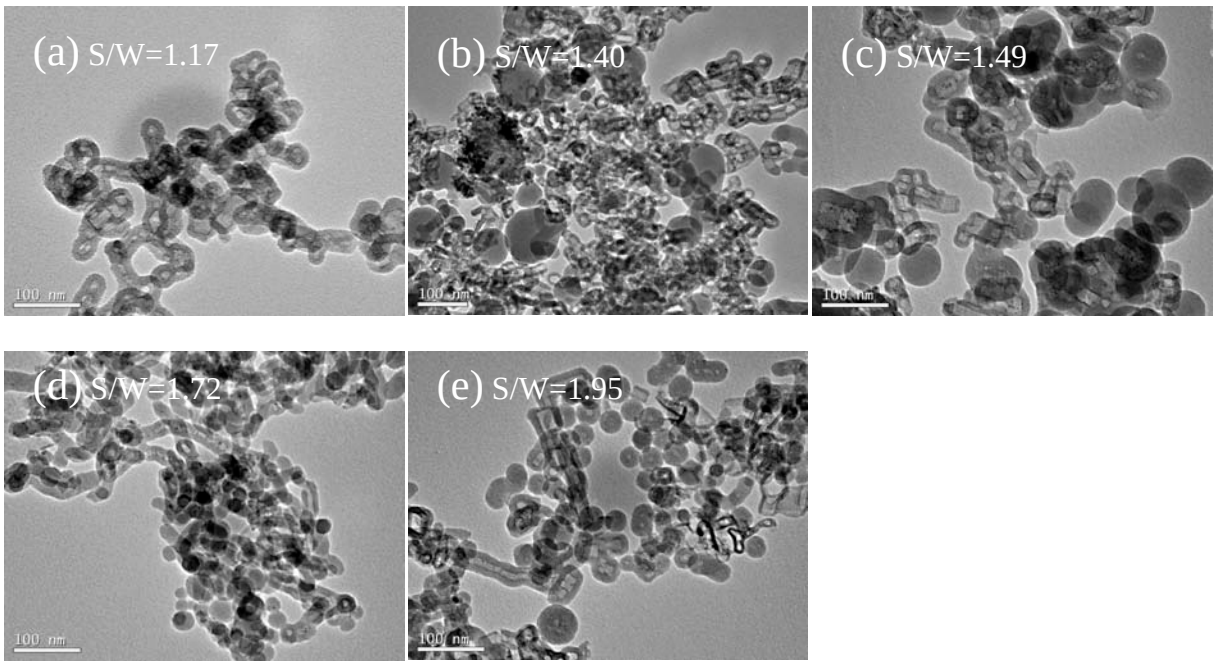

Figure 79: *TEM images when surfactant/water<2(a) S/W=1.17 (b) S/W=1.4 (c) S/W=1.49 (d) S/W=1.72 (e) S/W=1.95*

B.3 FORMATION OF CAVITY STRUCTURE

To see whether the cavity structure is formed because of the surfactant removal, the TEM picture of the core shell material is taken before calcination to compare the one after calcination. The cavity structure in Figure 80-left indicates the cavity formation occurs during solution synthesis. The blurred image is due to the effect of the surfactant before calcination.

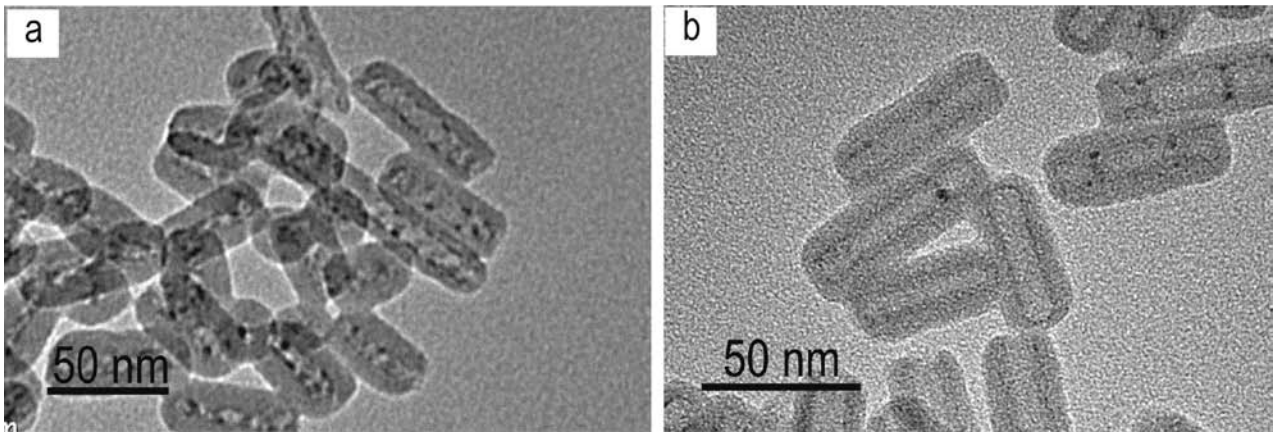

(Images provided by courtesy of R. Lu)

Figure 80: *TEM images of Ni@SiO_2 (left) before calcination and (right) after calcination at 500°C*

B.4 SHELL THICKNESS

B.4.1 Reaction time

Figure 81 shows an example of the growth of silica shell as a function of reaction time. Even though different amounts of TEOS (20g) are used, we observed the same trend that shell thickness increases as a function of time at initial stage while the cavity dimension is constant (Figure 82). After 5 hours, the shell thickness is independent of the reaction time due to the insufficient availability of water.

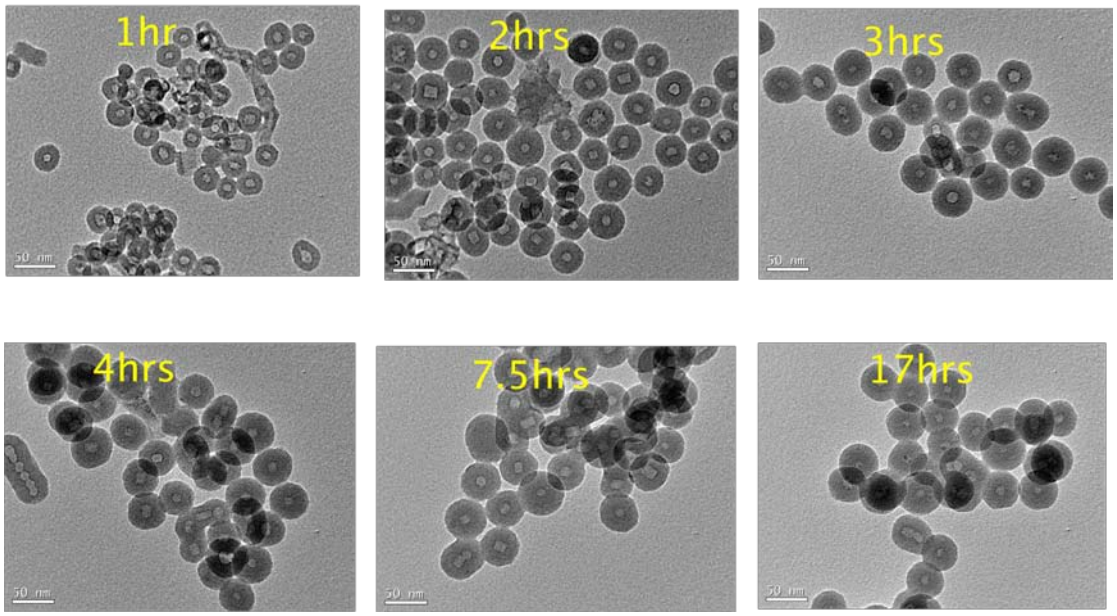

Figure 81: *TEM images of Ni@SiO_2 with different reaction times (using 20g TEOS)*

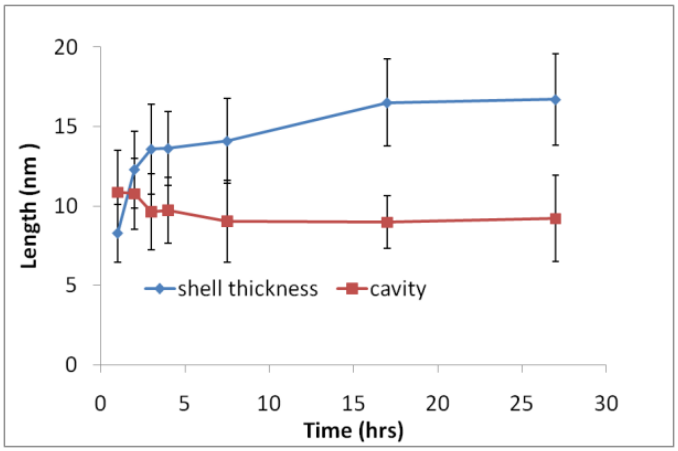

Figure 82: *Silica shell thickness and cavity dimensions as a function of reaction time. Synthesis condition: 20g TEOS, 3mL 16.5M ammonia solution, reaction time from 1hr to 27hrs at 50°C.*

B.4.2 Ammonia concentrations

The following images show that the silica shell thickness increases initially with increasing ammonia concentrations, reaching a plateau above the ammonia concentration of 4mol/L. Since the ammonia serves as a catalyst for TEOS hydrolysis, a higher concentration will facilitate hydrolysis process. However, the growth of silica shell is limited by the availability of both water and TEOS amount and hence eventually will slow down.

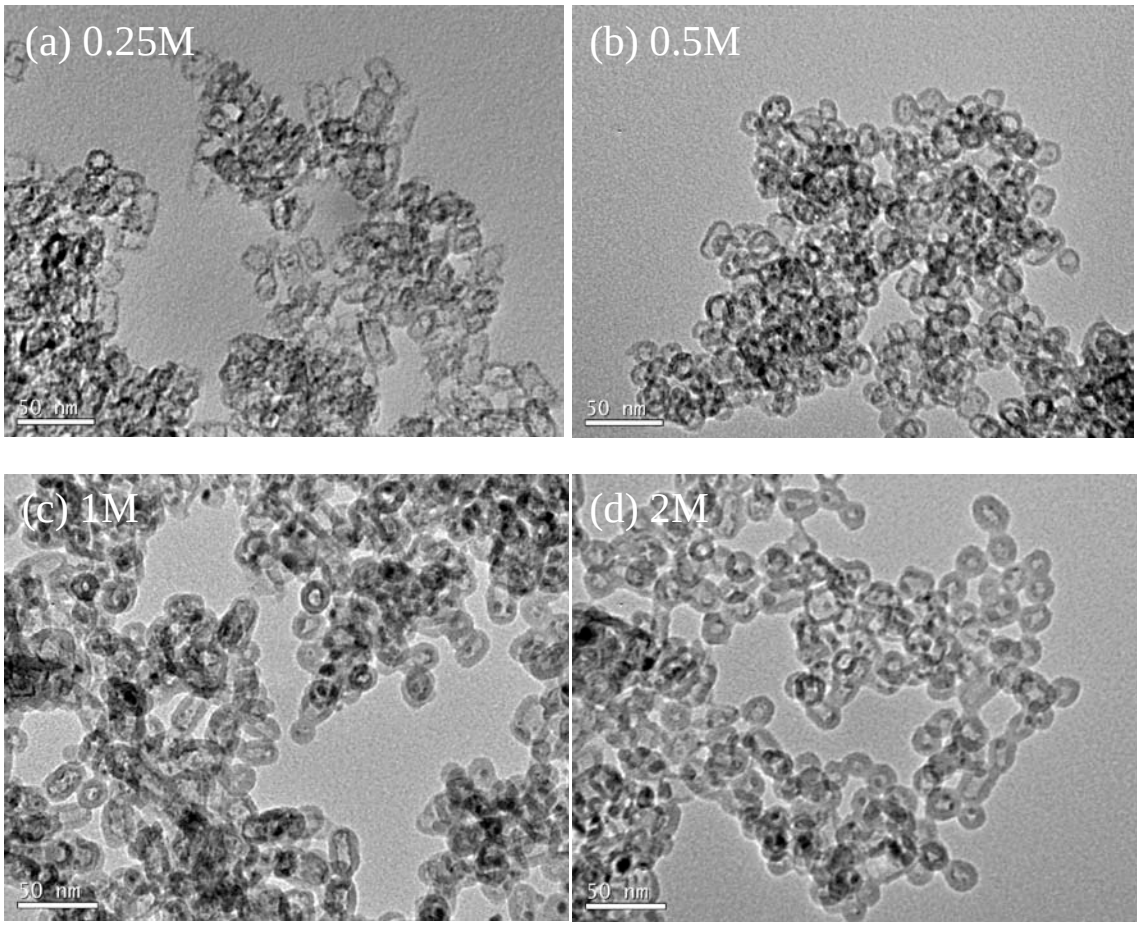

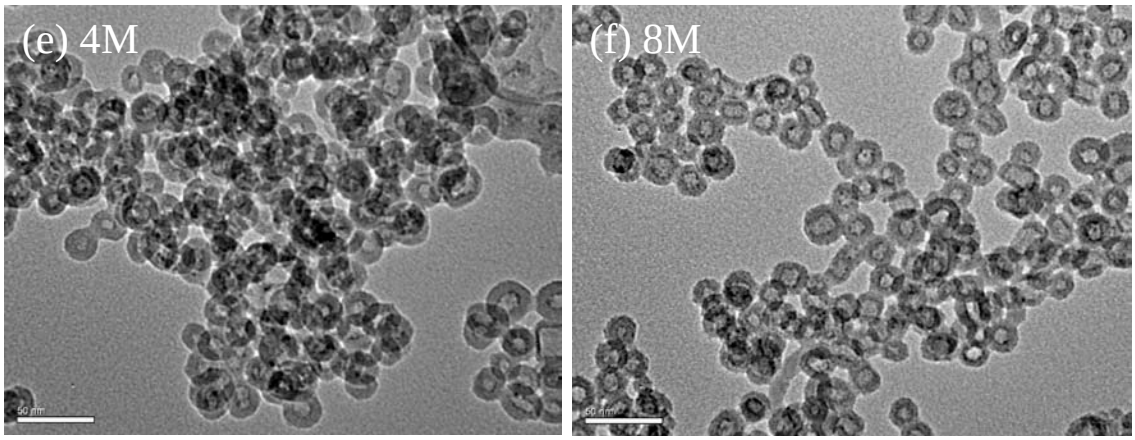

Figure 83: *TEM images of Ni@SiO_2 synthesized using different ammonia concentrations (a-f)*

B.4.3 Insufficient time or TEOS amount

The following images show that core shell material synthesized with a reaction time less than 1 hour while using standard amount of TEOS (10g) or with 1g TEOS while using standard reaction time (2 hours). The under-developed silica shell in Ni@SiO_2 is due to the insufficient time or TEOS amount for the shell growth.

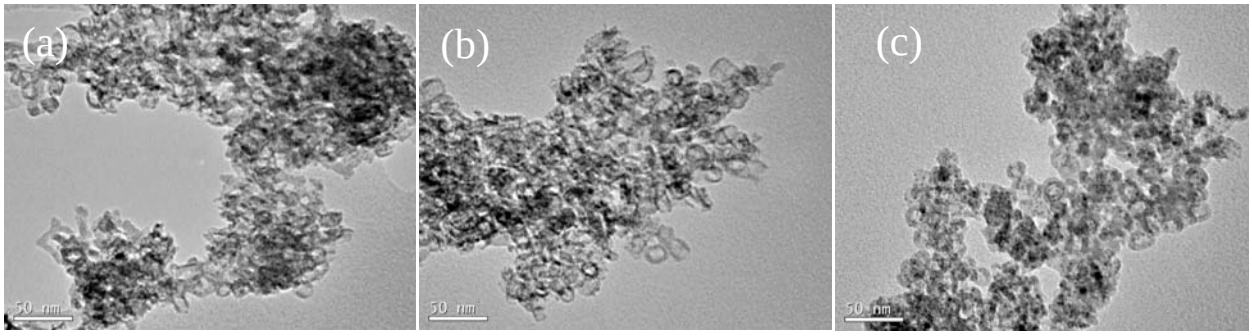

Figure 84: *TEM images of Ni@SiO_2 synthesized with reaction time (a) 20min (b) 40min, and TEOS amount (c) 1g*

B.4.4 Synthesis of shell thickness >20nm

The following TEM pictures materials with a silica shell thickness greater than 20nm. A narrow shell thickness distribution is hard to obtain when the shell is thicker than 20nm.

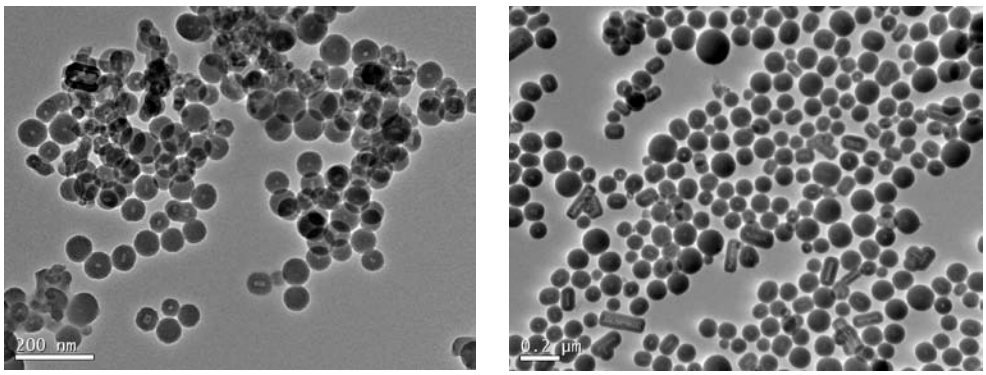

Figure 85: *(left) 4ml $NH_3.H_20$, 20g TEOS, 24hrs (shell thickness 24.3nm ±3.8nm); (right) 20g TEOS, 15.5g Brij 58, additional 2.1g H_2O*

B.5 NICKEL PARTICLE SIZE

B.5.1 Attempt to control nickel nucleation rate

Since the nickel particle size can be increased theoretically by decreasing the nucleation rate, the amount of reducing agent as well as its addition rate is adjusted to see whether larger nickel particles can be formed. A cavity structure is formed regardless of the change of hydrazine amount or its addition rate (Figure 86-a, b). Besides adjusting nucleation rate, the particle size could be theoretically also increased by increasing growth rate. An increase in growth rate can also be achieved by increasing nickel precursor concentrations. However, no larger nickel particles are formed at higher nickel nitrate concentrations (Figure 86-c, d). The results suggest

that the cavity structure is always formed in regardless of various nucleation or growth rates as long as the addition order nickel nitrate-hydrazine-ammonia solution is followed.

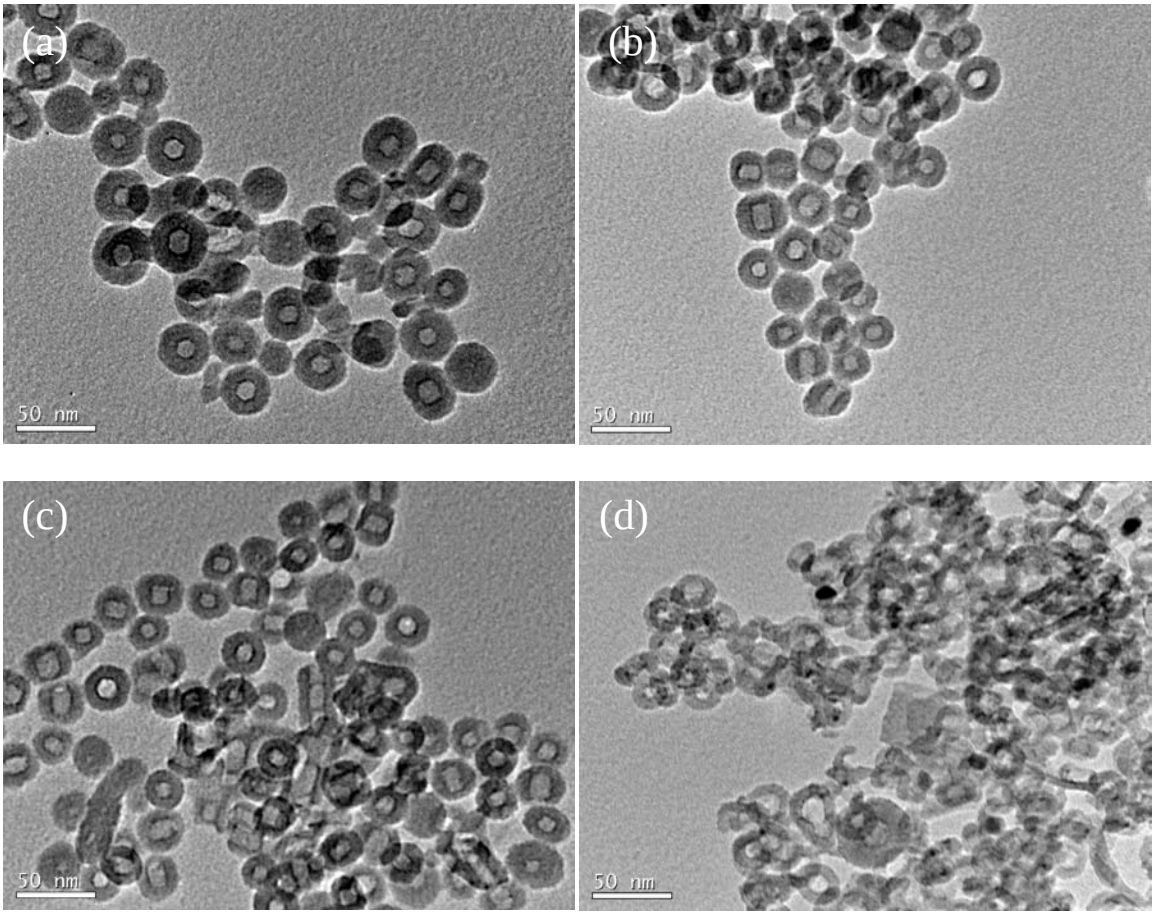

Figure 86: *(a) Hydrazine amount decreased to 0.5g; (b) hydrazine addition rate slowed down to 1 drop per minute; nickel nitrate concentration (c) 1.5M and (d) 4M*

B.5.2 Synthesis condition for particles size 1~7nm

The following table shows the synthesis parameters to obtain core shell materials with different nickel particle sizes ranging from 1nm to 7nm in non-cavity core shell materials.

Table 7: *Key synthesis parameters for particle size 1~7nm*

Particle size	Nickel conc.	Anhydrous hydrazine	Addition order
<d>= 1.23nm	1.5mL 0.8M	0	first nickel-then ammonia
<d>= 2.27nm	1.5mL 1M	0	first nickel-then ammonia
<d>= 2.95nm	1.5mL 1M	1.5mL	first nickel-then ammonia-then hydrazine
<d>= 4.12nm	1.5mL 4M	0	first nickel-then ammonia
<d>= 6.87 nm	1.5mL 4M	1.5mL	first nickel-then ammonia-then hydrazine
Other conditions: 10g TEOS with 2hrs hydrolysis time with the exception 1 hour hydrolysis for <d>=6.87nm			

B.6 OTHER SYNTHESIS PARAMETER

B.6.1 Different types of surfactant, nickel salt precursor, hydrazine and pH adjuster

Alternative chemicals in each step are also studied. Surfactant Brij 56 is used instead of Brij 58, for which the difference is the chain length. The cavity structure is still formed with an elongated shape (Figure 87-a). Nickel chloride is also used as salt precursor. A similar phenomenon to nickel nitrate is observed during the synthesis and the cavity structure is also formed (Figure 87-b). Even though the color of nickel chloride hydrate (yellowed pink) is different from nickel nitrate hydrate (green) due to different water coordination number, the green solution color from nickel ion is shown when both salts are dissolved in water. Hydrazine hydrate was used in the standard synthesis, the use of anhydrous hydrazine also creates the same structure as hydrazine (Figure 87-c). Ammonia is used to adjust the pH of the solution for faster hydrolysis. Other basic solution such as NaOH is also used to adjust the pH. However, irregular morphologies were generated possibly due to the ionic properties of NaOH (Figure 87-d).

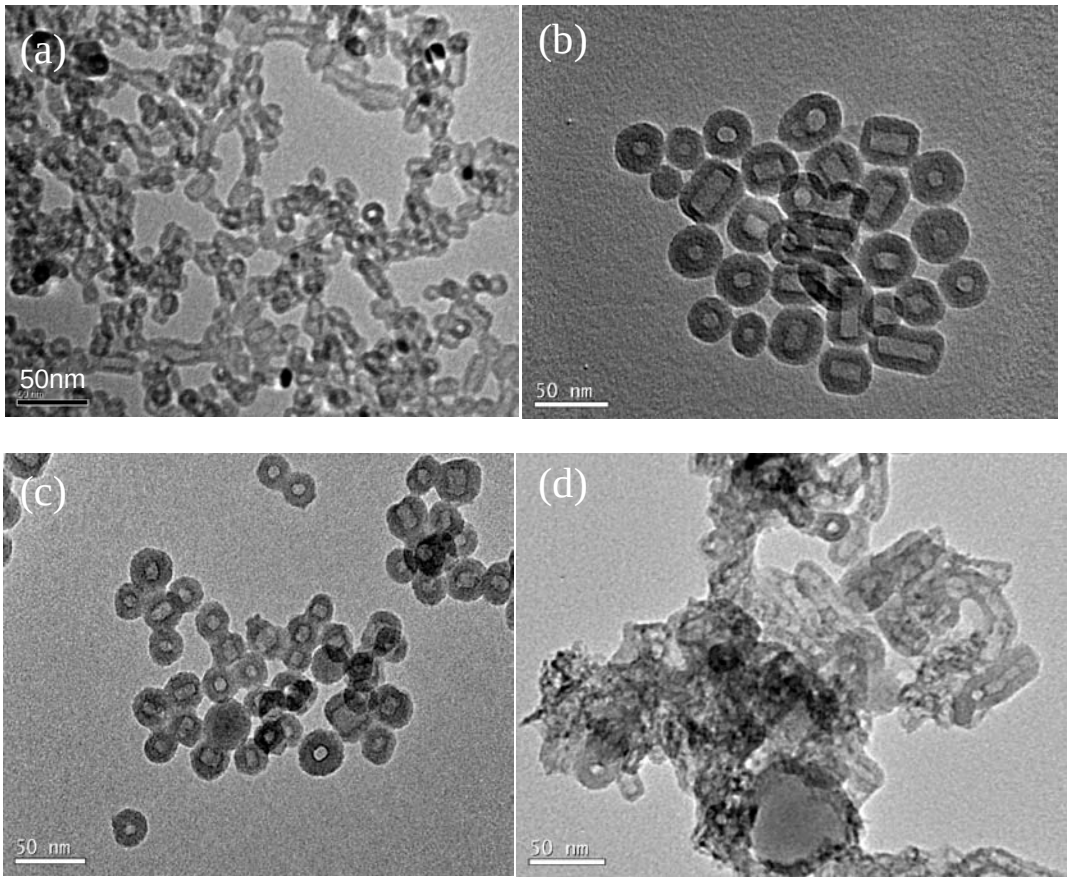

Figure 87: *(a) Use of Brij56; (b) Use of nickel chloride as salt precursor; (c) Use of anhydrous hydrazine; (d) Use of NaOH to adjust the pH*

B.6.2 Silica precursor type

The effort is also made to change the porosity of silica by using other silica precursor like (N-[3-(trimethoxysilyl)propyl]ethylenediamine) TSD or the porogen like C_{18}TMS [89] other than TEOS. Instead of the formation of core shell structure, 20nm nickel particles deposited on the silica are formed (Figure 88). Before adding the silica precursor, the solution color in each step is exactly as before. However, the pink color changes to a sky blue color after the addition of TSD or C_{18}TMS, which is different than the retained pink color after the addition of TEOS.

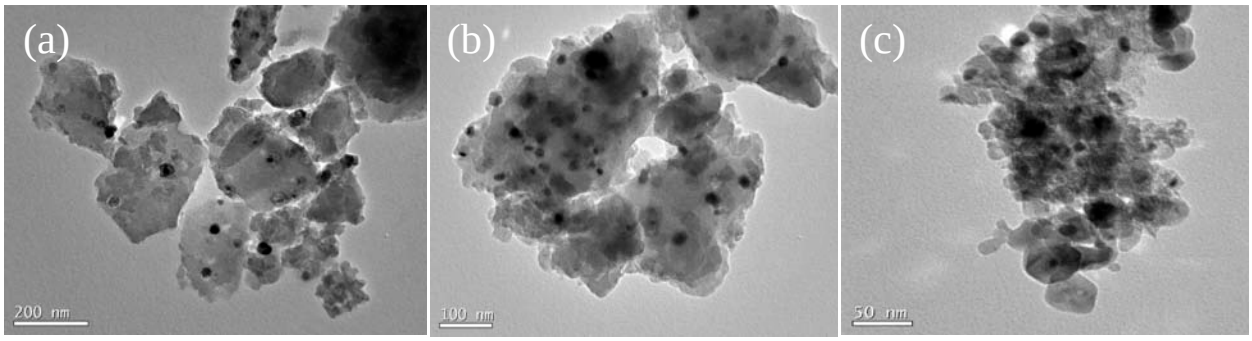

Figure 88: (*a) 5g TSD (b) 10g TSD (c) the mixture of 8g TEOS and 2g C_{18}TMS*

B.7 OTHER METAL CORES

B.7.1 Synthesis procedure for monometallic nanoparticles

To obtain other metal core silica shell materials, 1M stock solution of $Co(NO_3)_2$, $Cu(NO_3)_2$, $Pd(NO_3)_2$, $AgNO_3$ were used instead of 1M $Ni(NO_3)_2$. The rest of the procedure is exactly the same as described in section 2.1. The following figure shows the color of the powered sample before and after calcination.

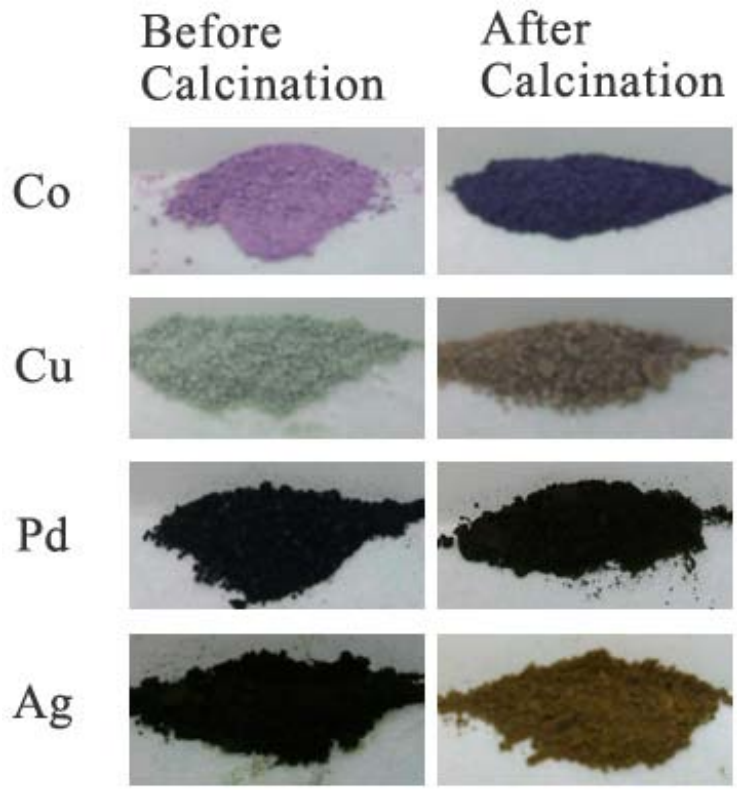

Figure 89: *The color of Co@SiO_2, Cu@SiO_2, Pd@SiO_2 and Ag@SiO_2 before and after air calcination*

B.7.2 Without hydrazine

In section 3.2.3, the cavity structure of Ni@SiO_2 changes to non-cavity structure in the absence of hydrazine. We would like to compare Pd@SiO_2 with and without hydrazine. No cavity is formed in Pd@SiO_2 without hydrazine. The reason could be that the Pd^{2+} is too easily to reduce just in the presence of ammonia solution.

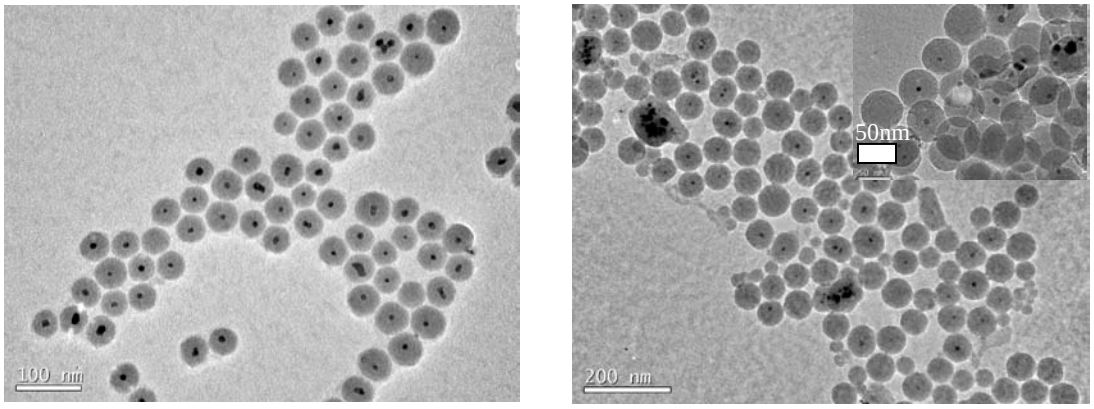

Figure 90: *(left) Pd@SiO_2 with hydrazine, (right) Pd@SiO_2 without addition of hydrazine*

B.7.3 Salt precursor concentration

Since Pd@SiO_2 does not have a cavity structure in the standard synthesis, we would like to see whether the cavity will be formed at a lower precursor concentration. The decrease in the Pd salt solution concentration only creates more silica particles without metals (Figure 91). This also reminds us that more pure silica structure without cavity structure at lower $Ni(NO_3)_2$ concentrations. The same trend is also observed in Ag@SiO_2 with different Ag salt concentrations (Figure 92).

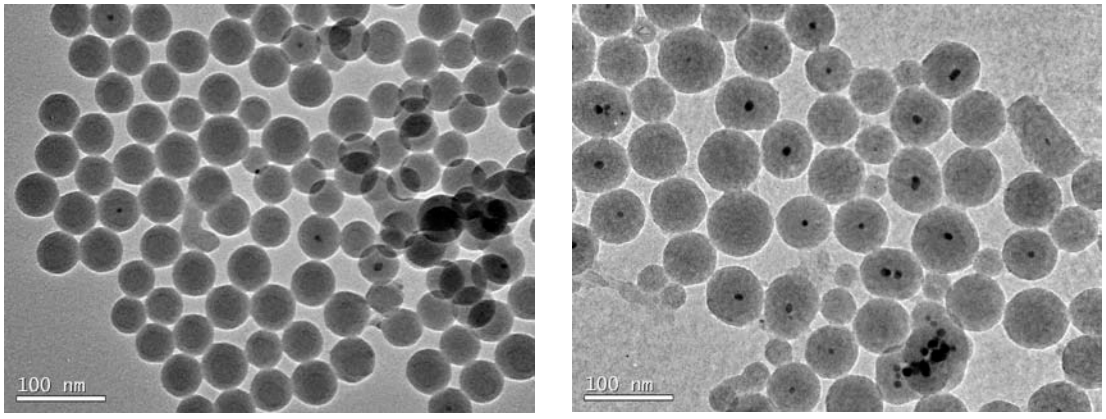

Figure 91: *Pd@SiO_2 with low Pd salt concentration (0.1M)*

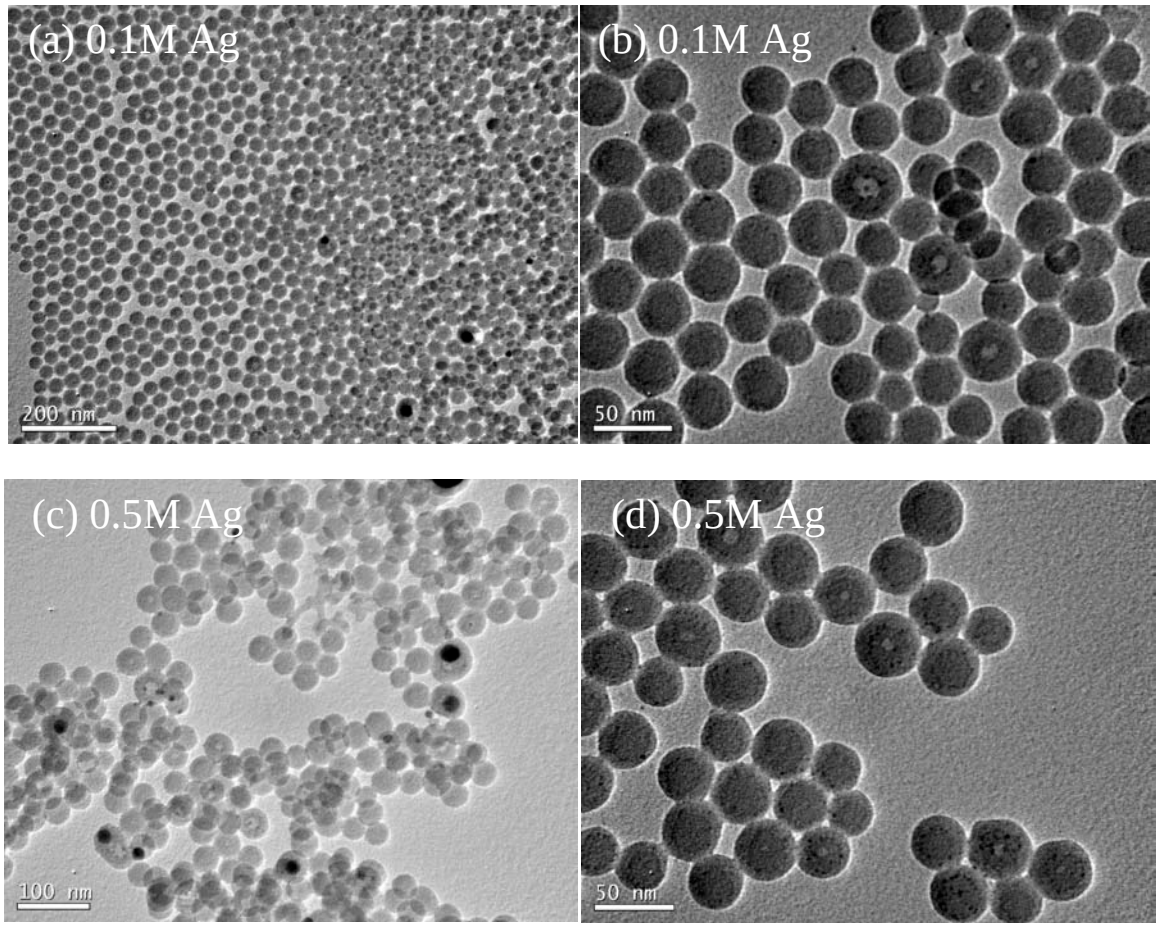

Figure 92: *Ag@SiO_2 with different precursor concentrations (a, b) 0.1M Ag (c, d) 0.5M Ag*

B.8 CORE SHELL USING STÖBER METHOD

B.8.1 Synthesis procedure NiPd coated silica using Stöber method

The synthesis of NiPd nanoparticles is followed by the recipe reported by Toshima's group [71]. Palladium (II) acetate (Aldrich) and $Ni(NO_3)_2 \cdot 6H_2O$ (Aldrich) were used as starting materials. 0.1767g $Pd(Ac)_2$ was dissolved in 50mL dioxane (Aldrich) and stirred for 1 day, resulting in a clear yellow solution. 0.145g $Ni(NO_3)_2 \cdot 6H_2O$ was dissolved in 300mL glycol at 80°C with stirring. 2g PVP with the molecular weight 55,000g/mol was added to the above

solution to make sure the molar ratio of PVP monomeric units to the both Ni^{2+} and Pd^{2+} metal ions is 14.3. To this solution, 48mL dioxane solution of $Pd(Ac)_2$ (15.6mmol/L) was added at ~0-5°C with stirring. The pH of the solution was adjusted to 9-11 by dropwise addition (about 150 drops with 2μL/drop) of an aqueous solution of sodium hydroxide (NaOH, 1M). The solution was stirred and refluxed at 198°C for 3 hours with a nitrogen flow passing through the reaction system to avoid the reoxidation of the nanoparticles during the synthesis. The color was a transparent black homogenous solution. Afterwards, 10mL solution was removed, washed, and redispersed with 40mL acetone for one time. It is noted that the reason to use acetone to precipitate the nanoparticles is that PVP can be dissolved in both ethanol and water but not in acetone. A TEM picture is taken afterwards to make sure the NiPd bimetallic nanoparticles are formed. The most critical step is to add the right amount of NaOH to adjust the pH of the solution. The successful synthesis of bimetallic NiPd protected PVP leads to a stable black solution. The NaOH is added dropwise while counting the drops. For example, 330 drops of NaOH solution was added one time, the precipitation at the bottom of the flask is observed with the indication of the failed synthesis.

To coat the silica shell on the NiPd nanoparticles, 4mL D.I water was added to the precipitated nanoparticles. The solution is transferred to the mixture with 64g ethanol and 23g ammonia solution. With stirring, 1.5mL TEOS in 8mL ethanol was added to the solution at room temperature and reacted for 1 hour. The solution is washed, precipitated and redispersed with ethanol afterwards.

(Special thanks to the help of A. Cao)

B.8.2 Silica shell-reaction time in Stöber method

In Stöber method, the hydrolysis takes place very fast. Figure 93 shows the silica shell thickness of bimetallic NiPd@SiO_2 is the same at 30 minutes reaction time as that of 20 hours reaction time. Other parameters (e.g. the ammonia concentration) instead of the reaction time need to be adjusted to modulate the shell thickness.

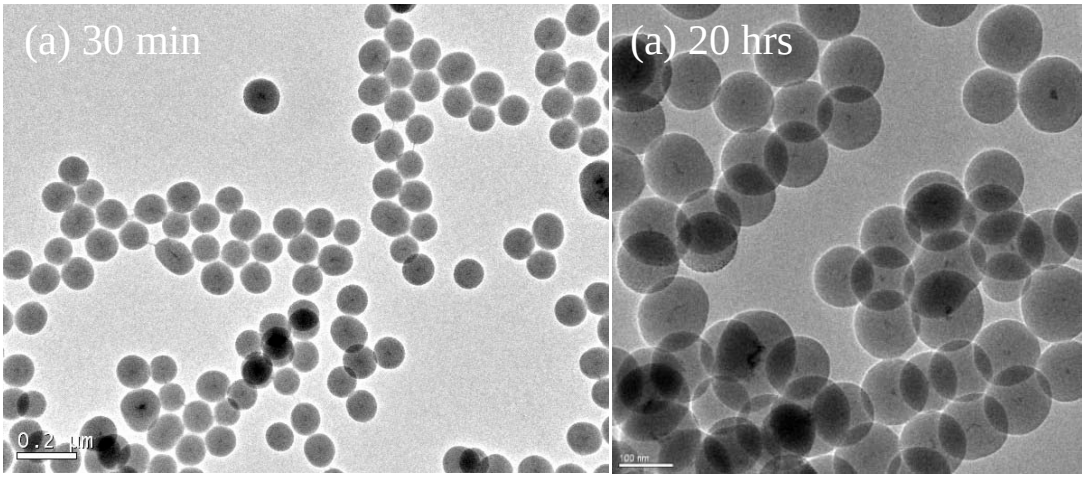

Figure 93: *Silica shell thickness with reaction time in Stöber method (a) 30min (b) 20hrs*

APPENDIX C

ETCHING

C.1 CAVITY STRUCTURE

C.1.1 Acids

Figure 94-97 show the TEM pictures of the Ni@SiO_2 after 1 hour and 24 hours etching with and without stirring using different types of acids. The core shell structure does not change after etching process. Even though the loss of nickel clusters are hard to spot in TEM images, a decrease in nickel loading as a function of etching time in Figure 98 indicates the nickel particles are indeed etched away.

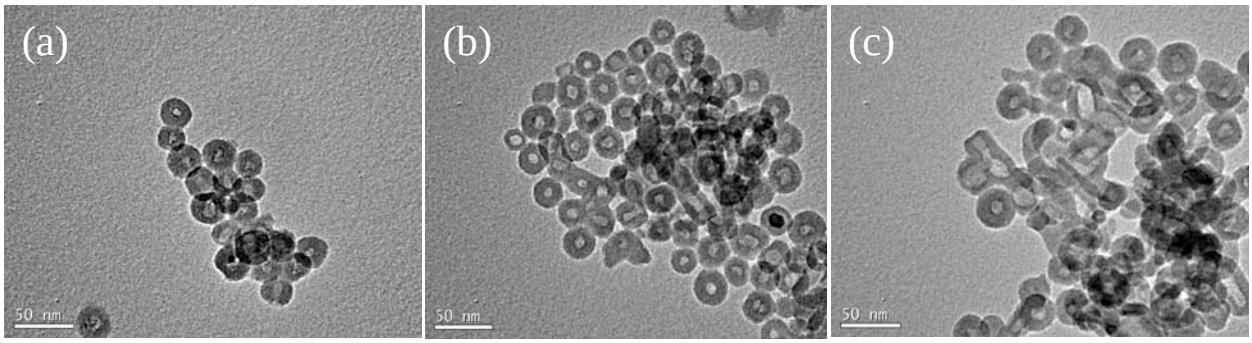

Figure 94: *3M HCl with different etching time (a) without stirring-1hr; (b) without stirring-24 hrs; (c) with stirring-24hrs*

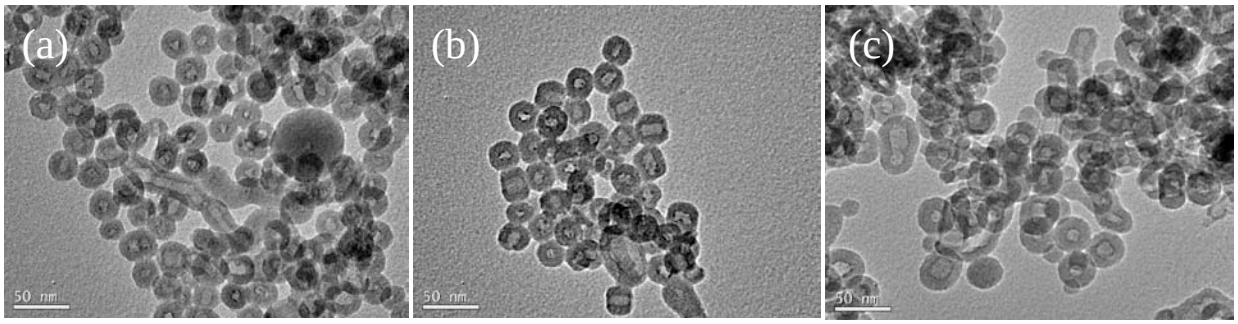

Figure 95: *3M HNO_3 with different etching time (a) without stirring-1hr; (b) without stirring-24 hrs; (c) with stirring-24hrs*

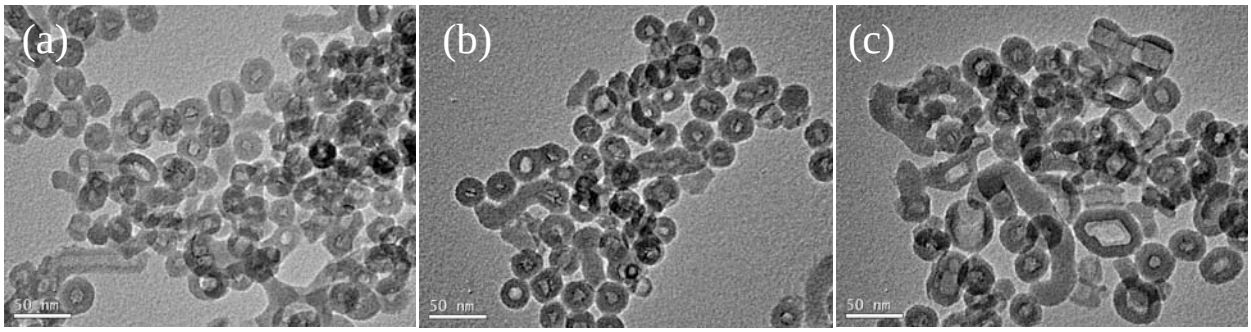

Figure 96: *3M H_2SO_4 with different etching time (a) without stirring-1hr; (b) without stirrin-24 hrs; (c) with stirring-24hrs*

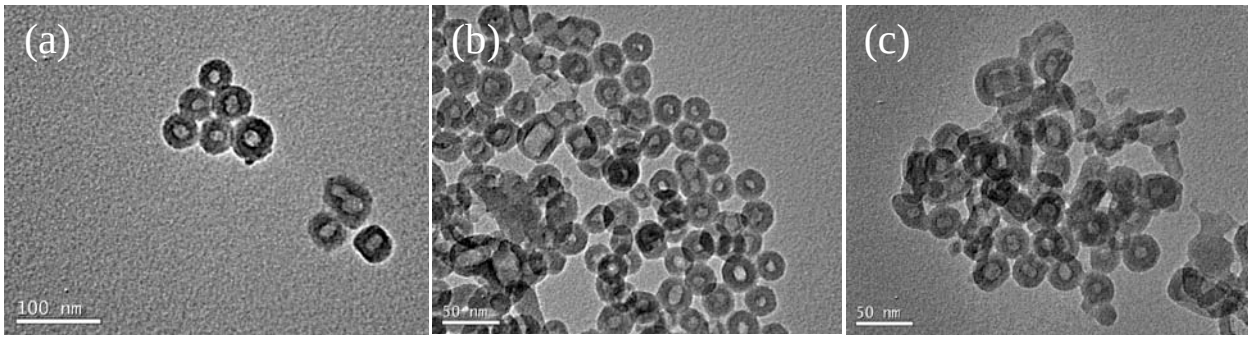

Figure 97: *Highly concentrated 12M HCl with different etching time (a) without stirring-1hr; (b) without stirring-24hrs; (c) with stirring-24hrs*

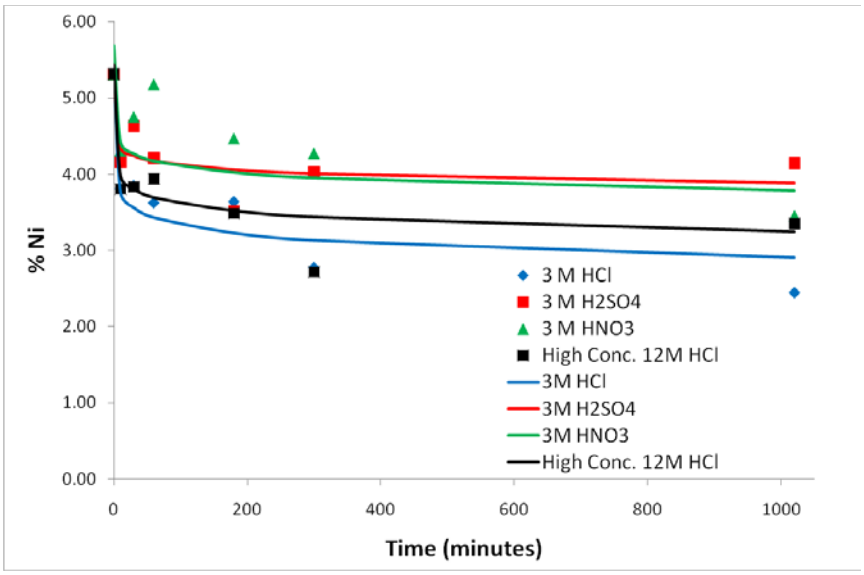

Figure 98: *Nickel loading determined by EDX as a function of etching time with different acids*

C.1.2 Uncontrollable etching process

Figure 99 shows the difficulty of controlling etching rate and degree of etching to achieve complete removal external nickel particles while retaining all internal nickel particles. As seen in Figure 99-a,b, ome internal nickel particles are etched away while a significant amount of nickel is still sitting outside of the silica shell even after 1 hour. Even though no external nickel is present after 2 hour etching, a large amount of internal nickel is depleted as well.

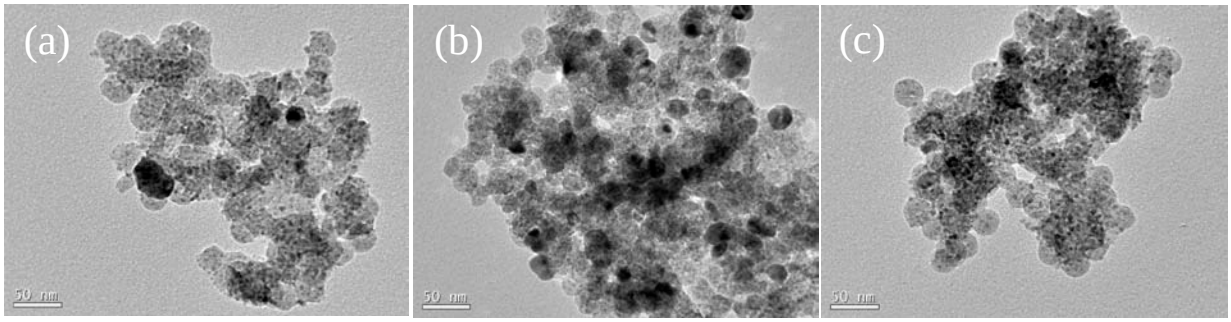

Figure 99: *TEM pictures of non-cavity sample with etching time (a) 10min (b) 65min (c) 120min*

APPENDIX D

CHARATERIZATION

D.1 XRD

Figure 100 demonstrates that small sized nickel particles are very easily oxidized after exposure to air. NiO peaks were observed even when the sample is isolated in a vial for one week. It is suggested that XRD should be performed as soon as the sample is reduced. The same observation is also reported in literature that 5nm nickel particles will have NiO pattern within 1 day [64].

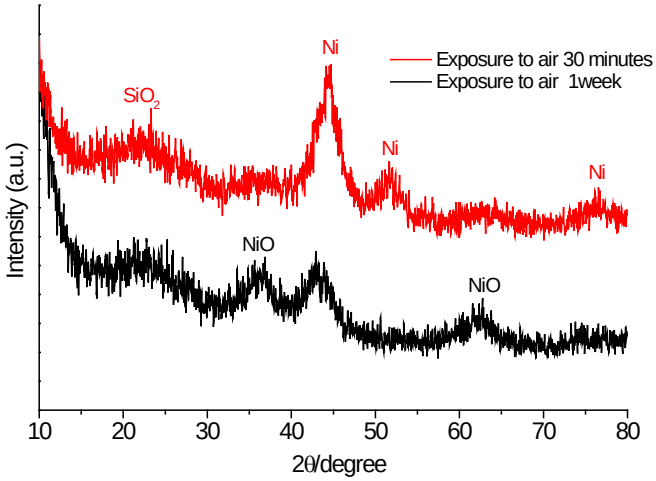

Figure 100: *XRD pattern of fully reduced Ni/SiO_2 after exposure to air for 30min and 1 week*

D.2 TPO

There is no pronounced O_2 consumption peak in core shell materials. The reason could be that nickel clusters in core shell materials are easily oxidized after exposure to air at room temperature.

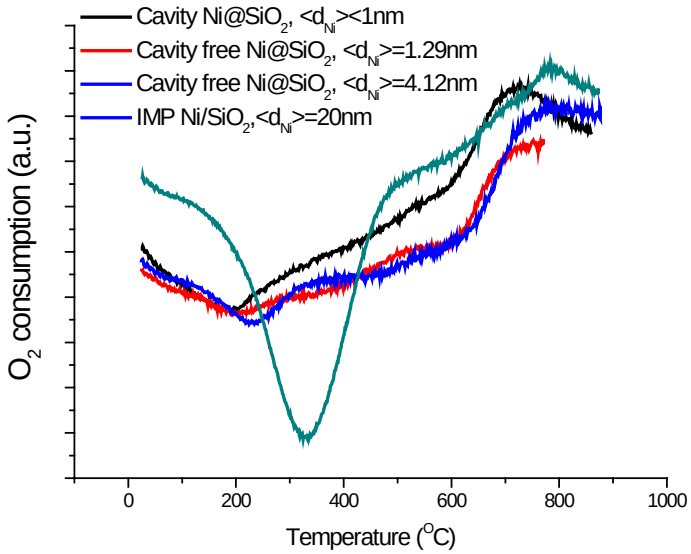

Figure 101: *TPO of cavity Ni@SiO₂, non-cavity Ni@SiO₂ with different nickel sizes in comparison with IMP-Ni/SiO₂*

APPENDIX E

THERMAL STABILITY

E.1.1 Treated in air

In Chapter 4.0, the stability of core shell material is studied in a H_2 environment. Minimal sintering of nickel particles in the air is also observed. The majority of sub-nanometer nickel clusters are maintained at temperatures as high as 800°C.

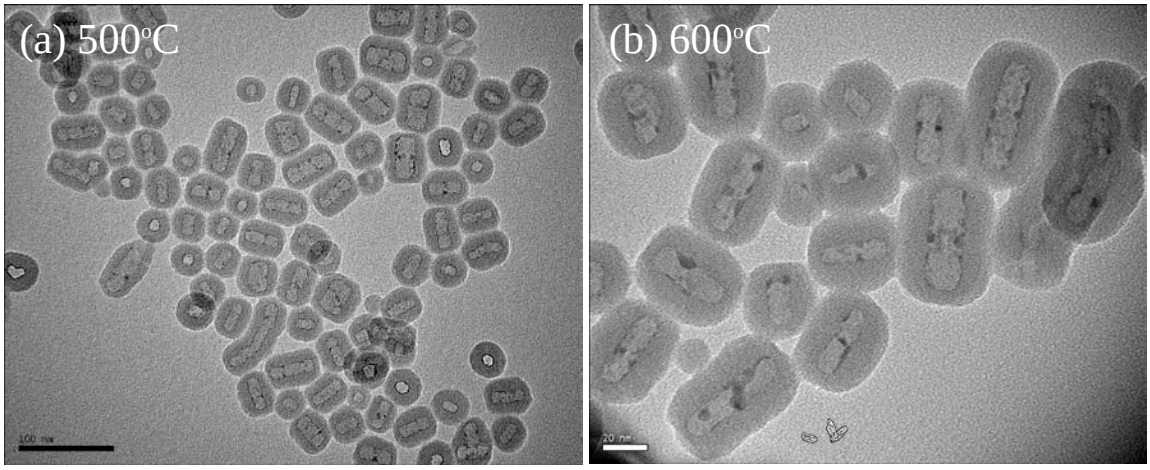

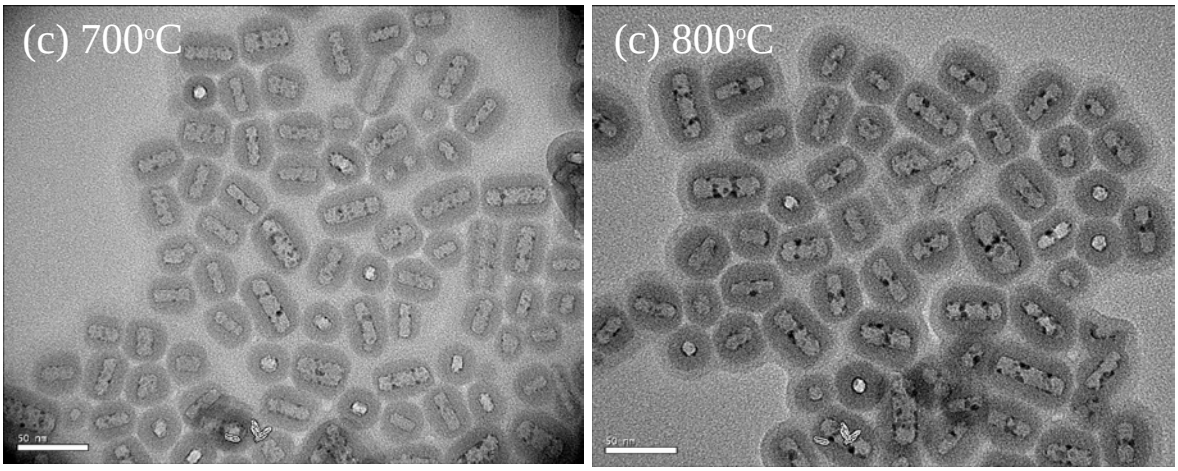

Figure 102: *Elongated Ni@SiO_2 treated in the air at each different temperature for 2hrs*

E.1.2 BET surface area for different shell thickness

The BET surface area was measured of Ni@SiO_2 with different silica shell thicknesses after thermal treatment at various temperatures (from 200-800°C) in air for 2 hours. The surface area reaches its maximum at 400°C and decreases thereafter (Figure 103-left). This maximum surface area is achieved due to the complete removal of surfactant, which produces a porous structure in the silica shell. The decrease in surface area indicates that this porous structure is sintered above 400°C. However, the surface area gradually drops only by 20% after 12 hours thermal treatment at 800°C (Figure 103-right). The silica support obtained in our method is much more stable compared than that synthesized by modified Stöber method, where surface area drops from 320m^2/g to nearly zero from 400°C to 800°C [80].

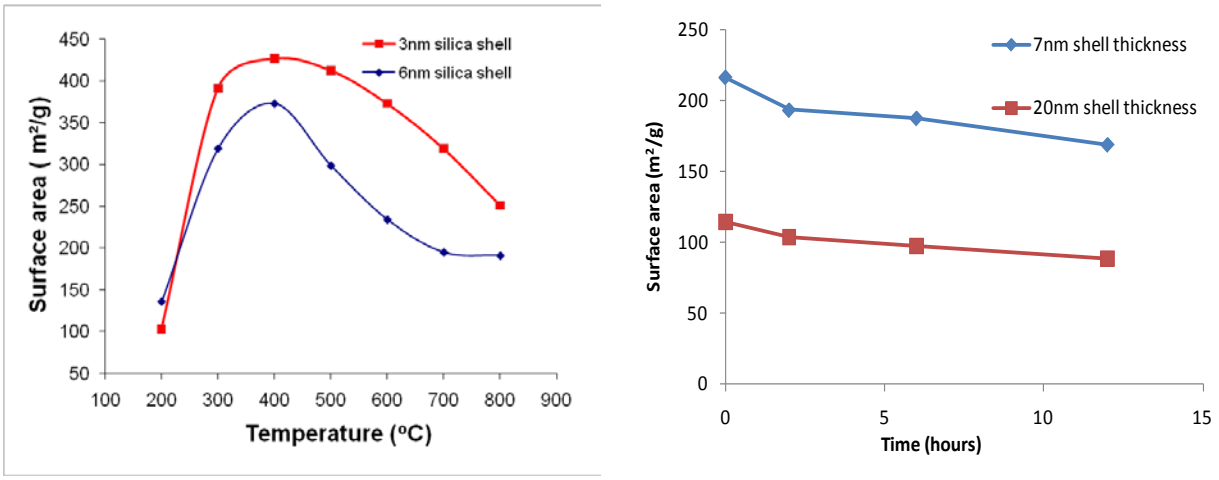

Figure 103: *BET surface area of $Ni@SiO_2$ (left) with 3nm and 6nm shell thickness after calcination at different temperatures for 2hrs in air; (right) with 7nm and 20nm shell thickness after calcination at 800°C for different period of time in air*

E.1.3 Sintering at 800°C as a function of time

A nickel sintering study at 800°C as a function of time ranging from 2 to 12 hours is also performed. Even though there is a slight increase in nickel particle size, the sintered nickel particles move towards the center of silica particles.

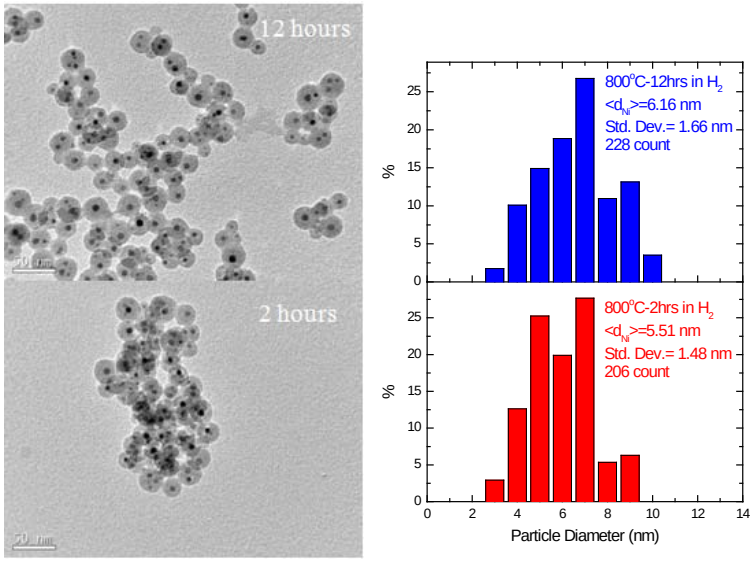

Figure 104: *TEM images and particle size distribution of 4nm $Ni@SiO_2$ after thermal treatment at 800°C in H_2 for 2hrs and 12hrs*

APPENDIX F

F.1.1 Catalysts information

Figure 105 shows the TEM pictures of the catalysts with controlled shell thickness from ~3-20nm used in the reactions. Table 8 lists the nickel loading and BET surface are of the corresponding samples.

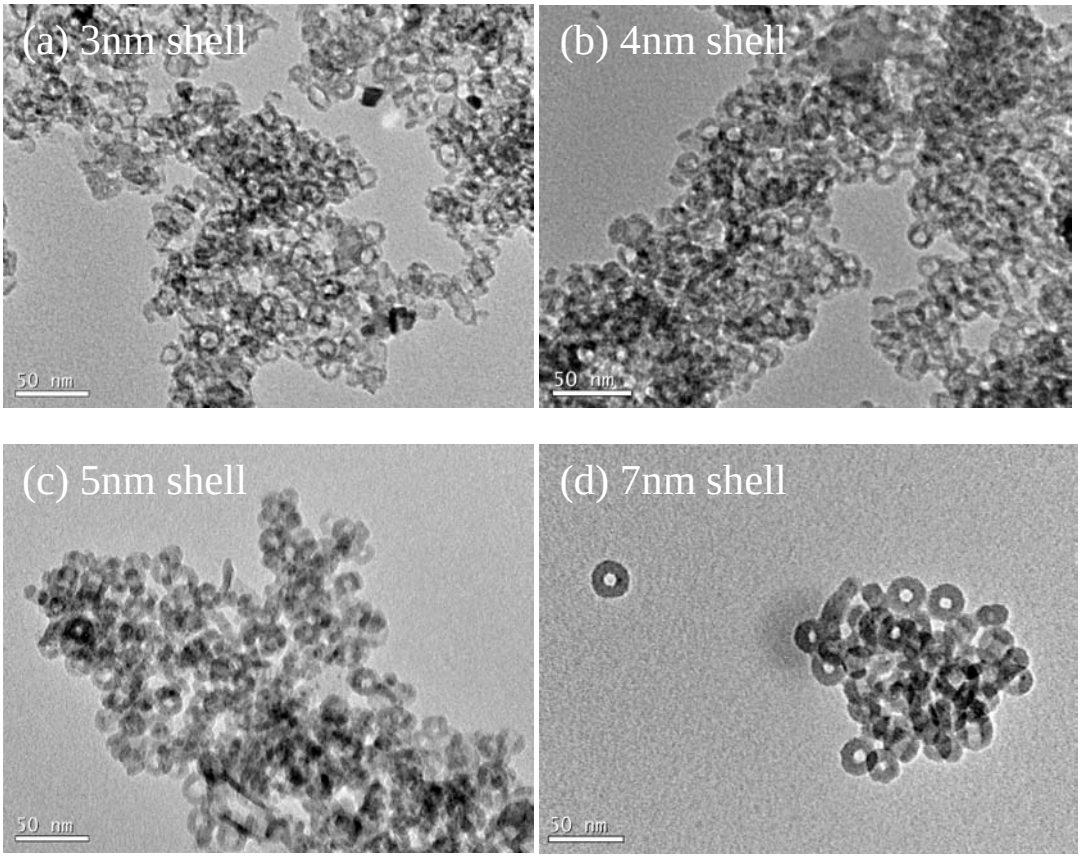

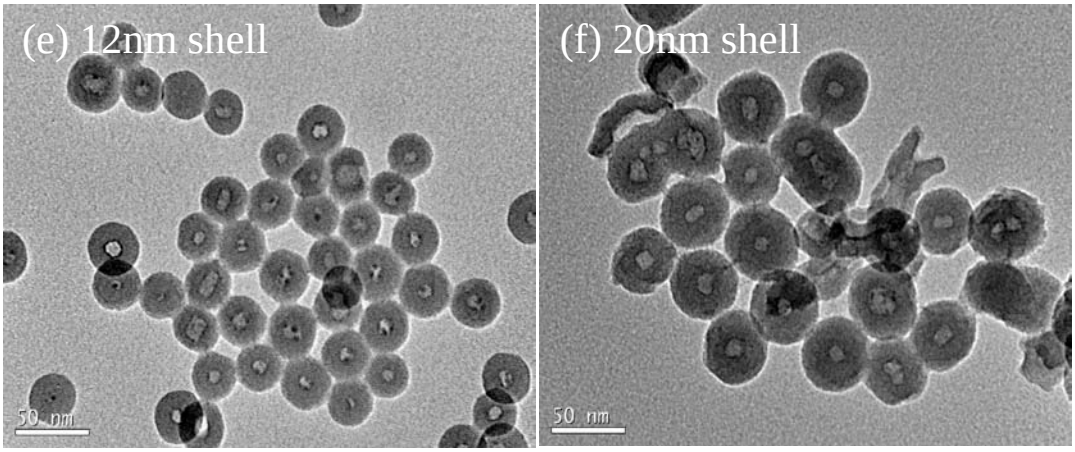

Figure 105: *TEM pictures of Ni@SiO_2 with the controlled shell thickness from 3nm to 20nm*

Table 8: *BET surface area and nickel loading of the materials used for reactions*

Silica shell thicknesses	BET surface area (m^2/g)	Nickel loading
3nm	285	5%
5nm	239	4%
7nm	217	4%
10nm	164	4%
12nm	114	3.5%
20nm	73	1.2%

F.1.2 Feed in ratio of CO methanation reaction

Different H_2/CO ratios are studied to obtain reasonable CO conversion. Minimal change in CO conversion is observed when H_2/CO ratio is higher than a stoichiometric ratio of 3.

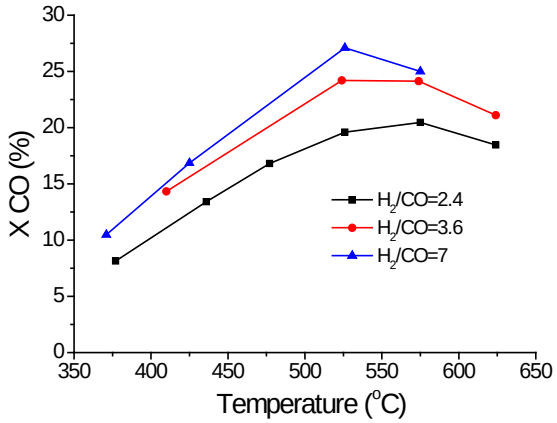

Figure 106: *Impact of different H_2/CO ratios on the CO conversions of cavity-Ni@SiO_2 with 7nm shell thickness*

F.1.3 Robustness of hysteresis in CPOM reaction

The unchanged reactivity and selectivity in the extinction curve at different temperature points as low as 500°C indicates the robustness of the hysteresis loop in core shell materials.

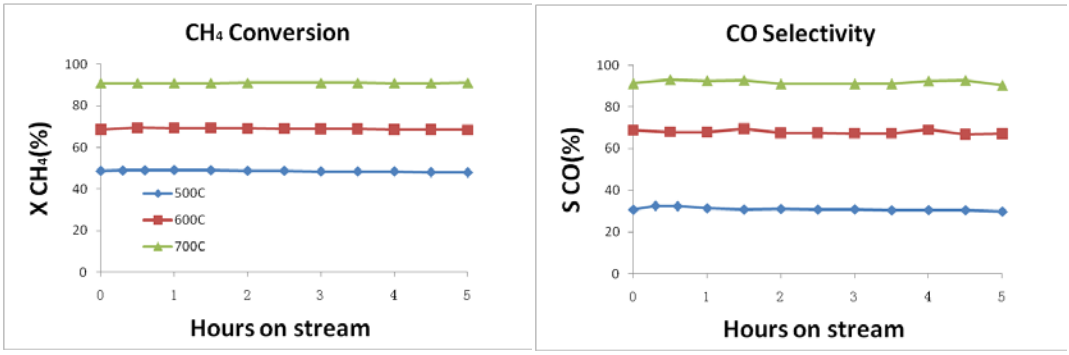

Figure 107: *Methane conversion and carbon monoxide selectivity of cavity-Ni@SiO_2 at different temperatures in the extinction operation for 5hrs (CH_4/O_2=2)*

F.1.4 Calculation of O_2 depletion

The amount of O_2 depletion during the dip is calculated by the integration of peak area. The flow rate of different O_2 level is determined by GC and denoted as below:

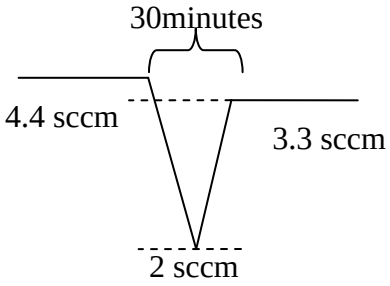

$$\Delta m_{o_2}(\text{reaction}) = \Delta V_{o_2} \times t \times \rho_{o_2}/2 = (3.3\text{-}2) \times 30 \times (1.43 \times 10^{-3})/2 = 0.025\text{g}$$

The O_2 amount for oxidizing nickel catalyst is calculated based on 0.03g catalyst with 5% nickel loading. The calculation is as below

$$\Delta m_{o_2}(\text{Ni oxidation}) = m_{Ni}/ MW_{Ni} \times MW_O = (0.03 \times 5\%)/58 \times 16 = 0.004\text{g}$$

The result suggests that the consumption of O_2 is one order of magnitude higher than the amount for complete nickel oxidation.

BIBLIOGRAPHY

1. Kumar, S.A. and M.I. Khan, *Heterofunctional Nanomaterials: Fabrication, Properties and Applications in Nanobiotechnology.* Journal of Nanoscience and Nanotechnology, 2010. **10**(7): p. 4124-4134.

2. Lazaro, M.J., et al., *Carbon Nanofiber Growth Optimization for Their Use as Electrocatalyst Support in Proton Exchange Membrane (PEM) Fuel Cells.* Journal of Nanoscience and Nanotechnology, 2009. **9**(7): p. 4353-4359.

3. Kanwar, J.R., G. Mahidhara, and R.K. Kanwar, *Recent Advances in Nanoneurology for Drug Delivery to the Brain.* Current Nanoscience, 2009. **5**(4): p. 441-448.

4. Iskandar, F., *Nanoparticle processing for optical applications - A review.* Advanced Powder Technology, 2009. **20**(4): p. 283-292.

5. Balogh, L.P., T.O. Ely, and W.G. Lesniak, *Composite Nanoparticles for Cancer Imaging and Therapy: Engineering Surface, Composition, and Shape*, in *Nanomedicine Design of Particles, Sensors, Motors, Implants, Robots, and Devices*. 2009, Artech House. p. 95-126.

6. Wang, S., et al., *Phase-selectivity photocatalysis: a new approach in organic pollutants' photodecomposition by nanovoid core(TiO2)/shell(SiO2) nanoparticles.* Chemical Communications, 2008(32): p. 3756-3758.

7. Plata, D.L. and et al., *Industrially synthesized single-walled carbon nanotubes: compositional data for users, environmental risk assessments, and source apportionment.* Nanotechnology, 2008. **19**(18): p. 185706.

8. Hansen, S., et al., *Categorization framework to aid exposure assessment of nanomaterials in consumer products.* Ecotoxicology, 2008. **17**(5): p. 438-447.

9. Valden, M., *Onset of Catalytic Activity of Gold Clusters on Titania with the Appearance of Nonmetallic Properties.* Science, 1998. **281**(5383): p. 1647-1650.

10. H.S.Bengaard, J.S., J.R. Rostrup-Nielsen, *Steam Reforming and Graphite Formation on Ni Catalysts.* Journal of Catalysis, 2002. **209**(2): p. 365-384.

11. http://www.azonano.com/news.asp?NewsID=10850, *Global Nanocatalysts Market Projected to Reach $6.0 Billion by 2015*. 2010.

12. http://www.bccresearch.com/report/NAN028A.html, *Nanocatalysts report hightlights* 2010.

13. Nanda, K.K., et al., *Higher Surface Energy of Free Nanoparticles.* Physical Review Letters, 2003. **91**(10): p. 106102.

14. Campbell, C.T., S.C. Parker, and D.E. Starr, *The Effect of Size-Dependent Nanoparticle Energetics on Catalyst Sintering.* Science, 2002. **298**(5594): p. 811-814.

15. Buffat, P. and J.P. Borel, *Size effect on the melting temperature of gold particles.* Physical Review A, 1976. **13**(6): p. 2287.

16. Sanders, T., P. Papas, and G. Veser, *Supported nanocomposite catalysts for high-temperature partial oxidation of methane.* Chemical Engineering Journal, 2008. **142**(1): p. 122-132.

17. Sanders, T., *Nanocomposite catalytic materials for clean energy processes*. 2008, University of Pittsburgh.

18. Ikeda, M., et al., *Thermal stability of an SiO2-coated Rh catalyst and catalytic activity in NO reduction by CO.* Chemical Communications, 2001(23): p. 2512-2513.

19. Park, J.-N., et al., *Synthesis and characterization of sintering-resistant silica-encapsulated Fe3O4magnetic nanoparticles active for oxidation and chemical looping combustion.* Nanotechnology, 2010. **21**(22): p. 225708.

20. Jung-Nam, P., et al., *Highly Active and Sinter-Resistant Pd-Nanoparticle Catalysts Encapsulated in Silica.* Small, 2008. **4**(10): p. 1694-1697.

21. Joo, S.H., et al., *Thermally stable Pt/mesoporous silica core–shell nanocatalysts for high-temperature reactions.* Nature Materials, 2008. **8**(2): p. 126-131.

22. Arnal, P.M., M. Comotti, and F. Schüth, *High-Temperature-Stable Catalysts by Hollow Sphere Encapsulation.* Angewandte Chemie, 2006. **118**(48): p. 8404-8407.

23. Güttel, R., M. Paul, and F. Schüth, *Ex-post size control of high-temperature-stable yolk–shell Au@ZrO2 catalysts.* Chemical Communications, 2010. **46**(6): p. 895.

24. Hori, K., et al., *Preparation of silica-coated Pt metal nanoparticles using microemulsion and their catalytic performance.* Science and Technology of Advanced Materials, 2006. **7**(7): p. 678-684.

25. V. Suryanarayanan, A.S.N., Renjis T. Tom and T. Pradeep, *Porosity of core–shell nanoparticles.* Journal of Materials Chemistry, 2004. **14**: p. 2661-2666.

26. Ryoo, M., *The effect of mass transfer on the catalytic combustion of benzene and methane over palladium catalysts supported on porous materials.* Catalysis Today, 2003. **83**(1-4): p. 131-139.

27. Park, J.C., et al., *Ni@SiO2 yolk-shell nanoreactor catalysts: High temperature stability and recyclability.* Journal of Materials Chemistry, 2010. **20**(7): p. 1239.

28. Park, J.-N., et al., *Highly Active and Sinter-Resistant Pd-Nanoparticle Catalysts Encapsulated in Silica.* Small, 2008. **4**(10): p. 1694-1697.

29. Nguyen, S.V., et al., *Mesoporous silica supported LaCoO3 perovskites as catalysts for methane oxidation.* Microporous and Mesoporous Materials, 2002. **54**(1-2): p. 51-61.

30. M. T. Tavaresa, I.A., C. A. Bernardoa and J. R. Rostrup-Nielsen, *Carbon formation and CO methanation on silica-supported nickel and nickel-copper catalysts in CO + H2 mixtures.* Journal of Catalysis, 1996. **158**(2): p. 402-410

31. Sehested, J., et al., *Methanation of CO over Nickel: Mechanism and Kinetics at High H2/CO Ratios.* The Journal of Physical Chemistry B, 2004. **109**(6): p. 2432-2438.

32. Gierlich, H.H., et al., *Deactivation Phenomena of a Ni-based Catalyst for High Temperature Methanation*, in *Studies in Surface Science and Catalysis*, B. Delmon and G.F. Froment, Editors. 1980, Elsevier. p. 459-469.

33. McCarty, J.G. and H. Wise, *Hydrogenation of surface carbon on alumina-supported nickel.* Journal of Catalysis, 1979. **57**(3): p. 406-416.

34. Chang-jun Liu, J.Y., Jiaojun Jiang, and Yunxiang Pan *Progresses in the preparation of coke resistant Ni-based catalyst for steam and CO2 reforming of methane.* ChemCatChem 2011. **3**: p. 529-541.

35. Trimm, D.L., *Coke formation and minimisation during steam reforming reactions.* Catalysis Today, 1997. **37**(3): p. 233-238.

36. Claridge, J.B., et al., *A study of carbon deposition on catalysts during the partial oxidation of methane to synthesis gas.* Catalysis Letters, 1993. **22**(4): p. 299-305.

37. Sehested, J., *Four challenges for nickel steam-reforming catalysts.* Catalysis Today, 2006. **111**(1-2): p. 103-110.

38. York, A.P.E., et al., *Methane Oxyforming for Synthesis Gas Production.* Catalysis Reviews: Science and Engineering, 2007. **49**(4): p. 511 - 560.

39. Aiello, R., et al., *Hydrogen production via the direct cracking of methane over Ni/SiO2: catalyst deactivation and regeneration.* Applied Catalysis A: General, 2000. **192**(2): p. 227-234.

40. Zhang, T. and M.D. Amiridis, *Hydrogen production via the direct cracking of methane over silica-supported nickel catalysts.* Applied Catalysis A: General, 1998. **167**(2): p. 161-172.

41. Koo, K., et al., *CeO2 Promoted Ni/Al2O3 Catalyst in Combined Steam and Carbon Dioxide Reforming of Methane for Gas to Liquid (GTL) Process.* Catalysis Letters, 2009. **130**(1): p. 217-221.

42. Laosiripojana, N. and S. Assabumrungrat, *Methane steam reforming over Ni/Ce-ZrO2 catalyst: Influences of Ce-ZrO2 support on reactivity, resistance toward carbon formation, and intrinsic reaction kinetics.* Applied Catalysis A: General, 2005. **290**(1-2): p. 200-211.

43. Miao, Q., et al., *Partial oxidation of methane to syngas over nickel-based catalysts modified by alkali metal oxide and rare earth metal oxide.* Applied Catalysis A: General, 1997. **154**(1-2): p. 17-27.

44. Kim, P., *Synthesis and characterization of mesoporous alumina with nickel incorporated for use in the partial oxidation of methane into synthesis gas.* Applied Catalysis A: General, 2004. **272**(1-2): p. 157-166.

45. Hou, Z., et al., *Deactivation of Ni catalysts during methane autothermal reforming with CO2 and O2 in a fluidized-bed reactor.* Journal of Catalysis, 2007. **250**(2): p. 331-341.

46. Lercher, J.A., et al., *Design of stable catalysts for methane-carbon dioxide reforming*, in *Studies in Surface Science and Catalysis*, W.N.D.E.I. Joe W. Hightower and T.B. Alexis, Editors. 1996, Elsevier. p. 463-472.

47. Duprez, D., et al., *Deactivation of steam-reforming model catalysts by coke formation : I. Kinetics of the Formation of Filamentous Carbon in the Hydrogenolysis of cyclopentane on Ni/Al2O3 Catalysts.* Journal of Catalysis, 1990. **124**(2): p. 324-335.

48. Demicheli, M.C., et al., *Deactivation of Steam-Reforming Model Catalysts by Coke Formation .II. Promotion with Potassium and Effect of Water.* Journal of Catalysis, 1994. **145**(2): p. 437-449.

49. Damyanova, S., et al., *MCM-41 supported PdNi catalysts for dry reforming of methane.* Applied Catalysis B: Environmental, 2009. **92**(3-4): p. 250-261.

50. Yoshida, K., et al., *Oxidative steam reforming of methane over Ni/Al2O3 modified with trace Pd.* Applied Catalysis A: General, 2008. **351**(2): p. 217-225.

51. García-Diéguez, M., et al., *Characterization of alumina-supported Pt, Ni and PtNi alloy catalysts for the dry reforming of methane.* Journal of Catalysis, 2010. **274**(1): p. 11-20.

52. Nowosielska, M., W. Jozwiak, and J. Rynkowski, *Physicochemical Characterization of Al2O3 Supported Ni-Rh; Supported Ni–Rh Systems and their Catalytic Performance in CH4/CO2 Reforming.* Catalysis Letters, 2009. **128**(1): p. 83-93.

53. Jones, G., et al., *First principles calculations and experimental insight into methane steam reforming over transition metal catalysts.* Journal of Catalysis, 2008. **259**(1): p. 147-160.

54. Matsumura, Y., *Steam reforming of methane over nickel catalysts at low reaction temperature.* Applied Catalysis A: General, 2004. **258**(1): p. 107-114.

55. Berrocal, G.P., et al., *Novel supports for nickel-based catalysts for the partial oxidation of methane.* Catalysis Today, 2010. **149**(3-4): p. 240-247.

56. Song, Y., et al., *Partial Oxidation of Methane to Syngas over Ni/Al2O3 Catalysts Prepared by a Modified Sol-gel Method.* Energy & Fuels, 2009. **23**(4): p. 1925-1930.

57. Christian Enger, B., R. Lødeng, and A. Holmen, *A review of catalytic partial oxidation of methane to synthesis gas with emphasis on reaction mechanisms over transition metal catalysts.* Applied Catalysis A: General, 2008. **346**(1-2): p. 1-27.

58. C.B. Murray, S.S., Hugh Doyle,and T. Betley, *Monodisperse Fe, Co, Ni.Nanoparticles and Their Assembly into Nanoparticle Superlattices.* MRS BULLETIN, 2001: p. 985-991.

59. Hou, Y., et al., *Size-controlled synthesis of nickel nanoparticles.* Applied Surface Science, 2005. **241**(1-2): p. 218-222.

60. Chen, D.-H. and S.-H. Wu, *Synthesis of Nickel Nanoparticles in Water-in-Oil Microemulsions.* Chemistry of Materials, 2000. **12**(5): p. 1354-1360.

61. Wu, S.-H. and D.-H. Chen, *Synthesis and characterization of nickel nanoparticles by hydrazine reduction in ethylene glycol.* Journal of Colloid and Interface Science, 2003. **259**(2): p. 282-286.

62. C.B. Murray, S.S., Hugh Doyle, and T. Betley *Monodisperse 3d Transition-Metal (Co, Ni, Fe) Nanoparticles and Their Assembly into Nanoparticle Superlattices.* MRS Bulletin, 2001: p. 985-991.

63. Carenco, S., et al., *Controlled Design of Size-Tunable Monodisperse Nickel Nanoparticles.* Chemistry of Materials, 2010. **22**(4): p. 1340-1349.

64. J. Park, E.K., *Monodisperse Nanoparticles of Ni and NiO: Synthesis, Characterization, Self-Assembled Superlattices, and Catalytic Applications in the Suzuki Coupling Reaction.* Advanced Materials, 2005. **17**(4): p. 429-434.

65. Winnischofer, H., et al., *Chemical Synthesis and Structural Characterization of Highly Disordered Ni Colloidal Nanoparticles.* ACS Nano, 2008. **2**(6): p. 1313-1319.

66. Sidhaye, D.S., *Preparation of Nearly Monodisperse Nickel Nanoparticles by a Facile Solution Based.* J. Phys. Chem. C, 2009.

67. Schimpf, S., C. Louis, and P. Claus, *Ni/SiO2 catalysts prepared with ethylenediamine nickel precursors: Influence of the pretreatment on the catalytic properties in glucose hydrogenation.* Applied Catalysis A: General, 2007. **318**: p. 45-53.

68. Pina, G., C. Louis, and M.A. Keane, *Nickel particle size effects in catalytic hydrogenation and hydrodechlorination: phenolic transformations over nickel/silica.* Physical Chemistry Chemical Physics, 2003. **5**(9): p. 1924-1931.

69. Paolo Burattin, M.C., and Catherine Louis, *Ni/SiO2 Materials Prepared by Deposition-Precipitation Influence of the Reduction Conditions and Mechanism of Formation of Metal Particles.* Journal of Physical Chemistry B, 2000. **104**(45): p. 10482-10489.

70. Paolo Burattin, M.C., and Catherine Louis, *Metal Particle Size in Ni/SiO2 Materials Prepared by Deposition−Precipitation: Influence of the Nature of the Ni(II) Phase and of Its Interaction with the Support.* Journal of Physical Chemistry B, 1999. **103**(30): p. 6171–6178.

71. Ping Lu, N.T., *Polymer-protected Ni Pd bimetallic nano-clusters Preparation, characterization and catalysis for hydrogenation of nitrobenzene.* J. Phys. Chem. B 1999. **103**: p. 9673-9682.

72. Alonso, F., et al., *Nickel nanoparticles in hydrogen-transfer reductions: Characterisation and nature of the catalyst.* Applied Catalysis A: General, 2010. **378**(1): p. 42-51.

73. Graf, C., et al., *A General Method To Coat Colloidal Particles with Silica.* Langmuir, 2003. **19**(17): p. 6693-6700.

74. Liz-Marzan, L.M., M. Giersig, and P. Mulvaney, *Synthesis of Nanosized Gold-silica Core-shell Particles.* Langmuir, 1996. **12**(18): p. 4329-4335.

75. Joo, S.H., et al., *Thermally stable Pt/mesoporous silica core-shell nanocatalysts for high-temperature reactions.* Nat Mater, 2009. **8**(2): p. 126-131.

76. Lu, Y., et al., *Synthesis and Self-Assembly of Au@SiO2 Core-shell Colloids.* Nano Letters, 2002. **2**(7): p. 785-788.

77. Gorelikov, I. and N. Matsuura, *Single-Step Coating of Mesoporous Silica on Cetyltrimethyl Ammonium Bromide-Capped Nanoparticles.* Nano Letters, 2007. **8**(1): p. 369-373.

78. Botella, P., A. Corma, and M.T. Navarro, *Single Gold Nanoparticles Encapsulated in Monodispersed Regular Spheres of Mesostructured Silica Produced by Pseudomorphic Transformation.* Chemistry of Materials, 2007. **19**(8): p. 1979-1983.

79. Nooney, R.I., et al., *Self-Assembly of Mesoporous Nanoscale Silica/Gold Composites.* Langmuir, 2003. **19**(18): p. 7628-7637.

80. Chou, K.-S. and C.-C. Chen, *Fabrication and characterization of silver core and porous silica shell nanocomposite particles.* Microporous and Mesoporous Materials, 2007. **98**(1-3): p. 208-213.

81. Takenaka, S., et al., *Synthesis of carbon nanotube-supported Pt nanoparticles covered with silica layers.* Carbon, 2008. **46**(2): p. 365-368.

82. Takenaka, S., et al., *Structures of Silica-Supported Co Catalysts Prepared Using Microemulsion and Their Catalytic Performance for the Formation of Carbon Nanotubes through the Decomposition of Methane and Ethylene.* The Journal of Physical Chemistry C, 2007. **111**(21): p. 7748-7756.

83. Teruoki Tago, T.H., Kanta Miyajima, Masahiro Kishida, Shizuka Tashiro, Katsuhiko Wakabayashi, *Novel Synthesis of Silica-Coated Ferrite Nanoparticles Prepared Using Water-in-Oil Microemulsion.* Journal of American Ceramic Society 2002. **85**(9): p. 2188-2194.

84. Matsune, H., et al., *Network structure consisting of chain-like arrays of gold nanoparticles and silica layer prepared using a nonionic reverse-micelle template.* Journal of Nanoparticle Research, 2006. **8**(6): p. 1083-1087.

85. Tago, T., et al., *Synthesis of silica-coated rhodium nanoparticles in reversed micellar solution.* Journal of Materials Science, 2002. **37**(5): p. 977-982.

86. Joongoo, L., P. Ji Chan, and S. Hyunjoon, *A Nanoreactor Framework of a Au@SiO2 Yolk/Shell Structure for Catalytic Reduction of p-Nitrophenol.* Advanced Materials, 2008. **20**(8): p. 1523-1528.

87. Kamata, K., Y. Lu, and Y. Xia, *Synthesis and Characterization of Monodispersed Core-Shell Spherical Colloids with Movable Cores.* Journal of the American Chemical Society, 2003. **125**(9): p. 2384-2385.

88. Kim, J.Y., S.B. Yoon, and J.-S. Yu, *Fabrication of nanocapsules with Au particles trapped inside carbon and silica nanoporous shells.* Chemical Communications, 2003(6): p. 790-791.

89. Chen, Y., et al., *Hollow/Rattle-Type Mesoporous Nanostructures by a Structural Difference-Based Selective Etching Strategy.* ACS Nano, 2009. **4**(1): p. 529-539.

90. Tierui, Z., et al., *Formation of Hollow Silica Colloids through a Spontaneous Dissolution-Regrowth Process.* Angewandte Chemie, 2008. **120**(31): p. 5890-5895.

91. Hah, H.J., et al., *New synthetic route for preparing rattle-type silica particles with metal cores.* Chemical Communications, 2004(8): p. 1012-1013.

92. Yin, Y., *Formation of Hollow Nanocrystals Through the Nanoscale Kirkendall Effect.* Science, 2004. **304**(5671): p. 711-714.

93. Kim, S., et al., *IR Spectroscopic Observation of Molecular Transport through Pt@CoO Yolk-shell Nanostructures.* Journal of the American Chemical Society, 2007. **129**(30): p. 9510-9513.

94. Djéga-Mariadassou, G. and M. Boudart, *Classical kinetics of catalytic reactions.* Journal of Catalysis, 2003. **216**(1-2): p. 89-97.

95. Langmuir, I., *The mechanism of the catalytic action of platinum in the reactions 2Co + O2= 2Co2 and 2H2+ O2= 2H2O.* Transactions of the Faraday Society, 1922. **17**: p. 621-654.

96. Berlowitz, P.J., C.H.F. Peden, and D.W. Goodman, *Kinetics of carbon monoxide oxidation on single-crystal palladium, platinum, and iridium.* The Journal of Physical Chemistry, 1988. **92**(18): p. 5213-5221.

97. Allian, A.D., et al., *Chemisorption of CO and Mechanism of CO Oxidation on Supported Platinum Nanoclusters.* Journal of the American Chemical Society, 2011. **133**(12): p. 4498-4517.

98. Eichler, A. and J. Hafner, *Reaction channels for the catalytic oxidation of CO on Pt(111).* Surface Science, 1999. **433-435**: p. 58-62.

99. Zhang, C.J. and P. Hu, *Why Must Oxygen Atoms Be Activated from Hollow Sites to Bridge Sites in Catalytic CO Oxidation?* Journal of the American Chemical Society, 2000. **122**(9): p. 2134-2135.

100. Hammer, B., *The NO+CO Reaction Catalyzed by Flat, Stepped, and Edged Pd Surfaces.* Journal of Catalysis, 2001. **199**(2): p. 171-176.

101. A. G. Bosch-Driebergen, M.N.H.K., A. Dreumel, R. M. Wolf, F. C. M. J. M. Delft and B. E. Nieuwenhuys, *CO oxidation over silica supported Pt-Rh alloy catalysts.* Catalysis Letters, 1989: p. 73-80.

102. Somorjai, G. and C. Kliewer, *Reaction selectivity in heterogeneous catalysis.* Reaction Kinetics and Catalysis Letters, 2009. **96**(2): p. 191-208.

103. Mondal, K.C., et al., *Carbon microsphere supported Pd catalysts for the hydrogenation of ethylene.* Catalysis Communications, 2008. **9**(4): p. 494-498.

104. Koh, H.-P. and R. Hughes, *Kinetics of ethylene hydrogenation over a supported nickel catalyst.* Journal of Catalysis, 1974. **33**(1): p. 7-16.

105. Duca, et al., *Computational studies on surface reaction mechanisms : ethylene hydrogenation on platinum catalysts.* 1999: p. 473.

106. Niemantsverdriet, R.A.v.S.a.J.W., *Chemical Kinetics and catalysis* 1995, Plenum Press: New York p. 56.

107. Pauls, A.C., E.W. Comings, and J.M. Smith, *Kinetics of the hydrogenation of ethylene: On a nickel catalyst.* AIChE Journal, 1959. **5**(4): p. 453-457.

108. P. Sabatier and J.B. Senderens, C.R.A.S.P., p. 514., 1902.

109. I. Chorkendorff, H.N., ed. *Concepts of Modern Catalysis and Kinetics*. 2007, Wiley.

110. A. Harms, B.H., E. Jørn and A. Skov, Oil and Gas Journal, 1980. **78**: p. 120.

111. Dry, M.E., *Present and future applications of the Fischer-Tropsch process.* Applied Catalysis A: General, 2004. **276**(1-2): p. 1-3.

112. Görke, O., P. Pfeifer, and K. Schubert, *Highly selective methanation by the use of a microchannel reactor.* Catalysis Today, 2005. **110**(1-2): p. 132-139.

113. Choudhury, M.B.I., et al., *Preferential methanation of CO in a syngas involving CO2 at lower temperature range.* Applied Catalysis A: General, 2006. **314**(1): p. 47-53.

114. Van Hardeveld, R. and F. Hartog, *The statistics of surface atoms and surface sites on metal crystals.* Surface Science, 1969. **15**(2): p. 189-230.

115. Thomas P. Beebe, D.W.G., Bruce D. Kay, and John T. Yates, *Kinetics of the activated dissociative adsorption of methane on the low index planes of nickel single crystal surfaces* Journal of Chemical Physics, 1987. **87**(4): p. 2305-2315.

116. Kelley, R.D. and D.W. Goodman, *Catalytic methanation over single crystal nickel and ruthenium: Reaction kinetics on different crystal planes and the correlation of surface carbide concentration with reaction rate.* Surface Science, 1982. **123**(2-3): p. L743-L749.

117. Abild-Pedersen, F., et al., *Methane activation on Ni(1 1 1): Effects of poisons and step defects.* Surface Science, 2005. **590**(2-3): p. 127-137.

118. Andersson, M., et al., *Structure sensitivity of the methanation reaction: H2-induced CO dissociation on nickel surfaces.* Journal of Catalysis, 2008. **255**(1): p. 6-19.

119. Rostrup-Nielsen, J.R., K. Pedersen, and J. Sehested, *High temperature methanationSintering and structure sensitivity.* Applied Catalysis A: General, 2007. **330**: p. 134-138.

120. R.Z.C. van Meertena, A.H.G.M.B., P.F.M.T. van Nisselrooija and J.W.E. Coenena, *Structure sensitivity and crystallite size change of nickel during methanation of CO H2 on nickel-silica catalysts.* Surface Science, 1983. **135**(1-3): p. 565-579.

121. Weng, W.-Z., et al., *Effects of calcination temperatures on the catalytic performance of Rh/Al2O3 for methane partial oxidation to synthesis gas.* Catalysis Today, 2006. **117**(1-3): p. 53-61.

122. Zhang, Y.H., et al., *Deactivation studies over NiO/gamma-Al2O3 catalysts for partial oxidation of methane to syngas.* Catalysis Today, 2000. **63**(2-4): p. 517-522.

123. Kirchhoff, M., U. Specht, and G. Veser, *Engineering high-temperature stable nanocomposite materials.* Nanotechnology, 2005. **16**(7): p. S401-S408.

124. Kobayashi, Y., et al., *Effect of NiO content in mesoporous NiO-Al2O3 catalysts for high pressure partial oxidation of methane to syngas.* Applied Catalysis A: General, 2011. **395**(1-2): p. 129-137.

125. Horiguchi, J., et al., *Mesoporous NiO-Al2O3 catalyst for high pressure partial oxidation of methane to syngas.* Applied Catalysis A: General, 2011. **392**(1-2): p. 86-92.

126. Qiu, Y., J. Chen, and J. Zhang, *Effect of Calcination Temperature on Properties of Eggshell Ni/MgO–Al2O3 Catalyst for Partial Oxidation of Methane to Syngas.* Catalysis Letters, 2009. **127**(3): p. 312-318.

127. Jiang, Z., et al., *Catalytic Partial Oxidation of Methane over Ni-Based Catalysts Derived from Ni-Mg/Al Ternary Hydrotalcites.* Energy & Fuels, 2009. **23**(3): p. 1634-1639.

128. Enger, B.C., R. Lødeng, and A. Holmen, *Modified cobalt catalysts in the partial oxidation of methane at moderate temperatures.* Journal of Catalysis, 2009. **262**(2): p. 188-198.

129. Slagtern, Å., et al., *Catalytic partial oxidation of methane over Ni-, Co- and Fe-based catalysts.* Catalysis Today, 1998. **46**(2-3): p. 107-115.

130. VANLOOIJ F, V.J., STOBBE ER, et al., *Mechanism of the partial oxidation of methane to synthesis gas on a silica-supported nickel catalyst.* CATALYSIS TODAY, 1994. **21**(2-3): p. 495-503.

131. Hu, Y.H. and E. Ruckenstein, *Catalyst Temperature Oscillations during Partial Oxidation of Methane.* Industrial & Engineering Chemistry Research, 1998. **37**(6): p. 2333-2335.

132. Takenaka, S., et al., *Specific performance of silica-coated Ni catalysts for the partial oxidation of methane to synthesis gas.* Journal of Catalysis, 2007. **245**(2): p. 392-400.

133. Mitri, A., et al., *Reverse-flow reactor operation and catalyst deactivation during high-temperature catalytic partial oxidation.* Chemical Engineering Science, 2004. **59**(22-23): p. 5527-5534.

134. Sehested, J., J. Gelten, and S. Helveg, *Sintering of nickel catalysts: Effects of time, atmosphere, temperature, nickel-carrier interactions, and dopants.* Applied Catalysis A: General, 2006. **309**(2): p. 237-246.

135. Au, C.T., Y.H. Hu, and H.L. Wan, *Pulse studies of CH4 interaction with NiO/Al2O3 catalysts.* Catalysis Letters, 1994. **27**(1): p. 199-206.

136. Diskin AM, C.R., Ormerod RMZ, *The oxidative chemistry of methane over supported nickel catalysts.* CATALYSIS TODAY, 1998. **46**(2-3): p. 147-154

137. Chu, W., W. Yang, and L. Lin, *The partial oxidation of methane to syngas over the nickel-modified hexaaluminate catalysts BaNiyAl12-yO19-[delta]*. Applied Catalysis A: General, 2002. **235**(1-2): p. 39-45.

138. Utaka, T., et al., *Partial oxidation of methane over Ni catalysts based on hexaaliminate- or perovskite-type oxides.* Applied Catalysis A: General, 2003. **247**(1): p. 125-131.

139. Lu, Y., Y. Liu, and S. Shen, *Design of stable Ni catalysts for partial oxidation of methane to synthesis gas.* Journal of Catalysis, 1998. **177**(2): p. 386-388.

140. Provendier, H., et al., *Stabilisation of active nickel catalysts in partial oxidation of methane to synthesis gas by iron addition.* Applied Catalysis A: General, 1999. **180**(1-2): p. 163-173.

141. Choi, J.-Y., et al., *A Chemical Route to Large-Scale Preparation of Spherical and Monodisperse Ni Powders.* Journal of the American Ceramic Society, 2005. **88**(11): p. 3020-3023.

142. Rasband, W. *ImageJ Software* *http://rsb.info.nih.gov/ij/*. 2011

143. Liu, T., C. Snyder, and G. Veser, *Catalytic Partial Oxidation of Methane:Is a Distinction between Direct and Indirect Pathways Meaningful?* Industrial & Engineering Chemistry Research, 2007. **46**(26): p. 9045-9052.

144. Jin, R., et al., *Mechanism for catalytic partial oxidation of methane to syngas over a Ni/Al2O3 catalyst.* Applied Catalysis A: General, 2000. **201**(1): p. 71-80.

145. Matsoukas, T. and E. Gulari, *Dynamics of growth of silica particles from ammonia-catalyzed hydrolysis of tetra-ethyl-orthosilicate.* Journal of Colloid and Interface Science, 1988. **124**(1): p. 252-261.

146. Chang, C.-L. and H.S. Fogler, *Controlled Formation of Silica Particles from Tetraethyl Orthosilicate in Nonionic Water-in-Oil Microemulsions.* Langmuir, 1997. **13**(13): p. 3295-3307.

147. Chang, C.-L.F., H. Scott Fogler *Kinetics of silica particle formation in nonionic W/O microemulsions from TEOS.* Materials, Interfaces, and Electrochemical Phenomena 1996. **42**(11): p. 3153-3163.

148. Capek, I., *Preparation of metal nanoparticles in water-in-oil (w/o) microemulsions.* Advances in Colloid and Interface Science, 2004. **110**(1-2): p. 49-74.

149. Jae-Young, C., et al., *A Chemical Route to Large-Scale Preparation of Spherical and Monodisperse Ni Powders.* Journal of the American Ceramic Society, 2005. **88**(11): p. 3020-3023.

150. Boudjahem, A.-G., et al., *Study of Support Effects on the Reduction of Ni2+ Ions in Aqueous Hydrazine.* Langmuir, 2003. **20**(1): p. 208-213.

151. Gustafsson, M., et al., *Novel Polynuclear Nickel(II) Complex: Hydrazine, Sulfato, and Hydroxo Bridging in an Unusual Metal Hexamer. Crystal Structure and Magnetic Properties of [Ni6(N2H4)6(SO4)4(OH)2(H2O)8](SO4)(H2O)10.* Inorganic Chemistry.

152. Park, J.W., et al., *Preparation of fine Ni powders from nickel hydrazine complex.* Materials Chemistry and Physics, 2006. **97**(2-3): p. 371-378.

153. Wu, X.-J. and D. Xu, *Formation of Yolk/SiO2 Shell Structures Using Surfactant Mixtures as Template.* Journal of the American Chemical Society, 2009. **131**(8): p. 2774-2775.

154. http://chemprof.tripod.com/redtable.htm.

155. Yan, Q., et al., *Synthesis and Assembly of Monodisperse High-Coercivity Silica-Capped FePt Nanomagnets of Tunable Size, Composition, and Thermal Stability from Microemulsions.* Advanced Materials, 2006. **18**(19): p. 2569-2573.

156. Lu, P., et al., *Polymer-Protected Ni/Pd Bimetallic Nano-Clusters: Preparation, Characterization and Catalysis for Hydrogenation of Nitrobenzene.* The Journal of Physical Chemistry B, 1999. **103**(44): p. 9673-9682.

157. Tezuka, S., et al., *Studies on Selective Adsorbents for Oxo-Anions, NO3- Adsorptive Properties of Ni-Fe Layered Double Hydroxide in Seawater.* Adsorption, 2005. **11**(0): p. 751-755.

158. J. van de Loosdrecht, A.M.v.d.K., A. J. van Dillen and J. W. Geus, *Metal–Support Interaction Titania-Supported and Silica-Supported Nickel Catalysts.* Journal of Catalysis, 1997. **170**(2): p. 217-226.

159. B. Mile, D.S., M.A. Zammitta, A. Lovell, M. Webbb, *TPR studies of the effects of preparation conditions on supported nickel catalysts.* Journal of Molecular Catalysis, 1990. **62**(2): p. 179-198

160. Jankovic, B., B. Adnadevic, and S. Mentus, *The kinetic study of temperature-programmed reduction of nickel oxide in hydrogen atmosphere.* Chemical Engineering Science, 2008. **63**(3): p. 567-575.

161. Ryoji Takahashi, S.Y., *nanosized nickel silica catalyst prepard by homogeneous precipitation in wet silica gel.* Journal of Nanoscience and Nanotechnology, 2001. **1**: p. 169-176.

162. Infantesmolina, A., *Nickel supported on porous silica as catalysts for the gas-phase hydrogenation of acetonitrile.* Journal of Catalysis, 2004. **225**(2): p. 479-488.

163. D.J. Lensveld, J.G.M., A.J. van Dillen and K.P. de Jong, *Synthesis and characterisation of MCM-41 supported nickel oxide catalysts.* Microporous and Mesoporous Materials, 2001: p. 401-407.

164. Takanabe, K., K. Nagaoka, and K.-i. Aika, *Improved resistance against coke deposition of titania supported cobalt and nickel bimetallic catalysts for carbon dioxide reforming of methane.* Catalysis Letters, 2005. **102**(3): p. 153-157.

165. Rynkowski, T.P.a.J., *Temperature-programmed reduction and temperature-programmed oxidation of nickel and copper-nickel catalysts with addition of palladium supported on alumina.* Reaction Kinetics and Catalysis Letters, 1984. **24** p. 187-191.

166. Bridier, B., N. López, and J. Pérez-Ramírez, *Partial hydrogenation of propyne over copper-based catalysts and comparison with nickel-based analogues.* Journal of Catalysis, 2010. **269**(1): p. 80-92.

167. Hinrichsen, O., T. Genger, and M. Muhler, *Chemisorption of N2O and H2 for the Surface Determination of Copper Catalysts.* Chemical Engineering & Technology, 2000. **23**(11): p. 956-959.

168. Zhang, J., H. Wang, and A.K. Dalai, *Effects of metal content on activity and stability of Ni-Co bimetallic catalysts for CO2 reforming of CH4.* Applied Catalysis A: General, 2008. **339**(2): p. 121-129.

169. Bartholomew, C.H. and R.B. Pannell, *The stoichiometry of hydrogen and carbon monoxide chemisorption on alumina- and silica-supported nickel.* Journal of Catalysis, 1980. **65**(2): p. 390-401.

170. Kim, H.W., K.M. Kang, and H.-Y. Kwak, *Preparation of supported Ni catalysts with a core/shell structure and their catalytic tests of partial oxidation of methane.* International Journal of Hydrogen Energy, 2009. **34**(8): p. 3351-3359.

171. Takehira, K., *Autothermal reforming of CH4 over supported Ni catalysts prepared from Mg–Al hydrotalcite-like anionic clay.* Journal of Catalysis, 2004. **221**(1): p. 43-54.

172. Liu, D., et al., *Carbon dioxide reforming of methane to synthesis gas over Ni-MCM-41 catalysts.* Applied Catalysis A: General, 2009. **358**(2): p. 110-118.

173. Bartholomew, C.H., *Sintering Kinetics of Supported Metals: Perspectives from a Generalized Power Law Approach* Studies in Surface Science and Catalysis, 1994. **88**: p. 1-18.

174. Patterson, A.L., *The Scherrer Formula for X-Ray Particle Size Determination.* Physical Review, 1939. **56**(10): p. 978.

175. Wanke, S.E., Flynn, Peter C. , *SINTERING OF SUPPORTED METAL CATALYSTS.* Catal Reviews, 1975. **12**: p. 93-135.

176. Liu, D., et al., *MCM-41 supported nickel-based bimetallic catalysts with superior stability during carbon dioxide reforming of methane: Effect of strong metal–support interaction.* Journal of Catalysis, 2009. **266**(2): p. 380-390.

177. Christensen, K., et al., *Effect of supports and Ni crystal size on carbon formation and sintering during steam methane reforming.* Applied Catalysis A: General, 2006. **314**(1): p. 9-22.

178. Borowiecki, T., *Nickel catalysts for steam reforming of hydrocarbons; size of crystallites and resistance to coking.* Applied Catalysis, 1982. **4**(3): p. 223-231.

179. Wang, R., et al., *Effect of metal-support interaction on the catalytic performance of Ni/Al2O3 for selective hydrogenation of isoprene.* Journal of Molecular Catalysis A: Chemical, 2011. **344**(1-2): p. 122-127.

180. Shang, R., et al., *Carbon dioxide reforming of methane to synthesis gas over Ni/Si3N4 catalysts.* International Journal of Hydrogen Energy, 2011. **36**(8): p. 4900-4907.

181. Zhang, L., et al., *Effect of preparation method on structural characteristics and propane steam reforming performance of Ni-Al2O3 catalysts.* Journal of Molecular Catalysis A: Chemical, 2009. **297**(1): p. 26-34.

182. Bharadwaj, S.S. and L.D. Schmidt, *Catalytic partial oxidation of natural gas to syngas.* Fuel Processing Technology, 1995. **42**(2-3): p. 109-127.

183. Pena, M.A., J.P. Gomez, and J.L.G. Fierro, *New catalytic routes for syngas and hydrogen production.* Applied Catalysis a-General, 1996. **144**(1-2): p. 7-57

184. Deluga, G.A., et al., *Renewable Hydrogen from Ethanol by Autothermal Reforming.* Science, 2004. **303**(5660): p. 993-997.

185. Liguras, D.K., K. Goundani, and X.E.X.E. Verykios, *Production of hydrogen for fuel cells by catalytic partial oxidation of ethanol over structured Ru catalysts.* International Journal of Hydrogen Energy, 2004. **29**(4): p. 419-427.

186. Friedle, U. and G. Veser, *A counter-current heat-exchange reactor for high temperature partial oxidation reactions: I. Experiments.* Chemical Engineering Science, 1999. **54**(10): p. 1325-1332.

187. York, A.P.E., T.C. Xiao, and M.L.H. Green, *Brief overview of the partial oxidation of methane to synthesis gas.* Topics in Catalysis, 2003. **22**(3-4): p. 345-358.

188. Michael, B.C., A. Donazzi, and L.D. Schmidt, *Effects of H2O and CO2 addition in catalytic partial oxidation of methane on Rh.* Journal of Catalysis, 2009. **265**(1): p. 117-129.

189. http://www.metalprices.com/.

190. Torniainen, P.M., X. Chu, and L.D. Schmidt, *Comparison of monolith-supported metals for the direct oxidation of methane to syngas.* Journal of Catalysis, 1994. **146**(1): p. 1-10.

191. Xiao, T.-c., et al., *Study on the mechanism of partial oxidation of methane to synthesis gas over molybdenum carbide catalyst.* Physical Chemistry Chemical Physics, 2002. **4**(18): p. 4549-4554.

192. Chen, D., et al., *Synthesis of carbon nanofibers: effects of Ni crystal size during methane decomposition.* Journal of Catalysis, 2005. **229**(1): p. 82-96.

193. Konovalova, N.D., et al., *Kinetics of the oxidation of CO on Ni/Al2O3 in excess oxygen.* Theoretical and Experimental Chemistry, 1994. **29**(4): p. 233-236.

194. D. Brennan, D.O.H., and B. M. W. Trapnell, *The Calorimetric Determination of the Heats of Adsorption of Oxygen on Evaporated Metal Films.* Proceedings of the Royal Society of London, 1960(256): p. 81-105.

195. A.K. Santra, D.W.G., *Catalytic oxidation of CO by platinum group metals: from ultrahigh vacuum to elevated pressures.* Electrochimica Acta, 2002(47): p. 3595-3609.

196. Hertl, W. and R.J. Farrauto, *Mechanism of carbon monoxide and hydrocarbon oxidation on copper chromite.* Journal of Catalysis, 1973. **29**(2): p. 352-360.

197. Dry, M.E. and F.S. Stone, *Oxidation reactions catalyzed by doped nickel oxide.* Discussions of the Faraday Society, 1959. **28**: p. 192-200.

198. Subbotin, A., B. Gudkov, and V. Yakerson, *Temperature hysteresis phenomena in heterogeneous catalysis.* Russian Chemical Bulletin, 2000. **49**(8): p. 1373-1379.

199. Gudkov, B., A. Subbotin, and V. Yakerson, *On the phenomena of temperature hysteresis in hydrogenation reactions over heterogeneous catalysts.* Reaction Kinetics and Catalysis Letters, 1999. **68**(1): p. 125-132.

200. Zhu, T. and M. Flytzani-Stephanopoulos, *Catalytic partial oxidation of methane to synthesis gas over Ni-CeO2.* Applied Catalysis A: General, 2001. **208**(1-2): p. 403-417.

201. Choudhary, V.R., A.M. Rajput, and V.H. Rane, *Low-temperature catalytic selective partial oxidation of methane to carbon monoxide and hydrogen over nickel/ytterbium sesquioxide.* The Journal of Physical Chemistry, 1992. **96**(22): p. 8686-8688.

202. Jun, J.H., et al., *Nickel-calcium phosphate/hydroxyapatite catalysts for partial oxidation of methane to syngas: characterization and activation.* Journal of Catalysis, 2004. **221**(1): p. 178-190.

203. Dissanayake, D., et al., *Partial oxidation of methane to carbon monoxide and hydrogen over a Ni/Al2O3 catalyst.* Journal of Catalysis, 1991. **132**(1): p. 117-127.

204. Lu, Y., et al., *Mechanistic investigations on the partial oxidation of methane to synthesis gas over a nickel-on-alumina catalyst.* Applied Catalysis A: General, 1998. **174**(1-2): p. 121-128.

205. Maurice Rigby, E.B.S., William A. Wakeham, and Geoffrey C. Maitland, *The Forces between Molecules*. 1986: Oxford University Press.

206. Available from: http://www.nitk.ac.in/assets/files/MetMat/Dr.AS/XPS.pdf.

207. Kustov, A.L., et al., *CO methanation over supported bimetallic Ni-Fe catalysts: From computational studies towards catalyst optimization.* Applied Catalysis A: General, 2007. **320**: p. 98-104.

208. Ginsburg, J.M., et al., *Coke Formation over a Nickel Catalyst under Methane Dry Reforming Conditions: Thermodynamic and Kinetic Models.* Industrial & Engineering Chemistry Research, 2005. **44**(14): p. 4846-4854.

209. Guo, J., et al., *Dry reforming of methane over nickel catalysts supported on magnesium aluminate spinels.* Applied Catalysis A: General, 2004. **273**(1-2): p. 75-82.

210. Bernardo, C.A., I. Alstrup, and J.R. Rostrup-Nielsen, *Carbon deposition and methane steam reforming on silica-supported Ni---Cu catalysts.* Journal of Catalysis, 1985. **96**(2): p. 517-534.

211. Vincenzo Roberto Calderone, A.P.P., *Design of Colloidal Pt Catalysts Encapsulated by Silica Nano Membranes for Enhanced Stability in H2S Streams.* Catalysis Letters, 2010. **137**: p. 132-140.